Inverse Problems in Soft Tissue Elastography using Boundary Element Methods

Hans-Uwe Berger

A thesis presented for the degree of
Doctor of Philosophy
in
Mechanical Engineering
at the
University of Canterbury,
Christchurch, New Zealand.

9th March 2009

Abstract

Elastography is an emerging functional imaging technique of current clinical research interest due to a direct relation between mechanical material parameters, especially the tissue stiffness, and tissue pathologies such as cancer. Digital Image Elasto-Tomography (DIET) is a new method that aims to develop elastographic techniques and create a simplified, improved breast cancer screening process. The elastic material information of breast tissue is reconstructed in the DIET concept from mechanically excited steady-state harmonic motion observed on the surface of the breast. While this inversion process has been traditionally approached using finite element methods, this surface-orientated problem is naturally suited to the use of Boundary Element Methods (BEMs) requiring the discretization only on the surface of the domain and on the interface of a potential inclusion. As only approximate information is available about breast tissue material parameters, this thesis presents the development of BEM based inverse problem algorithms suitable for the reconstruction of all material parameters in a proportionally damped isotropic linear elastic solid, where only the material density is known. The highly nonlinear identification process of a potential inclusion is treated through the combination of a systematic Grid-Search with gradient descent techniques. This algorithm is extended to a three-step algorithm that performs a background material parameter estimation before the subsequent identification of an inclusion and thus provides a confident indication for the differentiation between cancerous and healthy breast tissue. The development of these algorithms is illustrated by several simulation studies highlighting important reconstruction behaviors relevant to the elastographic inverse problem. A first experimental test on a silicon based breast phantom is presented.

Acknowledgements

This section expresses my appreciation to a number of people associated with this research through all forms of technical, emotional or any other kind of support, without which this thesis would have likely been much more of a long lasting and torturing experience.

I would like to extend my sincere gratitude to both my supervisors, Prof. Geoff Chase and Dr. Eli Van Houten, for providing me with the required guidance throughout the completion of this work. I appreciate having had advice in both experienced guidance and overview as well as in detailed technical matters. Thanks also for hours of proofreading and resulting suggestions to my *germenglish* writing style.

Significant thanks is also due to two individuals, Prof. P.K. Banerjee and G. Dargush from the State University of New York at Buffalo, allowing me to spent a number of months under their guidance. The difficult implementation of the BEM has been successfully achieved due to their valuable advice, practical experience and not at last the willingness to spend a number of hours with me to help debugging my computer code. Despite the cold winter months, this stay has been an extremely enjoyable and professionally stimulating time for me.

The DIET system development team consists of a number of people whose significant contributions to the system as a whole need to be acknowledged. In particular, people that I was able to directly work with include Ashton Peters, Richard Brown, Chris Hann and Bob Broughton. However, further contributions have been made over the years by lab staff and a number of students, to a large part being on exchange from their overseas universities.

On a personal side, I have received the continuing backing and encouragement from my family throughout the duration of this work, in particular from my wonderful partner, Sarah, and my parents, Heinz and Ursula. For this indispensable support and your loving partnership I am especially grateful.

Last but not least I want to thank a number of very important friends, Joost, Anja, Nicolas & Naomi, Ben & Danielle, Christoph, Raghu: Your close friendship has made my life very enjoyable over this time period through all activities we shared between bbq's and pizza, home-handyman projects and strenuous tramping and mountaineering trips.

Contents

List of Figures

List of Tables

Nomenclature

In this thesis, in general, lower and upper case letters in normal font denote a scalar quantity, bold lower case letters denote a vector quantity and bold capital letters denote a matrix quantity. Subscripts i, j, k or other refer to a specific entry in a vector or a matrix, or are used to denote tensor quantities. If superscripts $(.)^I$ or $(.)^{II}$ are used, they refer to region-specific parameters (i.e. the background and inclusion specific parameters) in the region-based formulation of the BEM.

Acronyms

BEM	Boundary Element Method
BIE	Boundary Integral Equation
CG	Conjugate Gradient Method
DIET	Digital Image Elasto-Tomography
DOS	Diffuse Optical Spectroscopy
DOT	Diffuse Optical Tomography
EIT	Electrical Impedance Tomography
FDM	Finite Difference Method
FEM	Finite Element Method
IE	Integral Equation
MPI	Message Passing Interface
MRI	Magnetic Resonance Imaging
MRE	Magnetic Resonance Elastography
PDE	Partial Differential Equation
US	Ultrasound
USCT	Ultrasound Computer Tomography
USE	Ultrasound Elastography

Roman Symbols

$\mathbf{A}$	System matrix of a linear system of equations
$\|A\|$	Pseudo-amplitude of frequency response
a_i	Ellipse semi-axis parameters in cartesian space
$\tilde{\mathbf{b}}$	Right hand side vector of a linear system of equations
b_i	Body force components
c_{ij}	Geometric boundary constant
c_s	Shear (or secondary) wave speed
c_p	Longitudinal pressure (or primary) wave speed
D_{ij}	Block-diagonal terms if $\mathbf{F}$-matrix
$\mathcal{D}$	Diagonal scaling matrix
$\mathbf{d}$	Distance vector
E	Young's Modulus of elasticity (complex)
$E_{\mathcal{R}}$	Real part of Young's Modulus
$E_{\mathcal{I}}$	Imaginary part of Young's Modulus
E_{ijkl}	Elasticity tensor
$\mathbf{e}$	Displacement error
$\mathbf{F}$	Matrix of integrated traction solution
F_{ij}	Fundamental Kelvin solution for tractions
f	Actuation frequency
$\mathbf{G}$	Matrix of integrated displacement solution
G_{ij}	Fundamental Kelvin solution for displacements
$\boldsymbol{\nabla}_\theta \Psi$	Gradient of the objective function, Ψ, with respect to $\boldsymbol{\theta}$
g_i	Inequality constraint function
$\boldsymbol{\mathcal{H}}$	Approximate Hessian matrix to the objective functionΨ
h	Step size in the calculation of a finite difference Jacobian
h_i	Equality constraint function
$\boldsymbol{\mathcal{J}}_F$	Inverse problem Jacobian matrix to function F, taken with respect to the reconstruction variables, $\boldsymbol{\theta}$
$\|J(\boldsymbol{\eta})\|$	Jacobian determinant of the coordinate transformation from cartesian to intrinsic coordinate space
N_m	Number of measurements
N_θ	Number of reconstruction variables
$\mathbf{n}$	Surface normal vector
n_i	Surface normal vector components
P	Location of the center of an inclusion

$\mathbf{p}^{(k)}$	Vector of descent- or search direction in the k^{th} iteration
$\underline{\mathbf{q}}^{\star}$	Surface point, reconstructed from a measured motion path
$\underline{\tilde{\mathbf{q}}}^{\star}$	Correlated surface point on a mesh obtained by nonlinear reconstruction from $\underline{\mathbf{q}}^{\star}$
R	Radial size of an inclusion
S	Surface
T	Time period of a harmonic oscillation
$\mathbf{t}$	Traction vector
t_i	Surface traction component
$\mathbf{u}$	Complex displacement vector
$\mathbf{u}^{\star}$	Nodal reference displacements from measurement or simulation
$\hat{\mathbf{u}}$	Complex valued displacement amplitudes
u_i	Displacement components
$\underline{\hat{\boldsymbol{u}}}^{\star}$	Displacement amplitudes reconstructed from measured motion path (complex)
V	Volume
$\mathbf{x}$	Cartesian coordinate space
$\tilde{\mathbf{x}}$	Vector of unknown quantities
x_i	Cartesian coordinate components
$\tilde{\mathbf{y}}$	Vector of known quantities
$\mathbf{z}_{\mathbf{q}}(t)$	Motion path of the point $\mathbf{q}$
$\mathbf{z}^{\star}_{\mathbf{q}}(t_j)$	Measured position of point $\mathbf{q}$ at time t_j with respect to global coordinate system

Greek Symbols

α	Inertial damping parameter
β	Viscous damping parameter
Γ	Wavelength
γ	Tikhonov regularization parameter
$\Delta(\mathbf{x}, \boldsymbol{\xi})$	Dirac delta, (unit) impulse, applied at point $\boldsymbol{\xi}$ in direction $\mathbf{x}$
δ_{ij}	Kronecker delta symbol
ζ	Proportional damping ratio
$\epsilon^{(j)}$	Stopping threshold for gradient descent iteration
ϵ_{rel}	Relative error in a reconstruction solution
ε_{ij}	Lagrangian strain tensor

ζ	Damping ratio
$\boldsymbol{\eta}$	Localized (intrinsic) coordinate space
η_i	Gauss points on a normalized intrinsic coordinate interval
$\boldsymbol{\theta}$	Generalized vector of relevant (material and geometric) reconstruction variables
$\boldsymbol{\theta}^\star$	Vector of relevant reference or solution parameters
$\tilde{\boldsymbol{\theta}}$	Vector of relevant solution parameters obtained by converged reconstruction
ϑ	Rotation of an elliptical inclusion in space
λ	First Lamé's constant
μ	Shear modulus, second Lamé's constant
ν	Poisson ratio
$\boldsymbol{\xi}$	Source point of unit impulse
ρ	Density (complex)
$\rho_{\mathcal{R}}$	Real part of density
$\rho_{\mathcal{I}}$	Imaginary part of density
ϱ	Step size parameter in Gauss-Newton algorithm
σ_{ij}	Cauchy stress tensor
τ	Generalized time, time step
$\phi_k(\boldsymbol{\eta})$	k^{th} quadratic basis function in intrinsic coordinates
$\boldsymbol{\varphi}$	Phase angle in a damped time-harmonic motion
$\underline{\boldsymbol{\varphi}^\star}$	Phase angle reconstructed from measured motion path
Ψ	Displacement error functional
Ω	Rotational actuation frequency

Chapter 1

Introduction

In the relatively new field of biomedical engineering, soft tissue elastography is an emerging technique targeted at the imaging of bio-mechanical elastic tissue properties. The technique is intended to contribute significantly to earlier cancer diagnosis and by implication improved cancer survival rates.

Worldwide, cancer is a serious public health concern, causing about 13% of the total number of deaths. In western societies, the rates of cancer cases per year exceed 4% of the total population, with more than 2.8 million new cases in Europe in 2006 and more than 1.4 million new cases in the Unites States predicted for 2008 [1, 2].

Cancer in general is a tissue disease that is caused by abnormal growth behavior of cells, meaning in particular uncontrolled cell multiplication and prolonged cell life spans. This process is often initiated by genetic defects in the cell caused by carcinogenic products. In the early stages, this cell growth is, for most cancer types, a localized process, forming hard tumors. However, as the disease progresses tumors can metastasize, which refers to the process of cancer cells breaking away from the original tumor and distributing throughout the whole body via the blood or lymph system [3].

1.1 Breast Cancer

Due to there being well over 100 different types, cancer is usually classified by the part of the body that is affected by the primary tumor. While lung cancer remains the type of cancer with the highest mortality rate, breast cancer was estimated in Europe in 2006 to be the most common form of cancer. Breast cancer makes up a total of 13.5% of all cancer cases and, is a concern for approximately 10% of the total female population in the western world [1, 2].

The female breast consists of a number of different tissues. Glandular tissues, consisting mainly of lobular and ductal tissue that are responsible for milk production and storage, are surrounded by a layer of subcutaneous fat [4]. A cross section of the female breast illustrates the basic breast anatomy, and is shown in Figure 1.1 [5].

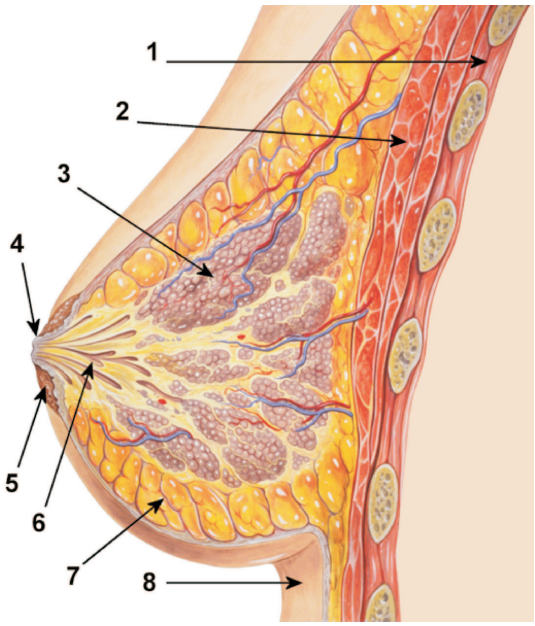

Legend:
1 - Chest wall/rib cage
2 - Pectoralis muscle
3 - Lobules
4 - Nipple
5 - Areola
6 - Lactiferous ducts
7 - Fatty tissue
8 - Skin

Figure 1.1 Basic breast anatomy

Most breast cancers are believed to originate in the lobular and ductal tissue, and are classified according to their initial tissue type, *ductal* and *lobular carcinoma* [6].

Once detected, a combination of diagnostic tools, mammography, sonography and tissue punch biopsy are employed to create a complete diagnosis and classification of the tumor. This diagnosis is used to determine an appropriate treatment plan. The so called TNM system is the widely accepted standard for the classification of malignant breast cancers and provides detailed information on the cancer's characteristics. This information is parameterized: T indicates the size of the primary tumor, N is a measure of its invasiveness and the degree of spread to regional lymph nodes, and M is an indication for the presence of metastasis. Additional parameters are available, but not compulsory. Using the TNM system, the tumor is further ranked 0 – IV in a more general and easier to understand staging system [7]. This system is illustrated in Table 1.1 and relates to the size and location of the tumor and thus level of disease progression.

Stage	Description
0	Indicates the existence of a small tumor *in situ*, that is localized and has not yet affected its surrounding tissue
I	Carcinoma, larger than stage 0, but less than 2 cm in diameter. The neighboring tissue may be affected, but not yet the lymph nodes
II & III	Locally advanced cancer that has spread past the originating region to the surrounding breast tissue, and has affected the regional lymph nodes. The degree to which the lymph system is affected differentiates between stage II and III
IV	Indicates severely advanced cancer with metastasis spread to other organs of the body

Table 1.1 Staging system for the classification of breast tumors

The treatment of breast cancer depends to a large degree on the stage classification and the history of cancer cases in the patient and the patient's family. At low stages, 0, I or II, carcinoma may be removed by surgery. This operation is called lumpectomy, referring to the local characteristics of the tumor, and is usually accompanied with treatments of radiotherapy and/or chemotherapy. The chances of survival from cancers at this stage are very high with a five year survival rate of over 95% [8]. Higher stage breast cancers usually require a complete mastectomy, meaning the removal of the entire breast, in addition to an intense treatment plan of radio-, hormone- and chemotherapy. There are cases where even the second breast is removed as a precautionary measure, when there exists a distinct cancer history in the patient's family. If a cancer has reached the stage of metastasis (stage IV), survival odds are greatly decreased with a five year survival rate of only 20% [9]. Cases where the disease has metastasized and spread to other vital organs are likely to be terminal.

1.2 Breast Cancer Screening Technology

A number of carcinogenic products and behaviors have been identified as increasing the risk of breast cancer. Lifestyle factors that have been found to decrease the risk of breast cancer include regular exercise, healthy diet and avoidance of alcohol consumption [10]. However, such factors only minimize the cancer risk and cannot guarantee to exclude a potential occurrence.

When cancer does occur, survival rates are heavily dependent on the stage of the cancer at the time of detection. It is thus a basic rule that the earlier a tumor is detected the more effective the countermeasures taken, and hence, the better the survival rate. Therefore, there is obviously great interest in detecting cancer as early as possible [6].

With regard to early breast cancer detection, women of all ages are recommended to be aware of any change happening to the outer appearance of the breast at all times. In particular, changes in color or shape, or the appearance of small lumps in the breast and under the armpits are indications for a potentially cancerous tumor. It is recommended that women aged 35 years and older should examine the breast by manual palpation techniques for the potential presence of lumps monthly [11]. Although up to 70% of breast cancer cases are detected by self-palpation, the method's effectiveness is often questioned [12, 13], as tumors often become palpable only once they have reached a distinct size.

To improve the ability of early breast cancer recognition, particularly at its earliest stages where the tumor is significantly small and survival rates are highest, a number of large scale screening methods have been developed. The performance criteria for such screening methods are specificity and sensitivity. Sensitivity is a measure of the rate of correct identifications of females with breast cancer, and specificity means the rate of correct identifications of females without breast cancer. Hence, a low sensitivity indicates a large number of false negatives, and thus undetected progress of the disease. In contrast, low specificity indicates a large number of false positives, creating unnecessary anxiety and further testing for the patient. Therefore, a quality screening method must demonstrate both high sensitivity and specificity before considering factors related to invasiveness, cost, comfort and availability.

1.2.1 Mammography

Mammography has become a widely established breast cancer screening technique. In many western countries, organized programs offer regular (annually or up to five year intervals) screening of women, particularly to those in the highest risk groups, aged 50 – 69 years [14]. In essence, mammography is a low-powered x-ray technique. A mammogram is a 2D projection of an x-ray through the human breast, and is captured while the breast is compressed in the mammography device. This process is performed once in the horizontal, and once in the vertical direction, to avoid missing blind angles. Despite breast compression being un-

comfortable or even painful for the patient, it is an important factor with regard to the quality of the resulting images [15,16]. The mammograms are then visually interpreted by a radiologist, who decides if follow-up examinations are required.

Traditional film based mammography is currently being replaced by more advanced digital mammography [17,18]. Digital mammography offers particular advantages with respect to immediate display, storage, and image enhancements through specialized image processing of the acquired mammograms. Figure 1.2 shows two mammograms of the same healthy breast, captured using digital mammography on the left, and traditional film based mammography on the right [19]. The differences in clarity due to image enhancement are evident.

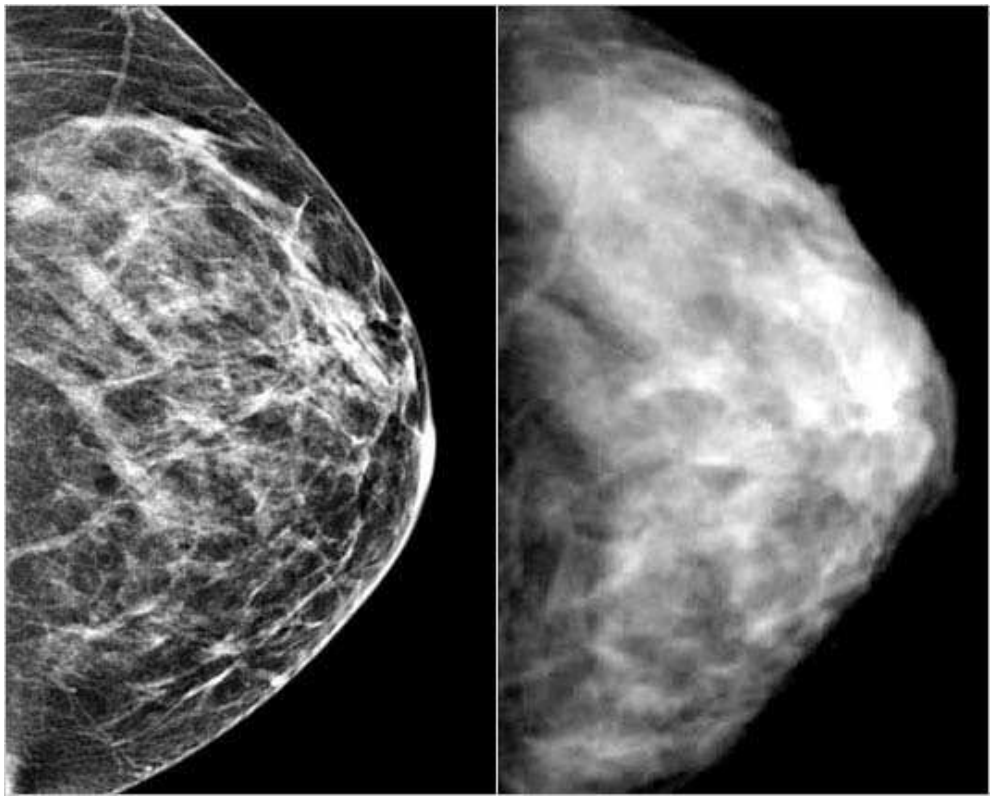

Figure 1.2 Mammogram of a healthy breast acquired by digital mammography (left) and by traditional, film based mammography (right)

A history of controversy on mammographic screening exists in the literature. On one side of this debate the usefulness of the method in the prevention of breast cancer deaths is questioned. In particular, it is argued that mammography is an invasive screening technique, as the patient is subjected to small amounts of radiation, which in itself increases risk. In addition, mammography is not recommended for young women, where breast tissue is predominantly glandular

tissue [20]. The reliability of interpretation of mammograms also remains an issue, despite the improved picture quality of digital mammography [10]. More specifically, the interpretation of mammograms is a difficult process and even skilled and experienced radiologists are subject to human error [21]. Fatigue or lack of attention also appears to contribute to the number of false negative results [22,23]. Finally, on follow-up assessments of large scale screening programs, some authors found no reliable evidence that screening for breast cancer reduces the mortality rate [24, 25]. However, on the other side of this debate it still appears that most articles in the literature support positive findings and earlier cancer detection due to mammographic screening, and highlight a resulting (up to) 25% decrease in mortality rate [14, 26].

1.2.2 Alternative Breast Screening Methods

Besides mammography, there are a number of suitable imaging technologies for breast cancer screening. None of them are as established as mammography, but they still show potential for population screening applications. At a minimum, these methods are complimentary applications to mammographic screening, as they utilize and examine different physical principles for the cancer detection problem [17].

The most promising of these procedures are introduced briefly in the following list. It is interesting to note that all of these methods are non-invasive. Some techniques, such as Ultrasonography or Magnetic Resonance Imaging, are already in long term use as routine diagnostic tools. Other techniques stem from totally different, non-medical backgrounds.

- **Ultrasound** (US) is a technique based on the capture of the echoes of high frequency sound waves transmitted into the body. Changes in tissue cause reflections from different distant boundaries, producing in a two dimensional image (sonogram) in real time. This technique is used widely in the monitoring of developing babies, as well as the detection of kidney stones and prostate, ovary and breast cancer. Particularly in the latter applications, US is used to determine the size and location of a tumor. US has also become a standard tool in the classification of the tumor's nature, specifically if it is malignant or benign. The primary drawback of US is the resolution of the images produced, which creates difficulties in their interpretation [27].

- **Ultrasound Computer Tomography** (USCT) is a recent imaging technique that uses a large number of transducers arranged in a cylindrical fashion around the complete breast. USCT is capable of producing 3D high resolution images with high image quality intended for early breast cancer diagnosis [28]. However, this technique is currently still at an early stage of its development.

- **Magnetic Resonance Imaging** (MRI) is well suited to imaging soft tissues, particularly when the tissue would be otherwise difficult to scan such as the brain, which is shielded by the skull bones. The body in question is placed in a powerful magnetic field that causes hydrogen nuclei in the tissue to align. Overlaying a second, pulsing, electromagnetic field perpendicular to the main field causes the hydrogen nuclei to oscillate, and emit a radio-frequency signal that can be measured. The result is a number of two-dimensional, *sliced* images of the tissue in high resolution. Contrast enhanced MRI was found to be capable of detecting very small breast cancer lesions [29, 30]. However, the key limitation is that MRI breast imaging comes with a low specificity [31], and potentially bringing with it a large number of unnecessary surgeries. Furthermore, the costs involved in a single scan are very high (recent estimates are 800.00 $US on average in the USA) The high cost of the equipment and resulting relative dearth of facilities would also inhibit the ability to screen large numbers. These factors make the method prohibitive for large scale population screening [32]. However, MRI has noted functional advantages and is rapidly becoming an important tool in the assessment and staging of cervical, ovary or prostate cancer [33].

- **Thermography**, or thermal imaging, is a technique that makes use of the heat radiating properties of the skin. The emissions can be measured using heat sensors operated at infrared frequencies. It is well known that tumors cause a higher than normal metabolism and increased blood flow in the affected region, resulting in locally higher surface temperatures of the skin. Hence, the diagnostic potential for cancer screening using breast thermography [34]. However, despite significant improvements in the technique since its development in the 1950s, a significant disadvantage of the method remains its low sensitivity in the case of small tumors or tumors that are located deep within the breast tissue. At this stage, thermography is suggested as a method that is complementary to mammography [35–37].

- **Electrical Impedance Tomography** (EIT) is based on the electrical properties of tissues, where considerable differences exist between the electrical conductivity or impedance of normal and pathological tissue [38]. In principle, EIT uses a pair of electrodes placed on the skin to apply a small current, while the resulting voltages are measured. The solution of the inverse problem of the governing Laplace equation allows the construction of images showing the distribution of electrical impedance throughout the tissue. Therefore, the technique has potential for a variety of medical applications, and is promising for the detection of breast cancer [39,40]. Current drawbacks of the method are its low spatial resolution, and particularly in medical applications, a large variability of images between subjects [41]. Due to its ill-posed, inverse problem and its similar solution strategy, EIT is closely related to Elastography (introduced in Section 1.3).

- **Positron Emission Tomography** (PET) produces images of biochemical and functional processes within the body that are visualized by measurements of the emissions of a weakly radioactive substance administered to the patients bloodstream. In modern machines PET is performed using a CT x-ray scanner. While applications of PET are found in the areas of neurology, cardiology, atherosclerosis and vascular disease, this technique is frequently used in the imaging of tumors and metastasis. PET is rated non-invasive despite the exposure of the patient to radioactive substance, but is, however, recommended to be performed only retentively. Hence, it may not necessarily be suitable for use as a breast cancer screening tool on a regular basis.

- Optical Imaging methods, in particular **Diffuse Optical Tomography** (DOT) and **Diffuse Optical Spectroscopy** (DOS), exist in the breast imaging field, where they are also called Optical Mammography. These methods take advantage of the diffusive nature of light propagation through tissue. A variety of optical approaches use near-infrared light or laser to illuminate the breast, while observing the resulting trans-illuminations or reflection patterns. Spatial information is gathered, as high optical contrast is observed in blood-rich areas of the breast, such as tumors [42]. Furthermore, spectral information, including changes in wavelength and scattering effects, provide measures associated with oxygenation, water and hemoglobin concentration. These can directly be used for diagnostic purposes [43]. Contrast agents that accumulate in cancerous tissue can be used

for image enhancement, particularly in the detection of small lesions [44]. Disadvantages of this approach include low spatial resolution of the images obtained and a limited depth to which light can penetrate the tissue [45,46].

1.3 The Concept of Elastography

The presence of a stiffness contrast between healthy and cancerous tissue has been recognized for a long time. However, the quantitative knowledge of the elastic material parameters of soft tissues have been studied only recently, where elastic property values of different soft tissues from the breast, liver, prostate and others, have been evaluated in a variety of experimental tests [47–49]. For healthy breast tissue, absolute values for Young's Modulus were reported between 2–12 kPa for fatty tissue, 20–66 kPa for glandular tissue, and 96–244 kPa for fibrous breast tissue. Results also showed that values for an isotropic Young's Modulus, E, depend to a large degree on the testing modality employed. Nonlinear material behavior was also found to occur as a function of actuation frequency and compression history of the test samples [50, 51].

Despite large differences in the stiffness values obtained with different mechanical testing modalities, all tests commonly confirmed a significant contrast comparing healthy and cancerous tissues. Stiffness values for cancerous tissues were observed to be between 5–12 times greater in stiffness [52,53]. Thus, a range of 5–10 times is an accepted stiffness contrast.

The clinical use of this characteristic has been limited to the detection of near-surface cancers by palpation methods. Therefore, research efforts in recent years aim to make better use of this property by means of both quantitative and qualitative assessment of the elastic properties or property distribution of soft tissues. This novel technology is called *Elastography* after early development by Ophir *et al.* [54].

Today, a variety of elastographic methods have emerged. However, all these methods are based on a similar principle. Specifically, the tissue in question is actuated mechanically, while the resulting displacements or strains are measured. These measurements are subsequently converted to elastic property information usually via some form of inverse problem solution or approximation. Comparative studies have commonly found significant improvements of elastographic methods over traditional screening or diagnostic tools. [31, 55, 56]. The most common

differentiation of elastographic methods is made with respect to the modality used for imaging the displacement response due to mechanical tissue actuation.

1.3.1 Ultrasound Elastography

Ultrasound Elastography (USE) is the earliest and, by today, the most advanced elastographic technique. Classic ultrasound techniques are used as the imaging tool measuring the displacement response. Ophir *et al.* correlated images that were measured before and after a static or quasi-static mechanical compression to obtain an image of strain. Assuming constant stress throughout the image, a description of the elastic material parameter could easily be obtained using basic laws of linear elasticity [54, 57, 58].

Similarly, Lerner *et al.* used doppler based methods to obtain strain images of harmonically excited tissue [59, 60]. This technique is known as Sonographic Imaging. While those early techniques suffered from both low contrast and spatial resolution, they clearly showed significant potential for use in prostate, liver and particularly breast cancer detection in a clinical study [61].

By today, strain-based USE techniques have experienced significant progress with advancements to three-dimensional, freehand elastography being performed in real time. Progress has also been made in the resolution issue by the use of drop-out corrections and frame filtering techniques. However, robustness and spatial resolution remain problems [62–66].

Figure 1.3 shows the sonogram and corresponding elastogram in (a) the case of a benign and (b) for a malignant breast tumor in vivo [67]. In both cases, the tumors are clearly identified. Additionally, relative size comparison between the tumors visible in a sonogram and a elastogram may provide grounds for the differentiation between benign and malignant cases.

Besides strain-based USE, model-based approaches have been made to improve on the assumption of uniform stress. This approach introduces the requirement to solve the resulting ill-posed inverse problem that has been shown to have several exact solutions and is therefore non-unique. However, this undesirable quality can be circumvented through selection of robust inverse algorithms [68–70]. A study comparing the quality of both strain and model based USE is provided in detail by Doyley *et al.* [71].

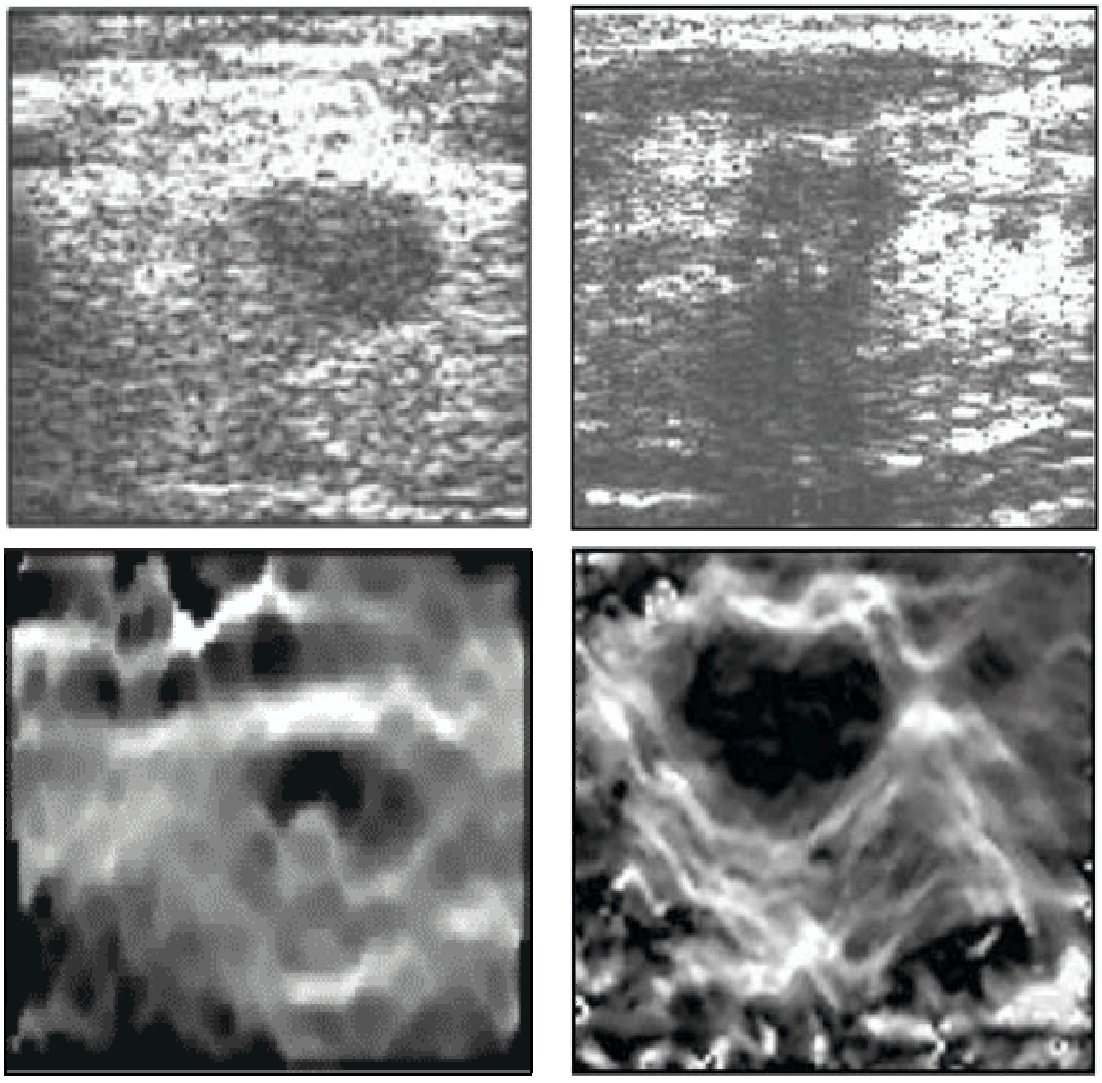

(a) (b)

Figure 1.3 Two sonograms of the breast (top) and their corresponding elastograms (bottom) showing (a) a benign tumor and (b) a malignant tumor in vivo (invasive ductal carcinoma)

1.3.2 Magnetic Resonance Elastography

Magnetic Resonance Elastography (MRE) is an approach to elastography that uses MRI for the measurement of tissue displacements from mechanical actuation. Thereby, the full 3D displacement field is obtained from the typical 2D MR-measurements in a *slicewise* fashion. It delivers accurate, high resolution displacement images for an elastographic inverse problem.

While initial approaches to MRE used similar strain-based techniques as are employed in USE in quasi-static and harmonic tissue actuation [50, 72], this exceptionally large, data-rich problem has led to the development of special optimization algorithms. Van Houten *et al.* developed a reconstruction scheme

that solves the elastic inverse problem on small, overlapping subzones of the full three-dimensional volume [73–75]. This algorithm has been shown to successfully detect lesions up to 4–5 mm in diameter. Other quality results could also be achieved by filtering compression waves out of the MR data and thus reducing the problem size, as was successfully demonstrated by Sinkus *et al.* and Manduca *et al.* [76–79].

Figure 1.4 shows examples of elastograms obtained with MR techniques. Figure 1.4 (a) illustrates the three-dimensional character of elastograms determined from full volume MRI and is shown in a slicewise fashion. Figure 1.4 (b) shows the detail of one cross-sectional (*slice*) of a breast, where a highlighted area of increased shear stiffness, μ, clearly corresponds to the location of an invasive tumor.

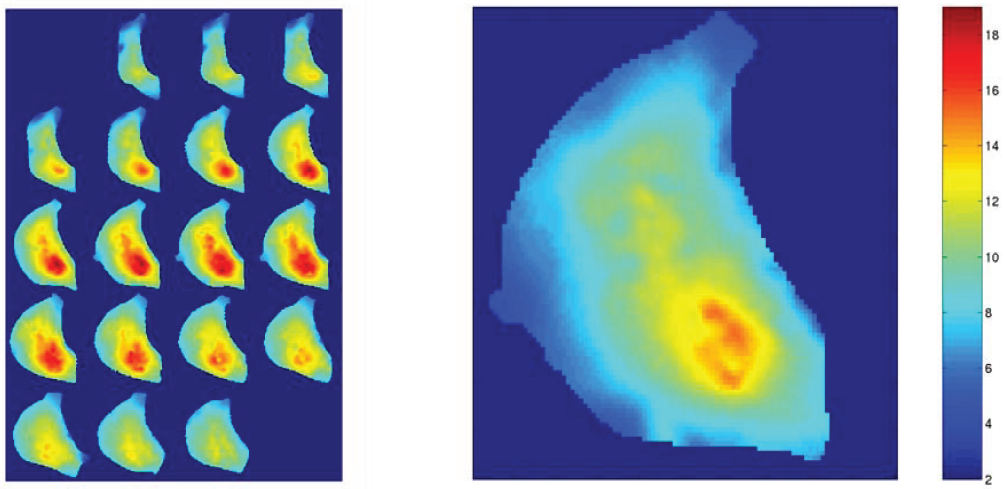

(a) (b)

Figure 1.4 Elastograms for shear stiffness (μ $[kPa]$) obtained with MR Elastography techniques — (a) shows the three-dimensional character of MR images and (b) shows a single slice, where an area of high shear stiffness clearly indicates the presence of an invasive tumor.

1.3.3 Current Research in Elastography

Despite the apparent clinical advantages of the resulting images, elastography is still considered a novelty that has not yet fully matured. Hence, it is not yet implemented as a regular screening tool in any diagnostic facility. However, research continues towards the advancement of these techniques in key problem areas.

Most model based elastography techniques require intensive computing time caused by the difficult, nonlinear reconstruction process. As a result, these reconstructions often require computationally expensive stochastic optimization techniques. This computational time requirement alone represents a hurdle that needs to be overcome for the practical use of such methods in clinical applications.

Where USE is promoted as a reasonably advanced method, the specific techniques are currently being tuned for the specific diagnostic applications, such as prostate, liver or breast cancer. Further improvements to spatial resolution and robustness of the technique are also the subject of current research [80–84].

In MRE, research currently focuses on better model representation such as the incorporation of porous media models or the better characterization of attenuation behavior of soft tissues [85, 86]. Improvement of the time intensive image acquisition process is also desired [87] in addition to improving the MR compatible actuation systems [88].

1.4 Digital Image Elasto-Tomography

Digital Image Elasto-Tomography (DIET) is a recent, alternate elastographic method aimed at the development of a portable, low-cost breast cancer screening system that avoids the discomforts and X-ray invasiveness of mammographic scans. A DIET breast cancer test is achieved by mechanical actuation of the breast, while only surface motion is measured using calibrated digital cameras. Based only on this surface motion data, a model based inversion process is employed to obtain an elastographic image of the full three-dimensional volume that can be used for diagnostic interpretation. The development of the complete system can therefore be divided into two major areas, motion capture and elasticity reconstruction. This process is illustrated in Figure 1.5.

The current system assumes the patient is lying horizontally (face down) with the the breast exposed to appropriate lighting and an array of digital cameras capable of taking images of the complete free surface area. A mechanical actuator, placed in contact with a fraction of the breast surface, allows sinusoidal actuation at a specific amplitude and frequency. After brief transient motion has died out, the digital cameras are used to take images at several points in time over a complete motion period, T. Images are taken in time-steps, $T + \Delta t$, where $\Delta t = T/N_p$ and N_p is the number of samples taken by using a strobe light to *freeze* the steady state response at those points. This approach enables the use

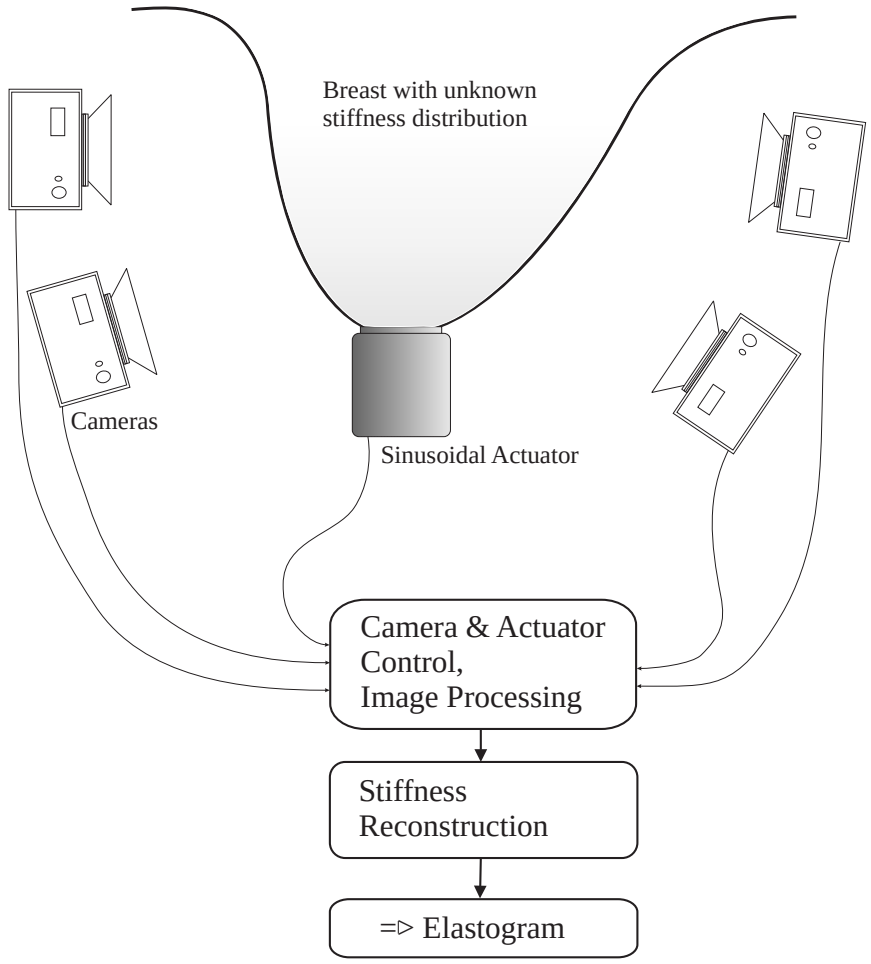

Figure 1.5 Concept of the DIET system: image capture to elastogram

of digital cameras without high speed capabilities and extends the image capture time only sightly.

The cameras, previously calibrated in their position and orientation with respect to a global coordinate system by use of a three-dimensional reference object, produce only two-dimensional images. However, the knowledge of the calibration parameters of each camera allow the determination of the three-dimensional position of each point on the breast surface that is located in the intersecting fraction of a pair of images taken by two different cameras. Image processing tools are then used to track the position of any such point from subsequent images over the period of a complete oscillation. Tracking the motion of a large set of points that are distributed over the entire surface area delivers a full three-dimensional description of the surface motion.

Once image capture is completed, motion data of each sampled point is converted into a complex valued displacement description. Using a model based forward calculation of the scanned and discretized geometry with an initial material parameter configuration, a comparison between measured and calculated surface displacements can be used to define an error function. This error function provides the basis for optimization algorithms that are subsequently used to systematically update the model's material parameters until the error tends to a minimum or zero. The material description found in this minimal error state includes full volume stiffness information, a 3D elastogram, that can be used for clinical interpretation.

1.4.1 Initial State of the DIET System

At the beginning of the work at hand, the DIET system has been a theoretical concept with first proof of concept studies performed in numerical simulation by Peters *et. al* [89]. This first study used a standard Finite Element Method (FEM) in an undamped, compressible formulation, but near incompressibility, with linear tetrahedral elements. A quarter of a semi-spherical domain was used to compute the surface displacements resulting from longitudinal, harmonic actuation in the z-direction from the underside.

A number of cases were simulated with different inclusion sizes, locations and different stiffness values. To simulate nonhomogeneous material with variation in elasticity, the shear modulus, μ, was extended in the FEM formulation using an isoparametric formulation, such that the stiffness variation is given over each element in terms of its interpolating shape function and nodal shear modulus values, μ_i. Simulated data was corrupted in each case by adding normal distributed noise with a resulting standard deviation of 5%.

Using a gradient descent algorithm for this nonlinear problem, reconstructions were performed for the stiffness values of three different regions within the domain associated with regions of fatty, glandular and cancerous tissue according to the forward simulations. Initial stiffness parameter values were chosen in the the range of healthy tissue. The results of those reconstructions indicated the feasibility of the reconstruction method from surface data only, with 17 out of 27 inclusions successfully identified.

This numerical study highlighted several issues, including high sensitivity to start values and limited success rates in the reconstruction of large inclusions. In

contrast, small inclusions were identified more successfully, even at deep locations within the simulated tissue, which was a counter-intuitive result.

A second, more general proof of concept study was then carried out using a dual mesh scheme which allowed more accurate simulations of model displacements, while supporting material variation on a second, coarser mesh. This approach enabled the reconstruction of nodal values for shear modulus over the entire domain [90]. Several levels of coarseness were tested in the reconstruction of a model with a single, medium sized inclusion. The majority of results were reported to reconstruct stiff regions within the domain, but often failed to converge in the correct locations. However, some results identified the inclusion correctly, as shown in Figure 1.6, where the original map of elastic properties used for forward simulation is shown (a) together with the elastic reconstruction results (b). This behavior was interpreted to be due to the severe nonlinear characteristics of the error function which possessed a relatively large number of local minima.

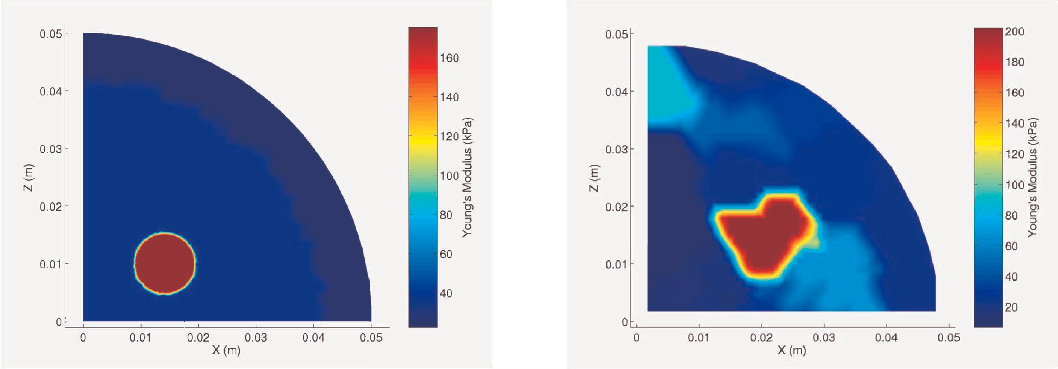

(a) (b)

Figure 1.6 Proof of concept studies: (a) shows the elastic parameters used for forward simulated as a cross section through the model and (b) shows the elastic parameters obtained from reconstruction from surface motion data.

1.4.2 Parameter Reconstruction from Boundary Data

Parallel to the continuing development of the DIET image capture system, this thesis deals with the development of an elastic parameter reconstruction scheme. In the sense of surface based reconstruction, a variety of inverse problems exist in engineering fields that have successfully attempted to reduce specific, full volume based reconstruction methods to surface based inverse methods. These kind of surface based inverse problems are often (with few exceptions) attempted using Boundary Element Methods (BEMs) for the forward solution.

BEM techniques offer a range of computational advantages. The most significant advantage of BEM is that discretisation is only required on the surface of the domain, keeping the resulting system matrices relatively small. Further advantages arise in reduced computational costs due to a reduction in the size of the system matrices and potential advantages in re-computation of forward solutions using only partially updated system matrices. Hence, BEM appear to be naturally suited to the kind of surface based inverse problem, as they take the entire problem to the surface and drastically reduce the number of parameters to be reconstructed.

A brief review on inverse problems, particularly those using BEM, of relevance to this thesis, are presented here. Further details on BEM algorithms and specifics are left for subsequent chapters.

Potential Theory and Acoustic Inverse Problems

Many of the surface based inverse problems are based on potential theory, as given in applications governed by the Laplace Equation or some variation thereof [91, 92]. An advantageous factor here is that the number of degrees of freedom per discretization point is only one. Hence, the resulting system matrices are relatively small. In addition, the Laplace Equation can be solved very accurately with BEMs, even at very imprecise discretization levels with constant elements [93].

Examples of such inverse potential problems would include EIT, where the electrical impedance or resistance of a material is reconstructed from voltages measured on the surface of the domain in question (see Section 1.2.2). EIT has been studied for a long time and is well presented in the literature [39–41, 94]. Thermal problems are another significant type inverse potential problem, where temperature measurements allow the reconstruction of heat fluxes [95, 96], or the determination of internal heat sources [97].

Similar inverse problems appear also in the field of acoustics. Based on the Helmholtz Equation, measured field pressures are used to reconstruct the vibro-acoustic field generated by arbitrary structures that vibrate within an infinite medium [98]. The detection of acoustic sources in such structures, for example specific areas of a car engine, are useful in the design of products that can be optimized with respect to minimal generation of vibro-acoustic noise [99, 100]. Here, the BEM performs to its full potential with discretization required only for

the surface of the vibrating structure and accurate computations of an objective function that is defined at distant points approaching relative infinity.

Shape-Related Optimization Problems

A large range of DIET-related inverse problems in the field of elasticity are concerned with the optimization of the shape of a product with respect to some cost function, such as an optimal stress distribution with minimal use of material or similar objectives. This kind of inverse problem is often called *optimal design* or *shape sensitivity analysis* and also includes the attempt to identify defects, such as cracks, inclusions and cavities. The BEM is also effective in solving this kind of reconstruction problem, as changes with respect to the discretized boundary are obtained easily without the requirement of repeatedly re-meshing the full volume.

Early attempts for the identification of cavities have been made by Tanaka *et al.* [101], using a Taylor series expansion of the BEM for harmonic elastodynamics in conjunction with a constant boundary element formulation. Convergence was shown only for problems where quality start values were available. The relatively low discretization level will also have been insufficient in this elasticity problem. Burczyński *et al.* have developed a general approach for shape sensitivity analysis for static and vibration problems with BEMs, using the adjoint method for first order Jacobian calculations [102]. These studies were extended by sensitivity analysis for defect shape identification by comparison to known eigenfrequencies obtained by the BEM. This approach enabled analytic sensitivity expressions for eigenfrequencies in the use of optimizations methods [103].

Recent contributions in this category are the work of Rus and Gallego, who developed calculations of inclusion and cavity shape sensitivities for both bounded and unbounded solids in two dimensions with arbitrary defect shapes by direct differentiation of the Boundary Integral Equation [104]. A similar problem has been researched by Mallardo *et al.*, who investigated a given circular inclusion in a rigid and in a deformable state with respect to its location within a domain to obtain optimal structural stiffness. The objective function in this case was defined as the accumulated strain energy of the displaced system [105].

Material Parameter Identification Problems

The reconstruction of material parameters in engineering fields has always been dominated by experimental and destructive testing. However, the development of

nondestructive testing procedures, known as the *Identification Inverse Problem*, has been motivated by demands in other fields, specifically in clinical applications (see Section 1.3) and from quality assurance applications, where material parameter values show some degree of variation due to inexact manufacturing processes, as occur for example in the manufacturing of composite materials.

Besides those inverse problems mentioned in Section 1.3 on Elastography, in particular USE and MRE, only a few attempts appear in the literature using FEMs for these identification problems. An early study by Schnur *et al.* developed a FEM-based approach for the identification of elastic material properties of a two-dimensional elastic solid from displacement measurements on the fraction of the boundary with Neumann (traction) boundary conditions. Further, the identification of a circular inclusion and its elastic properties has been incorporated using automatic finite element mesh generation during the optimization process with a modified Levenberg-Marquardt algorithm [106, 107].

More recently, Liu *et al.* developed a general framework for the three-dimensional tomography-based elastographic reconstruction of anisotropic material parameters from displacement measurements on the boundary and the interface between the inclusion and surrounding material. A gradient based optimization method was used with analytic gradients obtained by an adjoint method. Simulation studies indicated that isotropic material parameters can be identified uniquely for both tissue and inclusion, but anisotropic reconstructions require at least multiple data sets obtained at different loading conditions [108].

BEMs have also been popular in the identification of material parameters from boundary data. In isotropic material identification, Mallardo *et al.* have attempted similar approaches to Schnur *et al.* in determining the position and shear modulus of a deformable inclusion in 2D from static loads in simulation [105]. Similarly, Marin *et al.* used the simulation of elastic waves to determine the Poisson ratio and shear modulus of an isotropic solid from boundary tractions and displacements [109]. A reconstruction problem of isotropic Lamé constants with a radial dependency was solved for a spherical geometry [110].

Other studies have used the BEM for the identification of the anisotropic material parameters of 2D plates from boundary measurements [111, 112], which have shown to be nonunique [113]. They thus required a computationally intensive genetic algorithm combined with a nonlinear least square method for successful reconstruction. Similarly, orthotropic material parameters have been reconstructed in the case of 2D plates [114, 115]. However, the identification of

3D anisotropic material parameters, was targeted only recently by Heyliger *et al.*, who approached this problem by an algorithm based on the impact resonance of a specific rectangular parallelepiped [116].

1.5 An Approach to the DIET Inverse Problem with BEMs

Besides the continuing development of the image capture system [117] as well as elasticity reconstruction algorithms based on basic FEMs [118, 119], this thesis takes a separate identification approach using Boundary Element Methods. Thereby, the reconstruction of material parameters is performed in a more holistic sense, considering reconstructions of a full, unique set of isotropic material parameters including Young's modulus, Poisson ratio, density and viscous and inertial attenuation parameters. Furthermore, reconstruction of a potential lesion is considered through identification of the location and size of a circular/spherical inclusion with different material specifications using a region-based approach. These parameters are obtained in both two- and three-dimensional geometry cases from elastic steady-state time-harmonic motion measured on the surface.

The major proportion of this thesis was the implementation of both an efficient BEM for static and harmonic elasticity for 2D and 3D applications as well as the implementation of a flexible optimization scheme allowing for the above reconstruction investigation requirements. Besides a number of side programs for visualizations or preliminary data processing using MATLAB, this task was realized in an approximately 25.000 lines long code written in FORTRAN90. This thesis thus illustrates the abilities and the systematic growth and development of this program suite using realistic examples and findings of its application in a practical DIET system.

Chapter 2 introduces the classical BEM for both static and time-harmonic elasticity including some detail on the numerical techniques required for its successful implementation. Advantages over the FEM with respect to the forward as well as the inverse problems are discussed.

In Chapter 3, standard models as used in this thesis for numerical investigations in simulation are introduced together with typical characteristics of their forward solutions in ranges of material parameters that are plausible for biological soft tissues. In this regard, a study on errormaps associated with the inverse

problem is presented with the aim to identify critical parameters with nonlinear behavior, preliminary to the design of inverse algorithms.

Chapter 4 provides an overview and reasoning of the optimization methods chosen in this work, with details to the specific implementation used. This includes an algorithm to extract a number of minima out of a multi-dimensional errormap from a Grid-Search, as well as a gradient based Gauss-Newton technique with parameter scaling and Tikhonov regularization.

Chapter 5 presents systematic simulation case studies performed for the reconstruction of material parameters that characterize the elastic behavior of an isotropic, homogeneous, single domain (in 2D and 3D). These parameters include all parameters of a five material parameter model, the viscous and inertial damping parameters, α and β, Young's modulus, E, Poisson's ratio, ν, and the density, ρ. Reconstructions using the Gauss-Newton method and the BEM for harmonic elasticity were performed for single parameters as well as for combinations of up to all parameters at the same time.

Successful techniques for the identification of inclusion parameters are presented in Chapter 6. This includes a first study on the expectable reconstruction accuracy at the example of inclusion stiffness, E^{II}, in various cases with dependencies on inclusion size, location, attenuation effects, actuation type and frequency. After illustrating the reconstruction of single inclusion parameters, location, P, and size R, results are presented for the simultaneous reconstruction of P, R and E^{II}. The clinical use of these reconstructions is discussed.

Chapter 7 concludes the algorithm development with the illustration of a three-step inversion algorithm that combines the techniques developed in Chapters 5 and 6 resulting in the successful reconstruction of both background material and the relevant inclusion parameters.

The development of an imaging capture system [89, 120] parallel to this work has made experimental surface motion data available gathered from a silicon based breast phantom. Chapter 8 thus presents the algorithms developed to correlate the DIET-specific motion data measurements to a BEM surface. Preliminary results obtained from the application of these algorithms on a first experimental data set are also shown.

Concluding this work, Chapters 9 and 10 summarize the developments of this thesis and provide an overview of the future steps to be taken for the successful continuing development of the DIET system.

Chapter 2

The Boundary Element Method in Elasticity

The behavior of most physical systems, for example the deformation of a body subjected to a certain loading scenario, can be described by partial differential equations (PDEs). Often, their analytic solution is only possible in simple cases. In the late 1800's, progress toward the solution of more complicated cases was achieved by reformulating PDE's more practically as Integral Equations (IE). In Elasticity Theory, work on the wave equation by Helmholtz [121] in 1860 and Kirchhoff [122] in 1883, Somigliana [123] on Elastostatics in 1889 and Fredholm [124] in 1903 on IE solutions, form the basis of numerical solution methods, such as the Finite Element Method (FEM) and the Boundary Element Method (BEM). However, it was not until the invention of digital computers and the design of numerical algorithms that practical use of IE based methods commenced. Implementation of the BEM has been particularly difficult with early results in elasticity published by Banaugh and Goldsmith [125,126] in 1963. However, practical solutions remained elusive until Lachat and Watson's paper [127] in 1976. A review on the BEM development from the 1960's to today is found in [128].

Complete descriptions on the general BEM and its applications can be found in many textbooks. An excellent example is the work of P.K. Banerjee [93]. The somewhat complicated issue of computational implementation has only recently been published in comprehensive form by G. Beer [129], which covers important details of the numerical difficulties that are encountered.

For the sake of clarity and completeness, the derivation of the BEM in static and harmonic Elasticity will be reviewed here. This chapter also includes relevant details on its computer implementation related to the work presented in this thesis. Note that all derivations are carried out in indicial notation, and summation convention applies, unless stated otherwise.

2.1 Fundamentals in Elasticity

2.1.1 Governing Equations of Linear Elasticity

An elastic body in cartesian space $\mathbf{x}$, as shown in Figure 2.1, is described by the equations of equilibrium in tensor notation:

$$\sigma_{ij,j} + b_i = 0 \tag{2.1}$$

where b_i are the body forces. The stress components σ_{ij} are defined by Hooke's general law of Elasticity:

$$\sigma_{ij} = E_{ijkl}\varepsilon_{kl}, \tag{2.2}$$

where E_{ijkl} is the fourth order elasticity tensor, and the strain components ε_{ij} are assumed to be infinitesimally small:

$$\varepsilon_{ij} = \frac{1}{2}\left(u_{i,j} + u_{j,i}\right). \tag{2.3}$$

In Equation (2.3), $u_{i,j}$ represents the derivative of the displacement u_i in the x_j direction. For an isotropic material, Hooke's law reduces to:

$$\sigma_{ij} = \lambda\delta_{ij}\varepsilon_{kk} + 2\mu\varepsilon_{ij}, \tag{2.4}$$

where δ_{ij} is the Kronecker-delta, and μ and λ are Lamé's constants, related to a reduced Young's Modulus E of single order by:

$$\mu = \frac{E}{2(1+\nu)}, \quad \lambda = \frac{\nu E}{(1+\nu)(1-2\nu)}, \tag{2.5}$$

where ν is Poisson's ratio.

Using Equations (2.3) and (2.4), Equation (2.1) can be expressed in terms of displacements u, yielding Navier's Equation for Elastostatics:

$$(\lambda+\mu)u_{j,ji} + \mu u_{i,jj} + b_i = 0. \tag{2.6}$$

Equation (2.6) can easily be extended to the dynamic case through the consideration of an inertial forcing term, resulting in Navier's Equation for Elastodynamics:

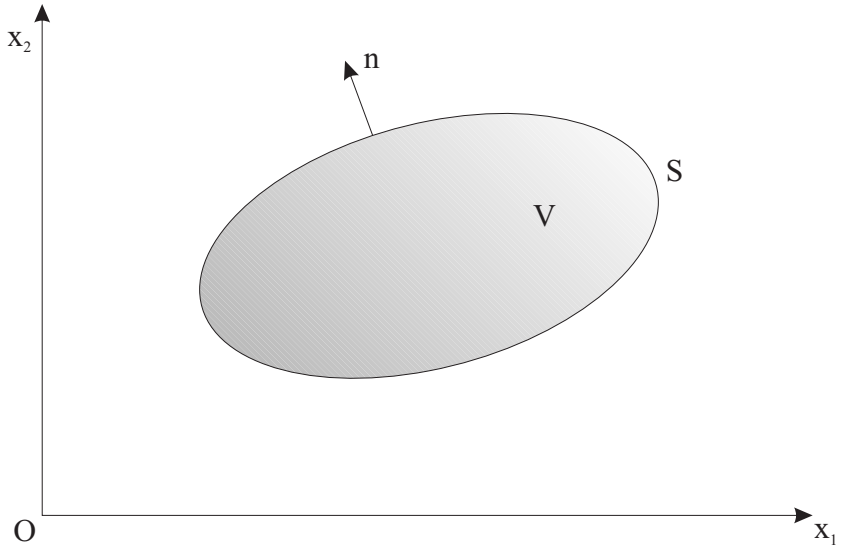

Figure 2.1 Elastic body in equilibrium, shown with volume V, surface S and surface normal vector n.

$$(\lambda + \mu)u_{j,ji} + \mu u_{i,jj} + b_i = \rho \ddot{u}_i, \tag{2.7}$$

where $\ddot{u}_i$ denotes the second time derivative of the displacement u_i. Furthermore, the incorporation of a velocity dependant energy dissipation term into Equation (2.7) yields:

$$(\lambda + \mu)u_{j,ji} + \mu u_{i,jj} + b_i = \rho \ddot{u}_i + \beta \dot{u}_i, \tag{2.8}$$

where β is the added coefficient for viscous damping effects.

Given a time-harmonic actuation, the steady-state displacement response is also a harmonic oscillation in the rotational frequency, Ω:

$$\begin{aligned} u_j &= \hat{u}_j \, e^{-i\Omega t}, \\ \dot{u}_j &= \frac{du_j}{dt} = -i\Omega \, \hat{u}_j \, e^{-i\Omega t}, \\ \ddot{u}_j &= \frac{d^2 u_j}{dt^2} = -\Omega^2 \, \hat{u}_j \, e^{-i\Omega t}, \end{aligned} \tag{2.9}$$

where $\hat{u}$ is the complex valued oscillation amplitude. In this case, it can be shown that the use of a complex valued elastic modulus, $E = E_{\mathcal{R}} + iE_{\mathcal{I}}$, and a

complex density, $\rho = \rho_{\mathcal{R}} + i\rho_{\mathcal{I}}$, produce attenuation effects of the same form seen in Equation (2.8). Hence, the simulation of damped motion behavior is possible without any modifications required in the subsequent derivations, other than the use of complex material parameters.

In this work, by default, a proportional damping model (Rayleigh Damping) was used for the calculation of the imaginary parts of E and ρ, with:

$$E = E_{\mathcal{R}}(1 + i\Omega\beta) \qquad \text{and} \qquad \rho = \rho_{\mathcal{R}}\left(1 - \frac{i\alpha}{\Omega}\right), \tag{2.10}$$

where β is a real valued viscous damping parameter and α a real valued inertial damping parameter. Note that as a consequence of using a complex valued E and ρ, the Lamé constants, μ and λ, will also be complex. The damping ratio ζ can then be defined analogous to a single degree of freedom model:

$$\zeta = \frac{1}{2}\left(\frac{\alpha}{\Omega} + \beta\Omega\right). \tag{2.11}$$

2.1.2 Formulation of the Boundary Integral Equation

Multiplying Equation (2.1) with an arbitrary function u_i^*, followed by integration over the problem domain, V, yields:

$$\int_V \left(\sigma_{ij,j} + b_i\right) u_i^* dV = 0. \tag{2.12}$$

Integration by parts is defined in general for two sufficiently smooth functions f and g:

$$\int_V f\frac{\partial g}{\partial x_i}dV = \oint_S f g n_i dS - \int_V g\frac{\partial f}{\partial x_i}dV. \tag{2.13}$$

where $\oint_S(\ldots)dS$ means the integration over the closed surface of the body, and n_j represents the surface normal in the x_j direction. It can be carried out on Equation (2.12) and leads to:

$$\oint_S \sigma_{ij}u_i^* n_j dS - \int_V \sigma_{ij}u_{i,j}^* dV + \int_V b_i u_i^* dV = 0, \tag{2.14}$$

Using the definition of the surface tractions t_i:

$$t_i = \sigma_{ij}n_j, \tag{2.15}$$

and the symmetric properties of the stress tensor ($\sigma_{ij} = \sigma_{ji}$), Equation 2.14 can be simplified to yield:

$$\oint_S t_i u_i^* dS + \int_V b_i u_i^* dV = \int_V \sigma_{ij} u_{i,j}^* dV. \tag{2.16}$$

Equation (2.16) represents the principle of virtual work, if the functions u_i^* are taken as the virtual displacements, and is the integral formulation used for the FEM in Elasticity.

Considering the symmetry of the derivatives $u_{i,j}^*$, which can be thought of as the virtual strain tensor:

$$u_{i,j}^* = \varepsilon_{ij}^* = \frac{1}{2}\left(u_{i,j}^* + u_{j,i}^*\right), \tag{2.17}$$

and using the symmetric properties of the elasticity tensor, E_{ijkl}, as follows:

$$\sigma_{ij}\varepsilon_{ij}^* = E_{ijkl}\varepsilon_{kl}\varepsilon_{ij}^* = \varepsilon_{kl}E_{klij}\varepsilon_{ij}^* = \varepsilon_{kl}\sigma_{kl}^* = \sigma_{ij}^*\varepsilon_{ij}, \tag{2.18}$$

then Equation (2.16) can be rewritten:

$$\oint_S t_i u_i^* dS + \int_V b_i u_i^* dV = \int_V \sigma_{ij}^* u_{i,j} dV. \tag{2.19}$$

Carrying out a second integration by parts on the right hand side term yields:

$$\oint_S t_i u_i^* dS + \int_V b_i u_i^* dV = \oint_S \sigma_{ij}^* u_i n_i dS - \int_V u_i \sigma_{ij,j}^* dV. \tag{2.20}$$

Assuming that all functions denoted by a * satisfy the same conditions as their analogous counterpart, such that:

$$t_i^* = \sigma_{ij}^* n_j, \quad \textit{and} \quad \sigma_{ij,j}^* + b_i^* = 0, \tag{2.21}$$

as would be the case, if u_i^* are interpreted as virtual displacements, then Equation (2.20) can be rewritten:

$$\oint_S t_i u_i^* dS + \int_V b_i u_i^* dV = \oint_S t_i^* u_i dS + \int_V b_i^* u_i dV. \tag{2.22}$$

Equation (2.22) represents Betti's theorem of reciprocal work, and forms the basis for BEM formulations in Elasticity.

Betti's theorem can be interpreted as relating two distinctly different states of loading and displacement of a body to each other, (u_i, t_i, b_i) and (u_i^*, t_i^*, b_i^*). More specifically, it states that the work performed by the load of state one on the displacements of state two is equal to the work performed by the load of state two on the displacements of state one.

All multiplications in Equation (2.22) can be replaced by convolution integrals, defined generally:

$$f(x_i,t) = g \star h = \begin{cases} 0 & t < 0 \\ \displaystyle\int_0^t g(x_i, t-\tau) h(x_i,t) d\tau & t > 0, \end{cases} \tag{2.23}$$

Furthermore, introducing initial conditions (u_{i0}, $\dot{u}_{i0}$, u_{i0}^* and $\dot{u}_{i0}^*$), generalizes Betti's theorem to the elastodynamic case:

$$\begin{aligned} &\oint_S t_i \star u_i^* dS + \int_V \left(b_i \star u_i^* + \rho \dot{u}_{i0} u_i^* + \rho u_{i0} \dot{u}_i^*\right) dV \\ &\quad = \oint_S t_i^* \star u_i dS + \int_V \left(b_i^* \star u_i + \rho \dot{u}_{i0}^* u_i + \rho u_{i0}^* \dot{u}_i\right) dV. \end{aligned} \tag{2.24}$$

If steady state, time harmonic motion is assumed, Equation (2.24) can be simplified by transformation to the frequency domain (Fourier space). In this space, it now reads exactly the same as Equation (2.22), only with time dependency transformed to a dependency on the actuation frequency, Ω.

2.1.3 Fundamental Solutions

The fundamental solutions to Navier's equation, $G_{ij}(\mathbf{x}, \boldsymbol{\xi})$ in Elastostatics and $G_{ij}(\mathbf{x}, \boldsymbol{\xi}, \Omega)$ in steady-state Elastodynamics, are often referred to as Kelvin solutions [130]. They belong to the family of Green's functions, representing the response (displacements $u_i(\mathbf{x})$) at any field point $\mathbf{x}$ due to a unit force $\delta(\boldsymbol{\xi})$ applied at the source point $\boldsymbol{\xi}$ anywhere in the domain, as illustrated in Figure 2.2. In the elastodynamic case, the loading term is a unit impulse, $\delta(\boldsymbol{\xi}, t)$, applied in $\boldsymbol{\xi}$ at time t. The corresponding solutions for tractions, $F_{ij}(\mathbf{x}, \boldsymbol{\xi})$ and $F_{ij}(\mathbf{x}, \boldsymbol{\xi}, \Omega)$, are derived via Hooke's law (Equation (2.4)) and the relationship between stress and traction (Equation (2.15)).

G_{ij} and F_{ij} are given in the following subsections explicitly for the $2D$ and $3D$ cases in Elastostatics and Elastodynamics in indicial notation. Note, it was found that many representations of these solutions in the literature contain ty-

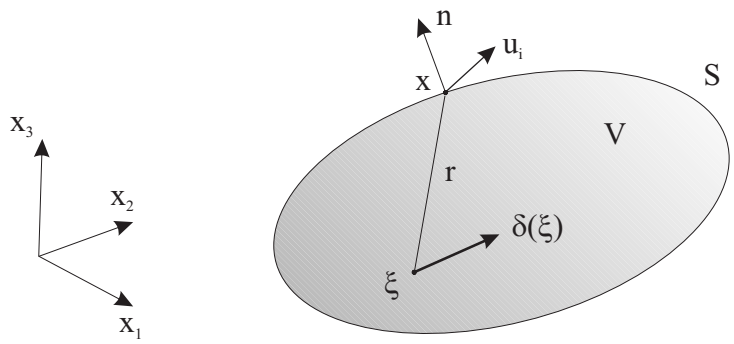

Figure 2.2 The Kelvin-solutions are determined due to unit force loading

pographical errors. The formulations given here are verified as correct. Note also that in the $2D$ case, the solutions are given for plain strain conditions. However, they can easily be converted to plain stress conditions, by substituting an effective Poisson's ratio, $\bar{\nu} = \nu/(1+\nu)$.

In all cases, $r = \sqrt{(x_i - \xi_i)(x_i - \xi_i)}$ is the radius between the source point $\boldsymbol{\xi}$ and the field point $\mathbf{x}$, where the outward pointing normal vector is $\mathbf{n}$. The radial derivative with respect to the outward normal can be determined using the summation rule:

$$\frac{\partial r}{\partial n} = \frac{\partial r}{\partial x_i}\, n_i, \qquad \text{where} \qquad \frac{\partial r}{\partial x_i} = r_{,i} = \frac{1}{r}\,(x_i - \xi_i).$$

The steady-state Elastodynamic solutions also contain additional parameters: The rotational actuation frequency, Ω; and the shear and longitudinal wave speeds defined by the material parameters. For isotropic material these wave speeds are given as:

$$c_s = \sqrt{\frac{\mu}{\rho}} \qquad \text{and} \qquad c_p = \sqrt{\frac{\lambda + 2\mu}{\rho}}, \tag{2.25}$$

where c_p is the longitudinal (or primary) wave speed and c_s is the shear (or secondary) wave speed.

It is important to note that the fundamental solutions G_{ij} are weakly singular, and the solutions F_{ij} are strongly singular, when the field point approaches the source point, i.e. as $r \to 0$. This singularity plays a major role in the implementation of the BEM.

Kelvin Solution for 2D Elastostatics

The Kelvin solution of Equation (2.6) is given in the two-dimensional case for displacements:

$$G_{ij}(\mathbf{x}, \boldsymbol{\xi}) = \frac{1}{8\pi\mu(1-\nu)} \left((3-4\nu)\, ln\left(\frac{1}{r}\right) \delta_{ij} + \frac{\partial r}{\partial x_i}\frac{\partial r}{\partial x_j} \right), \tag{2.26}$$

with the traction counterpart determined to be:

$$F_{ij}(\mathbf{x}, \boldsymbol{\xi}) = \frac{-1}{4\pi\,(1-\nu)\,r} \left(\frac{\partial r}{\partial n} \left((1-2\nu)\delta_{ij} + 2r_{,i}r_{,j} \right) + (1-2\nu)(n_j r_{,i} - n_i r_{,j}) \right). \tag{2.27}$$

Kelvin Solution for 3D Elastostatics

Similarly, the three-dimensional case displacement solution for Equation (2.6) is given as:

$$G_{ij}(\mathbf{x}, \boldsymbol{\xi}) = \frac{1}{16\pi\mu(1-\nu)}\frac{1}{r} \left((3-4\nu)\, \delta_{ij} + \frac{\partial r}{\partial x_i}\frac{\partial r}{\partial x_j} \right), \tag{2.28}$$

with the corresponding tractions:

$$F_{ij}(\mathbf{x}, \boldsymbol{\xi}) = \frac{-1}{8\pi(1-\nu)\,r^2} \left(\frac{\partial r}{\partial n} \big((1-2\nu)\delta_{ij} + 3r_{,i}r_{,j} \big) + (1-2\nu)(n_j r_{,i} - n_i r_{,j}) \right). \tag{2.29}$$

Kelvin Solution for 2D steady-state Elastodynamics

In the $2D$ elastodynamic case, Kelvin's solution to Equation (2.7) is given in Fourier-space. The the displacement solution is given:

$$G_{ij}(\mathbf{x}, \boldsymbol{\xi}, \Omega) = \frac{1}{2\pi\mu} \left(A\delta_{ij} - Br_{,i}r_{,j} \right), \tag{2.30}$$

with the traction counterpart given as:

$$F_{ij}(\mathbf{x}, \boldsymbol{\xi}, \Omega) =$$

$$\frac{1}{2\pi}\left\{P\left(\delta_{ij}\frac{\partial r}{\partial n} + r_{,j}n_i\right) + Q\left(r_{,i}n_j - 2r_{,i}r_{,j}\frac{\partial r}{\partial n}\right) + Rr_{,i}r_{,j}\frac{\partial r}{\partial n} + Sr_{,i}n_j\right\}. \tag{2.31}$$

The potential functions, A and B, for Equation (2.30) have the form:

$$A = K_0\left(\frac{i\Omega r}{c_s}\right) + \frac{c_s}{i\Omega r}\left\{K_1\left(\frac{i\Omega r}{c_s}\right) - \frac{c_s}{c_p}K_1\left(\frac{i\Omega r}{c_p}\right)\right\}, \tag{2.32}$$

$$B = K_2\left(\frac{i\Omega r}{c_s}\right) - \frac{c_s^2}{c_p^2}K_2\left(\frac{i\Omega r}{c_p}\right), \tag{2.33}$$

whereas Equation (2.31) consists of functions containing their derivatives:

$$P = \frac{\partial A}{\partial r} - \frac{B}{r}, \quad Q = -2\frac{B}{r}, \quad R = -2\frac{\partial B}{\partial r}, \quad \text{and} \tag{2.34}$$

$$S = \left(\frac{c_p^2}{c_s^2} - 2\right)\left(\frac{\partial A}{\partial r} - \frac{\partial B}{\partial r} - \frac{B}{r}\right), \tag{2.35}$$

where K_0, K_1 and K_2 are the modified Bessel functions of the second kind and order 0, 1 and 2, and i is the imaginary unit. Note that particular care must be taken in the implementation of these Bessel functions with respect to the use of different series expansions depending on the argument's size [131, 132].

Kelvin solution for 3D steady-state Elastodynamics

In the $3D$ elastodynamic case, the fundamental solutions are given:

$$G_{ij}(\mathbf{x}, \boldsymbol{\xi}, s) = \frac{1}{4\pi\mu}\left(A\delta_{ij} - Br_{,i}r_{,j}\right) \tag{2.36}$$

and:

$$F_{ij}(\mathbf{x}, \boldsymbol{\xi}, s) =$$

$$\frac{1}{4\pi}\left\{P\left(\delta_{ij}\frac{\partial r}{\partial n} + r_{,j}n_i\right) + Q\left(r_{,i}n_j - 2r_{,i}r_{,j}\frac{\partial r}{\partial n}\right) + Rr_{,i}r_{,j}\frac{\partial r}{\partial n} + Sr_{,i}n_j\right\}, \tag{2.37}$$

where the potential functions A and B are now given in terms of the Laplace transform parameter $s = k - i\Omega$ at $k = 0$:

$$A = \left(\frac{c_s^2}{s^2 r^2} + \frac{c_s}{sr} + 1 \right) \frac{e^{-sr/c_s}}{r} - \frac{c_s^2}{c_p^2} \left(\frac{c_p^2}{s^2 r^2} + \frac{c_p}{sr} \right) \frac{e^{-sr/c_p}}{r}, \tag{2.38}$$

$$B = \left(\frac{3c_s^2}{s^2 r^2} + \frac{3c_s}{sr} + 1 \right) \frac{e^{-sr/c_s}}{r} - \frac{c_s^2}{c_p^2} \left(\frac{3c_p^2}{s^2 r^2} + \frac{3c_p}{sr} + 1 \right) \frac{e^{-sr/c_p}}{r}. \tag{2.39}$$

In Equation (2.38) and (2.39), P, Q and R are the same functions defined in Equations (2.32)–(2.34) in the section on $2D$ Elastodynamics, and S is now defined:

$$S = \left(\frac{c_p^2}{c_s^2} - 2 \right) \left(\frac{\partial A}{\partial r} - \frac{\partial B}{\partial r} - \frac{2B}{r} \right). \tag{2.40}$$

2.2 Derivation of the Boundary Element Formulation

There exist a number of BEM formulations developed over the last 50 years. The formulation employed here is the so called *Direct* Boundary Element Formulation. Some other formulations come with apparent disadvantages, such as Trefftz's method [133], where the computation of a set of fictitious sources is required and convergence can be an issue [134]. Similarly, the less general *Indirect* BEM [135] makes use of an arbitrary set of functions with no direct physical interpretation. In the direct Boundary Element formulation, those fictitious sources are chosen on the boundary. Hence, the method comes with numerical difficulties in (for example) the evaluation of strongly singular integrals. However, convergence is guaranteed.

2.2.1 Direct Boundary Integral Equation

Starting with Betti's reciprocal work theorem (compare Equation (2.22)), the direct Boundary Integral Equation formulation can be derived by assuming one of the two states in Equation (2.22), indicated by * is known, and formulating a solution for the other state. Considering Equations (2.21), where the known solution must satisfy the governing equations exactly, it becomes apparent that

the $*$–solution must be a fundamental solution to the PDE. The Kelvin solutions G_{ij} and F_{ij}, provided in the foregoing section, satisfy this requirement with one exception in the singular source point, $\boldsymbol{\xi}$. If this singularity is treated separately, as will be shown below, one can choose:

$$u_i^* := G_{ij}(\mathbf{x}, \boldsymbol{\xi}) \quad \text{and} \quad t_i^* := F_{ij}(\mathbf{x}, \boldsymbol{\xi}). \tag{2.41}$$

Substituting Equation (2.41) into Betti's theorem (Equation (2.22)) yields:

$$\begin{aligned} &\oint_S F_{ij}(\mathbf{x}, \boldsymbol{\xi}) u_i(\mathbf{x}) dS(\mathbf{x}) + \int_V \delta_{ij} \Delta(\mathbf{x}, \boldsymbol{\xi}) u_i(\mathbf{x}) dV(\mathbf{x}) \\ &\quad = \oint_S t_i(\mathbf{x}) G_{ij}(\mathbf{x}, \boldsymbol{\xi}) dS(\mathbf{x}) + \int_V b_i(\mathbf{x}) G_{ij}(\mathbf{x}, \boldsymbol{\xi}) dV(\mathbf{x}). \end{aligned} \tag{2.42}$$

where the body force term b_i^* has been replaced by the unit forcing term $\Delta(\mathbf{x}, \boldsymbol{\xi})$. Using the properties of the Dirac Δ-function, and assuming, the source point, $\boldsymbol{\xi}$, is within the domain, the left hand side volume integral in Equation (2.42) can be solved as:

$$\int_V \delta_{ij} \Delta(\mathbf{x}, \boldsymbol{\xi}) u_i(\mathbf{x}) dV(\mathbf{x}) = \int_V u_j(\mathbf{x}) \Delta(\mathbf{x}, \boldsymbol{\xi}) dV(\mathbf{x}) = u_j(\boldsymbol{\xi}). \tag{2.43}$$

With this simplification, Equation (2.42) reduces to Somigliana's Identity:

$$u_j(\boldsymbol{\xi}) = \oint_S \left[G_{ij}(\mathbf{x}, \boldsymbol{\xi}) t_i(\mathbf{x}) - F_{ij}(\mathbf{x}, \boldsymbol{\xi}) u_i(\mathbf{x}) \right] dS(\mathbf{x}) + \int_V G_{ij}(\mathbf{x}, \boldsymbol{\xi}) b_i(\mathbf{x}) dV(\mathbf{x}) \tag{2.44}$$

In the direct boundary element formulation, the location of the source point, $\boldsymbol{\xi}$, is now chosen on the boundary, as shown in Figure 2.3. To accommodate this singularity in the surface integral in Equation (2.44), an infinitesimal adjustment, is made to the boundary, S, such that $S \to S + \delta S - \Delta S$ as illustrated in Figure 2.3. δS represents the fraction of a spherical surface with radius κ around $\boldsymbol{\xi}$, which is now excluded from the domain, V. The surface integrals on δS in Equation (2.44) can be solved analytically by substituting a relevant pair of fundamental solutions from Section 2.1.3, and taking the limit process $\kappa \to 0$. In this operation ΔS must be understood as that part of S within the sphere centered at $\boldsymbol{\xi}$. Hence, $S - \Delta S \to S$ as κ approaches zero and the limiting value of the integral must be taken as a Cauchy principle value, which yields:

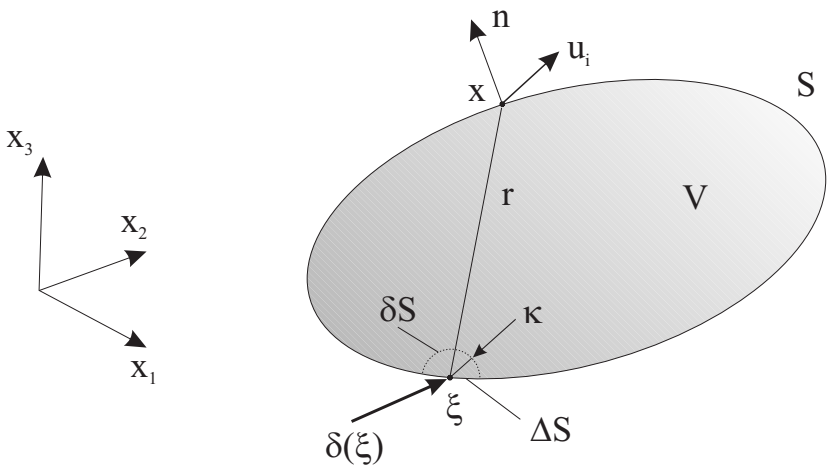

Figure 2.3 Unit force load on the boundary of the domain

$$\int_{\delta S} G_{ij}(\mathbf{x},\boldsymbol{\xi})t_i(\mathbf{x})dS = 0 \tag{2.45}$$

$$\int_{\delta S} F_{ij}(\mathbf{x},\boldsymbol{\xi})u_i(\mathbf{x})dS = c_{ij}u_i(\boldsymbol{\xi}), \tag{2.46}$$

where c_{ij} is a constant depending purely on the geometry of the body's surface in $\boldsymbol{\xi}$. Hence, the surface integrals in Equation (2.44) can be written:

$$\oint_S G_{ij}(\mathbf{x},\boldsymbol{\xi})t_i(\mathbf{x})dS = \int_S G_{ij}(\mathbf{x},\boldsymbol{\xi})t_i(\mathbf{x})dS \tag{2.47}$$

$$\oint_S F_{ij}(\mathbf{x},\boldsymbol{\xi})u_i(\mathbf{x})dS = c_{ij}u_i(\boldsymbol{\xi}) + \int_S F_{ij}(\mathbf{x},\boldsymbol{\xi})u_i(\mathbf{x})dS. \tag{2.48}$$

Considering these simplifications in Equation (2.44) finally yields the direct Boundary Integral Formulation for a body with arbitrary surface:

$$\begin{aligned} c_{ij}(\boldsymbol{\xi})u_i(\boldsymbol{\xi}) = &\int_S \left[G_{ij}(\mathbf{x},\boldsymbol{\xi})t_i(\mathbf{x}) - F_{ij}(\mathbf{x},\boldsymbol{\xi})u_i(\mathbf{x})\right] dS(\mathbf{x}) \\ &+ \int_V G_{ij}(\mathbf{x},\boldsymbol{\xi})b_i(\mathbf{x})dV(\mathbf{x}). \end{aligned} \tag{2.49}$$

In steady-state Elastodynamics, Equation (2.49) also depends on the actuation frequency, and can thus be written:

$$c_{ij}(\boldsymbol{\xi})u_i(\boldsymbol{\xi}) = \int_S \left[G_{ij}(\mathbf{x},\boldsymbol{\xi},\Omega)t_i(\mathbf{x}) - F_{ij}(\mathbf{x},\boldsymbol{\xi},\Omega)u_i(\mathbf{x})\right] dS(\mathbf{x}) + \int_V b_i(\mathbf{x})G_{ij}(\mathbf{x},\boldsymbol{\xi},\Omega)dV(\mathbf{x}). \tag{2.50}$$

It is worth noting that the coefficients, $c_{ij}(\boldsymbol{\xi})$, are the same in Equations (2.49) and (2.50). This becomes apparent considering the following integral:

$$\int_{\delta S} \left[F_{ij}(\mathbf{x},\boldsymbol{\xi},\Omega) - F_{ij}(\mathbf{x},\boldsymbol{\xi})\right] u_i(\mathbf{x})dS \to 0 \quad \text{for} \quad \kappa \to 0,$$

as the difference between $F_{ij}(\mathbf{x},\boldsymbol{\xi})$ and $F_{ij}(\mathbf{x},\boldsymbol{\xi},\Omega)$ is only weakly singular.

Since body forces are not relevant in this work, the term including b_i will be neglected in the following considerations, reducing the problem to one where only the surface of the geometry is relevant.

2.3 Numerical Implementation

2.3.1 General Problems (Single Region)

For the numerical implementation of the Boundary Integral Equation ((2.49) or (2.50)), the boundary of a single region problem is discretized in terms of $m = 1, ..., M$ boundary elements, as illustrated in Figure 2.4. For the present work, three-noded quadratic line elements have been used in $2D$ problems, and eight-noded quadratic surface elements of the Serendipity type in $3D$. Adopting the approach of isoparametric elements, as often seen in FEM [136, 137], the spatial coordinates, displacements and tractions on each element are given in terms of their interpolating shape functions, $\phi_k(\boldsymbol{\eta})$:

$$x_i^{(el)} = \phi_k(\boldsymbol{\eta})\, x_{ik} \tag{2.51}$$

$$u_i^{(el)} = \phi_k(\boldsymbol{\eta})\, u_{ik} \tag{2.52}$$

$$t_i^{(el)} = \phi_k(\boldsymbol{\eta})\, t_{ik}, \tag{2.53}$$

where $\boldsymbol{\eta}$ is an intrinsic coordinate system for each element, x_{ik} represent the nodal coordinates, u_{ik} the nodal displacements and t_{ik} the nodal tractions on an

element, each directed in the i^{th} cartesian coordinate direction. Neglecting body forces, Equation (2.49) can then be written:

$$\begin{aligned} c_{ij}(\boldsymbol{\xi})u_i(\boldsymbol{\xi}) + \sum_{m=1}^{M} \int_{S_m} F_{ij}(\mathbf{x}(\boldsymbol{\eta}), \boldsymbol{\xi})\phi_k(\boldsymbol{\eta})u_{ik} dS_m(\mathbf{x}(\boldsymbol{\eta})) \\ = \sum_{m=1}^{M} \int_{S_m} G_{ij}(\mathbf{x}(\boldsymbol{\eta}), \boldsymbol{\xi})\phi_k(\boldsymbol{\eta})t_{ik} dS_m(\mathbf{x}(\boldsymbol{\eta})). \end{aligned} \tag{2.54}$$

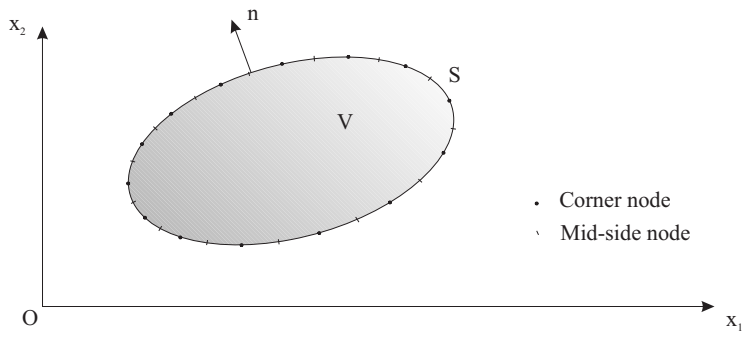

Figure 2.4 Body discretized by quadratic boundary elements.

Since surface integrals in the BEM can be integrated analytically only in simple cases, such as the discretisation with constant elements, the use of higher order elements necessitates the employment of numerical integration. In this work, integration was performed with Gaussian Quadrature [138], defined in general for one dimension:

$$\int_{-1}^{1} f(\eta)d\eta \simeq \sum_{i=1}^{N} w_i f(\eta_i), \tag{2.55}$$

where w_i are the Gaussian weights and the integrand is evaluated at the optimized Gauss point locations, η_i. The geometric transformation of the integrals from cartesian coordinates, $\mathbf{x}$, to intrinsic space, $\boldsymbol{\eta}$, is achieved by expressing the surface element dS as:

$$dS(\mathbf{x}(\boldsymbol{\eta})) = |J(\boldsymbol{\eta})|d\boldsymbol{\eta}. \tag{2.56}$$

where the determinant of the coordinate transform Jacobian,$|J|$, is given in the case of a $3D$ surface element:

$$|J(\boldsymbol{\eta})| = \begin{vmatrix} \frac{\partial x_1'}{\partial \eta_1} & \frac{\partial x_1'}{\partial \eta_2} \\ \frac{\partial x_2'}{\partial \eta_1} & \frac{\partial x_2'}{\partial \eta_2} \end{vmatrix}, \tag{2.57}$$

where x_1' and x_2' are local cartesian axes located in the tangential plane of an element at point (η_1, η_2). In the $2D$ case Equation (2.57) reduces to:

$$|J(\eta)| = \sqrt{\left(\frac{\partial x_1'}{\partial \eta}\right)^2 + \left(\frac{\partial x_2'}{\partial \eta}\right)^2}. \tag{2.58}$$

The partial derivatives $(\partial x_i'/\partial \eta_j)$ are obtained by differentiating the surface element shape functions of Equation (2.51). Considering Equations (2.55)–(2.58), Equation (2.54) can be written:

$$\begin{aligned} c_{ij}(\boldsymbol{\xi})u_i(\boldsymbol{\xi}) + \sum_{m=1}^{M} \left\{ u_{ik} \int_{-1}^{1} F_{ij}(\mathbf{x}(\boldsymbol{\eta}), \boldsymbol{\xi}) \phi_k(\boldsymbol{\eta}) |J(\mathbf{x}(\boldsymbol{\eta}))| d\boldsymbol{\eta} \right\} \\ = \sum_{m=1}^{M} \left\{ t_{ik} \int_{-1}^{1} G_{ij}(\mathbf{x}(\boldsymbol{\eta}), \boldsymbol{\xi}) \phi_k(\boldsymbol{\eta}) |J(\mathbf{x}(\boldsymbol{\eta}))| d\boldsymbol{\eta} \right\}. \end{aligned} \tag{2.59}$$

Now all coefficients of Equation (2.59) can be evaluated using every node $j = 1, ..., N$ as a collocation point. One can therefore rewrite the problem in matrix form:

$$\mathbf{F}\,\mathbf{u} = \mathbf{G}\,\mathbf{t}, \tag{2.60}$$

where u is a vector containing all nodal surface displacements, t contains the corresponding traction values, and the coefficients c_{ij} have been absorbed in $\mathbf{F}$. Note that $\mathbf{G}$ must be a rectangular matrix, as traction values are given as nodal values corresponding to a specific element. This approach thus allows for discontinuities between each element. Such jumps in traction values occur often, particularly at corners of a geometry. However, displacement values cannot allow discontinuities between elements. Thus, $\mathbf{F}$ is a square matrix.

Boundary conditions can be prescribed on the surface as either tractions or displacements, and are applied for each boundary element. For a well posed problem in linear elasticity, the boundary of the domain, S, can, for each coordinate direction, be divided into two regions, S_d and S_t, where S_d defines the portion of the boundary on which displacements are known and S_t defines the portion of the boundary on which tractions are known. Equation (2.60) can thus, schematically,

be rearranged column-wise:

$$\begin{bmatrix} \mathbf{G}_{S_d,S_d} & \mathbf{F}_{S_d,S_t} \\ \mathbf{G}_{S_t,S_d} & \mathbf{F}_{S_t,S_t} \end{bmatrix} \begin{Bmatrix} \mathbf{t}_{S_d} \\ \mathbf{u}_{S_t} \end{Bmatrix} = \begin{bmatrix} \mathbf{F}_{S_d,S_d} & \mathbf{G}_{S_d,S_t} \\ \mathbf{F}_{S_t,S_d} & \mathbf{G}_{S_t,S_t} \end{bmatrix} \begin{Bmatrix} \mathbf{u}_{S_d} \\ \mathbf{t}_{S_t} \end{Bmatrix}, \tag{2.61}$$

which is a well posed matrix equation of the form:

$$\mathbf{A}\,\tilde{\mathbf{x}} = \mathbf{B}\,\tilde{\mathbf{y}}, \tag{2.62}$$

where unknown quantities, $\tilde{\mathbf{x}}$, sorted on the left hand side and known quantities, $\tilde{\mathbf{y}}$, sorted on the right hand side. Hence, Equation (2.61). Equation (2.62) can now be simplified to:

$$\mathbf{A}\,\tilde{\mathbf{x}} = \tilde{\mathbf{b}}, \tag{2.63}$$

where this formulation can be readily solved with a standard linear algebra solver.

2.3.2 Inclusion Problems

The general BEM is valid for bodies of homogeneous material only, because the fundamental solutions from Section 2.1.3 do not allow for material-related nonlinearities or heterogeneities. Therefore, the solution of inclusion problems requires the simulation of two or multiple regions and their coupling. This process is illustrated in Figure 2.5, where two regions are denoted by superscripts I and II. Each region has its own set of material parameters. Note that the boundary of region I consists of S_a and S_b, where the boundary of region II is only S_b.

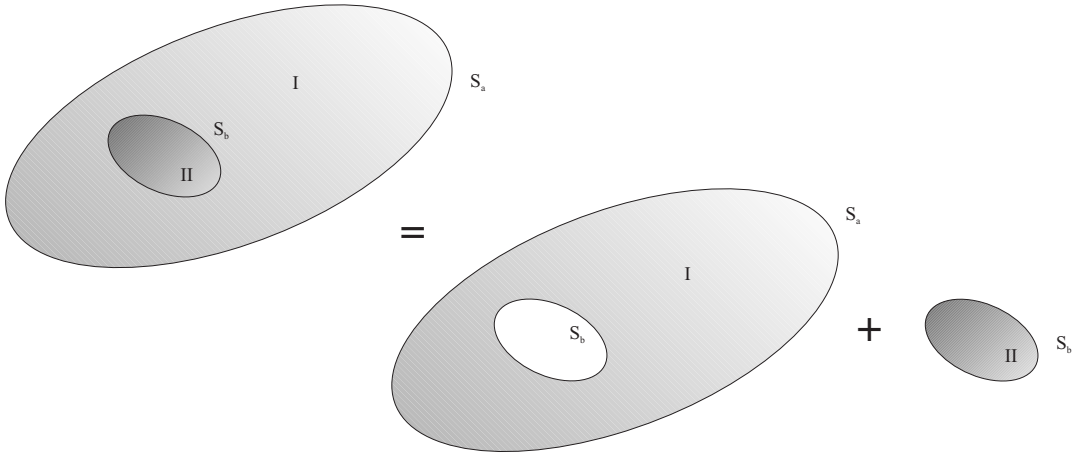

Figure 2.5 Superposition of BEM-regions for an inclusion problem

Due to the absence of boundary conditions on the interface of the regions, coupling is achieved by enforcing two conditions on the interface, displacement compatibility and Newton's third law:

$$\begin{aligned} u_b^I &= u_b^{II} \\ t_b^I &= -t_b^{II}. \end{aligned} \tag{2.64}$$

The integral equation for region I (compare Equation (2.49)) can thus be written for a body containing a hole:

$$\begin{aligned} c_{ij}(\boldsymbol{\xi})u_i^I(\boldsymbol{\xi}) = &\int_{S_a} \left[G_{ij}^I(\mathbf{x},\boldsymbol{\xi})t_i^I(\mathbf{x}) - F_{ij}^I(\mathbf{x},\boldsymbol{\xi})u_i^I(\mathbf{x})\right] dS_a(\mathbf{x}) \\ &+ \int_{S_b} \left[G_{ij}^I(\mathbf{x},\boldsymbol{\xi})t_i^I(\mathbf{x}) - F_{ij}^I(\mathbf{x},\boldsymbol{\xi})u_i^I(\mathbf{x})\right] dS_b(\mathbf{x}). \end{aligned} \tag{2.65}$$

The equation for the interior region, II, that fills the hole in regions I similarly reads:

$$c_{ij}(\boldsymbol{\xi})u_i^{II}(\boldsymbol{\xi}) = \int_{S_b} \left[G_{ij}^{II}(\mathbf{x},\boldsymbol{\xi})t_i^{II}(\mathbf{x}) - F_{ij}^{II}(\mathbf{x},\boldsymbol{\xi})u_i^{II}(\mathbf{x})\right] dS_b(\mathbf{x}), \tag{2.66}$$

Solving Equations (2.65) and (2.66) for $j^I = 1, ..., N$ and $j^{II} = 1, ..., N^{II}$, where N is the total number of nodes and N^{II} the number of nodes on the interface, a matrix equation is obtained for each system:

$$\begin{bmatrix} \mathbf{G}_{aa}^I & \mathbf{G}_{ab}^I \\ \mathbf{G}_{ba}^I & \mathbf{G}_{bb}^I \end{bmatrix} \begin{Bmatrix} \mathbf{t}_a^I \\ \mathbf{t}_b^I \end{Bmatrix} = \begin{bmatrix} \mathbf{F}_{aa}^I & \mathbf{F}_{ab}^I \\ \mathbf{F}_{ba}^I & \mathbf{F}_{bb}^I \end{bmatrix} \begin{Bmatrix} \mathbf{u}_a^I \\ \mathbf{u}_b^I \end{Bmatrix}, \tag{2.67}$$

and

$$\mathbf{F}_{bb}^{II}\,\mathbf{u}_b^{II} = \mathbf{G}_{bb}^{II}\,\mathbf{t}_b^{II}. \tag{2.68}$$

If the interface is assumed to be smooth and without corners, the matrices ($\mathbf{G}_{bb}^I$ and $\mathbf{G}_{bb}^{II}$) can be assembled as square matrices, while the other block matrices in $\mathbf{G}^I$ remain rectangular. $\mathbf{G}_{bb}^{II}$ can now be inverted, solving Equation (2.68) for the unknown interface tractions:

$$\mathbf{t}_b^{II} = \left[\mathbf{G}_{bb}^{II}\right]^{-1} \mathbf{F}_{bb}^{II}\,\mathbf{u}_b^{II}. \tag{2.69}$$

Substituting Equation (2.69) in Equation (2.67), and then into the compatibility

conditions (Equation (2.64)), yields:

$$\begin{bmatrix} \mathbf{G}_{aa}^{I} \\ \mathbf{G}_{ba}^{I} \end{bmatrix} \left\{ \mathbf{t}_{a}^{I} \right\} = \begin{bmatrix} \mathbf{F}_{aa}^{I} & \mathbf{F}_{ab}^{I} + \mathbf{G}_{ab}^{I} \left[\mathbf{G}_{bb}^{II}\right]^{-1} \mathbf{F}_{bb}^{II} \\ \mathbf{F}_{ba}^{I} & \mathbf{F}_{bb}^{I} + \mathbf{G}_{bb}^{I} \left[\mathbf{G}_{bb}^{II}\right]^{-1} \mathbf{F}_{bb}^{II} \end{bmatrix} \left\{ \begin{array}{c} \mathbf{u}_{a}^{I} \\ \mathbf{u}_{b}^{I} \end{array} \right\}, \tag{2.70}$$

which has the same form as Equation (2.62) and can be solved after applying the boundary conditions prescribed on S_a.

2.3.3 Numerical Techniques in the Implementation

As seen in the derivation of the BEM, there are difficulties to be expected in the numerical implementation. In particular, weakly and strongly singular integrals need to be evaluated. However, the conditioning of the resulting matrix system requires special treatment for the accurate solution of the BEM forward problem. These techniques are particularly relevant in the time-harmonic case.

2.3.3.1 Integration Accuracy

Maintaining sufficient and uniform accuracy of the numerical integration of the matrix components in G_{ij} and F_{ij}, is and essential component of the BEM solution process that must be handled with some precision. Sufficient integration accuracy is obviously closely related to achieving correct solutions from BEMs. The uniformity of this accuracy close-to and far-from singularities also plays a critical role in the solution process. However, as large differences in these accuracies lead to bad conditioning of the matrix system which in turn leads to accumulation of error in the solution.

Based on the error estimate of Gaussian quadrature, Lachat and Watson [127] have developed a formula to estimate the integration order required to maintain a uniform error level close-to and far-from singularities. This estimation process has been employed in this work. The method takes into account a characteristic size of an element and the distance between source and field point to obtain the number of Gauss points required for a given collocation point and element combination.

2.3.3.2 Evaluation of weakly singular and near-singular Integrals

In the vicinity of the collocation point, where the distance between source and field point becomes very small, the fundamental solutions turn singular. The

technique mentioned above is then not sufficient for the accurate evaluation of the surface integrals, even if an extremely fine discretisation is used.

In this case, a graded sub-segmentation scheme similar to the one suggested by Manolis *et al.* [139] has been employed, where the number of subdivisions depends on the minimum distance of the singularity from the surface element subject to integration. Starting from the singularity or the point on an element closest to the singularity in intrinsic space, the segmentation scheme in subdivides the element in the $3D$ case first into small triangles immediately surrounding singularity and then into rectangles away from the singularity. This is illustrated in Figure 2.6, where subdivision examples for the case of a near-singular (a), and a singular (b) surface element are shown. The sub-segmentation in $2D$ is performed analogous on line elements.

Therefore, this sub-segmentation requires a second, linear transformation to the numerical integration range. The rectangular sub-elements are mapped linearly to the unit-square, while the triangular sub-elements are mapped as such

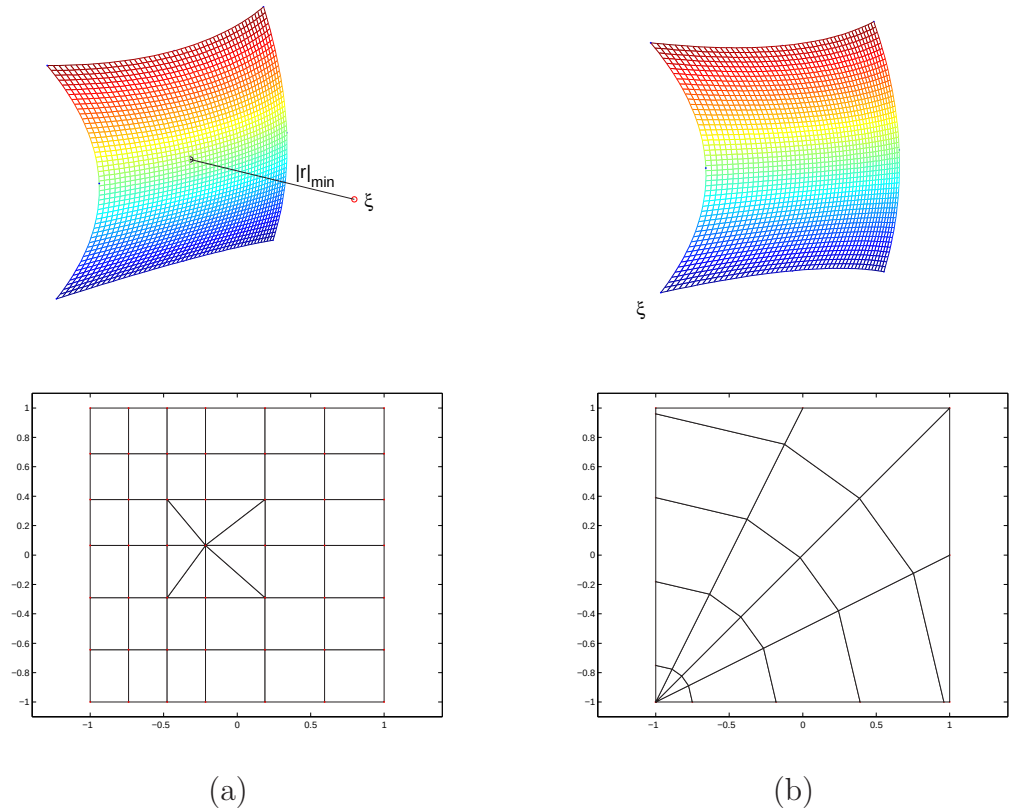

Figure 2.6 Sub-segmentation of a near-singular quadratic element in intrinsic space from the point closest to the singularity in $\boldsymbol{\xi}$ (a), and sub-segmentation of a singular element with singularity in a corner node (b)

that the singular point is stretched along a side of the unit-square [136]. This special transformation introduces a second Jacobian term of order r and, hence, cancels the weak singularities in the G_{ij} kernel and in the product of the F_{ij} kernel with shape functions that equal zero at point $\boldsymbol{\xi}$.

2.3.3.3 Evaluation of strongly singular Integrals

Special treatment is also required in the evaluation of the strong singularities caused by the F_{ij} kernels (Cauchy Principle Value (CPV) Integrals), where the polynomial approximation of Gaussian quadrature does not provide results with sufficient accuracy. While a direct approach exists for the computation of Cauchy principle value integrals in the BEM [140], this issue is avoided here by using an implicit approach, the well known principle of Rigid-Body-Motion. This principle states that a rigidly displaced (static) body gives rise to no stress. Therefore, tractions on the boundary must be zero. Thus, when substituting $\mathbf{u} = 1$ and $\mathbf{t} = 0$ into Equation (2.60), the diagonal block matrices D_{ij} (in $\mathbf{F}$), that contain the free term coefficients c_{ij} and the CPV integrals, can be evaluated for each equation of collocation at node l as:

$$D^s_{ijl} = -\sum_{k=1,\, k\neq l}^{N} F^s_{ijkl}, \tag{2.71}$$

where the superscript ^{s} denotes the static case.

However, in the dynamic case, the rigid body motion principle does not apply. Here, it is important to note that strong singularity occurs only in one part of the summation, where the shape function is the one belonging to the singular node. All other shape functions have the value zero here, and hence, the singularity is canceled. Denoting the singular shape function as $\hat{\phi}$, one can formulate the diagonal block matrix terms of equation of collocation, l, for the static case as:

$$D^s_{ijl} = c_{ijl} + \int_S F^s_{ijl}(\mathbf{x}, \boldsymbol{\xi})\, \hat{\phi}\, dS, \tag{2.72}$$

where $\hat{\phi}$ is zero over all boundary elements except for those of which $\boldsymbol{\xi}$ is a point. The same terms for the harmonic case (superscript ^{h}) are written as:

$$D^h_{ijl} = c_{ijl} + \int_S F^h_{ijl}(\mathbf{x}, \boldsymbol{\xi}, \Omega)\, \hat{\phi}\, dS, \tag{2.73}$$

and combining Equation (2.72) with Equation (2.73), yields the diagonal block matrices for the time-harmonic case:

$$D^h_{ijl} = D^s_{ijl} + \int_S \left[F^h_{ijl}(\mathbf{x}, \boldsymbol{\xi}, \Omega) - F^s_{ijl}(\mathbf{x}, \boldsymbol{\xi})\right] \hat{\phi}\, dS, \tag{2.74}$$

where D^s_{ijl} is evaluated by Equation (2.71) and the remaining integral can be evaluated using Gaussian quadrature as described above, as the subtracted expression is only weakly singular.

2.3.3.4 Scaling

Considering Equation (2.60), the terms in the **F** and **G** matrices can be noted to be of several orders different in magnitude, characterized by the presence of a shear modulus term in the denominator of the displacement solution. To avoid significant numerical error from round-off, scaling should be introduced prior to solving the matrix equation. In this work, the shear modulus, μ, has been used as a scaling factor, and Equation (2.60) was modified to the form:

$$\mathbf{F}\,\mathbf{u} = [\mu\,\mathbf{G}] \left(\frac{1}{\mu}\,\mathbf{t}\right). \tag{2.75}$$

2.4 Computational Advantages of the BEM

On the one hand, the BEM in general comes with a number of disadvantages to the programmer, such as the sensitivity to the implementation of its numerical integration scheme. The method requires dealing with complex valued, fully populated, system matrices, where only those sophisticated integral solution techniques yield a numerically stable system. Hence, the practical implementation is unforgiving to human error. In contrast, BEMs also offers large rewards, both, in terms of its use in forward solutions as well as in inverse problems; advantages that can not be achieved as easily with alternative solution methods, such as Finite Difference Methods (FDM) or Finite Element Methods (FEM). Some of those advantages and differences have been mentioned previously in chapter 1 in relation to the application in a DIET-system. However, a closer inspection of the BEM's computational details provides insight into additional available benefits. These advantages are discussed in this section in greater detail.

Although not relevant to the application of the BEM in the DIET problem treated in this work, it is worth mentioning that the BEM only comes to its

full potential when calculations of infinite or semi-infinite domains are required. This occurs due to the characteristic reduction to surface modeling only. In this case, no further assumptions to the extent of the discretization are needed (as is required for example in FEM), as the fundamental solutions satisfy the PDE exactly, even in infinite space. Hence, a great deal of potential discretization error can be entirely avoided.

2.4.1 Advantages of the BEM Forward Problem

Accuracy of the BEM Solution

The BEM is known for high accuracy of its solutions. Since the governing equations are satisfied within the domain exactly, the only errors that appear are due to inaccurate discretisation of the boundary and the approximations made in the numerical evaluations of the boundary integrals.

Given the implementation used in this work, with adequate discretisation using quadratic surface elements and the sophisticated integration scheme using sub-segmentation and prescribed integration accuracy, the potential error in the forward solution is minimized. Hence, only very small levels of numerical error should be expected from the model. Note that the use of the sub-division procedure also introduces the advantage that even reasonably coarse discretisation will provide converged solutions. Therefore, the size of system matrices can be kept small, with resulting small memory and solution time requirements.

Surface Meshing

The most obvious advantage of BEMs in general is the simplicity of the discretisation of the problem domain. In particular, only the geometry's boundaries require meshing, which is a significant reduction in comparison to full volume methods. This advantage comes with apparent time savings in the preparation of surface data.

A large scale breast screening application with a DIET-system requires a model-based numerical investigation to evaluate the potential presence of a stiff inclusion within a breast. Repeated for a large number of patients, this investigation likely represents a significant computational cost. Hence, the BEM discretization of the object of interest is advantageous in this case.

The particular size of a breast may change from case to case. However, the resulting number of fundamental shapes for a given size may be smaller. Hence, there may only be the need for a small number of scalable baseline meshes, from which the nodal coordinates could be adjusted to the specific patient case. Alternatively, the breast surface could easily be scanned by the available camera and imaging system [117], and automatically turned into a surface mesh by means of a simple and fast algorithm.

In comparison, the preparation of a mesh required in the full volume FEM analysis case appears to be more difficult. In particular, one cannot easily modify or adjust a given volumetric mesh by the assignment of new surface data. Complications are well known to arise from the distortion of elements or bad dimension ratios [135] in complex geometries. A surface scan by the camera system is of course possible in this case also. However, the additional step of obtaining a permissible and useful volumetric mesh discretisation should still be required for every patient.

Geometrical Damping

The fundamental solutions (Equations (2.26) – (2.37)) are given for the general case with complex valued density and elastic modulus. The undamped case is given for $E^I = 0$ and $\rho^I = 0$. However, the solutions still satisfy the radiation condition [141] automatically, meaning that energy radiated from the sources must scatter to infinity, and no energy may radiate from infinity. This property is often referred to as *geometrical damping* and can be interpreted for a closed domain as meaning that damping always exists in a sense of small energy dissipation due to radiation from the domain's boundary. This affect occurs directly in the BEM solution, where the *undamped* case is still complex-valued, and where the simulation of resonant behavior does not necessarily lead to infinitely large displacements.

Incompressibility

The simulation of nearly incompressible ($\nu \to 0.5$) and incompressible ($\nu = 0.5$) material is difficult in FEM. In particular, Lamé's constant λ approaches an infinite value and therefore creates a singularity in the FEM system equations. Special FEM formulations that consider pressure terms are required to obtain solutions in these conditions [142].

BEM formulations, in contrast, do not have singular characteristics in incompressible cases, as can be noted by inspection of the fundamental solutions in Equations (2.26)–(2.37). In fact, terms containing λ cancel and simplify the solutions in both static and time-harmonic elasticity. Care needs to be taken only in the evaluation of the longitudinal wave speed, c_p, which is well known for most materials from experimental measurements.

Plane Strain and Plane Stress

The Kelvin solutions in $2D$ are derived using plane strain assumptions. However, the simulation of plane stress conditions is again easily achieved, by substituting ν by an effective Poisson's ratio $\tilde{\nu}$ [93]:

$$\tilde{\nu} = \frac{\nu}{1+\nu}. \tag{2.76}$$

2.4.2 Advantages of the BEM in Inverse Problems

Inverse problems often require a large number of repeated evaluations of an objective function to determine the best choice of the parameters governing the problem behavior [143]. If the objective function requires the use of numerical procedures, such as the FEM or BEM, their forward solution often significantly dominates the overall computational costs. Hence, there is great interest in keeping the time-requirements for such solutions low, in particular by reducing the number of forward solutions required or their computational costs.

Reduction of Number of Variables

In the FEM approach to Elastography, the domain is discretized with volumetric elements, a popular choice being tetrahedral elements [118]. To allow for variation in the distribution of elastic parameters over the volume, an isoparametric approach was taken (compare Equation (2.51)). For example, the variation of the shear modulus is described via interpolation over an element using nodal values μ_i and the the local shape functions ϕ_i:

$$\mu = \phi_i \, \mu_i. \tag{2.77}$$

Hence, the number of parameters for shear modulus in the inverse problem is the same as the number of nodes, and can easily exceed several tens of thousands

[144]. The resulting FEM-based inverse problem therefore has large storage and CPU requirements.

In a BEM approach, a region-approach is compulsory due to the inhomogeneity in material parameters. However, this approach in turn means a dramatic reduction of variables in the inverse problem. In the case of one spherical inclusion, the variables are now limited to only the material parameters of each region, some of which can be assumed known, and the location and size of the inclusion. If the inclusion is parameterized as an ellipse or ellipsoid, the angular orientation within the domain introduces an additional variable.

The parametrization of an interior domain in the usual FEM-based approach is still possible by selecting the material properties for individual nodes based on shape functions within the domain [89]. However, this approach does not allow for an exact definition of material boundaries as discretization is still based on the existing nodal distribution, which will lead to a zigzag appearance along material boundaries. In contrast, the BEM-based approach, by definition, provides smooth and exact material boundaries.

Interface Meshing

As mentioned previously, meshing of surfaces in the BEM is achieved with little difficulty. This easier meshing is also of advantage in the inverse problem, where the mesh of the interface between material regions can require repeated modification. The adjustment of geometric parameters, such as an inclusion's location, size or rotation, is a fast operation that is easily handled by subroutines within the general inversion algorithm.

Computational Time Savings

The BEM also offers a number of gains in terms of computational time, particularly, when the solution of BEM-regions is required with respect to changes in only few variables. Starting with the basic region based problem, such as the examples shown in Figure 2.7, a number of significant computational savings can be identified, where updated solutions can be obtained without having to re-simulate the entire problem. This is the case, when material parameters are changed only in one region, and the mesh is not alternated, or only a fraction of the mesh is alternated. Further cases will always be a combination of those two cases described here.

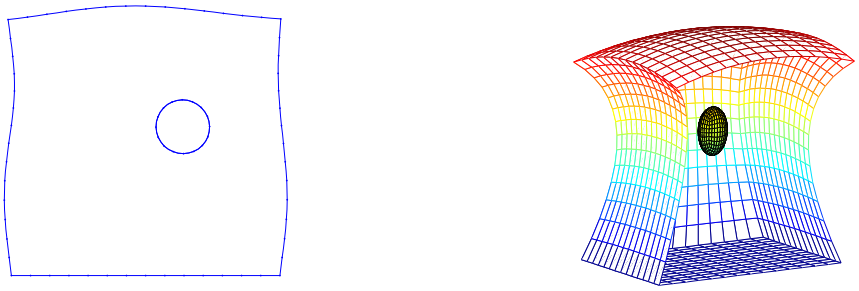

Figure 2.7 A $2D$ and $3D$ geometry used for investigation on computational time-savings

To illustrate the power of the computational savings, some numerical investigations with the harmonic BEM implementation were carried out on a 1.9GHz AMD Opteron machine. Two sample geometries, one $2D$ and one $3D$ case were chosen, each containing an inclusion. They are displayed in Figure 2.7 in a dynamically displaced state.

A first solution was determined by calculating and solving the complete system equations, where the regional matrices $\mathbf{G}^I$, $\mathbf{F}^I$, $\mathbf{G}^{II}$ and $\mathbf{F}^{II}$ from Equation (2.67) were saved in memory. A solution update was then determined by only calculating the system matrices for the interior region, $\mathbf{G}^{II}_{bb}$ and $\mathbf{F}^{II}_{bb}$, to mimic testing a new inclusion stiffness and re-solving the system. This test was repeated ten times for each geometry at two different discretisations. Table 2.1 shows the average of the resulting time requirements for the complete solution and the solution by updating only the relevant system matrices.

	Number of Elements			Solution Time [sec]		relative computation time
	Reg. I	Reg. II	total	complete	update	
$2D$	36	8	44	0.124	0.018	14.5%
	325	25	350	7.25	2.0	27.6%
$3D$	30	24	54	31.02	10.28	33.1%
	294	24	318	275.56	25.09	9.1%

Table 2.1 Average computational solution-time consumption by updating only matrices of region II.

It is clearly seen that in any of the cases simulated, there are significant computational time savings. The best improvement was obtained for the 3D geometry, with a very fine discretization. The solution update needed only 9.1% of the solution time required for total system.

When material parameters are kept constant, but the mesh configuration is changed, then only those boundary integrals affected by the change need to be re-calculated. Given, for example, a change in the interface mesh, such as a modification of S_b in Figure 2.5, the matrices $\mathbf{F}^I_{aa}$ and $\mathbf{G}^I_{aa}$ in Equation (2.67) can be saved and only the remaining matrices require recomputing. Numerical testing of time saving benefits of this method was repeated on the same sample geometries as used in the tests above, but for the special case of a rigid translation of the interface mesh within the domain, mimicking the testing of a new inclusion location. The specific block matrices that require recomputing, are then $\mathbf{G}^I_{ab}$ and $\mathbf{G}^I_{ba}$, as well as $\mathbf{F}^I_{ab}$ and $\mathbf{F}^I_{ba}$. The matrices $\mathbf{G}^I_{bb}$, $\mathbf{G}^{II}_{bb}$, $\mathbf{F}^I_{bb}$ and $\mathbf{F}^{II}_{bb}$ are not affected, as there is no modification to the discretisation of region II. Table 2.2 shows the average of the time requirements for the complete and updated solutions, where the tests were again repeated ten times.

	Number of Elements			Solution Time [sec]		relative computation time
	Reg. I	Reg. II	total	complete	update	
$2D$	36	8	44	0.12	0.043	35.8%
	325	25	350	7.24	2.96	40.9%
$3D$	30	24	54	31.58	19.73	62.5%
	294	24	318	276.08	48.68	17.63%

Table 2.2 Average computational solution-time consumption when updating only relevant block matrices, given a rigid displacement of the interface mesh.

As can be seen, significant time savings can be achieved when only updating the relevant parts of the system matrices. Clearly, the savings depend on the relative size of the regions. The best improvement is observed again for the $3D$ case, where the number of elements of the interior region is small in comparison to the total number of elements, and only 17.6% of the total solution time was required for the solution update.

2.5 Summary

In this chapter, the BEM for the application in static and time-harmonic Elasticity has been reviewed in detail, with a complete derivation of the boundary integral equation given. Particular numerical techniques required for its successful implementation have been documented, such as the solution of weakly and strongly singular integrals and techniques for the appropriate conditioning of the system.

A number of advantages have been discussed that make the use of the BEM practical, particularly for inverse problems like those found with DIET, where nearly incompressible conditions apply and a large number of solutions must be calculated. It has been shown that these solutions can be determined efficiently by updating only relevant portions of the system matrices. As a result, large amounts of computational efforts can be saved, creating a potentially more feasible or tractable inverse problem environment using the BEM.

Chapter 3

Preliminary Considerations

Prior to approaching the development of inverse strategies and algorithms to solve the DIET problem, this chapter provides a comprehensive insight to the general behavior to be expected in both the forward and inverse BEM solutions. The first section introduces the geometric models used as standard models for numerical investigations in subsequent chapters, as well as mechanical material parameters plausible for human breast tissue. In this context, dynamic characteristics of the forward solution are presented. The second section analyzes the surface motion error functional that governs the inverse problem, and is defined as the difference between the measured and simulated surface motion. These fundamental considerations facilitate a strategic approach to the design of appropriate inverse solvers. They also highlight key parameters and problem areas involved in this computational problem.

3.1 Standard Models

This thesis deals primarily with standardized geometries in two and three dimensions which are used for numerical investigations. They have been chosen in analogy to the experimental DIET system currently used to obtain gelatine phantom-data [144]. This section provides an overview of the geometric models, the material parameters involved in the problem, and some impressions of the characteristics in the dynamic behavior of their forward BEM solutions.

3.1.1 Geometries

The two-dimensional models were a square geometry of 0.07m side-lengths, and a semi-ellipse of 0.07m base-length and 0.05m height, meshed with three-noded

quadratic line-elements. They are displayed in Figure 3.1, where an example of an inclusion is shown in the square geometry.

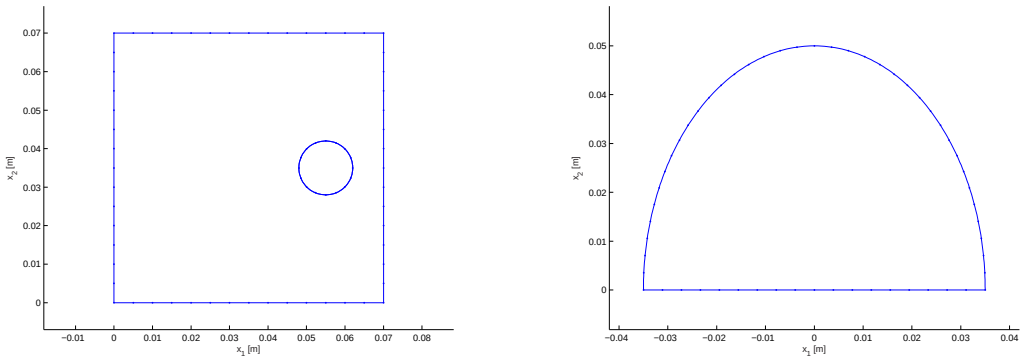

Figure 3.1 Two-dimensional standard geometries used for numerical investigations.

The three-dimensional models were a cylindrical geometry of 0.07m base-diameter and a height of 0.07m, as well as a semi-ellipsoidal geometry with a circular base of 0.07m in diameter and a height of 0.05m. Both are meshed with eight-noded quadratic surface elements of the Serendipity type [136] and are shown in Figure 3.2. A section of the outer surface is cut out of the hemispherical geometry to illustrate the presence of an ellipsoidal inclusion, meshed with 24 quadratic surface elements.

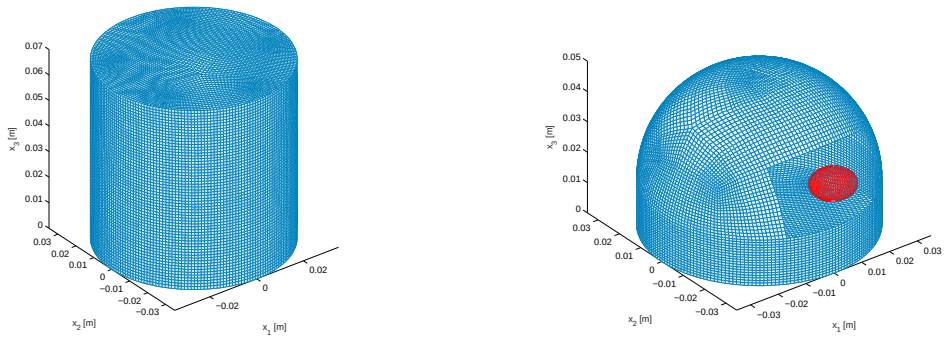

Figure 3.2 Three-dimensional standard geometries used for numerical investigations.

Harmonic Actuation of the models was applied in all cases with a maximum frequency, f, of $100Hz$ from the bottom side of the model by prescribing Dirichlet-type boundary conditions. Typically, longitudinal input boundary displacements were applied as an amplitude operating sinusoidally in the x_3 direction at frequency Ω, with zero displacements applied in the x_1 and x_2 directions. Traction-free boundary conditions (Neumann-type) were applied to the remaining surfaces

in all coordinate directions. Hence, in physical terms, a typical longitudinal wave is induced, where the wavelength Γ can be evaluated as:

$$\Gamma = \frac{c}{f}, \tag{3.1}$$

where the frequency $f = \Omega/2\pi$, and c is chosen the longitudinal wave velocity c_p in this case.

3.1.2 Model Parameters and Assumptions

The parameters relevant to this problem and its eventual inverse problem solution are the mechanical material parameters for both regions and the geometrical parameters that describe the inclusion location and dimension.

3.1.2.1 Mechanical Material Parameters

A complete material description of a homogeneous, isotropic material is provided by three independent material parameters. These parameters are chosen, in this work, as Young's modulus, E, Poisson ratio, ν, and density, ρ. All remaining material constants relevant in the BEM solution, μ, λ, c_p and c_s can be determined from these three fundamental parameters using Equations (2.5) and (2.25).

Internal attenuation effects are also apparent in the dynamics of biological tissues, but only the real part of the elastic modulus $E_{\mathcal{R}}$ has been shown relevant for clinical interpretation in breast cancer diagnosis [54]. Thus, numerical investigations here are always carried out with respect to $E_{\mathcal{R}}$, while the imaginary part $E_{\mathcal{I}}$ was assigned automatically using the viscous damping parameter β and Equation (2.10). For the sake of a clearer interpretation of results, this separation was also applied to the density parameters, $\rho_{\mathcal{R}}$ and $\rho_{\mathcal{I}}$, using an inertial damping parameter, α. A damping ratio, ζ, can then be obtained from Equation (2.11).

Since an inclusion is small in comparison to the background region, global attenuation effects will largely depend on the damping parameters of the region immediately around the inclusion. It was, therefore, assumed that the values of α and β do not change between the background and the inclusion. However, the damping ratio is expected to take significant values in a real situation. Therefore, a complete material model is defined, when α and β are given in terms of the entire volume, and $E_{\mathcal{R}}$, ν and $\rho_{\mathcal{R}}$ are given independently in terms of each region, indicated with superscript ^{I} for the background region and ^{II} for an inclusion.

The material parameters for breast tissue are known to vary within a range of values, due to structural changes of tissue with age, menstrual cycle and other physiological changes [145]. Plausible values [52] for the material are given:

- $E^I_{\mathcal{R}} \in [20,\ 30]kPa$
- $\rho^I_{\mathcal{R}} \in [950, 1050]kg/m^3$
- $\nu^I \in [0.45, 0.5]$
- $\zeta \in [5, 50]\%$
- $E^{II}_{\mathcal{R}} \in [20,\ 250]kPa$
- $\rho^{II}_{\mathcal{R}} \in [950, 1050]kg/m^3$
- $\nu^{II} \in [0.45, 0.5]$

Considering these material parameters, the mesh was found to be convergent in case of shear actuation with $f = 100Hz$, when the characteristic length of an element was no longer than $0.01m$. This characteristic length is hence approximately one third of a shear wavelength, given above parameters.

3.1.2.2 Geometric Parameters

The shape of a cancerous lesion within the breast will vary arbitrarily in specific cases, but can generally be described as ellipsoidal without significant loss of accuracy. Hence, the geometric parameters required for the unique definition of the inclusion is the location P within the geometry, the elliptical axes parameters, a_i, and a rotation ϑ in space, as illustrated in Figure 3.3. Note, that the two-dimensional case requires only one rotation $\vartheta = \vartheta_1$ and the three-dimensional case requires two rotations $\vartheta = (\vartheta_1,\ \vartheta_2)^T$ to fully define an elliptical body in two- or three-dimensional space in the sense of Euler's rotational coordinate transformation.

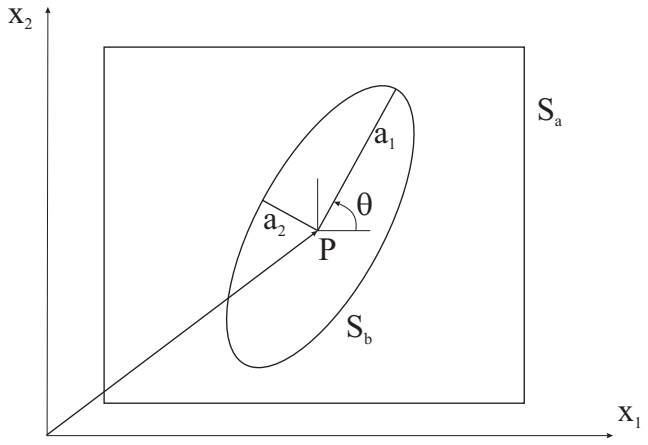

Figure 3.3 Parametric definition of an elliptic inclusion in a $2D$ domain.

3.1.3 Forward-Solution Characteristics

A typical response for the four test-geometries introduced in section 3.1.1, is shown in Figure 3.4. All solutions shown are simulation results corresponding to a sinusoidal actuation at the geometries' bottom side with an amplitude of $1mm$, although the actuation direction, and frequency, as well as the material properties, vary from case to case.

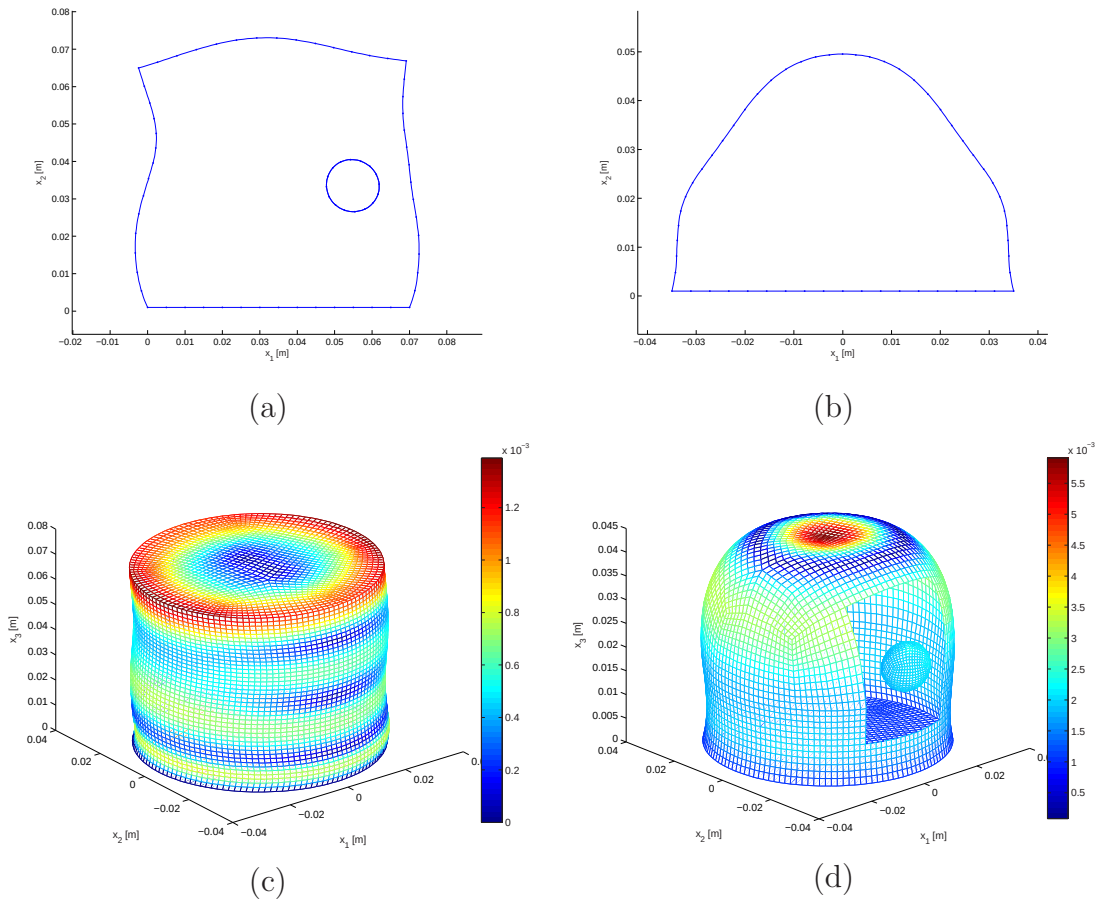

Figure 3.4 Typical displacement solutions for 2D and 3D test geometries in different parameter configurations.

In Figure 3.4 (a), material parameters were chosen at $E^I_{\mathcal{R}} = 30kPa$, $\nu^I = 0.49$, $\rho^I_{\mathcal{R}} = 950kg/m^3$, and $E^{II}_{\mathcal{R}} = 200kPa$, $\nu^{II} = \nu^I$, $\rho^{II}_{\mathcal{R}} = \rho^I_{\mathcal{R}}$ at $\alpha = 1$ and $\beta = 1 \cdot 10^{-4}$ at vertical actuation with $f = 50Hz$ (damping ratio $\zeta = 1.73\%$). Despite the outer geometry being perfectly symmetric in shape, it can clearly be recognized that the dynamic displacements are not symmetric, due to the presence of a circular inclusion of $7mm$ radial size and with a ten times stiffer elastic modulus than its surrounding.

The BEM solution of the homogeneous, semi-elliptical domain, shown in Figure 3.4 (b), was obtained using $E_{\mathcal{R}} = 18kPa$, $\nu = 0.45$ and $\rho_{\mathcal{R}} = 1000kg/m^3$ at low damping, $\alpha = 1$ and $\beta = 5 \cdot 10^{-5}$, and vertical actuation with $f = 100Hz$ ($\zeta = 1.65\%$). As expected, a longitudinal wave-pattern with symmetry to the semi-ellipse's vertical center axis can clearly be seen.

Figure 3.4 (c) shows the displacement results of the cylindrical geometry, subjected to a shear actuation applied at its bottom side in the x_1-direction ($x_2 = x_3 = 0$) at $f = 50Hz$. Material parameters were chosen $E_{\mathcal{R}} = 20kPa$, $\nu = 0.45$ and $\rho_{\mathcal{R}} = 1000kg/m^3$, with increased damping at $\alpha = 30$ and $\beta = 3 \cdot 10^{-4}$ ($\zeta = 9.49\%$). A regular shear-wave pattern can be seen to propagate along the cylinder surface, as expected for this homogeneous geometry.

The semi-ellipsoidal geometry in Figure 3.4 (d) was calculated using $E^I_{\mathcal{R}} = 20kPa$, $\nu^I = 0.48$, $\rho^I_{\mathcal{R}} = 1000kg/m^3$, and $E^I I_{\mathcal{R}} = 200kPa$, $\nu^{II} = \nu^I$, $\rho^{II}_{\mathcal{R}} = \rho^I_{\mathcal{R}}$ at $\alpha = 0$ and $\beta = 2.5 \cdot 10^{-5}$ for a vertical actuation at $f = 50Hz$ ($\zeta = 0.39\%$). In this three-dimensional case, the stiff inclusion was an ellipsoid with semi-axes $\mathbf{a} = (5, 6, 7)^T mm$ and 30° rotation in ϑ_1 and ϑ_2. Here, the inclusion does not appear to have large effects on the global displacement patterns. However, inspection of the displacement values at the surface near to the inclusion highlights clear differences, when compared to the homogeneous (no inclusion) case.

The effect of heavy internal damping is illustrated in Figure 3.5, where $\alpha = 120$ and $\beta = 5 \cdot 10^{-4}$ ($\zeta \approx 25\%$). Simulation parameters have been chosen at $E_{\mathcal{R}} = 20kPa$, $\nu = 0.5$ and $\rho_{\mathcal{R}} = 1000kg/m^3$ at the same shear actuation conditions, as applied in Figure 3.4 (c), but at frequency $f = 75Hz$. It can be seen that shear waves of the same characteristic establish on the geometry's surface. However, they attenuate quickly and are clearly recognized only up to about half the geometry's height.

3.1.4 Frequency Response

To illustrate the frequency characteristics of the models, a pseudo-amplitude response, $|A|$, was defined as the Euclidian norm over the vector of absolute nodal displacements of a mesh, $|\mathbf{u}|$:

$$|A| = \sqrt{|\mathbf{u}|^T |\mathbf{u}|}. \tag{3.2}$$

This pseudo-amplitude is a summation, rather than a true frequency response function, and characterizes the relative vibration amplitudes. Therefore, it facil-

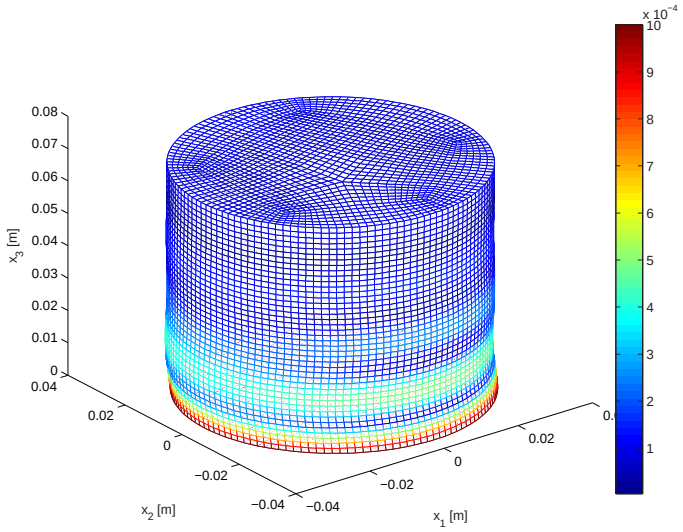

Figure 3.5 Attenuated motion behavior of a 3D cylinder shear actuated at its bottom side at $f = 75Hz$ and damping ration of $\zeta \approx 25\%$.

itates the identification of resonant frequencies for a given model in response to the actuation applied.

Simulations were carried out for the models introduced in the previous section using the same material parameters as described for the forward simulations in Figure 3.4 (a)–(d). However, a constant damping ratio was applied over the frequency range of interest, $f \in [1, 120]Hz$. It was assumed that the inertial and viscous damping parameters have equal influence on the motion behavior, thus $\alpha/\Omega = \beta\Omega$. The parameters α and β were then calculated from a prescribed damping ratio, ζ:

$$\alpha = \zeta\Omega \quad \text{and} \quad \beta = \frac{\zeta}{\Omega}. \tag{3.3}$$

Figure 3.6 shows the frequency response of the square geometry containing an inclusion. Figure 3.6 (a) shows the undamped case ($\zeta = 0\%$) and 3.6 (b) the response at a damping ratio of $\zeta = 10\%$. The undamped case clearly shows rich dynamic behavior, with a large number of resonant frequencies in the simulated range. There is also a number of relatively small peaks present in the pseudo-amplitude. For an increase in the damping ratio, it is recognized that the higher modes in particular are damped quickly and the overall amplitude response is decreased at high frequency. At $\zeta = 10\%$, only one resonant mode at $f_r \approx 24Hz$ remains significant in the simulated frequency range, whereas other

modes at higher frequencies have largely been damped out. This significant peak corresponds to the case, where the wavelength, Γ, is approximately half of the geometries height, and hence, waves originating at the actuation side are superposed with those waves reflected from the opposite side.

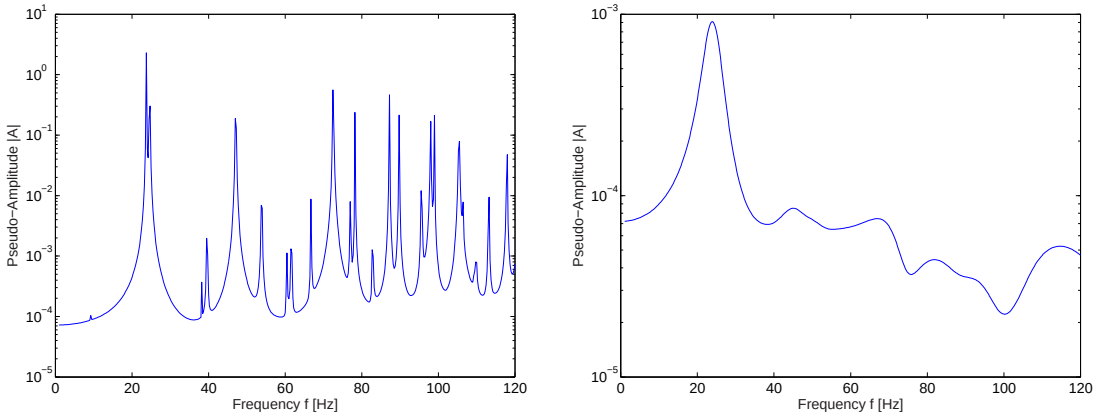

(a) $\zeta = 0\%$ (b) $\zeta = 10\%$

Figure 3.6 Pseudo frequency-response, $|A|$ (in meters), of a 2D cylinder containing a circular, stiff inclusion, in longitudinal actuation from the bottom side.

In contrast, Figure 3.7 illustrates the frequency response for the homogeneous semi-elliptical geometry. There are still a large number of resonant areas in the simulated frequency range, but this number appears to be significantly lower than in the case of the rectangular domain. The same decrease in high frequency amplitude is observed for an increase of damping ratio. At $\zeta = 10\%$, there is again only one dominant mode at $f_r \approx 26.5Hz$. However, a distinct anti-resonant frequency has appeared at $f_a \approx 70Hz$.

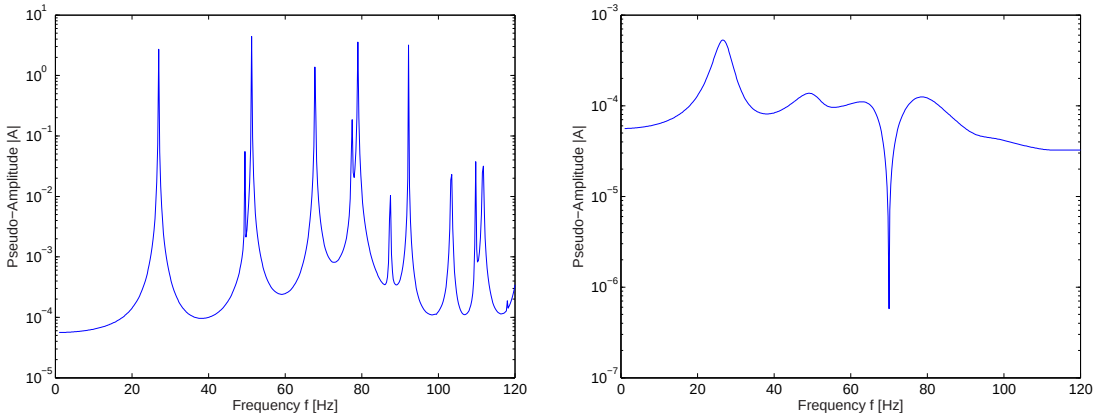

(a) $\zeta = 0\%$ (b) $\zeta = 10\%$

Figure 3.7 Pseudo frequency-response, $|A|$ (in meters), of a homogeneous 2D semi-ellipse in longitudinal actuation.

The frequency response in the $3D$ case appears very similar to the $2D$ case. Figure 3.8 shows the pseudo-amplitude response from the homogeneous cylindrical geometry in shear actuation at $\zeta = 0$ (a), and $\zeta = 10\%$. It is notable that the motion behavior here is richer than that observed with longitudinal actuation and there exists a much larger number of resonant areas responding to the shear actuation. In the damped case, two distinct frequencies at $6.5Hz$ and $17.5Hz$ remain resonant, and anti-resonant areas emerge at much lower frequency than in the longitudinal case.

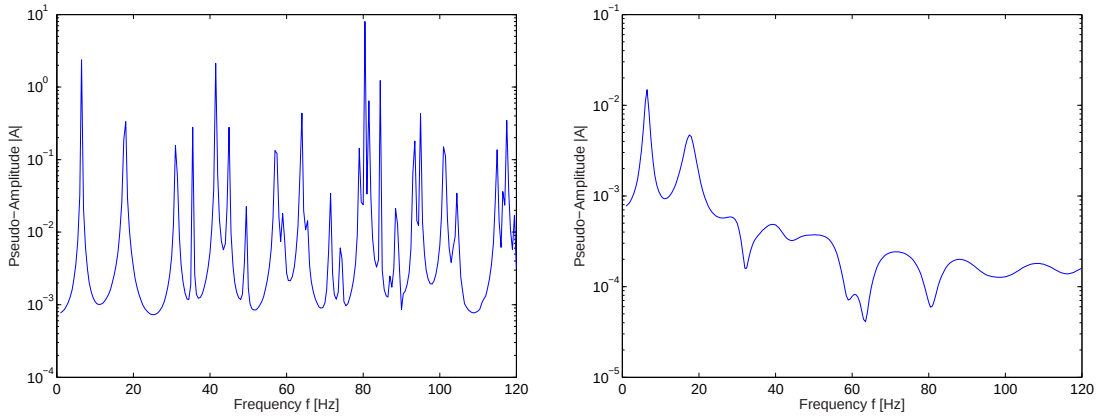

(a) $\zeta = 0\%$ (b) $\zeta = 10\%$

Figure 3.8 Pseudo frequency-response, $|A|$ (in meters), of a homogeneous 3D cylinder in shear actuation.

Figure 3.9 illustrates the pseudo-amplitude response for the semi-ellipsoidal geometry with an inclusion of ellipsoidal shape, as introduced in Figure 3.4 (d). Similar to the frequency response of the previous geometries, damping shows greater effect in the upper end of the frequency range, where two distinct anti-resonant areas appear. It is interesting to note that the undamped case again shows a large number of small peaks, which have the appearance of a disturbance of the global response.

3.1.5 Discussion

In this section, a definition and brief dynamic overview was provided of the models predominantly used for numerical investigations in this thesis. It includes the fundamental definition of the material and geometric parameters involved in the BEM forward and inverse problems. Some characteristic forward solution cases for different material and geometric conditions were shown together with their

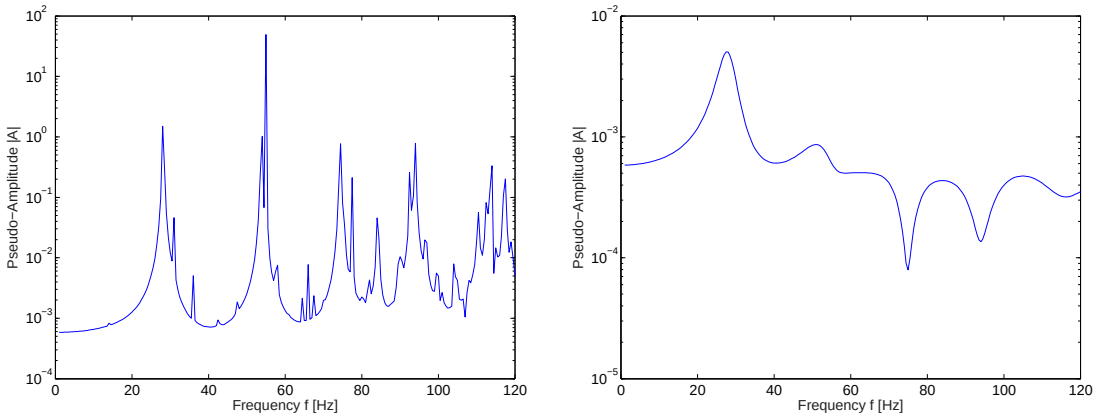

(a) $\zeta = 0\%$ (b) $\zeta = 10\%$

Figure 3.9 Pseudo frequency-response, $|A|$ (in meters), of a 3D semi-ellipsoid with an ellipsoidal inclusion in longitudinal actuation.

frequency response. The following discussions contains points that are of interest with respect to the reconstruction algorithm to be designed and are noted:

- The parametric definition of an inclusion as an ellipse or an ellipsoid, in 2D or 3D cases respectively, allows the approximation of a wide range of shapes in the model that can be forward solved uniquely. However, it is apparent that same uniqueness will be lost in the inverse problem, as the same elliptic shape may be produced with several different combinations of parameters. Bound constraints may therefore have to be introduced to any inverse problem, but may not be advantageous with respect to the performance of the algorithm. However, since the practical goal of this application is an indication for the potential presence of a stiff inclusion, this non-uniqueness may be irrelevant, so long as convergent behavior of the conversion algorithm is still maintained.

- Because the inverse problem is solely orientated on the surface motion error, it is important to maximize the amount of information available at the boundaries. Rich dynamic behavior is observed at higher frequencies, where wavelengths become small. However, these frequencies appear to be heavily attenuated when simulated at the higher damping ratios expected in tissue. Hence, higher frequency actuation may not be ideal for this application. In contrast, it has also been observed that shear actuation introduces very rich motion patterns on the surface, due to the short shear wave lengths, c_s.

- To maximize surface motion information, the actuation frequency, Ω, should also be chosen carefully. It could be advantageous to use actuation frequen-

cies that are at or near resonant areas, to maximize the resulting amplitudes. As a side effect, this approach could also decrease the measurement error relative to the motion amplitudes. Anti-resonant frequencies should be strictly avoided.

- There is an interesting observation in the pseudo-frequency response function $|A|$, where a large number of small peaks appear in cases where an inclusion is present. These peaks may be interpreted as a disturbance of the homogeneous system due to the presence of the second inclusion stiffness value and the resulting presence of a second set of wave speeds. These disturbances are quickly diminished once damping is introduced to the system. Hence, they may not be able to be measured in a real situation. However, they may give rise to a potential approach in solving this problem kind.

3.2 Surface Motion Error Analysis

The surface motion error forms the primary functional for the elastic reconstruction problem in the DIET-system. It is defined as the difference between motion data gathered from a surface measurement and surface motion calculated from forward simulations with different parameter configurations. This section explores the surface motion error function for the DIET problem. The goal is to determine and define the key parameters and specific requirements for the setup of an effective BEM-based reconstruction algorithm for the DIET problem. Errormaps are therefore constructed and examined with respect to the material and geometric parameters involved in the inverse problem.

3.2.1 Methods and Errormap Simulations

The BEM, introduced in chapter 2, was used to determine the quadratic surface motion error functional, Ψ, defined:

$$\Psi = \mathbf{e}^H \mathbf{e}, \tag{3.4}$$

where $\mathbf{e}^H$ is the Hermitian transpose of the displacement error, defined:

$$\mathbf{e} = \mathbf{u}^\star - \mathbf{u}, \tag{3.5}$$

where $\mathbf{e}$ is the difference of the steady-state harmonic surface motion, $\mathbf{u}^\star$, given at a certain configuration of initial values (reference-values) of material and geometrical parameters, $\boldsymbol{\theta}^\star$, and the surface motion, $\mathbf{u}$, resulting from a changed parameter configuration $\boldsymbol{\theta}$.

Errormaps in this initial examination were obtained using $2D$ geometries, to keep the computational effort to a minimum, while providing high resolution results. They also simplify some of the visualizations and the analysis of the results, without any loss of generality. For this purpose, the square and semi-elliptical geometries shown in Figure 3.1, have been chosen. Each geometry is harmonically actuated at its bottom side in the x_2-direction with an amplitude of 1mm at a frequency of $50Hz$.

Several different configurations were employed for the reference configuration. In the first configuration, a single homogeneous body is simulated. In the other configurations, a single circular inclusion was inserted into the geometry at one of three different locations indicated in Figure 3.10, with radial sizes ranging between 1mm and 5mm for the single inclusion used.

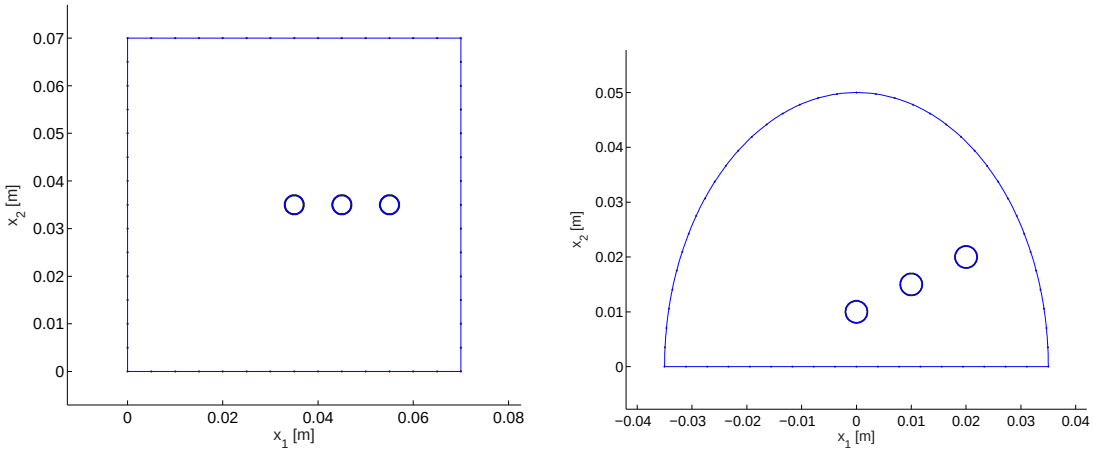

Figure 3.10 Inclusion locations used in the $2D$ reference geometries for the analysis of errormaps.

Assuming the body's behavior to be governed by the equation for harmonic linear elasticity in Equation (2.7), seven parameters of interest, $\boldsymbol{\theta}^\star$, were chosen as being most relevant in this problem:

- $E^I_{\mathcal{R}}$ = Young's Modulus of the outer region,
- ν = Poisson's ratio, assumed to be equal for region I and II,

- $\rho_{\mathcal{R}}$ = Density, also assumed to be the same for both regions,
- β = the viscoelastic damping parameter, similarly assumed to affect both regions equally,
- R = Radial size of the inclusion,
- $E^{II}_{\mathcal{R}}$ = Young's modulus of the interior region,
- P = Location of the inclusion within the given geometry.

Note that the inclusion's location, P, is a generalized parameter that fully presents the two- or three-dimensional spatial description of the inclusion's position within the domain. All remaining material parameters, namely the shear modulus μ, the wave speeds c_s and c_p, and Lamé's constant λ are therefore defined in terms of each region. Similarly, the interface between the inclusion and the outer region is defined in parametric form and easily meshed, given the number of elements to be used on the interface mesh.

Maps of the error-metric Ψ for particular parameters were obtained by repeatedly comparing motions, $\mathbf{u}^{\star}$, calculated for a reference property description, to motions, $\mathbf{u}$, generated from variations in the relevant parameter over a range of plausible values, $\boldsymbol{\theta}$. Results of this investigation can be plotted as two-dimensional contour plots of the multidimensional error function within the plane corresponding to the selected parameters.

The first 15 parameter pairs were determined by combining the first six parameters $E^{I}_{\mathcal{R}}$, ν, $\rho_{\mathcal{R}}$, β, R and $E^{II}_{\mathcal{R}}$, while maintaining the correct value $P^{\star}$ for the inclusion's location. An errormap in the spatial domain was generated by the variation of the location P alone, since this variation forms a two-dimensional errormap by itself (in the case of simulations in 2D). Note that the variation of P is restricted to a space within the overall volume, as no overlap is allowed to occur between the inner and outer region boundaries.

A third set of information about the error-domain was obtained by calculating the spatial errormap, while allowing variation in one of the remaining parameters, $E^{I}_{\mathcal{R}}$, ν, $\rho_{\mathcal{R}}$, β, R and $E^{II}_{\mathcal{R}}$. Extracting the minimum and maximum error value from each spatial errormap enabled a plot of the span of error values over a single parameter. Furthermore, since the minimum error value in each spatial errormap is to be interpreted as an indication for the solution of the inclusion location, $\bar{P}$, a spatial distance $|\mathbf{d}|$ between the identified location of minimum error, $\bar{P}$, and

the correct location $P^\star$ can be calculated for each non-spatial parameter $E^I_{\mathcal{R}}$, ν, $\rho_{\mathcal{R}}$, β, R and $E^{II}_{\mathcal{R}}$:

$$|\mathbf{d}| = |\bar{P} - P^\star|. \tag{3.6}$$

In all cases, the solution parameters $\boldsymbol{\theta}^\star$ were chosen at plausible for human breast tissue containing a stiff inclusion, and are listed in Table 3.1 together with the range of acceptable values for variation.

	Reference Configuration $\boldsymbol{\theta}^\star$	Range of Variation $\in$	Relative Variation
$E^I_{\mathcal{R}}$	$20\,kPa$	$[10, 20]\,kPa$	$\pm$ 50%
ν	0.45	$[0.4, 0.5]$	$\pm$ 11.1%
$\rho_{\mathcal{R}}$	$1000\,kg/m^3$	$[900, 1100]\,kg/m^3$	$\pm$ 10%
β	0.0005	$[0, 0.001]\,s/rad$	$\pm$ 100%
R	$3\,mm$	$[1, 10]\,mm$	-66.6%, +233.3%
$E^{II}_{\mathcal{R}}$	$50\,kPa$	$[15, 70]\,kPa$	-70%, +40%

Table 3.1 Simulation Parameters with their allowed Range of Variation investigated in the Errormaps

The errormaps resulting from the rectangular geometries are presented in the subsequent sections accompanied by a discussion. The semi-elliptical geometry and other similar test-geometries produced the same characteristics with only slight differences in the quantity of error-values, and are discussed in less detail. Note that each errormap highlights it's local minimum corresponding to the reference parameter $\boldsymbol{\theta}^\star$ with a light colored hexagram in the dark blue minimal error region. In the first set of maps shown, the local minimum is always identical to the global solution $\boldsymbol{\theta}^\star$.

3.2.2 Errormaps with Convex Characteristics

Figures 3.11 and 3.12 show the errormaps for all ten possible pairs of the parameters β, ν, $\rho_{\mathcal{R}}$, R and $E^{II}_{\mathcal{R}}$. Note that the color-coding in these Figures is scaled non-linearly to emphasize the characteristics of the error maps, rather than performing a qualitative analysis. Figures 3.11 (a) and (b) are only presented over a part of the variation, as their local maxima, located at the search limits, are several orders larger than the minimum, resulting in a misleading contour-plot despite the use of logarithmic scaling.

The maps containing the parameter E_{II} appear to have a constant behavior, when plotted versus β, ν and $\rho_{\mathcal{R}}$ as seen in Figure 3.11 (d), and Figures 3.12

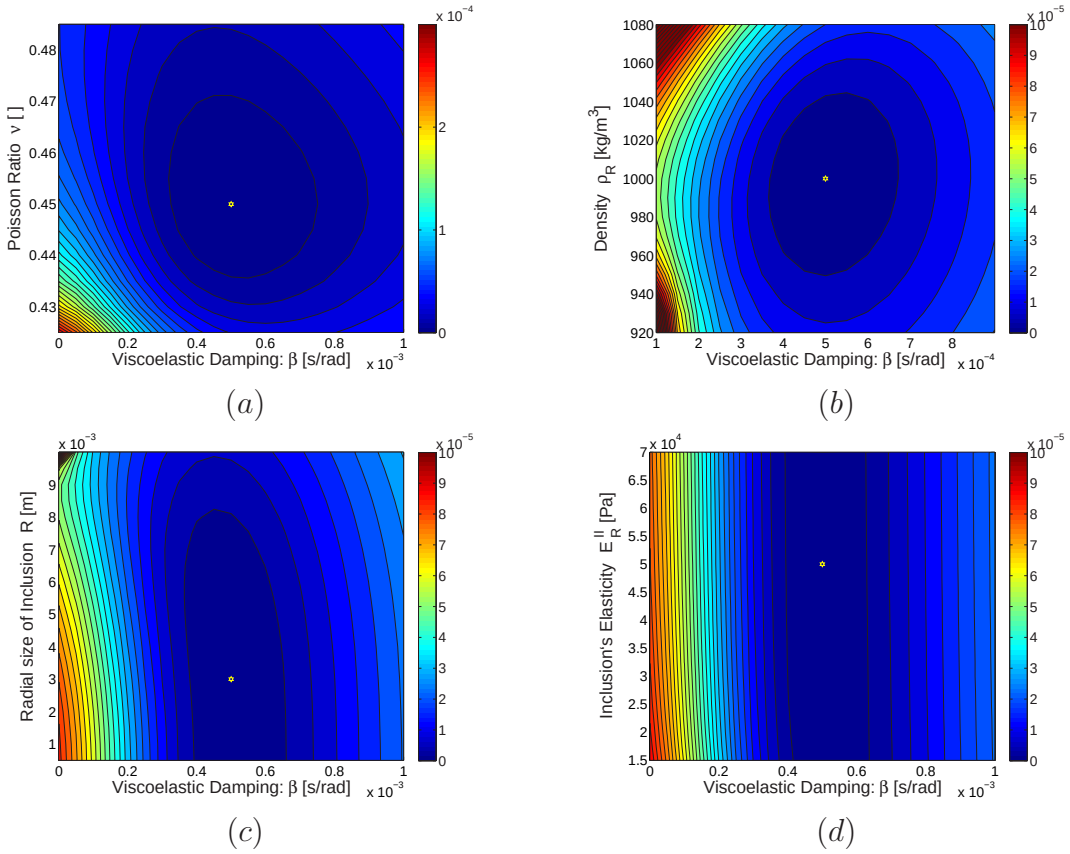

Figure 3.11 Errormaps with convex characteristics (first set in $[\beta, \nu]$, $[\beta, \rho_{\mathcal{R}}]$, $[\beta, \nu]$, $[\beta, R]$ and $[\beta, E^{II}_{\mathcal{R}}]$) with the error-value, Ψ, in m^2

(c) and (e). This result can be explained by the relatively small volume of the inclusion and its resulting small impact on the overall surface-motion. Similar behavior is observed for the inclusion's size R as seen in Figures 3.11 (c) and Figures 3.12 (b), (d) and (f). However, it can clearly be seen that the overall impact of the inclusion on the level of error-value increases strongly with increasing size, but not with decreasing size, where a limit value is reached when R approaches zero.

An interesting observation can also be made inspecting Figure 3.12 (f), the errormap of R vs. E_{II}. It can be seen that, again, a certain limit error value is reached when the inclusion's Young's Modulus reaches the value of the outer region, $E_I = E_{II} = 20kPa$. The error-value along the straight line $E_{II} = E_I$ is constant and independent of the size R of the inclusion. This line corresponds to the result for a single domain geometry without an inclusion and with an overall Young's modulus of $20\,kPa$.

In summary, all errormaps presented in Figures 3.11 and 3.12 commonly illustrate reasonably convex characteristics with one single minimum at the correct

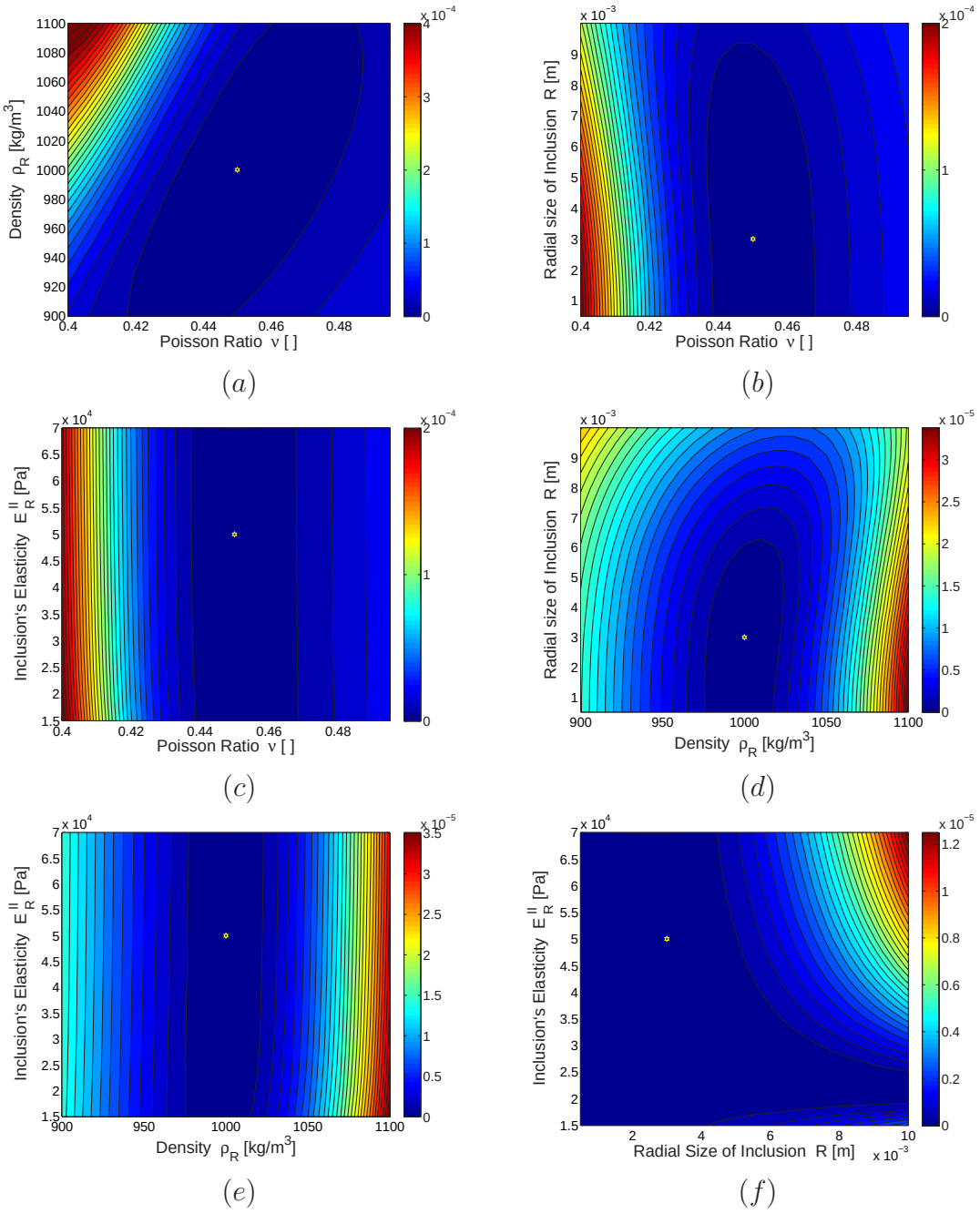

Figure 3.12 Errormaps with convex characteristics (second set in $[\nu, \rho_{\mathcal{R}}]$, $[\nu, R]$, $[\nu, E^{II}_{\mathcal{R}}]$, $[\rho_{\mathcal{R}}, R]$, $[\rho_{\mathcal{R}}, E^{II}_{\mathcal{R}}]$ and $[R, E^{II}_{\mathcal{R}}]$) with the error-value, Ψ, in m^2

value of $\boldsymbol{\theta}^{\star}$. If these parameters were to be used as variables in a gradient descent based inverse algorithm, with the purpose of identification from surface motion, it is expected (but cannot be guaranteed) that the optimization approach should be well behaved. This promise would be particularly valid, where the start-values are within the limits used here.

3.2.3 Nonlinear or Non-convex Errormaps

Figure 3.13 shows all combinations of β, ν, $\rho_{\mathcal{R}}$, R and $E^{II}_{\mathcal{R}}$ versus the outer region's Young's Modulus $E^{I}_{\mathcal{R}}$. The plot (a), β vs. $E^{I}_{\mathcal{R}}$, is again shown only over a part of the simulated range to better illustrate its behavior. All maps in Figure 3.13 illustrate *wall-like* nonlinear behavior, where one side of the error-domain has a steep peak with a local minimum on the other side of it. This behavior results in two or three distinct local minima within the search domain, including those at the boundary of the variable range.

In conclusion, if $E^{I}_{\mathcal{R}}$ was an unknown parameter to be found by gradient descent techniques, it is likely to be a non-convex problem. Hence, it will be possible to converge to a local minimum that is not the global solution to this inverse problem, if a poor start value is chosen.

3.2.4 Spatial Errormaps

Figure 3.14 shows two representative errormaps generated by a scan for the inclusion's position within the geometry. The range of locations was scanned between $P_{x_1}, P_{x_2} \in [0.015m, 0.055m]$. All other parameters, including material parameters, the inclusion's size and circular shape, were assumed to be known.

Figure 3.14 (a) shows a scan performed at an inclusion size of $R = 3mm$, and Figure 3.14 (b) at $R = 1mm$. A minimum distance of $12mm$, or $14mm$, respectively, is left between the inclusion's boundary and the edge of the outer geometry.

The solution in the first errormap in Figure 3.14 (a) is found correctly at $P = (0.045m, 0.035m)$ where the solution was simulated at $R = 3mm$. It can be clearly seen that this errormap demonstrates highly nonlinear behavior, with several distinct maxima and saddle-points. There are also five different local minima appearing over the domain, three of which are on the errormap's boundary. The global minimum appears to have the largest region of attraction. However, the overall maximum amplitude of error-values is very low, on the order of $10^{-7}\, m^2$.

Repeating the simulation at $R = 2mm$ yields the same qualitative results as shown in Figure 3.14 (a). However, Figure 3.14 (b) shows the results for a small inclusion of $R = 1mm$. Despite the global minimum being highlighted at the correct location and some degree of structure still being present, the errormap appears to consist primarily of numerical noise. The order of maximum motion difference has now dropped to $10^{-8}\, m^2$, reaching a similar accuracy to which the

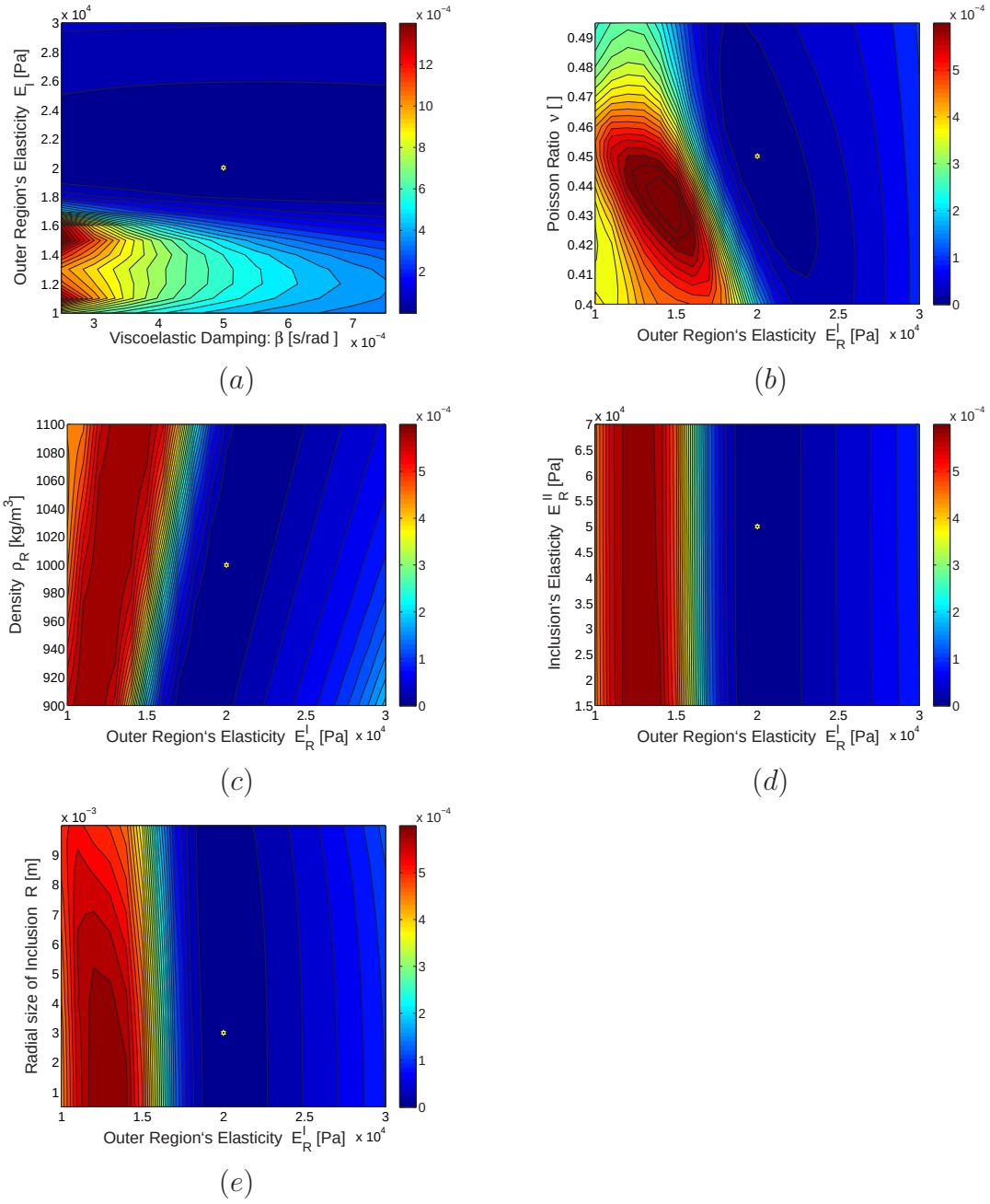

Figure 3.13 Errormaps with nonlinear characteristics (1), error-value, Ψ, given in m^2

integrals in the BIE (see Section 2.3) were evaluated. Thus, it can be stated that an inclusion of size $R = 1mm$ does not result in surface motion error large enough to realistically distinguish between error-values determined at different inclusion locations. All other scans performed for the different inclusion locations shown in Figure 3.10, as well as scans performed at sizes $R > 3mm$, lead to qualitatively similar results to those shown in Figure 3.14 (a).

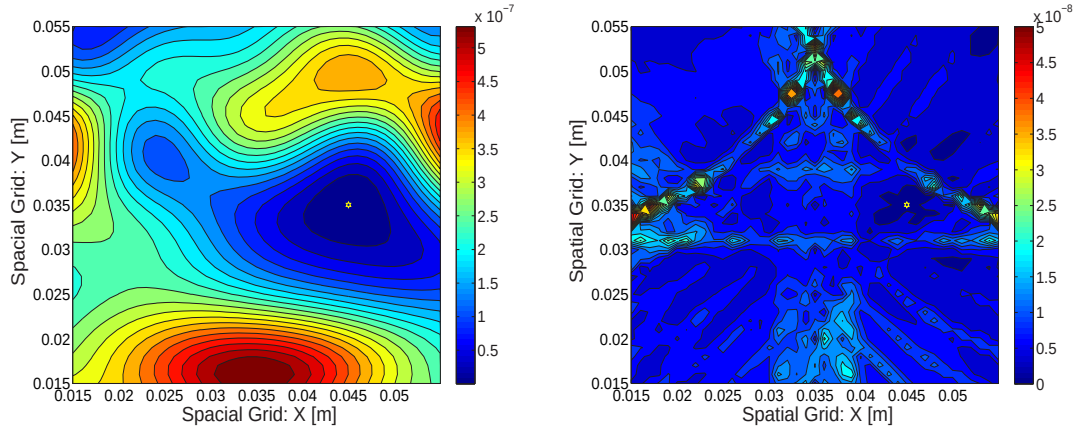

(a) (b)

Figure 3.14 Spatial errormap for the inclusion's location simulated at (a) R = 3mm and (b) R = 1mm, error-value, Ψ, given in m^2

Further investigating the spatial error domain, Figure 3.15 shows the span of minimum and maximum error-values recorded in a spatial errormap over each of the other six parameters. The second plot illustrates the spatial distance $|\mathbf{d}|$ between the inclusion location $\bar{P}$ indicated by the observed minimum error and the correct location $P^{\star}$. Figure 3.15 highlights that the error-span in the spatial errormaps is never very large compared to the overall change in error experienced over the varied parameter. Figures 3.15 (e) and (f) are the exceptions, as they are the maps for the inclusion parameters R and $E^{II}_{\mathcal{R}}$. These results confirm the previously observed tendencies to a constant error of $\Psi \approx 1.45 \times 10^{-7}$ when $R \to 0$ or $E^{I}_{\mathcal{R}} \to E^{II}_{\mathcal{R}}$.

It is observed in the plots of the error-span (Figure 3.15) that most parameters show a reasonably convex behavior, while nonlinearities are caused mainly by the outer region's Young's Modulus with error-values Ψ of the order $10^{-4}\, m^2$. Nonlinear behavior can also be expected from the inclusion's elasticity. However, the relatively small inclusion size does not have significant effect, as seen in the errorspan in Figure 3.15 (f), where values of Ψ are only of the order $10^{-7}\, m^2$.

The plots of parameter variation vs. distance $|\vec{d}|$ in Figures 3.15 (a)–(f) can be interpreted as a direct description of the quality of the location-solution obtained by spatial errormaps. These plots appear to be extremely sensitive and show several jumps in $|\mathbf{d}|$ due to abrupt changes in the location of the error minimum. Apart from Figure 3.15 (f), the inclusion's location is only obtained correctly once the other parameters are absolutely correct. In addition, even the slightest discrepancy can lead to an incorrect solution.

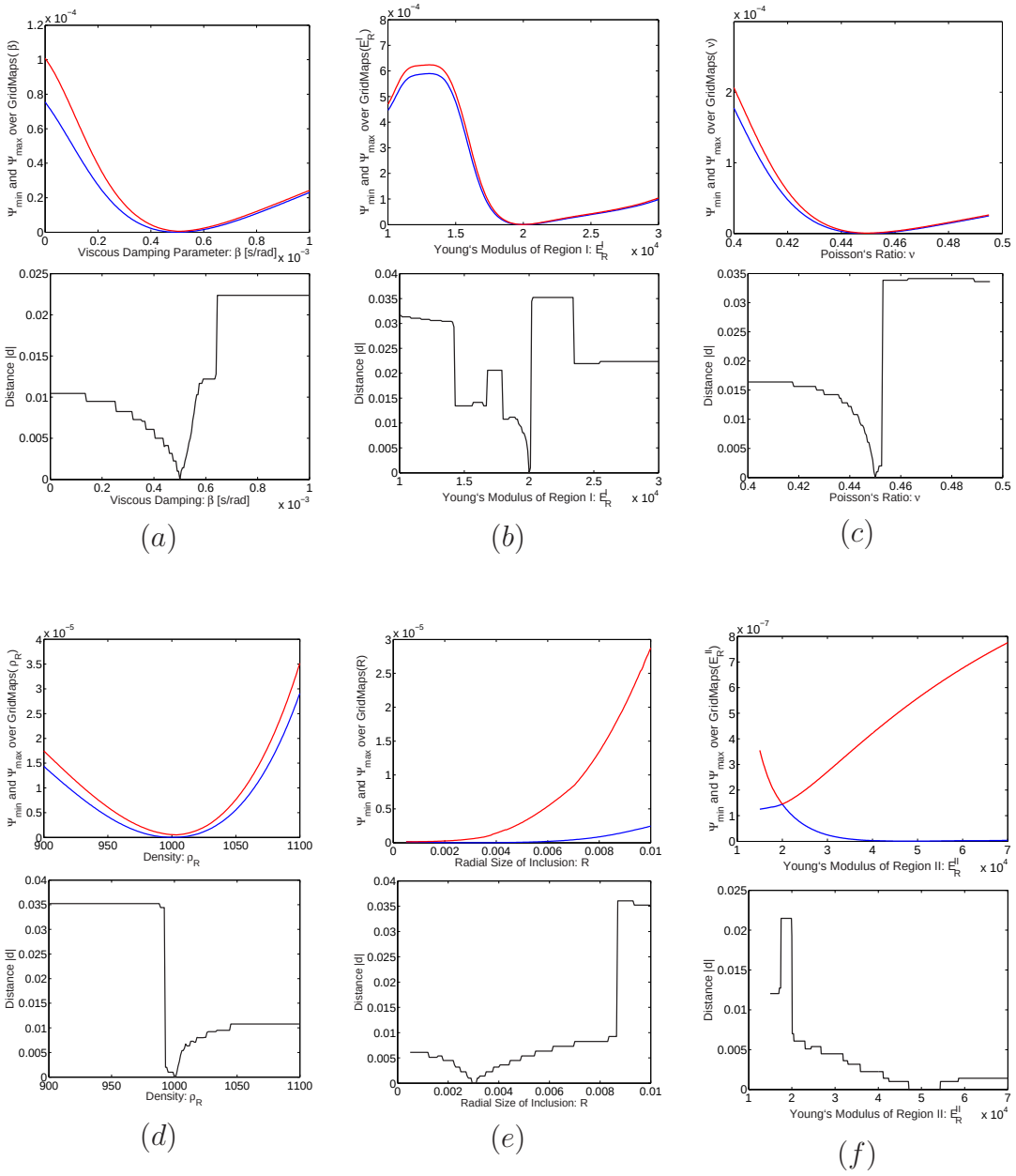

Figure 3.15 Characteristics of spatial errormaps and error in reconstructible inclusion location resulting from a systematic change of another problem parameter. Error-values, Ψ_{min} and Ψ_{max}, given in m^2.

In summary, it can be stated that a spatial grid search could successfully determine an inclusion's location from surface motion error, although the accuracy of this solution is dependent on a reasonable fit for all relevant parameters. However, inclusions smaller than $2mm$ in radial size appear to be below the limits of numerical accuracy with current methods.

3.3 Conclusions

The study of errormaps generated by surface motion error solely clearly shows the possibility of successfully using BEMs in the elastographic inverse problem to reconstruct material parameters and the location of an inclusion. The observations made by the inspections of the errormaps lead to the following conclusions:

- Independent of its relative location within the given geometry, inclusions smaller than $2mm$ in radius may likely not be able to be detected from global surface motion error only.
- Determining the location of a sufficiently large inclusion using surface motion error is a highly nonlinear problem that has the potential to be successfully solved, but requires accurate knowledge of the outer region's material parameters, particularly $E^I_{\mathcal{R}}$, ν, $\rho^I_{\mathcal{R}}$ and the damping behavior, as represented by β in the cases shown.
- The highly sensitive error domain with strong non-linear behavior indicates that the use of large scale grid-search or stochastic based reconstruction methods will likely be a necessity for the successful solution of this problem. However, the determination of an accurate solution with a gradient descent technique should be enabled once quality start values are found.

From the observations made in the general behavior of the forward solution, one can conclude that the successful reconstruction will be a challenge in the presence of intense internal damping effects, where motion disturbance generated by an inclusion may not be propagated to the surface. However, carrying out the inverse problem in the case of rich surface motion, as encountered for example near resonant frequencies or shear actuation, may support the reconstruction process. Use of motion error information obtained at multiple frequencies may also prove useful.

Chapter 4

Inversion Methods

The solution of the governing Equations (2.7) by a numerical method, such as the BEM, is the so called *Forward Problem*. It can be solved uniquely for every feasible set of material parameters and arbitrary geometries and leads to a linear system of equations of the type $\mathbf{A}\,\tilde{\mathbf{x}} = \tilde{\mathbf{b}}$. In the case of the elastodynamic BEM, the system matrix, $\mathbf{A}$, and the system right hand side, $\tilde{\mathbf{b}}$, are assembled as a combination of the BEM system matrices, $\mathbf{F}$ and $\mathbf{G}$, as shown in section 2.3.

$$\mathbf{A}(\boldsymbol{\theta})\,\tilde{\mathbf{x}} = \tilde{\mathbf{b}}(\boldsymbol{\theta}) \tag{4.1}$$

Hence, $\mathbf{A}$ and $\tilde{\mathbf{b}}$ are explicitly dependant on the material and geometric parameters, $\boldsymbol{\theta}$. However, the problem to be solved in the DIET system is the *Inverse Problem*. In particular, the reconstruction of the material and geometric parameters, $\boldsymbol{\theta}$, given the relevant (measured) surface displacements, $\mathbf{u}$, that are a part of $\tilde{\mathbf{x}}$ in Equation (4.1) and an approximate solution or start value $\boldsymbol{\theta}^{(0)}$. The direct inversion of Equation (4.1) appears untractable, given the highly nonlinear nature of the fundamental solutions (Equations (2.30)–(2.37)) that form the coefficient matrix $\mathbf{A}$ and the coefficient vector $\tilde{\mathbf{b}}$. Hence, the solution of the inverse problem requires a more sophisticated, numerical optimization technique.

This chapter provides a summary of the relevant methods in optimization theory that have been implemented in this thesis for the use in the BEM based DIET reconstruction problem. It is not within the scope of this thesis to comprehensively review optimization methods, nor to enhance best choice algorithms for the DIET inverse problem. The interested reader is referred to the large range of detailed literature on optimization problems available. For example, Horst and Pardalos [146] offer a comprehensive review in global optimization, and similarly, Nocedal and Wright [143] do the same for continuous optimization problems.

4.1 Optimization Theory and Application to DIET

Optimization can be defined in general terms as the approach to increase the performance or decrease the cost of a given system by systematically manipulating its input parameters. In mathematical terms, this process can always be formulated as a minimization technique performed on a given objective function, Ψ, with respect to the parameters, $\boldsymbol{\theta}$:

$$\boldsymbol{\theta}^{\star} = \arg\min_{\boldsymbol{\theta}} \left(\Psi \right), \tag{4.2}$$

where $\boldsymbol{\theta}^{\star}$ is the optimal solution that can, in general, also be subject to generalized equality constraints, $h_i(\boldsymbol{\theta})$, and inequality constraints, $g_i(\boldsymbol{\theta})$:

$$\begin{aligned} g_i(\boldsymbol{\theta}) &= 0 \\ h_i(\boldsymbol{\theta}) &\geq 0. \end{aligned} \tag{4.3}$$

The successful solution of Equation (4.2) depends greatly on the type of inverse problem. Those types can be differentiated into constrained or unconstrained problems, discrete or continuous optimization, local or global optimization, and stochastic or deterministic problems. Each problem area is well known and provides numerous optimization algorithms. However, those problem areas overlap greatly, and, in most cases, any selected algorithm will have to be tuned to the particular problem. The choice of the algorithm is also significant with respect to its performance in the problem. Therefore, the following section will discuss the specific type of problem faced in the DIET system and the resulting choice of algorithms.

4.1.1 Properties of the DIET Optimization Problem

An objective function has been introduced in Section 3.2, where a preliminary analysis was carried out on the error-function's general behavior. This objective function has been slightly modified for the optimization algorithms implemented in this thesis, but with no effect to its qualitative behavior. It is now defined as:

$$\Psi = \frac{1}{2}\, \mathbf{e}^{H} \mathbf{e}, \tag{4.4}$$

where $\mathbf{e}$ is the displacement error, defined as the difference between the measured steady-state, harmonic surface motion, $\mathbf{u}^\star$, and the surface motion, $\mathbf{u}$, resulting from a BEM forward simulation at a certain parameter configuration $\boldsymbol{\theta}$:

$$\mathbf{e} = \mathbf{u}^\star - \mathbf{u}(\boldsymbol{\theta}). \tag{4.5}$$

It is apparent that all material and geometric reconstruction variables, $\boldsymbol{\theta}$, as introduced in Chapter 3, are, in general, complex valued continuous variables. As all quantities are fully specified in the problem formulation (Equation (4.4)), the inverse solution of Equation 4.2 is deterministic. Furthermore, while Equation (4.4) is a quadratic function in $\mathbf{e}$, $\mathbf{u}(\boldsymbol{\theta})$, the forward solution resulting from the BEM system Equations (4.1), is extremely nonlinear in $\boldsymbol{\theta}$ due to the nature of the fundamental solutions. Thus, the BEM-based DIET inverse problem is a deterministic, continuous, nonlinear optimization problem.

In addition, it is recognized from discussion in the foregoing chapter, Section 3.2, that local optima exist, and uniqueness is not guaranteed. Furthermore, small changes in the measured data may well result in significant changes in the reconstruction variables, $\boldsymbol{\theta}$, indicating a lack of robustness. Hence, the DIET inverse problem is also *ill-posed* and *ill-conditioned*.

4.1.2 Constrained versus Unconstrained Optimization

Considering a physiologically reasonable range for the values in $\boldsymbol{\theta}$ is simultaneous to the introduction of inequality constraints. For the material parameters in the DIET problem, one could choose:

$$\left.\begin{array}{rcl} E^I_{\mathcal{R}} & \geq & 20kPa \\ \nu & \geq & 0.45 \\ \rho^I_{\mathcal{R}} & \geq & 950kg/m^3 \\ \zeta & \geq & 2\% \\ E^{II}_{\mathcal{R}} & \geq & 20kPa \end{array}\right\} \quad \text{and} \quad \left\{\begin{array}{rcl} E^I_{\mathcal{R}} & \leq & 30kPa \\ \nu & \leq & 0.5 \\ \rho^I_{\mathcal{R}} & \leq & 1050kg/m^3 \\ \zeta & \leq & 50\% \\ E^{II}_{\mathcal{R}} & \leq & 300kPa \end{array}\right. \tag{4.6}$$

Similarly, the geometric parameters could be constrained to:

$$\left.\begin{array}{rcl} a_i & \geq & 2mm \\ \vartheta_1 & \geq & 0 \\ \vartheta_2 & \geq & -\frac{\pi}{2} \end{array}\right\} \quad \text{and} \quad \left\{\begin{array}{rcl} a_i & \leq & 20mm \\ \vartheta_1 & \leq & \pi \\ \vartheta_2 & \leq & \frac{\pi}{2} \end{array}\right. \tag{4.7}$$

These simple, rather non-problematic constraints are easily transformed into the general case in Equation (4.3). Their consideration could possibly support the algorithm in cases. In particular, they may be useful where qualitatively bad start values were chosen for a non-convex problem, resulting in physically meaningless or clinically ambiguous results. However, use of constraints may also increase computational costs.

Rather than solving the fully constrained Lagrangian inverse problem, the constraints from Equations (4.6) and (4.7) can be transformed into penalty terms, $\mathcal{P}(\boldsymbol{\theta})$, or barrier terms, $\mathcal{B}(\boldsymbol{\theta})$:

$$\mathcal{P}(\boldsymbol{\theta}) = \sum_{i=1}^{m} \left(w_i \min\left\{0, g_i(\boldsymbol{\theta})\right\}\right)^2 \quad \text{and} \tag{4.8}$$

$$\mathcal{B}(\boldsymbol{\theta}) = -\sum_{i=1}^{m} \left(w_i \ln\left(g_i(\boldsymbol{\theta})\right)\right), \tag{4.9}$$

where m is the number of inequality constraints, and w_i are individual weights to be chosen depending on the importance of a certain constraint. The Barrier or Penalty terms can then be added to the objective function. For example:

$$\tilde{\Psi} = \frac{1}{2}\,\mathbf{e}^H\mathbf{e} + \frac{1}{\bar{\varrho}}\mathcal{B}(\boldsymbol{\theta}), \tag{4.10}$$

where $\bar{\varrho}$ is a series approaching zero in the iteration progress. This operation creates an unconstrained problem, approximately equivalent to the constrained problem. It can now be solved using the standard methods for unconstrained minimization without further manipulation [147].

In addition to the linear constraints shown in Equations (4.6) and (4.7), a geometric constraint appears in the BEM-based inverse problem that prevents the boundaries of the regions, background and inclusion, to overlap. This constraint is illustrated in Figure 4.1 and can be described:

$$\|\mathbf{d}\|_2 \geq d_{min}, \tag{4.11}$$

where $\mathbf{d}$ is the distance between the interface and the outer boundary and $\|.\|_2$ indicates the Euclidian vector norm. Assuming the outer and the inner geometry to be circular or spherical, with radius, R, and r, respectively, the distance, $\mathbf{d}$, in Equation (4.11) can be expressed in terms of the center coordinates, C and P,

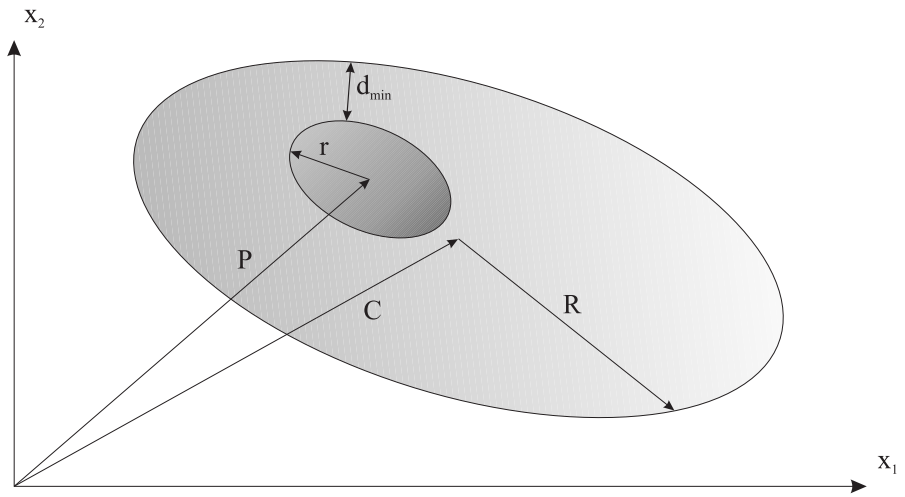

Figure 4.1 Geometric constraint to prevent overlapping boundaries between regions.

yielding:

$$\|C - P\|_2 \leq \|R\|_2 - d_{min} - \|r\|_2, \tag{4.12}$$

Equation (4.12) represents a nonlinear (quadratic) constraint with non-convex characteristics in the simplified, circular case. Further nonlinearities are to be expected in the case of arbitrary boundaries with corners, where $\mathbf{d}$ cannot be expressed analytically, and as a result, presents a sub-optimization problem. Therefore, the consideration of constraint (4.11) in the objective function may cause serious problems to the stability of an algorithm.

In the present work, the aim is to obtain fundamental investigations with interest in the behavior of all variables in $\boldsymbol{\theta}$. Therefore, constraints, such as these in Equations (4.6) and (4.7), were neglected in the error function to allow the algorithm the largest freedom. However, a fail-safe check has been considered in the gradient descent algorithm (see Section 4.3), where a new start value would be assigned for a reconstruction variable when an iteration results in the violation of a constraint or in physically meaningless parameter values. Additionally, the constraint (4.11) has been considered numerically such that the algorithms was not taking a step in the change of inclusion location, P, if a minimum distance, d_{min}, evaluated between the nodes of the inclusion and the outer boundary, was exceeded.

4.1.3 Global and Local Optimization

It has been shown in Section 3.2 that the objective function (error functional) possesses numerous local minima even within the plausible ranges for some parameters. In particular, the Young's modulus of each region and the position of a potential inclusion. Given exact data, $\mathbf{u}^\star$, only that solution with the lowest error value, $\Psi \rightarrow 0$, is the correct global minimum. However, it cannot be guaranteed that any good starting value will converge to this global solution. Therefore, it is of interest to know at least some number of solutions (if not all), as the global minimum can still be differentiated from other locally optimal solutions by the value of the error-function. Hence, the DIET inverse problem is in fact a global minimization problem. Furthermore, in the more realistic presence of noise due to measurement error, it may not be possible to decide with certainty, which one of a series of solutions is the right solution.

4.1.4 Problem Summary

In summary, it can be said that the DIET inverse problem requires at least a two-step algorithm. The task of the first part of this algorithm would be to supply a number of possible start values for $\boldsymbol{\theta}$ in the range of plausible values. The second step would be to run an algorithm that obtains a more precise solution for some or all of these starting values. The resulting error-values of the final solutions can then be used to determine the global solution, or in cases with measurement noise at least a strong indication of the global solution.

The first step must be an algorithm that is able to work out a number of start values that, in the optimal case, would converge to one locally optimal solution each. For this task, algorithms that use only objective function evaluations are suitable choices. Although there are a large number of genetic algorithms readily available that can to some degree rationally search the solution domain [148], it has been decided to use a different, systematic approach here, due to the advantages in computational speed of the BEM, as pointed out in Section 2.4. A Grid-Search is a complete search algorithm that scans the solution domain systematically within given box constraints [149]. Using grids that become progressively finer in zoomed areas of the solution domain, it is relatively straightforward to determine a large number of possible start values that will likely have their own local minimum. It is obvious that Grid-Search becomes extremely inefficient with the number of dimensions in the solution vector, as computational costs rise

exponentially. However, it may not be necessary to scan through all dimensions in $\boldsymbol{\theta}$. In addition, the Grid-Search can systematically take advantage of the BEM characteristics determined in Section 2.4.

The purpose of the second step algorithm is to obtain precise solutions, $\boldsymbol{\theta}^{\star}$, for each starting point or some selection thereof. This task is best achieved using a typical gradient descent based inverse technique. Obvious choices are the Conjugate Gradient Method (CG), which is known to be robust, and able to cope with computationally large problems.

However, the Gauss-Newton method is a similarly robust method that can achieve superlinear convergence rates [150]. The requirement of storing the approximate Hessian matrix may be a disadvantage to computational costs. However, it is not relevant in the BEM case, where the number of inverse parameters is expected to be relatively small.

Both the Grid-Search and Gauss-Newton methods, as well as some combinations of them, were implemented in the scope of this work[1]. They are described in detail in the following sections.

4.2 Grid-Search Implementation

The implementation of the Grid-Search algorithm was kept as general as possible. This approach maintains flexibility with respect to potentially changing research requirements. It is performed in the following three consecutive steps:

1. Setup of a feasible grid for the relevant material and geometric Grid-Search parameters, controlled by input file
2. Generation of a multi-dimensional errormap
3. Extraction of local minima from the errormap

The Grid-Search variables in this implementation were chosen as seven different solution parameters, θ_i, in particular:

- β: The viscoelastic damping parameter, which is assumed to affect both regions equally.

[1] A nonlinear CG method was also implemented, using a Newton-Raphson line search and the Fletcher-Reeves method for the iterative update of the residual, as suggested by Shewchuck [151]. However, several numerical experiments have shown that the Gauss-Newton method outperformed the CG method in convergence speeds in most cases. Hence, the research presented here is focussed on the use of the Gauss-Newton method.

- $E^I_{\mathcal{R}}$: Young's Modulus of the outer region, which has been found to be an important, nonlinear parameter.
- ν: Poisson's ratio, which is again assumed to be equal for regions I and II, as, to the best of the author's awareness, there have not been cases that indicated a change in poisson ratio due to a pathological change in tissue.
- $\rho_{\mathcal{R}}$: The density, which is similarly assumed to be the same for both regions.
- R: Inclusions have been assumed to be of circular or spherical shape only (radial size R), to keep the number of search parameters low.
- P: The location of the inclusion is varied within the complete geometry, and is provided with a minimum distance between the inner and outer boundaries.
- $E^{II}_{\mathcal{R}}$: Young's modulus of the interior inclusion region, which is also the most important parameter for clinical interpretation.

Each variable, apart from P, can be assigned its own upper and lower search limits, θ_i^{low} and θ_i^{up}, as well as an individual number of iterations, $N_{\theta_i} \geq 1$. All of these elements are assigned by a single input file.

The inclusion location, P, is a generalized variable that provides the two- or three-dimensional location coordinates, which were reduced to a one-dimensional array. The setup of a spatial grid is dependant on the geometry shape and size, and, in addition, a minimum distance, d_{min}, between the interface and outer boundary. Rather than a fixed number of discretization points, the resolution in P was therefore chosen to be determined by a maximum spatial step size, h_{max}, between two possible inclusion locations and the maximum inclusion size, R_{max}. The geometries for which this procedure was implemented are the typical test geometries presented in Section 3.1.1 (compare Figures 3.1 and 3.2). Figure 4.2 illustrates the setup of a spatial grid of circular inclusions within a rectangular geometry for two different resolutions, with the minimum distance, d_{min}, included. Figure 4.3 shows an example of the spatial grid performed for a semi-ellipsoidal domain in the negative x_3 direction, where only a fraction of the surrounding surface is plotted to allow a detailed view on the grid.

The generation of the grid-map of error values in step two is implemented in a straightforward nested loop, producing a seven-dimensional errormap. It is important to note that the order in which these parameter loops are performed is

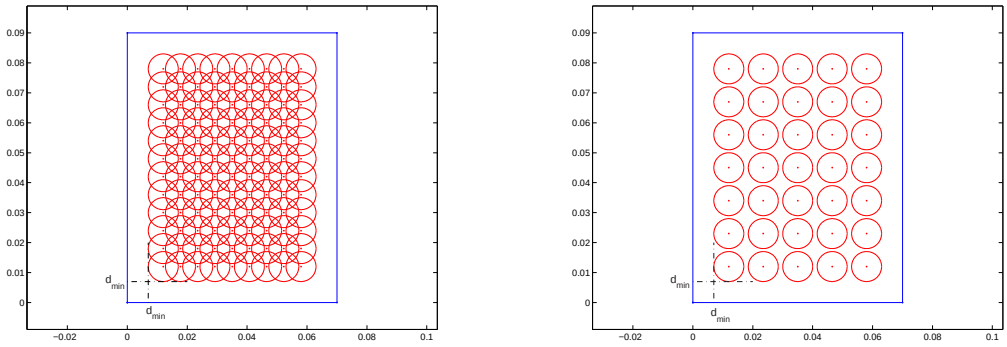

Figure 4.2 Setup of a spatial grid for a rectangular geometry in two different resolutions.

crucial for the computational efficiency of this algorithm, as described in Section 2.4. For best efficiency it is necessary to preserve the exact order as given in the foregoing solution parameter list, with β being the outermost and $E_{\mathcal{R}}^{II}$ being the innermost variable.

The output of this routine is a selection of the local minima, $\tilde{\boldsymbol{\theta}}$, in the non-linear errormap. These values are extracted in the third algorithm step. The extraction is achieved by a numerical procedure whose implementation is not straightforward, but can be illustrated using a simple one-dimensional example

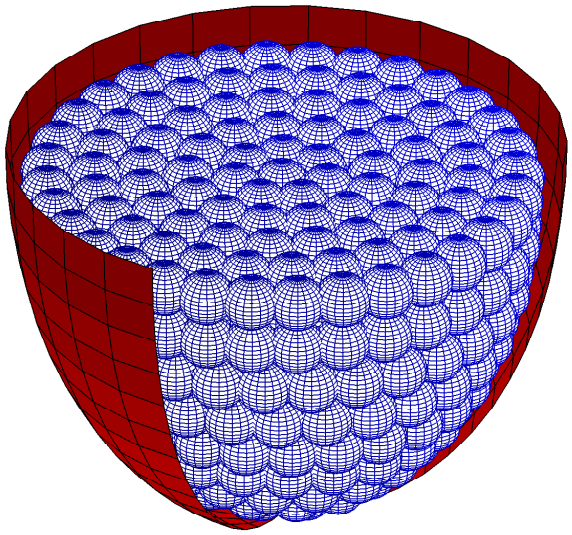

Figure 4.3 Setup of a spatial grid for a semi-ellipsoidal domain pointing in the negative x_3 direction.

Consider the discrete, one-dimensional errormap given in Figure 4.4. To start with, one of the local minima, $\tilde{\boldsymbol{\theta}}$, is selected and classed as an initial reference point, (1). From this reference point, neighboring points are selected and their error values are compared. If the error value of the neighboring point is higher than that of the reference point, then that neighboring point is selected as a reference and its neighbors are in turn compared. If the neighboring point has a lower error value than the reference this indicates descent and the search process is stopped in that direction.

By iteratively repeating this process, the entire *valley* relating to a particular local minimum can be deduced. In Figure 4.4, this *valley* is that section of the errorfunction, $|\Psi|$, between a and b, and is marked in red. The result is a reduced errormap that now consists only of those sections, marked in blue. The global minimum of this reduced errormap can now easily selected and saved as point (2). From here, the extraction procedure restarts for a maximum number of $N_{min} - 1$ times, to extract N_{min} local minima.

In this way, all local minima in the error map can be located and in turn used as starting points for the next stage of the global search algorithm. It is important to note that, as these minima were calculated at a prescribed search discretization, the global minimum found among the collection of $\tilde{\boldsymbol{\theta}}$, may not correspond to the true global minimum.

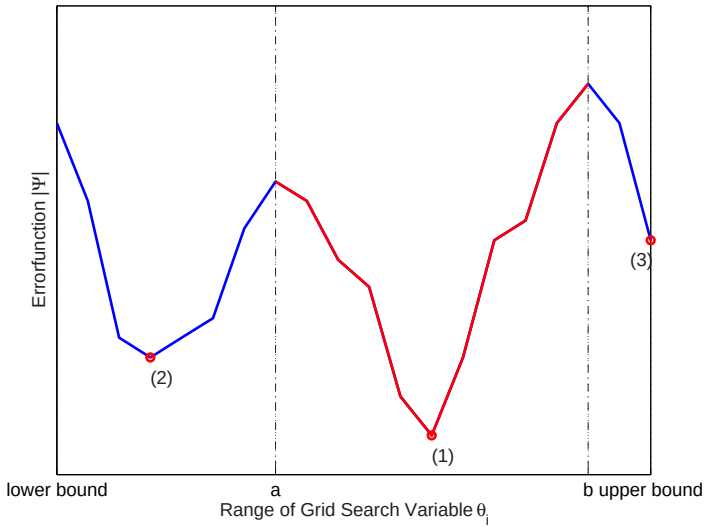

Figure 4.4 Illustration for the extraction of local minima (points (1), (2) and (3)) from a nonlinear error-function shown for a simplified 1D example.

In principle, there is no change to this extraction process in the multi-dimensional case. Starting at the minimum, $\tilde{\boldsymbol{\theta}}$, the new reference points are simply selected in all dimensions. Similarly, the *valleys* to be removed are now multi-dimensional.

The overall procedure can be illustrated in the simple flowchart shown in Figure 4.5. The only difficulty occurs in the selection of neighboring points in the location variable, P, where the grid that covers the geometrical domain is not always given in an evenly spaced, cartesian form, but rather in a circular or elliptical manner (compare to Figure 4.3). In this special case, the neighboring entries of a reference point in P are found based on the resolution of the geometrical grid, that is the maximum distance, h_{max}, between simulated inclusion locations.

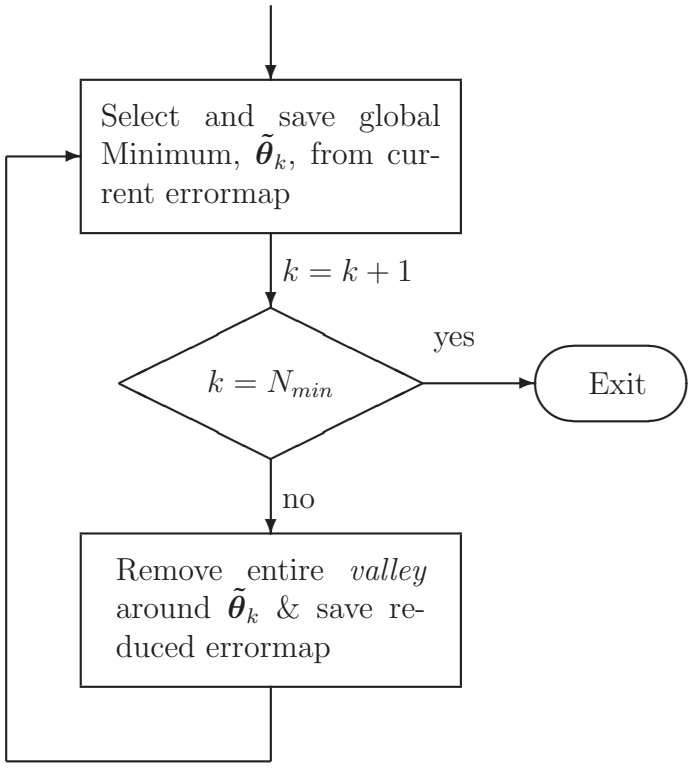

Figure 4.5 Flowchart for the extraction of multiple minima from a large nonlinear errormap in seven dimensions.

For a better understanding of the extraction process for multi-dimensional errormaps, a two-dimensional example is added in Figure 4.6 with several local minima in the coordinates x_1 and x_2. These kind of maps occur, for example, in the case of inclusions simulated at locations over the entire geometry. From top to bottom, Figure 4.6 illustrates the extraction process stepwise.

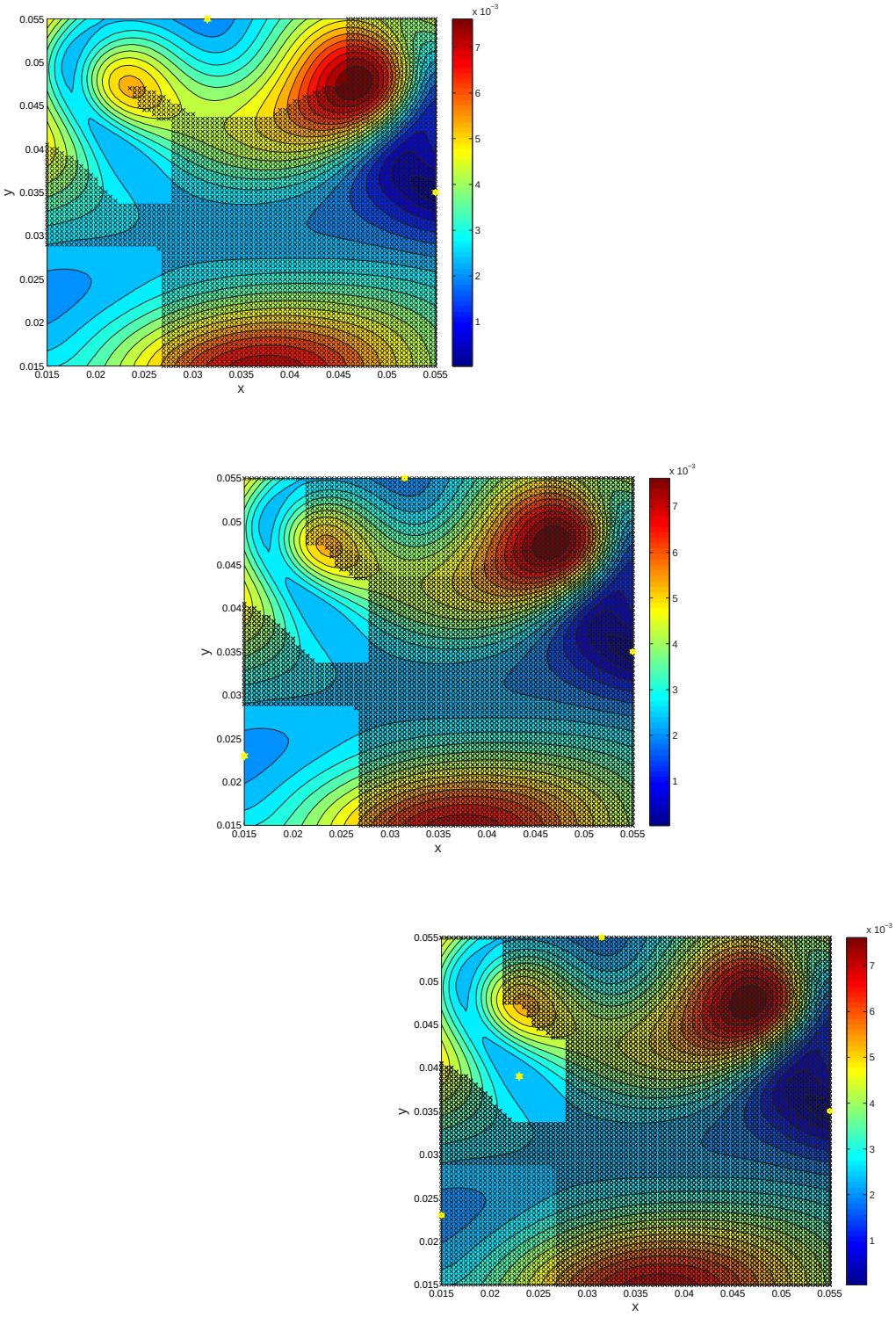

Figure 4.6 Process of the extraction of a number of local minima from a nonlinear spatial errormap in two dimensions. These plots illustrate the first three consecutive iterations of the extraction process.

In the first plot, the first minimum at $(x_{min}^{(1)},\ y_{min}^{(1)}) = (0.055,\ 0.035)$ is found before the first iteration. In this figure, it is highlighted with a yellow hexagon and is located in the area that constitutes the *valley* found during the first iteration, and is cross-hatched in grey. The second local minimum is found from the remaining errormap and is located at the top edge of the plot at $(x_{min}^{(2)},\ y_{min}^{(2)}) = (0.0315,\ 0.035)$. Starting at this minimum, the second iteration commences. This iteration results in the removal of an additional *valley* region, as well as in the detection of the third local minimum located at $(x_{min}^{(3)},\ y_{min}^{(3)}) = (0.015,\ 0.023)$. Similarly, after the third iteration the fourth local optimum is detected at $(x_{min}^{(4)},\ y_{min}^{(4)}) = (0.023,\ 0.039)$. It was chosen to not continue iterating in this case, although it would be possible to eliminate another valley of the errormap to find the last minimum. However, the three steps find three local minima after the first global minimum.

In summary, this extraction process can obtain all local minima from a multidimensional errormap, and is applied here in seven dimensions. The minima can be located either inside or at the boundary of the searched domain. Each one of the local minima represents an approximation to possible solutions of the inverse problem and will serve as a starting value for the more accurate determination of solutions using a gradient descent based procedure.

It is worth noting that the resolution of this GridSearch represents a critical tradeoff in terms of the inverse solution quality. While a very fine resolution will lead to highly increased computational time requirements, a too coarse resolution bears the risk to miss out minima including the global solution. An optimal GridSearch resolution may, however, be found. Alternatively, the use of other global optimization methods such as genetic algorithms, simulated annealing or similar techniques may be of potential in future developments of this reconstruction problem.

4.3 Gauss-Newton Algorithm

The Gauss-Newton method is a gradient descent technique applicable to a wide range of problems. It is derived from the Newton method and is suitable for nonlinear reconstructions, where the number of measurements, N_m, is greater than the number of reconstruction parameters, N_θ. The Gauss-Newton method was used in most investigations carried out for this work.

Consider an objective function, Ψ, defined as a quadratic in $F(\boldsymbol{\theta})$:

$$\Psi = \frac{1}{2} \left\| F(\boldsymbol{\theta}) \right\|^2. \tag{4.13}$$

It is desired to find a combination $\boldsymbol{\theta}^\star$ that minimizes Ψ, given a first approximation, $\boldsymbol{\theta}^{(0)}$. This minimization is equivalent to finding the zeros of $F(\boldsymbol{\theta})$. Linearizing $F(\boldsymbol{\theta})$ in the k^{th} iteration yields:

$$F(\boldsymbol{\theta}) \rightarrow F(\boldsymbol{\theta}^{(k)}) + \boldsymbol{\mathcal{J}}_F(\boldsymbol{\theta}^{(k)})\, \mathbf{p}^{(k)}, \tag{4.14}$$

where $\mathbf{p}^{(k)}$ is the descent- or search direction of the algorithm in $\boldsymbol{\theta}^{(k)}$ and $\boldsymbol{\mathcal{J}}_F(\boldsymbol{\theta}^{(k)})$ is the Jacobian matrix to the function F taken with respect to the reconstruction variables and evaluated in their k^{th} iteration, $\boldsymbol{\theta}^{(k)}$. The search direction, $\mathbf{p}^{(k)}$, is obtained be setting $F(\boldsymbol{\theta})$ in Equation (4.14) to zero and pre-multiplying with the hermitian transpose of the Jacobian, $\boldsymbol{\mathcal{J}}_F^H(\boldsymbol{\theta}^{(k)})$, to normalize the equation system to the number of reconstruction parameters, N_θ, yielding:

$$\underbrace{\boldsymbol{\mathcal{J}}_F^H(\boldsymbol{\theta}^{(k)})\, \boldsymbol{\mathcal{J}}_F(\boldsymbol{\theta}^{(k)})}_{\boldsymbol{\mathcal{H}}(\boldsymbol{\theta}^{(k)})}\, \mathbf{p}^{(k)} = - \underbrace{\boldsymbol{\mathcal{J}}_F^H(\boldsymbol{\theta}^{(k)})\, F(\boldsymbol{\theta}^{(k)})}_{\boldsymbol{\nabla}_\theta \Psi(\boldsymbol{\theta}^{(k)})}, \tag{4.15}$$

where $\boldsymbol{\mathcal{H}}(\boldsymbol{\theta}^{(k)})$ is the approximate Hessian matrix to the objective function, Ψ, and $\boldsymbol{\nabla}_\theta \Psi(\boldsymbol{\theta}^{(k)}) = \dfrac{\partial \Psi}{\partial \boldsymbol{\theta}}$ is the objective function gradient with respect to the reconstruction variables evaluated at $\boldsymbol{\theta}^{(k)}$. If the Hessian matrix is invertible, Equation (4.15) can be solved for the descent direction:

$$\mathbf{p}^{(k)} = - \left[\boldsymbol{\mathcal{H}}(\boldsymbol{\theta}^{(k)}) \right]^{-1} \boldsymbol{\mathcal{J}}_F^H(\boldsymbol{\theta}^{(k)})\, F(\boldsymbol{\theta}^{(k)}). \tag{4.16}$$

Using the descent direction from Equation (4.16), an iteration procedure is defined analogous to the Newton method for the parameter update:

$$\boldsymbol{\theta}^{(k+1)} = \boldsymbol{\theta}^{(k)} + \varrho^{(k)}\, \mathbf{p}^{(k)}, \tag{4.17}$$

where $\varrho^{(k)}$ is a parameter that can be chosen to manipulate the step length that the algorithm takes in the direction of descent. If $\varrho^{(k)} = 1$, the Gauss Newton method coincides with the standard Newton method.

Choosing the function $F(\boldsymbol{\theta})$ as the displacement error, $\mathbf{e}$, from Equation (4.5) and the objective function, Ψ, as given in Equation (4.4), the Gauss Newton method can be applied to the DIET problem. However, there are still a num-

ber of issues that needed to be addressed for numerical stability in its practical implementation to ensure computational efficacy and efficiency.

4.3.1 Line Search

Once a descent direction is obtained from the solution of Equation (4.16), a confirmation of the suitability of the search direction is advantageous before carrying out the iterative step. The product of the descent direction and the gradient represents the slope of the objective function in the search direction, evaluated in $\boldsymbol{\theta}^{(k)}$. Hence, the error value is decreased, when this product is negative:

$$\mathfrak{Re}\left\{\left(\mathbf{p}^{(k)}\right)^{H}\boldsymbol{\nabla}_{\theta}\Psi^{(k)}\right\} < 0. \tag{4.18}$$

However, the error function is still nonlinear along the search direction. To obtain an appropriate step length, $\varrho^{(k)}$, of descent along $\mathbf{p}^{(k)}$, a line search needs to be carried out for the error function along $\mathbf{p}^{(k)}$. It may appear generally desirable to descend as far as the minimum along this line. However, exact line search techniques have, in many cases, been found to be computationally more expansive than using only an approximate line search. Otherwise, an additional sub-minimization problem would need to be carried out to find that optimal step size. Hence, in this work, a simple, inexact backtracking algorithm was implemented, to satisfy:

$$\Psi\left(\boldsymbol{\theta}^{(k)}+\varrho^{(k)}\,\mathbf{p}^{(k)}\right) < \Psi\left(\boldsymbol{\theta}^{(k)}\right). \tag{4.19}$$

Assuming the standard Newton step length, $\varrho^{(k)}=1$, for the first iteration, the parameter update was executed, if Equation (4.19) was satisfied. Otherwise, the step length was decreased as in $\varrho^{(k)}=1/\varkappa_{ls}$, where $\varkappa_{ls}$ is the number of local iterations in the line search. This decrease was allowed a maximum number of times, $\varkappa_{max}$, before the algorithm was stalled, or stopped.

4.3.2 Tikhonov Regularization

To ensure Equation (4.16) is solvable, the Hessian must be positive definite. Unfortunately, this property cannot be guaranteed in this type of ill-posed optimization problem, where $\boldsymbol{\mathcal{H}}(\boldsymbol{\theta}^{(k)})$ is usually ill-conditioned, and leads to numerically

unstable behavior [152, 153]. Therefore, additional regularization techniques are required.

Tikhonov regularization is a very common regularization tool that is applied by assuming an extended objective function, defined as:

$$\Psi \rightarrow \widetilde{\Psi} = \frac{1}{2}\left\|F(\boldsymbol{\theta})\right\|^2 + \frac{1}{2}\gamma\left\|\boldsymbol{\theta} - \boldsymbol{\theta}^\star\right\|^2, \tag{4.20}$$

where γ is the Tikhonov weighting parameter.

Paradoxically, the added regularization term includes the solution, $\boldsymbol{\theta}^\star$, prior to its evaluation. However, the term $\|\boldsymbol{\theta} - \boldsymbol{\theta}^\star\|$ can be assumed to be small for any reasonable start value. Therefore, the complete regularization term can be neglected if the evaluation of the objective function is required. This term can also be neglected in the evaluation of the objective function gradient, $\boldsymbol{\nabla}_\theta\Psi$, but comes to full effect in the Hessian Matrix. The approximated Hessian matrix is now given:

$$\boldsymbol{\mathcal{H}}(\boldsymbol{\theta}^{(k)}) \rightarrow \widetilde{\boldsymbol{\mathcal{H}}}(\boldsymbol{\theta}^{(k)}) = \boldsymbol{\mathcal{J}}_F^H(\boldsymbol{\theta}^{(k)})\,\boldsymbol{\mathcal{J}}_F(\boldsymbol{\theta}^{(k)}) + \gamma\,\mathbf{I}, \tag{4.21}$$

where $\mathbf{I}$ is the identity matrix. Hence, the Tikhonov parameter is added only to the diagonal terms of the Hessian. In general, this technique adds a damping effect to the inversion of the Hessian matrix, which can thus be carried out with much improved numerical stability. For this study, the Tikhonov parameter was set to $\gamma = 1$ in the first iteration, but decreases with the number of Gauss-Newton iterations, $\gamma^{(k)} = 1/\varkappa_{GN}$, to limit its influence when the algorithm approaches the solution, $\boldsymbol{\theta}^\star$ [150].

4.3.3 Scaling

As previously noted, a small change in a solution parameter can lead to a large change in the resulting forward solution. In the DIET problem, it is observed that reconstruction variables can, in general, differ in size by several orders of magnitude. Thus, for example, a small change in the inclusion size (R, $O(10^{-3})$), has rather little influence with respect to the displacement solution, when compared to a change caused by a different elastic modulus ($E_{\mathcal{R}}$, $O(10^5)$).

When a Gauss-Newton iteration is carried out for more than one parameter, this property can have a significant influence on the speed of convergence of the different parameters. Some parameters may take overly large steps towards the

solution, while others appear to be static with almost no change towards the correct solution. This undesirable effect can be significantly reduced by scaling the solution variables to be of the same order, which is readily achieved by defining a scaled solution variable, $\bar{\boldsymbol{\theta}}$:

$$\boldsymbol{\theta} = \mathcal{D}\bar{\boldsymbol{\theta}}, \tag{4.22}$$

where $\boldsymbol{\mathcal{D}}$ is a matrix that contains the order of the variables included in the reconstruction process on its diagonal. The inverse algorithm solves now for the transformed reconstruction variable, $\bar{\boldsymbol{\theta}}$, that is scaled to order 1. Note that this scaling technique needs to be considered in the implementation of the Jacobian, $\boldsymbol{\mathcal{J}}_F$, and of course in the updating process of the true reconstruction variable, $\boldsymbol{\theta}$, whenever a forward solution is required.

4.3.4 Jacobian Calculation

The Jacobian matrix, $\boldsymbol{\mathcal{J}}_F$, is a matrix with as many rows as there are number of degrees of freedom on the geometry's surface, with as many columns as the number of reconstruction variables. In this work, reconstruction variables are specified by input file. Thus, the resulting size of the Jacobian matrix is flexibly allocated.

For the sake of simplicity in implementation, each column of the Jacobian matrix was approximated by means of a Finite Difference Method (FDM). The FDM is applied with respect to a reconstruction parameter and added column-wise to the Jacobian matrix. For most parameters, θ_i, a simple forward difference method was applied, defined:

$$\boldsymbol{\mathcal{J}}_F(\theta_i) = \frac{F(\theta_i + h) - F(\theta_i)}{h}, \tag{4.23}$$

where h is a finite difference step that is specific in its size to each reconstruction parameter, θ_i. Here, step sizes were chosen in the range of the product of the specific parameter's scaling factor times the square root of the machine precision (therefore around $1 \cdot 10^{-8}$), as suggested in [143].

However, inclusion related parameters, in particular the inclusion's Young's modulus, E_{II}, achieved better results when using a central difference method, defined:

$$\boldsymbol{\mathcal{J}}_F(\theta_i) = \frac{F(\theta_i + h) - F(\theta_i - h)}{2h}, \tag{4.24}$$

where the step size, h, was chosen as above.

In general, the computational requirement to calculate the Jacobian matrix is expensive. However, in these Jacobian calculations, one can make optimal use of partial system matrix updates, as outlined in Section 2.4.2, thus saving significant computational costs.

4.3.5 Stopping Criteria

The employment of stopping criteria is an important factor. It is particularly important where iterative search algorithms are applied to ill-posed problems and numerical algorithm behavior may thus be very unstable. Hence, several stopping criteria have been implemented in this work.

The algorithm was stopped from iterating, if a local minimum was found in the objective function. It was also stopped if further iterations would not result in any significant improvements, which occurs, if:

- The value of the objective function had decreased under a certain threshold: $\Psi \leq \epsilon$, where this threshold was usually chosen $\epsilon^{(1)} = 1 \cdot 10^{-12}$.
- The step of descent would become very small, that there is virtually no change or improvement towards a better material parameter solution. This can be expressed as $\varrho^{(k)} \, ||(\boldsymbol{\theta}^{(k+1)} - \boldsymbol{\theta}^{(k)})||_2 \rightarrow \epsilon^{(2)}$, where $||.||_2$ denotes the euclidian vector norm and $\epsilon^{(2)}$ was chosen $1 \cdot 10^{-8}$.

Both of these cases can be considered as a converged solution. However, in the event of numerically unstable cases, further fail-safe stopping criteria were implemented, including:

- The algorithm was constrained to a maximum number of iterations in the Gauss-Newton descent direction, $ii^{(GN)} \leq ii_{max}^{(GN)}$, where $ii_{max}^{(GN)}$ was usually chosen at 100 iterations, but adjusted in cases depending on the research goal.
- A maximum number of iterations in the line search would also trigger the algorithm to stop, $ii^{(LS)} \leq ii_{max}^{(LS)}$, with $ii_{max}^{(LS)}$ chosen at three to five times the number of reconstruction parameters.

4.4 Summary

Using the optimization techniques described in this chapter, a program suite has been developed and implemented in Fortran90 for numerical investigations of the ill-posed, non-linear and global DIET inverse problem, based on the BEM used for the required forward simulations. In particular, the program suite includes:

- A detailed a Grid-Search analysis in relevant material and geometric variables with the option to extract N_{min} local minima from the resulting multi-dimensional error map. The forward solution requirements in this technique have been optimized with respect to the computational time requirements.
- A Gauss-Newton gradient descent method to be used for the accurate reconstructions of any of the relevant parameters in any of their combinations. The technique has been implemented with a nonlinear backtracking line-search, a scaling technique for the reconstruction variables to normalize the inverse problem parameters to order one, and Tikhonov regularization to provide numerical stability in the algorithm.

Both methods have been implemented as autonomous subroutines that also enable the methods to be used in combined approaches. In particular, this means the accurate Gauss-Newton optimization of several local solutions obtained from a Grid-Search in the nonlinear variables.

Chapter 5

Reconstruction of Homogeneous Domain Parameters

The DIET system goal is to successfully screen for abnormal breast lumps. This goal includes identifying both cancer-suspicious cases and differentiating healthy cases with high specificity. In a first approximation, the healthy breast tissue case can be modeled as a homogeneous, elastic material with isotropic properties. A full material identification would therefore consider the reconstruction of five material parameters. In particular, these include the inertial and viscous damping parameters, α and β, Young's modulus of elasticity, E, Poisson's ratio, ν and the density, ρ.

The elastic parameters of breast tissue, Young's modulus, E, and shear modulus, G, are the most important parameters in the elastographic identification problem. Both are known to vary in both the long and short term. Little is known about the damping parameters. However, values for the density, ρ, are expected to be near those of water and fatty tissue and values of Poisson's ratio are expected to be near incompressibility.

That said, while some values may be reasonably well known, none of the material parameter values are known exactly. Each of them should be expected to have slightly different values from case to case. Therefore, it is of interest to know the behavior of a reconstruction process in all material parameters.

This chapter takes a closer inspection on the behavior of the reconstruction of material parameters of a homogeneous, isotropic domain from time-harmonic surface motion. For this purpose, the Gauss-Newton method is used, as described in Chapter 4 including parameter scaling and Tikhonov regularization in conjunction with the BEM for forward simulations. The general reconstruction setup is described in the first section. In the second section, reconstructions results are shown for single material parameters, while all remaining parameters are known

exactly. These first simulations prove the ability to reconstruct for such material parameters from harmonic surface motion and also verify the implementation of the algorithm. Further reconstructions were carried out to investigate the sensitivity of reconstructions with respect to start values and to test the performance of the identification procedure under the influence of noisy displacement data. The final section examines the performance of reconstructions carried out for multiple material parameters at the same time.

5.1 Reconstruction Setup

Reconstructions for material parameters were performed for all test geometries introduced in Section 3.1.1. The specific geometries include a 2D rectangle and a 2D semi-ellipse, as well as a 3D cylinder and a 3D semi-ellipsoid. Those geometries were first simulated at a harmonic actuation on the bottom side of $f = 50\ Hz$ with an amplitude of 1 mm in the vertical direction. The nodal displacement output, $\mathbf{u}$, of those simulations was used in the reconstruction algorithms as the reference displacements, $\mathbf{u}^\star$, instead of true surface displacement measurements.

The particular solution parameters, $\boldsymbol{\theta}^\star$, used in any forward simulation of the test geometries include the effects from the proportional damping parameters for inertial and viscous damping, α and β. They also are a function of the elastic modulus, E, the Poisson ratio, ν, and the density, ρ. The true (solution- or reference-) values for those parameters are shown in Table 5.1 together with the start values used for single material parameter reconstructions.

	Simulated Parameter (Solution, $\boldsymbol{\theta}^\star$)	Start Value, $\boldsymbol{\theta}^o$
α	15 rad/s	0 rad/s
β	0.0005 s/rad	0 s/rad
E	20 kPa	30 kPa
ν	0.45	0.5
ρ	950 kg/m^3	950 kg/m^3

Table 5.1 BEM-based material parameter identifications from harmonic surface displacements with a Gauss-Newton algorithm: Solution and start values for single material parameter reconstructions.

Several other solution values were also tested in reconstructions together with other start values. However, those initial guesses were always chosen in the range of expected material parameters for *region I*, as illustrated in Chapter 4, Equation 4.6. Reconstructions carried out in these different configurations produced, in

every case, the same qualitative results. Hence, the convergence results shown in this section should be understood to be representative for a broader behavior and set of results.

5.2 Reconstructions for Single Material Parameters

To show the ability to identify material properties from surface motion and to verify the implemented algorithm, this section contains a number of results from Gauss-Newton reconstructions for single material parameters. In particular, reconstructions were carried out for one single parameter with a start value from Table 5.1, where the solution values for all other material values were assumed to be known exactly.

5.2.1 Reconstruction Convergence Results

Figure 5.1 shows the convergence results obtained from the individual reconstructions for each material parameter, α, β, E, ν and ρ. All of these single parameter reconstructions clearly show convergent behavior to the correct solution values without exception and for all test geometries in two and three dimensions. In all cases, the algorithm stopped iterating once the displacement error, Ψ, (defined in Equation 4.4), achieved values lesser than $1 \cdot 10^{-11}\ m^2$. Only four iterations were required to achieve almost exact convergence in all parameters with the exception of elasticity, where one case, the 3D cylindrical geometry, required six iterations to converge to the same accuracy. This last case is shown in Figure 5.1 (e). Interestingly, it appears there is a difference in the convergence performance in elastic modulus between different geometries. Both the semi-elliptical and semi-ellipsoidal geometry performed better, requiring two and four iterations respectively less than the according geometries with corners.

5.2.2 Reconstruction Sensitivity to Start Values

The sensitivity of the algorithm's convergence with respect to start values was tested by repeating the single parameter reconstruction simulations using a range of initial guesses. In most of the material parameters, particularly α, β, ν and

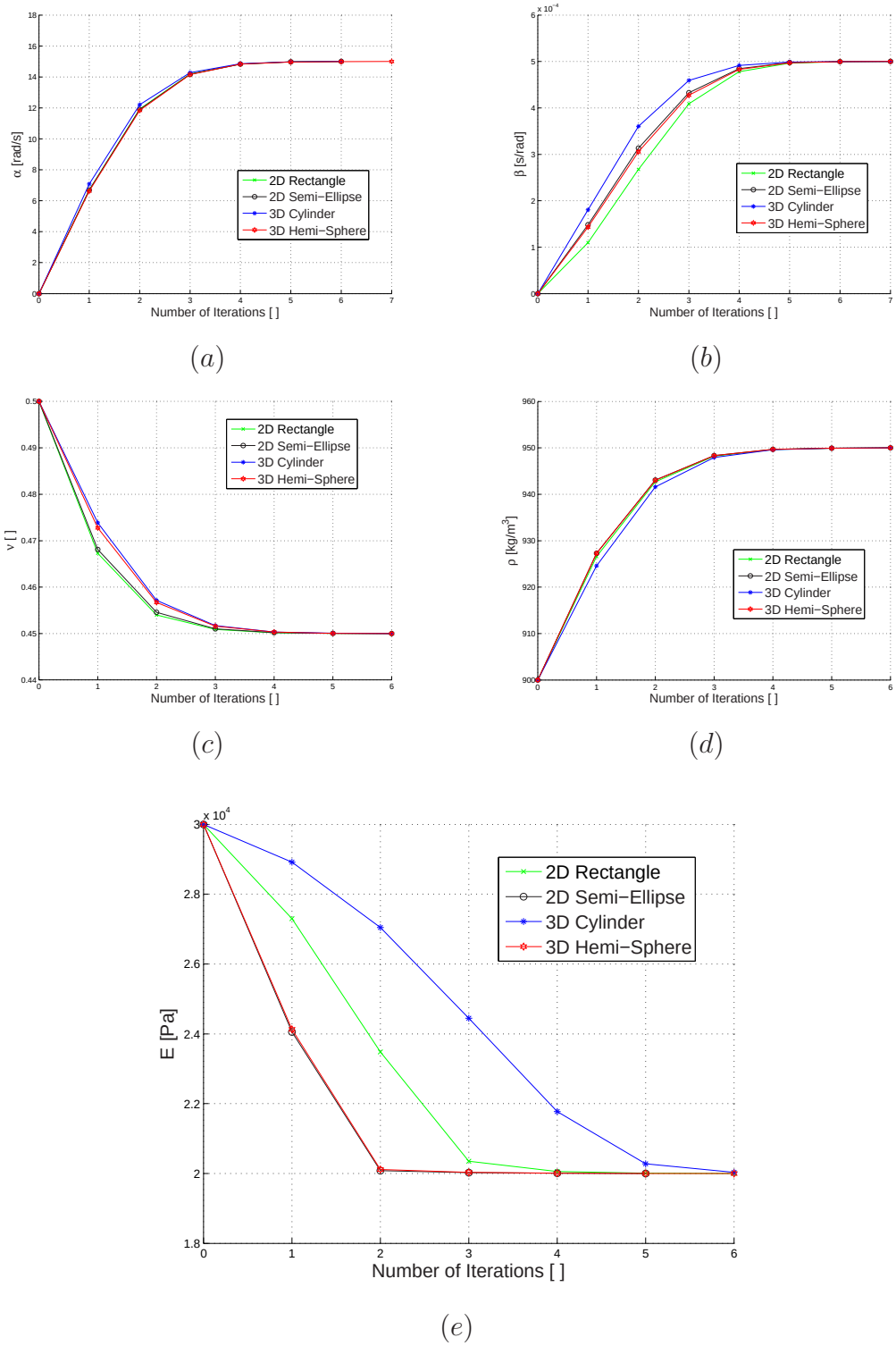

Figure 5.1 Convergence of reconstructions for single material parameter performed using four test geometries, (a) inertial damping parameter, α, (b) viscous damping parameter, β, (c) Poisson ratio, ν, (d) material density, ρ and (e) Young's modulus, E.

ρ, this range was chosen far wider than reasonable assumptions for breast tissue material parameters. The specific ranges are provided in Table 5.2.

Material parameter	Range of start values
α	$[0,\ 1500]\ rad/s$
β	$[0,\ 0.5]\ s/rad$
E	$[10,\ 200]\ kPa$
ν	$[0.1,\ 0.5]$
ρ	$[500,\ 1500]\ kg/m^3$

Table 5.2 Range of initial guesses used for testing of reconstruction sensitivity with respect to start values.

For the identification of single material parameters only the elastic modulus, E, shows significant sensitivity with respect to the initial guess. All other single parameter reconstructions (in α, β, ν and ρ) converged to their correct solution when a start value was chosen in the range illustrated in Table 5.2. In these cases, the convergence speed was still similar to those reconstructions shown in Figure 5.1 with only small numbers of iterations required.

In contrast, reconstructions for Young's modulus, E, exhibit local minima occurring below and above the correct solution value. Figure 5.2 shows an example for the convergence of reconstructions carried out for the 2D and 3D test geometries in the same conditions as described in Table 5.1, but with the start value $E = 200\ kPa$. The convergence to local minima in E of orders greater than $1 \cdot 10^7\ kPa$ and greater is evident. The reconstruction algorithm also required a much larger number of iterations before the process stopped due to failure in finding better solution approximations. It is also notable that despite the same initial guess, each test geometry converged to an entirely different solution with discrepancies of several orders in magnitude.

5.2.3 Reconstructions for Stiffness at Noisy Displacement Data

Accurate reconstruction of stiffness data is central to the DIET breast cancer screening concept. It is thus more important than the accurate reconstruction of other material parameters. As some error is to be expected in the motion data from the breast surface, a number of reconstruction simulations were carried out for the identification of elastic modulus in the presence of noisy displacement measurements.

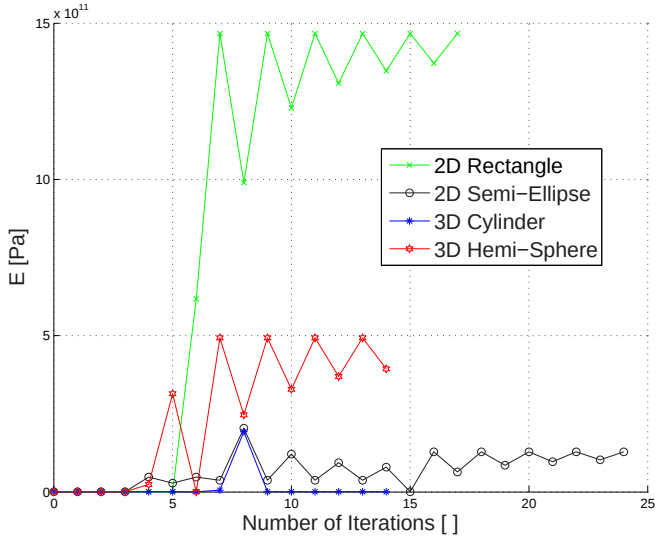

Figure 5.2 Sensitivity of reconstructions for Young's modulus with respect to start values results in convergence to local minima, where $E > 1 \cdot 10^{10}\ Pa$.

For this purpose, the 2D and 3D test geometries were simulated in the same solution configuration given in Table 5.1. These displacements were further corrupted in both real and imaginary part by adding uniformly distributed white noise up to $\pm 1\ mm$ at the maximum and in steps of $0.1\ mm$. This range of noise is chosen due to the current capabilities of the digital image capturing system [120], where measurement error is expected in the order of $0.1\ mm$. Hence the added noise is about one to ten times the motion error that might be expected.

The resulting nodal displacement data from these simulations have maximum absolute displacement amplitudes of the order of $1.6\ mm$ in the 3D cylindrical case, $2.2\ mm$ in both the 2D cases and $3.0\ mm$ in the 3D semi-ellipsoidal case. Hence, the relative amount of added noise is dependant on the geometry and can be quantified as in the range of up to 30% in the 3D hemispherical case. The 2D cases and the cylindrical geometry have similar relative errors of up to 45% and 62% respectively.

The resulting motion pattern of the noise-corrupted test geometries is illustrated in Figure 5.3. This figure shows the cylindrical sample geometry (a) without corruption, (b) with displacement noise up to $0.3\ mm$, and (c) with noise up to $1\ mm$ in amplitude. Where the motion pattern at zero noise level is still clearly defined in longitudinal waves along the cylinder's surface traveling in the vertical direction, the distortion becomes clearly visible even at small added noise amplitudes. Since noise is added randomly to the nodal values, the mesh now

contains elements with obvious discontinuities in the first spatial displacement derivatives (kinks), as can be seen in both corrupted geometries.

A reconstruction for the stiffness parameter, E, was then performed at each level of noise corruption for each of the 2D and 3D test geometries. For these reconstructions the start values from Table 5.1 were used. The results of these reconstructions are summarized in Figure 5.4.

Figure 5.4 (a) shows the relative error in the resulting converged stiffness value, ϵ_{rel}, that is defined as:

$$\epsilon_{rel} = \frac{|\mathfrak{Re}(\tilde{E}) - \mathfrak{Re}(E^\star)|}{|\mathfrak{Re}(E^\star)|},$$

where $\tilde{E}$ is the reconstructed stiffness value and $E^\star$ the true solution value known a priori from simulation. Figure 5.4 (b) illustrates the number of iterations to achieve a convergent stiffness value, $\tilde{E}$. It is notable that the number of iterations required to achieve a converged result in stiffness is much higher than in the noise-free case regardless of the amount of noise added. A general observation is that between four to eight times more iterations were required.

However, it is also clear that all of these reconstructions have converged to stiffness values reasonably close to the true solution. This convergence occurs even with highly corrupted motion data. The maximum relative error in the solution is only 3.5% and occurs in the sample reconstruction case for the 2D semi-elliptical geometry.

It can also be seen that the relative error tends to grow with increasing levels of noise. This error-growth may not necessarily proportional to the amount of noise added, but appears to occur in a span-like fashion. Some reconstructions afflicted by very high noise levels were still able to produce results with minimal error, where some other results indicate comparably high error values. Hence, the relative error is inconsistent as a strict function of the levels of added noise in the cases examined here.

5.3 Reconstructions for Multiple Parameters

This section examines the reconstruction behavior of the Gauss-Newton algorithm when multiple material parameters are reconstructed simultaneously. Two special cases are examined initially. The first case is the reconstruction of damping parameters, α and β. The second case is the reconstruction of Young's modulus

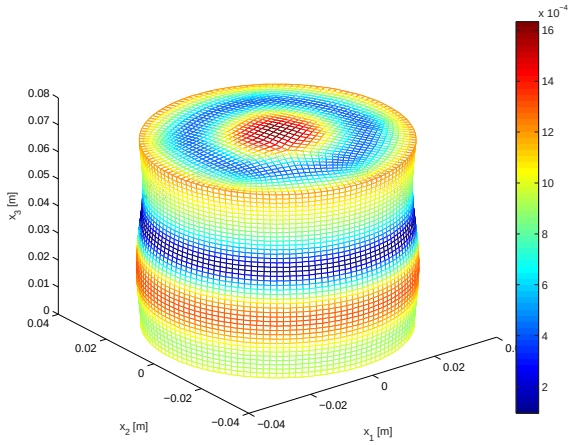

(a)

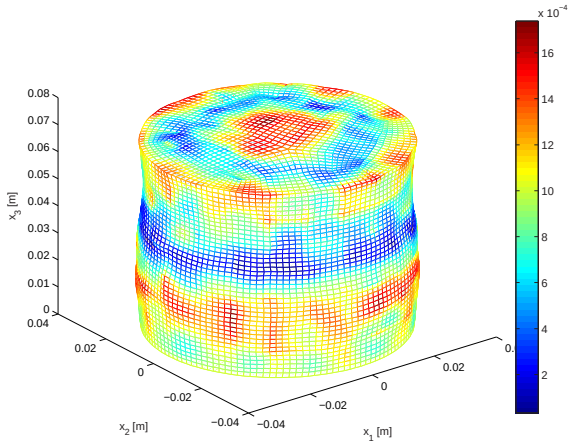

(b)

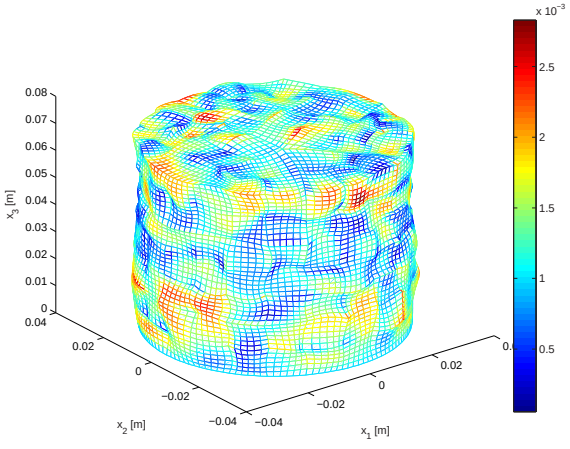

(c)

Figure 5.3 Surface motion at the example of a cylindrical geometry corrupted with uniformly distributed white noise at (a) 0 *mm*, (b) 0.3 *mm* and (c) 1 *mm* in amplitude. (The color coding shows the displacement amplitudes in [m]).

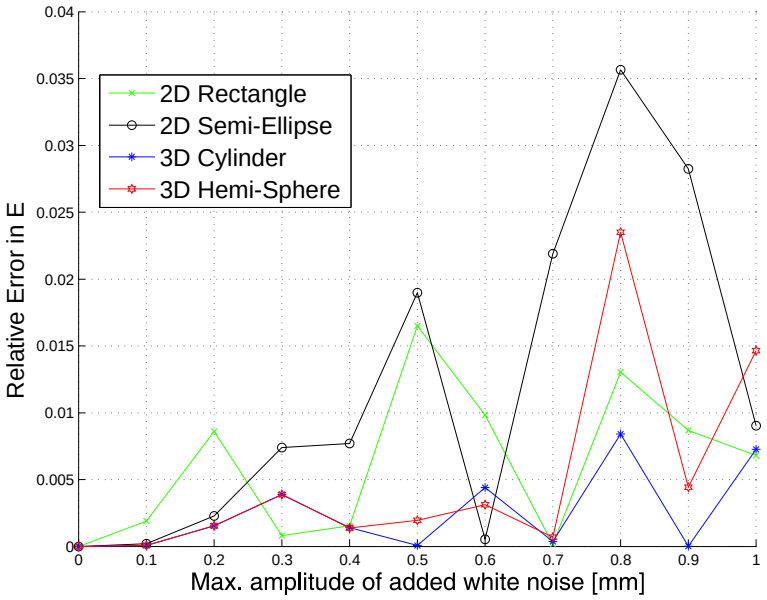

(a)

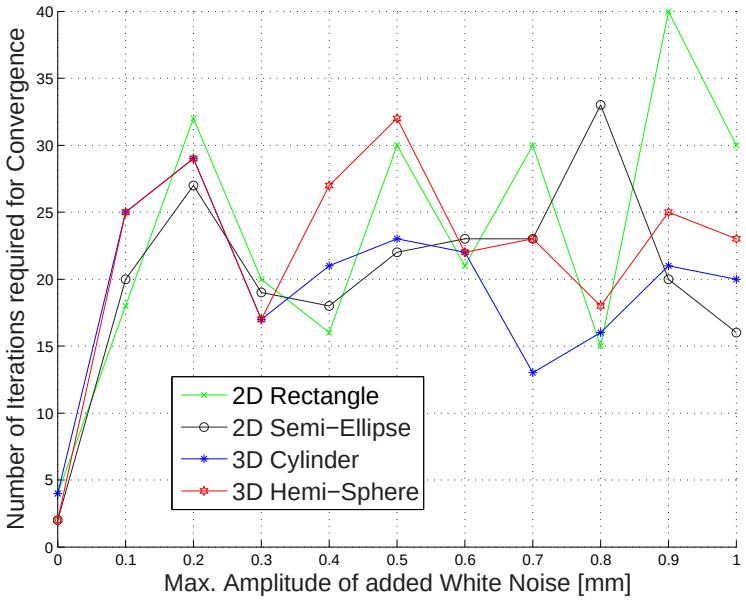

(b)

Figure 5.4 Reconstructions for Young's modulus, E, under the influence of noisy displacement data: (a) Relative error of the converged stiffness result, (b) number of required iterations for convergence.

and density, E and ρ. After these cases, reconstructions are attempted for a complete five-parameter model.

5.3.1 Reconstruction for Damping Parameters, α and β

Material reconstructions for both the inertial damping parameter, α, and viscous damping parameter, β, were conducted in several material configurations and with several start values. Figure 5.5 illustrates the general convergence behavior for reconstructions in α and β, where the solution configuration from Table 5.1 was used. The initial guess for α and β was zero for both, assuming an undamped material. However, exact knowledge is given for the real parts of density and elastic modulus, as well as the Poisson ratio.

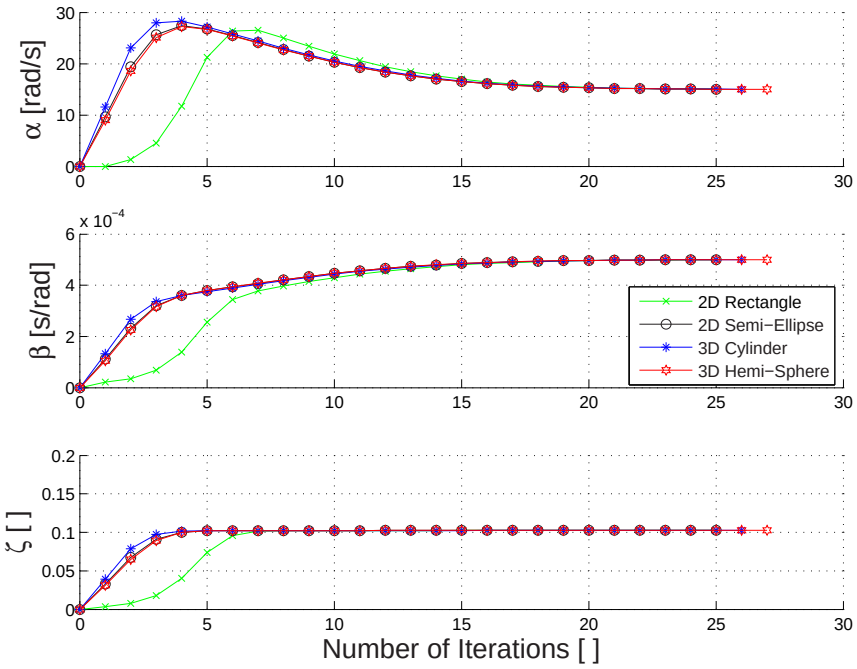

Figure 5.5 Reconstruction for both damping parameters causes convergence toward the correct damping ratio first, before the correct damping parameters, α and β are found.

It can be seen in Figure 5.5 (top and middle graph) that this reconstruction process achieves convergence to the correct values for both α and β. Simulating the same reconstruction with several different initial guesses always resulted in the same convergence behavior. Compared to reconstructions for single material parameters, the computational effort is significantly increased. The number of

iterations required to achieve a (very accurate) displacement error, $\Psi \leq 1 \cdot 10^{-}11$, is approximately 25, which is about four to six times greater than in the single parameter reconstruction case.

It is interesting to note that the reconstruction for α overshoots the final converged value during the early iterations. Similarly, the reconstruction for β appears to have a heavily damped convergence behavior. The bottom graph in Figure 5.5 shows the convergence behavior of the damping ratio, ζ, as calculated from the values of α and β during the inversion process using Equation 2.11. This graph clearly shows a very fast convergence to the correct damping ratio during the first few iterations. The number of iterations required is only four or six respectively, which is comparable to the performance seen in the case of single parameter reconstructions. This behavior was similarly observed by McGarry *et al.* in the case of reconstructions for damping parameters of a Rayleigh model using a FEM-based reconstruction algorithm for MRE [85].

5.3.2 Reconstruction for Material Parameters, E and ρ

An important reconstruction behavior is also found when carrying out simultaneous reconstructions for Young's modulus, E, and density, ρ, simultaneously, while α, β, and ν, are assumed to be known exactly. Figure 5.6 shows the general convergence behavior observed for these reconstruction cases, where the values from Table 5.1 were used.

Figure 5.6 clearly shows that convergence occurs for both reconstructed parameters, E and ρ. However, they have clearly not converged to correct values. The correct solution values are indicated in Figure 5.6 by a solid black line. The relative error in E and also in ρ in this particular reconstruction is significant with approximately 20% deviation from the solution in the case shown. However, the exact resulting values of E and ρ are sensitive to the initial values used in particular reconstructions.

In contrast, Figure 5.7 shows the convergence of the wave speeds, c_s and c_p, of the same reconstruction. These values are calculated from the material parameters obtained at each iteration using Equation 2.25. It can be seen that the wave speeds, c_p and c_s, converge to the correct values in a small number of iterations.

When correct values are obtained for c_p and c_s, in this type of reconstruction, the value of the displacement error function, Ψ, at these converged solutions

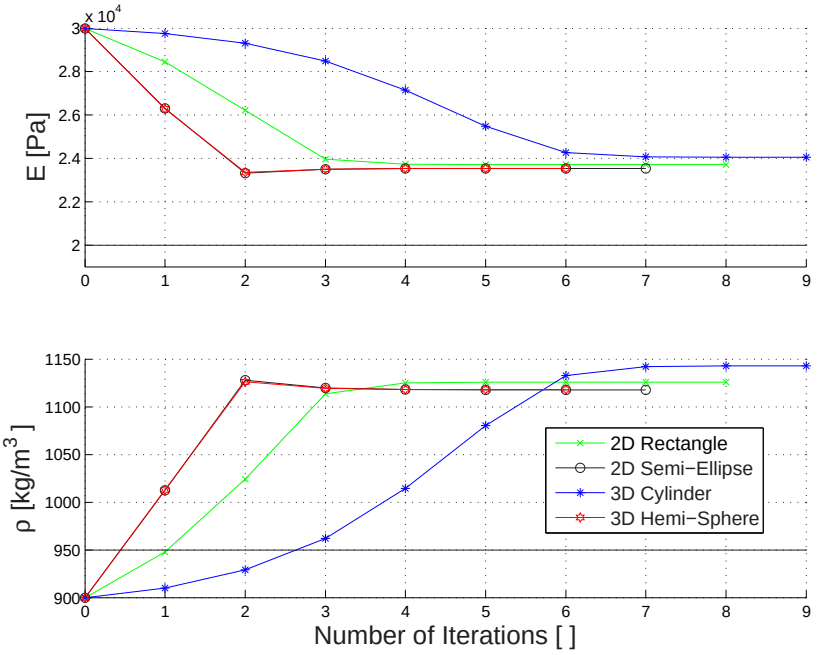

Figure 5.6 Convergence behavior of simultaneous reconstruction for material parameters E and ρ can cause convergence to incorrect solutions.

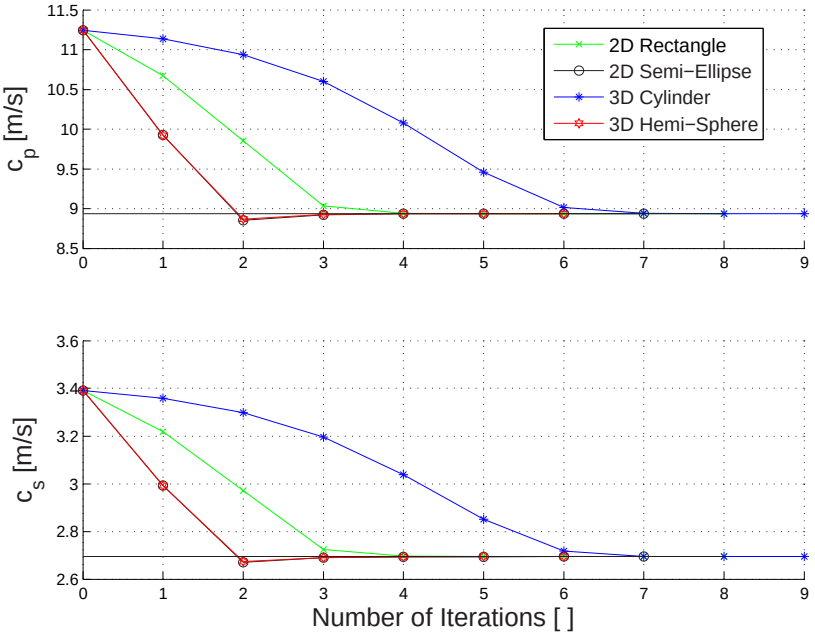

Figure 5.7 Reconstruction performed simultaneously for material parameters E and ρ causes convergence to incorrect solutions in E and ρ, but (b) to correct wave speeds, c_s and c_p.

becomes extremely small. In contrast to reconstructions for α and β, where additional iterations would finally yield the correct parameter values, the convergence to correct values in E and ρ does not necessarily occur. Forcing the iteration to continue until error values are near machine precision by setting the stopping criterium to $\Psi \leq \epsilon$, where $\epsilon = 1 \cdot 10^{-15}$, did not achieve better parameter identification in neither E or ρ. Scaling of the material parameters also has no effect here, as expected.

A confirmation of this reconstruction behavior can also be obtained by inspection of the equivalent errormap in Figure 5.8, where the objective function values, Ψ, from a comparison of the reference displacement solution at $E^\star = 25\ kPa$ and $\rho^\star = 950 kg/m^3$ with displacement solutions from simulations with variation in E and ρ are displayed. This errormap highlights the presence of an extended *valley* with minimal displacement error. This valley follows a straight line for which c_p and c_s are constant. That line passes through the correct solution values of E and ρ. Also, in this line, the displacement error is virtually zero, clearly indicating local, unidentifiable minima.

With respect to the inverse problem, this line clearly represents a line of non-unique solutions. The forward solution using any parameter combination of

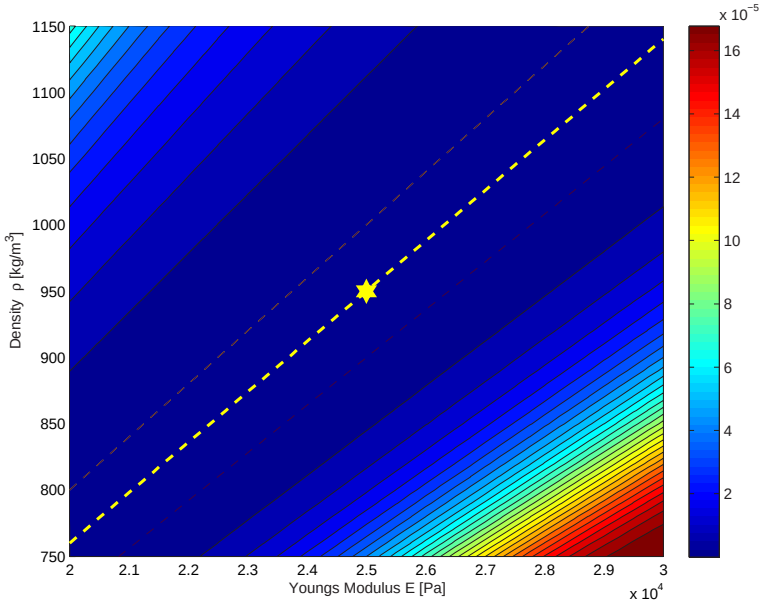

Figure 5.8 The errormap in E and ρ (for the 2D rectangle) illustrates the convergence behavior of those material parameters towards values on the yellow dashed line, where the wave speeds, c_s and c_p, assume the same values as obtained from the reference values, $E^\star = 25\ kPa$ and $\rho^\star = 950 kg/m^3$. This line represents non-unique solutions to the inverse problem.

E and ρ on this line essentially resembles the same displacement pattern on the geometry's surface, despite the differences in those two material parameter values. The result is a minimal to zero displacement error along the center line for all parameter values of E and ρ that result in the correct wave speeds. Furthermore, this reconstruction result is meaningful with respect to the composition of the fundamental solutions in harmonic Elasticity. Inspecting Equations 2.30–2.40, one can see that all significant components such as the arguments of the Bessel or exponential functions are expressed in terms of c_s and c_p, which can thus be interpreted as the dominant parameters.

As a secondary result, differences are repeatedly observed in the reconstruction performance between the different geometries. The 2D semi-elliptical and 3D semi-ellipsoidal geometry are almost identical in convergence behavior with small numbers of iterations required. The 2D rectangular and 3D cylindrical geometry both require more iterations. Furthermore, the descent towards the solution values in the case of the 3D cylinder is initially relatively flat, indicating more sensitivity in the start value of this particular geometry.

5.3.3 Reconstruction for the Complete Five Parameter Material Model

A set of reconstructions is discussed for the simulation of the complete five parameter material model, including α, β, E, ν and ρ. The general convergence behavior of such reconstructions is illustrated in Figures 5.9 and 5.10, where solution parameters and initial guesses were adapted entirely from Table 5.1. Again reconstructions were tested for all four test geometries.

The convergence behavior observed in these types of reconstructions is, in general, a superposition of the behavior encountered in the foregoing investigations (with an exception to the 3D cylindrical geometry). In Figure 5.9, it can be seen that all material parameters converge, but only the Poisson ratio is identified correctly. All other parameter values are incorrect. However, Figure 5.10 also illustrates the convergence of the damping ratio, ζ, calculated from α and β at every iteration, that is identified correctly. Similarly, the wave speeds, calculated from the material parameters at every iteration and shown in Figure 5.10[1],

[1]Note that in the some iterations, the Poisson ratio, ν, has a value of 0.5 for an incompressible material. Hence, the longitudinal wave speed, c_p, has a theoretical value of ∞, wich is numerically substituted with a large number. However, in Figure 5.10 this value was manually adjusted to not distort the expressiveness of this illustration.

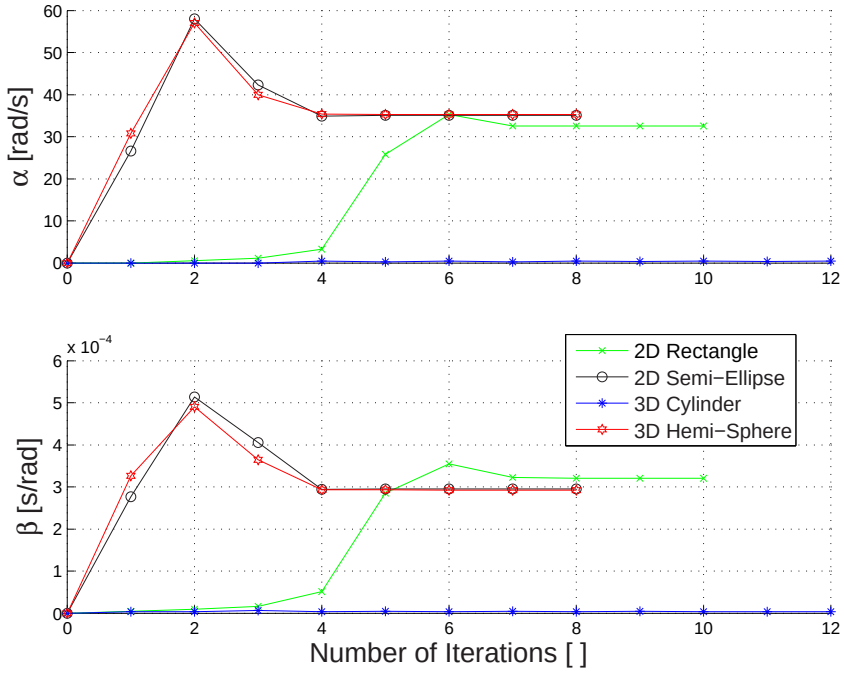

(a)

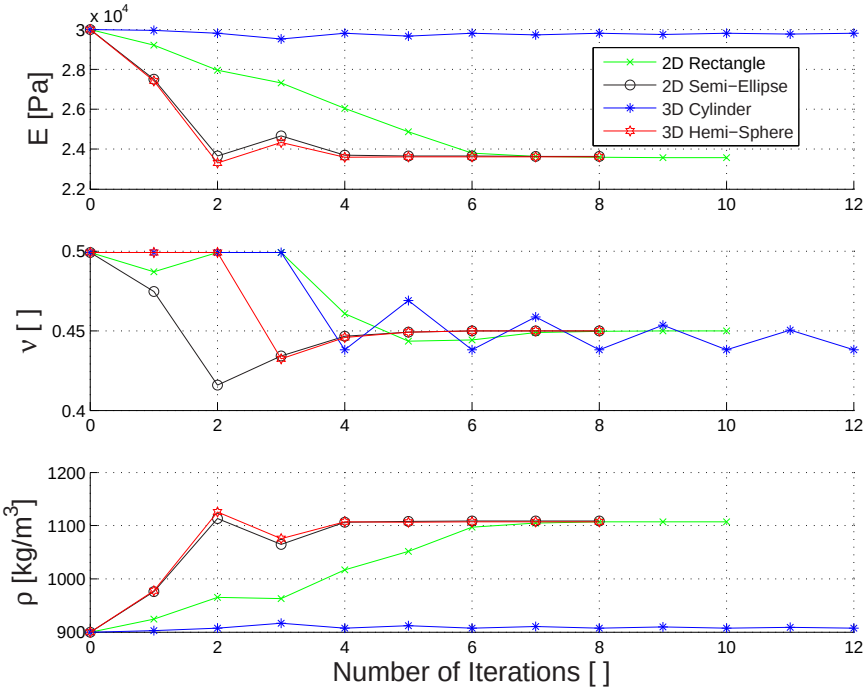

(b)

Figure 5.9 Reconstruction for material parameters of the full five parameter material model: (a) α and β, and (b) E, ν and ρ.

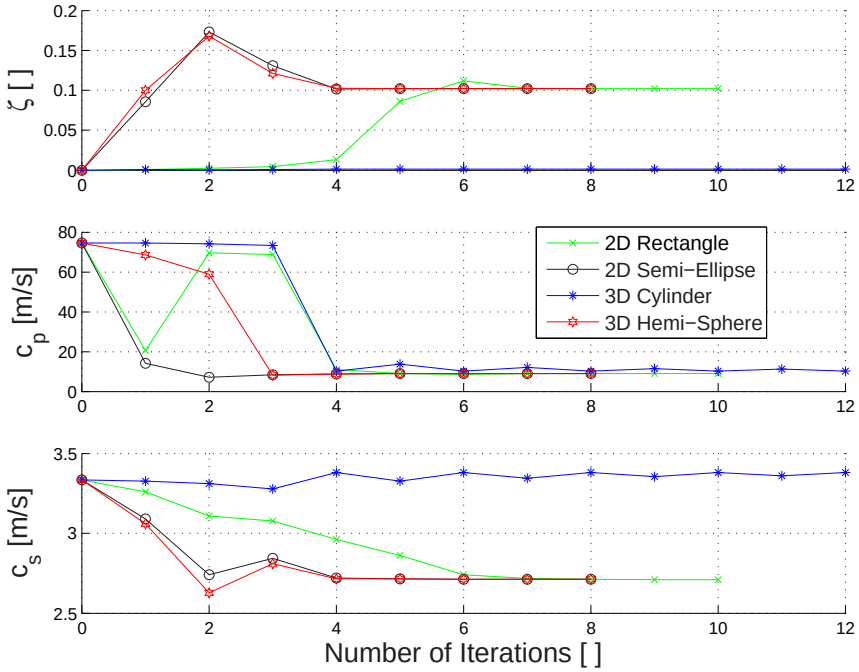

Figure 5.10 Convergence for ζ, c_p and c_s of the full five parameter material model.

are correctly identified. The incorrect values of E and ρ again lie on the line of constant wave speeds, c_p and c_s, through the correct solution.

An exception in this particular reconstruction is the cylindrical geometry, where damping parameters also fail to converge to the correct damping ratio. Furthermore, the convergence behavior in all other parameters is affected significantly. The Poisson ratio and the longitudinal wave speed are reconstructed only approximately, and the shear wave speed experiences no significant change from the initial guess. Where all other geometries have exited the iteration by achieving displacement error values to the demanded accuracy, the reconstruction in the 3D cylinder case stopped iterating due to failure to find a better approximation in the line search. This last result clearly indicates that a different local minimum was found that is not an element of the constant wave speed line.

5.3.4 Reconstruction for α, β, E and ν at known ρ

The reconstruction results obtained in both foregoing cases, particularly the failure to correctly identify the value of Young's modulus of elasticity, are unacceptable for the DIET application. However, it may not be necessary to reconstruct all

these material parameters. In particular, if there are reasonably accurate values available for the density, the convergence to incorrect values in elastic modulus may be avoidable. This approach is reasonable, as accurate values for ρ should be readily obtainable from (for example) ex-vivo testing.

To test the convergence behavior of the current material model with exact knowledge of the value of density, reconstructions were carried out with respect to α, β, E and ν. The convergence results can be seen in Figures 5.11 and 5.12.

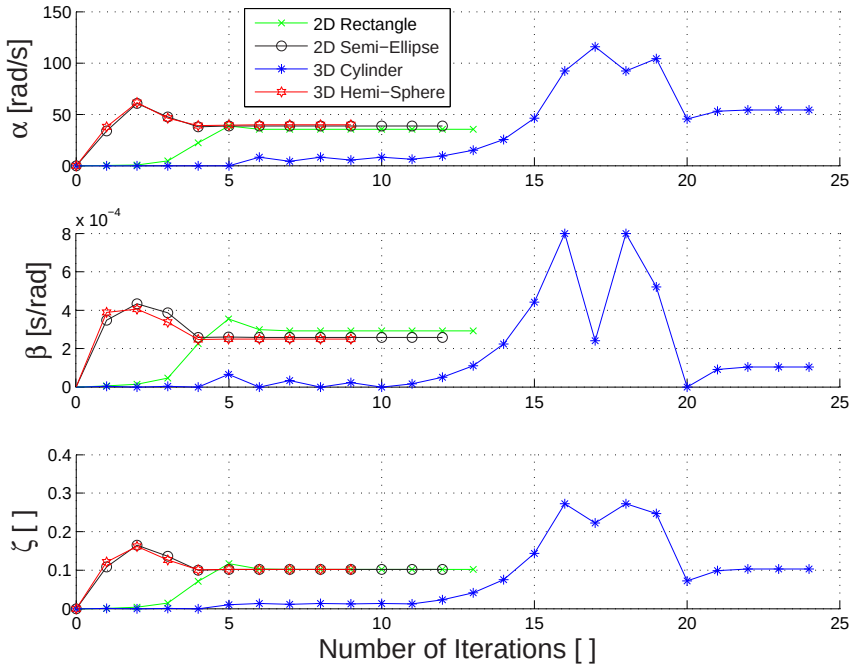

Figure 5.11 Reconstruction of the damping parameters, α and β, and the resulting damping ratio, ζ, in a reconstruction with known density, ρ.

Figure 5.11 shows, that the damping ratio, ζ, is identified correctly, but the exact damping parameters, α and β converged to an inaccurate local solution. However, it can be seen in Figure 5.12 (a) that now both the Poisson ratio, ν, and the elastic modulus are identified at their correct, global solutions. Similarly, the resulting wave speeds, c_p and c_s, in Figure 5.12 (b) are correct, as well.

The 3D cylindrical geometry is again an exception. First, it begins to show convergence to a local minimum. However, at a later iteration, convergence turns towards the correct solution values. Performance from that point is comparable to the performance of the other geometries. This reason for this behavior is likely the sensitivity with respect to start values for this particular geometry.

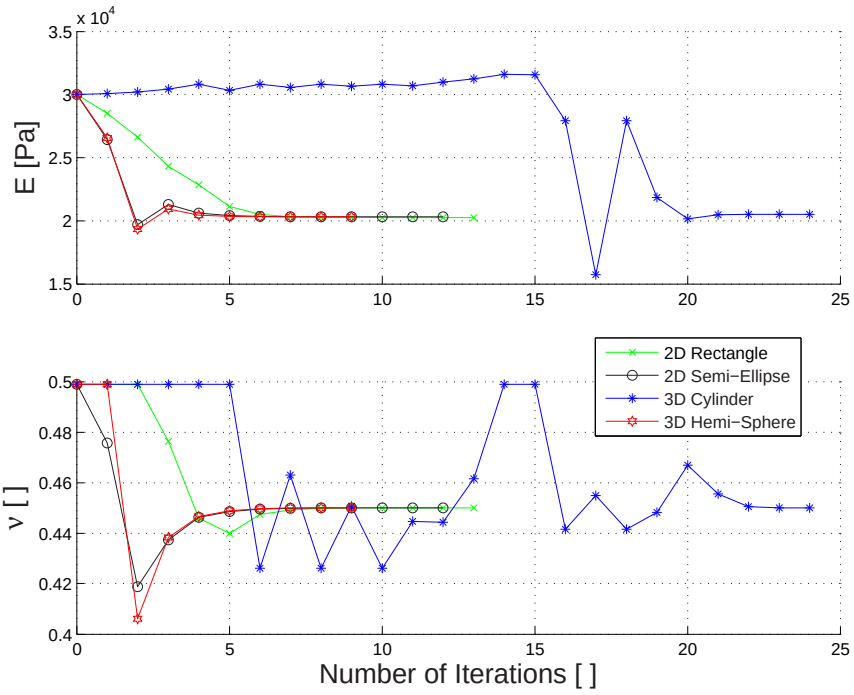

(a)

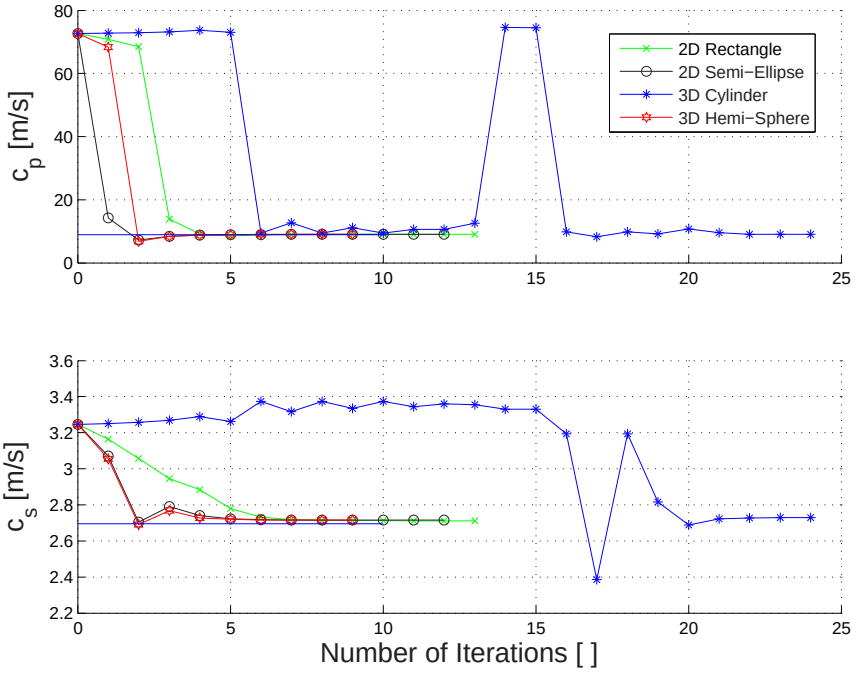

(b)

Figure 5.12 Convergence of (a) elastic modulus, E, and Poisson ratio, ν, and (b) the resulting wave speeds c_p and c_s in a reconstruction with known density, ρ.

5.4 Summary

Through a variety of simulation studies using the Gauss-Newton inversion method and the BEM for time-harmonic elasticity, it has been shown that the recovery of elastic material parameters of an isotropic, homogeneous solid is possible solely from surface motion. The following particular results are important:

- The identification of individual material parameters from a five parameter model including α, β, E, ν and ρ does not pose a difficult problem when all other parameters are known. Reconstructions are successful and converge to the correct parameter values even in the case of significantly corrupted displacement data with uniformly distributed noise up to 60%.

- Reconstructions carried out with respect to both damping parameters, α and β, while the remaining parameter values are known, result in convergence to the damping ratio, ζ, in the first few iterations, and achieve a small displacement error, Ψ, quickly. The correct values of α and β can be still successfully obtained by continuing the iteration process to extremely small values of Ψ. However, with respect to the clinical value of this inverse analysis it may well be sufficient to obtain only one damping parameter.

- Reconstructions that simultaneously identify Young's modulus and density, E and ρ, do converge, but not necessarily to their correct value. Instead, a convergence occurs to a solution for E and ρ that match the correct values of the longitudinal and shear wave speeds, c_p and c_s. In contrast to the recovery of damping parameters, where correct values can still be obtained, the correct identification of E and ρ is not possible by the use of a simple surface displacement error in this longitudinal actuation approach. This result is due to a vanishing displacement error along the line of constant wave speeds at different combinations of E and ρ. This inverse problem is not unique and, hence, requires a-priori knowledge or an assumption of either one parameter. Alternatively, the solution coefficients E and ρ could be replaced by E/ρ or by a wave speed, c_s or c_p.

- The simultaneous recovery of all five material parameters results in convergence behavior that represents a combination of those behaviors encountered for α, β and E, ρ independently. Convergence, in general, occurs to the correct damping ratio, ζ, and to the correct wave speeds, c_p and c_s. However, correct values are usually only obtained for the Poisson ratio,

ν, and not necessarily for other parameters, due to the non-uniqueness of solutions along the line of constant wave speeds. Additionally, the reconstructed results depend on the start value used with higher sensitivity than in prior scenarios.

- The problem of non-uniqueness is avoidable, if either the elastic modulus or the density are known or reasonably estimated prior to reconstruction. The reconstruction for α, β, E and ν at known values of ρ, successfully identifies correct solutions for elastic modulus, Poisson ratio and damping ratio, but still fails to correctly identify the correct damping parameters, α and β.

- Significant differences in the overall convergence behavior between two- or three-dimensional geometries could not be observed. However, convergence behavior may depend to some degree on the geometry type, where some differences can occur in the convergence speed. For example, the convergence performance of the 2D semi-spherical and the 3D semi-ellipsoidal geometry appears to be better than the performance of the 2D rectangular and 3D cylindrical geometry. The 3D cylindrical geometry appear to be more sensitive to start values than the remaining test geometries. This behavior could be due to the presence of corners on the free surface of the geometries and, hence, different wave reflection and scattering in these areas. Therefore, the displacement error function in these type of geometries may potentially contain more intense nonlinear characteristics and a larger amount of local solutions.

5.5 Conclusions for the Application in DIET

In a DIET breast cancer screening system, one critical function is the successful identification of healthy patients with a high specificity. Breast with healthy tissue may be approximated by a homogeneous, elastic and isotropic material. Material reconstruction techniques applied to such healthy cases in a DIET system are at the minimum required to correctly identify the elastic parameters from time-harmonic surface motion.

In this chapter, it has been demonstrated that this requirement is met by the techniques used, in several configurations, particularly if elasticity is reconstructed as a single parameter. If further parameters, such as the inertial and

viscous damping parameters and Poisson's ratio are also unknown, the techniques applied here are still successful in the reconstruction of the elastic parameters. Despite failure to identify the damping parameters correctly, the damping ratio is still obtained correctly, which may be sufficient.

However, in all cases, it is necessary to know at least the density value rather accurately, to avoid a problem from non-uniqueness and, therefore, to ensure reliable results in elasticity information. Additionally, knowing more accurate estimates of the values for damping parameters may be of advantage to decrease computational efforts and ensure convergence to correct values for elasticity.

Chapter 6

Identification of Inclusion Parameters

Successful screening equally requires: 1) successful recognition of non-cancerous cases; and 2) successful detection of cancerous lesions. Optimally, cancerous lesions would be identified with the high sensitivity and small size required for accurate early detection.

The presence of a cancerous lesion can be modeled by a stiff inclusion embedded in a homogeneous domain. The shape of this inclusion can be assumed to be spherical or ellipsoidal in the full volume 3D case, or circular or elliptical in the reduced 2D problem. The main requirements for a reconstruction algorithm to detect these cancerous cases would be the identification of the stiffness, size and location of an inclusion. Accurate identification of the presence of an inclusion with high stiffness contrast would be the minimum clinical goal.

For reconstructions of inclusion-related parameters the BEM for inclusions[1] is used as described in Chapter 2. An advantageous side-effect of this formulation is that this inclusion case includes the identification of healthy patients. For example, the convergence of the inclusion stiffness to the same value of the healthy background tissue is equivalent to the simulation of a single, homogeneous domain. Thus, the identification of a healthy patient can be achieved via an inclusion case. A similar result would include the convergence of the inclusion size to a minimal value.

While an approach to the recognition of non-cancerous cases was treated in Chapter 5, this chapter explores several reconstructions for inclusion cases using the Grid-Search and Gauss-Newton algorithms described in Chapter 4, as well as combinations of these two methods.

[1]Note that the same notation is used here for region-based parameters as was introduced in Section 2.3, where, if applicable, superscript $(.)^I$ refers to parameters associated with background parameters and $(.)^{II}$ refers to inclusion parameters.

First, investigations are made to obtain an indication of the reconstruction accuracy that can be expected in a best case scenario. This investigation is performed by example for the most important parameter, the inclusion's Young's modulus, E, with all other parameters known. However, a variety of scenarios are considered that account for different inclusion locations and sizes, in different material and actuation configurations.

Second, a strategy is proposed for the successful reconstruction of various inclusion parameters, with knowledge of the background material parameters. This strategy uses a combination of both Grid-Search and gradient descent based techniques. This combination is used to overcome the hurdles created by the highly nonlinear errormaps of the objective function, Ψ.

6.1 Accuracy of Inclusion Stiffness Reconstructions

This section aims to estimate the accuracy of reconstructions for inclusion related parameters in a best case scenario. Such a best case occurs when only one inclusion parameter requires reconstruction and all remaining parameters are known exactly. This task is performed by example for the inverse identification of the elastic material parameter of a lesion, E^{II}. The BEM for inclusions in Section 2.3 is used in conjunction with the Gauss-Newton inverse algorithm described in Section 4.3.

For this purpose, a multitude of inverse problems were setup that considered reconstructions for E^{II} at inclusion locations distributed over the entire spatial domain of the test geometries. A variety of scenarios were then simulated to investigate the reconstruction behavior with respect to change in the inclusion size, the actuation frequency, the type of actuation, and the damping ratio.

The 2D test geometries with rectangular and semi-elliptical shape of Section 3.1.1 were used primarily for these investigations. This choice was taken due to the simplicity in visualizing results and the faster calculation of the computationally smaller 2D problem. However, some reconstructions were also performed for the 3D geometries to confirm the similarity of the result trends.

6.1.1 Reconstruction Setup

To perform this extensive number of simulations, a program was set up that performed reconstructions systematically for a circular inclusion located at any location of a complete spatial grid within the given domain. This program is best illustrated by the pseudo-code in Table 6.1. In general, it first sets up the spatial grid depending on the geometry type and the inclusion size, R, as described in Section 4.2 with a minimum distance between the geometry's and the inclusion's boundaries. After simulating the harmonic forward displacement solution, $\mathbf{u}$, for one of the inclusion locations, P, the program saves those displacements as the reference displacements, $\mathbf{u}^\star$. It then uses them in a Gauss-Newton inverse algorithm for the reconstruction of inclusion stiffness, E^{II}.

(1) Load mesh and boundary conditions from Input files, load all input parameters ($\boldsymbol{\theta}^\star$, Ω, ...)
(2) Setup a feasible spatial grid according to the geometry type and depending on the inclusion size, R
(3) *FOR ALL* inclusion locations, *DO*:
    (a) Mesh the circular inclusion surface for the given size, R
    (b) Simulate the forward solution with given material parameters and save the displacements, $\mathbf{u}$, as the reference displacements, $\mathbf{u}^\star$
    (c) Load start value for E_0^{II}
    (d) Perform Gauss-Newton reconstruction algorithm for E^{II}
    (e) Save reconstruction results in an array
END DO
(5) Write reconstruction results to file

Table 6.1 Illustration of the program procedure for the reconstructions of inclusion elasticity, E^{II}, at multiple locations, P.

For all forward simulations in Step (3 b) of Table 6.1 that generate reference displacements, $\mathbf{u}^\star$, the same background material parameters were used. These values are specified in Table 6.2. The inclusion's density, ρ^{II}, Poisson ratio, ν^{II} and damping parameters, α^{II} and β^{II}, were assumed to have the same value as the material of region I. Hence, in all reconstructions in step (3 d) of the program, all material parameters, as well as the inclusion size and location, were known. Thus, only the inclusion stiffness, E^{II}, was reconstructed.

Parameter	Solution value ($\boldsymbol{\theta}^\star$)
E^I	25 kPa
ν^I	0.48
ρ^I	950 kg/m^3

Table 6.2 Background material parameter values for the generation of surface motion that were subsequently used in the reconstruction of the inclusion stiffness, E^{II}.

The program outlined in Table 6.1 was executed in a variety of scenarios. These scenarios characterize the reconstruction behavior in E^{II} with respect to systematic changes in the actuation frequency, f, the radial inclusion size, R, the actuation type, and the damping ratio, ζ. The specific damping parameters were assumed to equally contribute to the damping ratio, so that $\zeta = \alpha/\Omega = \beta\Omega$. Thus, the values of α and β were calculated depending on the actuation frequency to maintain an equivalent damping ratio over all simulations.

Reconstructions were also performed for two values of inclusion stiffness E^{II}. One value, $E^{II} = 30\ kPa$, simulates a healthy case with similar parameter values as healthy breast tissue. The other value, $E^{II} = 150\ kPa$, simulates a cancerous case. The reconstruction start value was $E^{II^0} = 50\ kPa$ between these target values. Specific values of all simulation parameters used for the reconstructions are given in Table 6.3.

Parameter	Value
Actuation frequency, f	50, 73, 100 [Hz]
Radial size, R	3, 5, 7 [mm]
Damping ratio, ζ	10, 20, 30, 40, 50 [%]
Actuation type	*Longitudinal* actuation in vertical (x_3) direction, *shear* actuation in horizontal (x_1) direction (each with an amplitude of 1 mm)
Inclusion modulus, $E^{II^\star}$	30, 150 [kPa]
Start value, E_0^{II}	50 [kPa]

Table 6.3 Variation of parameters for which reconstructions for inclusion elasticity, E^{II}, was investigated.

6.1.2 Reconstruction Results

The results of these investigations are illustrated in this section as plots of the test geometry indicated by its boundary mesh. Within the geometry, the grid points are plotted as dotted circles, $\odot$, each of which represents the center of an inclusion, for which a reconstruction in E^{II} was performed. Those plots are

furthermore arranged in figures with a matrix-like form. This raster illustrates the E^{II} reconstructions in a certain geometry for the three variations in the inclusion size and the three variations in actuation frequency, as denoted in Table 6.3. Thereby, the actuation type, the damping ratio, material parameters, and start value were kept at the same values.

The color-coding of the plotted grid points gives an indication for the accuracy of the reconstructions. In particular, the colors represent the relative error to which each reconstruction in E^{II} has converged at the time when the algorithm stopped iterating due to any of the stopping criteria listed in Section 4.3.5. This relative reconstruction error is defined:

$$\epsilon_{rel} = \frac{|E^{II\star} - \tilde{E}^{II}|}{E^{II\star}},$$

where $\tilde{E}^{II}$ is the converged, reconstructed value of E^{II}.

In summary, a blue ⊙ indicates a solution that has converged to an error of up to 5%. A red ⊙ indicates a failed reconstruction defined as an error greater than 25% of the reference value. Therefore, this failure criterion allows for an absolute reconstruction error of up to 7.5 kPa for the healthy case and 37.5 kPa in the cancerous case. From a computational point of view, this error range represents a reasonably generous framework, but should be acceptable from a clinical view. The detailed error ranges are listed in Table 6.4.

Color	Error range
blue ⊙	$\epsilon_{rel} \leq 5\%$
green ⊙	$5\% < \epsilon_{rel} \leq 10\%$
yellow ⊙	$10\% < \epsilon_{rel} \leq 15\%$
orange ⊙	$15\% < \epsilon_{rel} \leq 25\%$
red ⊙	$25\% < \epsilon_{rel}$

Table 6.4 Color-coding for the characterization of reconstruction accuracy in E^{II}.

Note that, for the sake of better comparability, the representation of reconstruction results is focussed here on the 2D-semi-elliptical test geometry.

6.1.2.1 Variation in Damping Ratio ζ

The most important result of these investigations are expected to be observed with changes in damping ratio, ζ. In particular, these values are expected to

characterize up to which levels of attenuation the reliable reconstruction of inclusion stiffness is possible. Figures 6.1–6.3 display the reconstructions for stiff inclusions ($E^{II} = 150\ kPa$) within the semi-elliptical geometry at three damping ratios, $\zeta = 10\%,\ 30\%$ and 50%, respectively. The actuation type in all of these figures was the DIET-typical longitudinal actuation in the vertical x_3-direction.

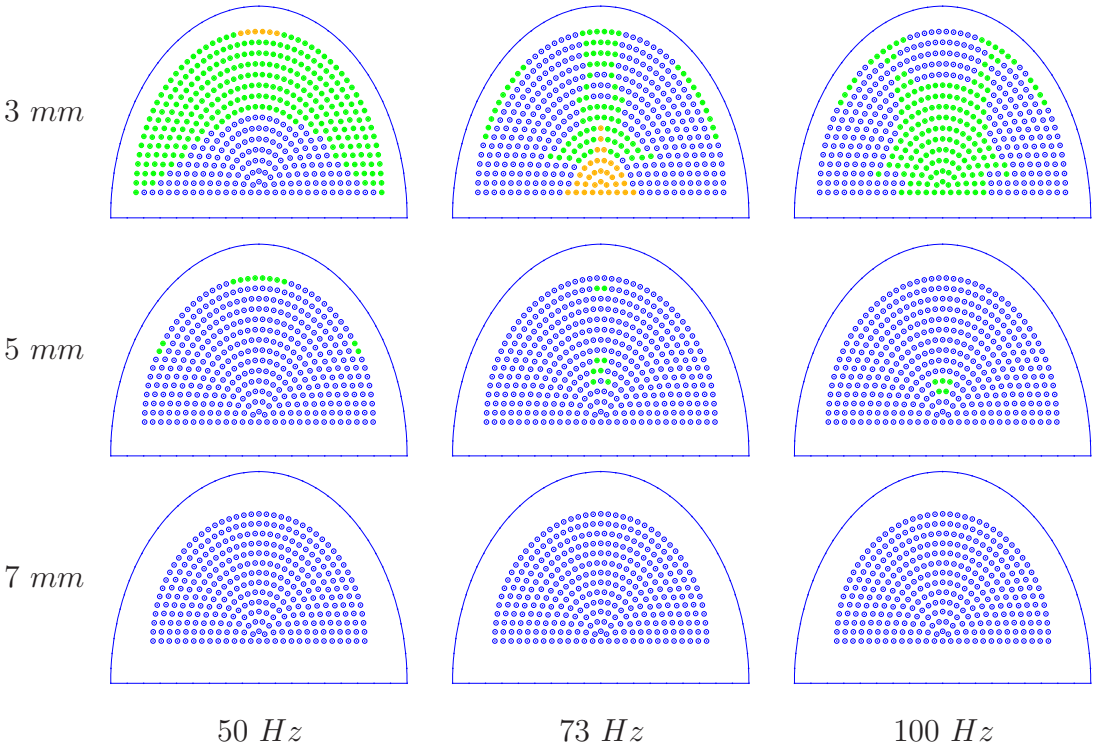

Figure 6.1 Stiffness reconstructions for circular, stiff inclusions (at $E^{II} = 150kPa$) within a 2D semi-ellipse with longitudinal actuation at a damping ratio of $\zeta = 10\%$.

E^{II} reconstructions at low damping levels (i.e. $\zeta = 10\%$, in Figure 6.1) achieve excellent convergent results. Regardless of the actuation frequency, the $R = 7\ mm$ inclusion size cases all converged to an error lesser than 5%. In the $R = 5\ mm$ cases, only a very few cases exceed the 5% margin. The $R = 3\ mm$ case, shows some areas with errors between 5% and up to 15% that cover larger areas of the spatial domain. The size and positions of those less accurate areas is different for each actuation frequency. However, at this damping level of $\zeta = 10\%$ no single reconstruction failures are observed.

When the influence from attenuation is increased to $\zeta = 30\%$, as shown Figure 6.2, E^{II}-reconstructions for the 7 mm inclusion case are still very good, with most locations returning reconstruction errors under 5%. A larger area of slightly increased error can be observed at an actuation frequency of 100 Hz. With decreasing inclusion sizes, $R = 3\ mm$ and 5 mm, areas with inaccurate

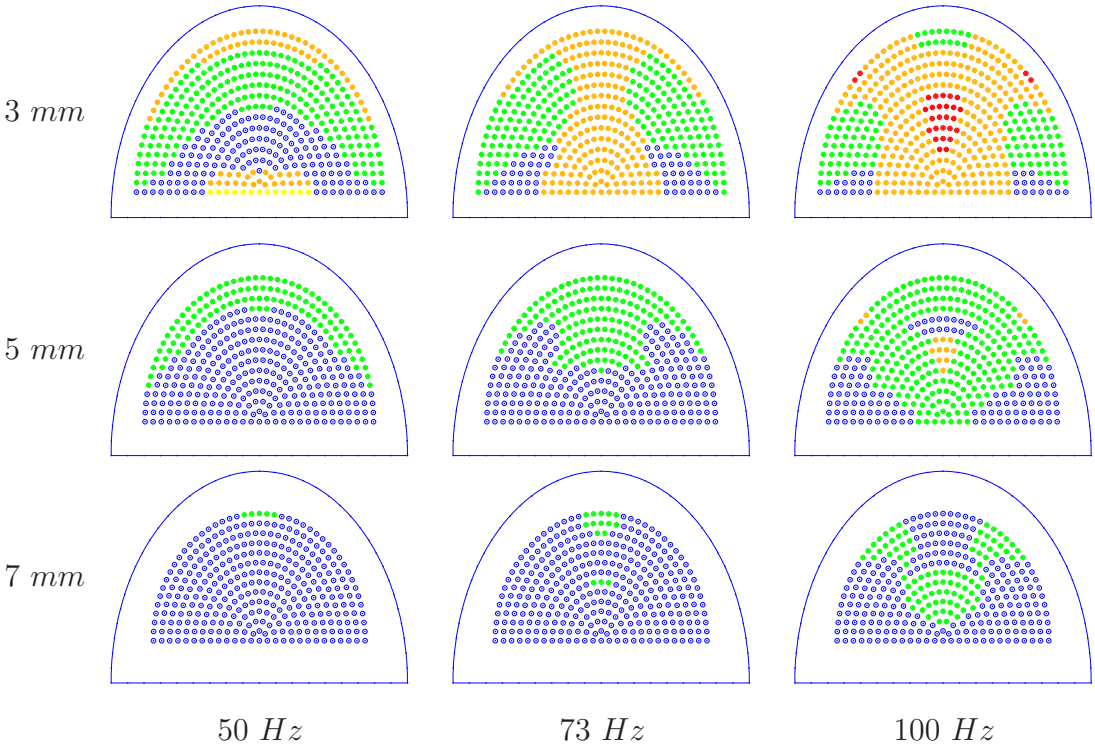

Figure 6.2 Stiffness reconstructions for circular, stiff inclusions (at $E^{II} = 150kPa$) within a 2D semi-ellipse with longitudinal actuation at a damping ratio of $\zeta = 30\%$.

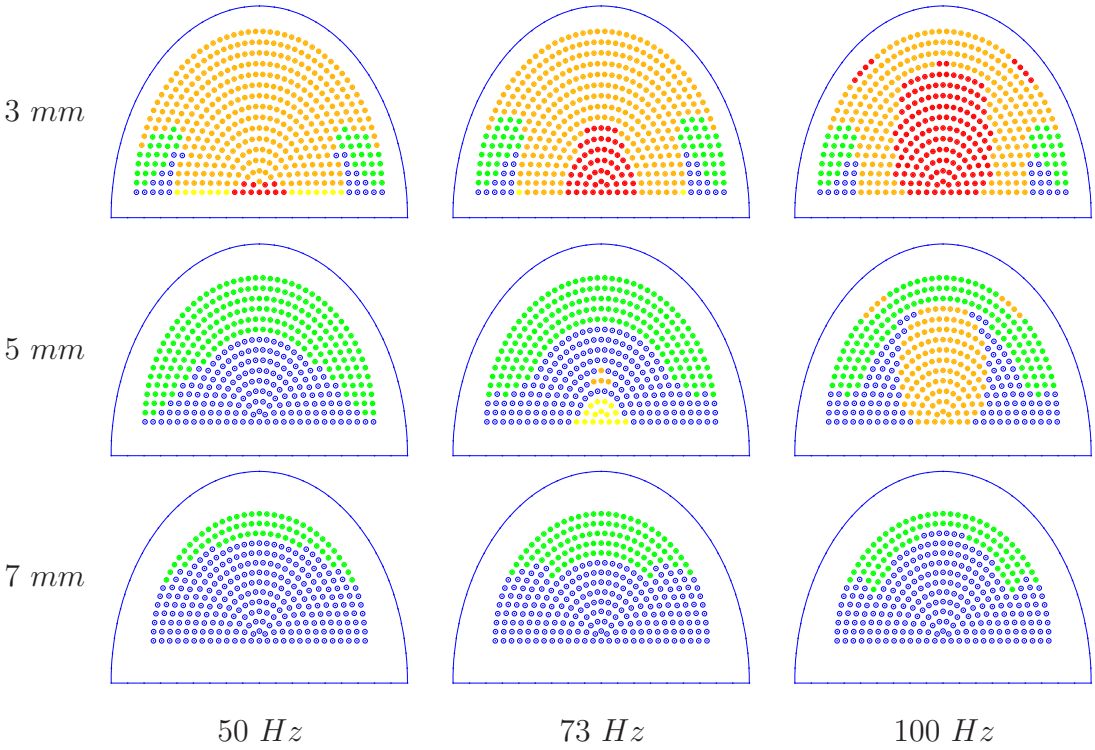

Figure 6.3 Stiffness reconstructions for circular, stiff inclusions (at $E^{II} = 150kPa$) within a 2D semi-ellipse with longitudinal actuation at a damping ratio of $\zeta = 50\%$.

reconstruction results increase in both size and error value. In the 3 mm case, in particular, there are now larger areas with reconstruction errors between 15% and 25%. In the 100 Hz actuation case, the first cases of reconstruction failure are observed in the middle and at the edge of the inclusion grid.

A further increase of the damping ratio to $\zeta = 50\%$ (see Figure 6.3) intensifies the effects described above. Where reconstructions in the large inclusion case ($R = 7$ mm) still show reasonably accurate results with errors under 10%, the smaller cases experience a clear decrease of reconstruction accuracy and efficacy. At $R = 3$ mm the greatest area of the grid converges with an error between 15% and 25%, but reconstruction failures now occur at all actuation frequencies. At $f = 50$ Hz, there are only very few reconstruction failures, but in the $f = 100$ Hz case, the number of failures makes up almost 30% of the entire grid.

Further results at this high damping ratio of $\zeta = 50\%$ and inclusion size of $R = 3$ mm are shown in Figures 6.4 and 6.5 for the same reconstruction scenario as in Figure 6.3. Here, the 2D rectangular geometry with longitudinal actuation and the 2D semi-elliptical geometry with shear actuation are examined. Each geometry is shown for reconstruction cases at 50 Hz and 100 Hz. All these highly damped cases clearly show a large number of failed reconstructions or, at the least, reasonably inaccurate reconstruction values. However, both geometries show better reconstruction results at the lower frequency of 50 Hz, when compared to those reconstructions at 100 Hz.

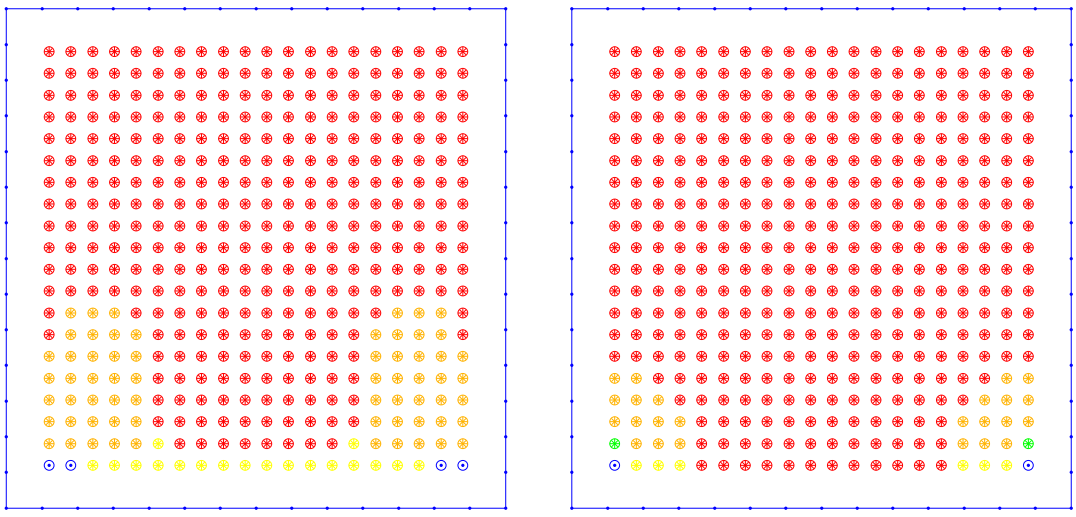

50 Hz 100 Hz

Figure 6.4 Stiffness reconstructions for circular, stiff inclusions (at $E^{II} = 150kPa$) at a damping ratio of $\zeta = 50\%$ within a 2D rectangular geometry with longitudinal actuation.

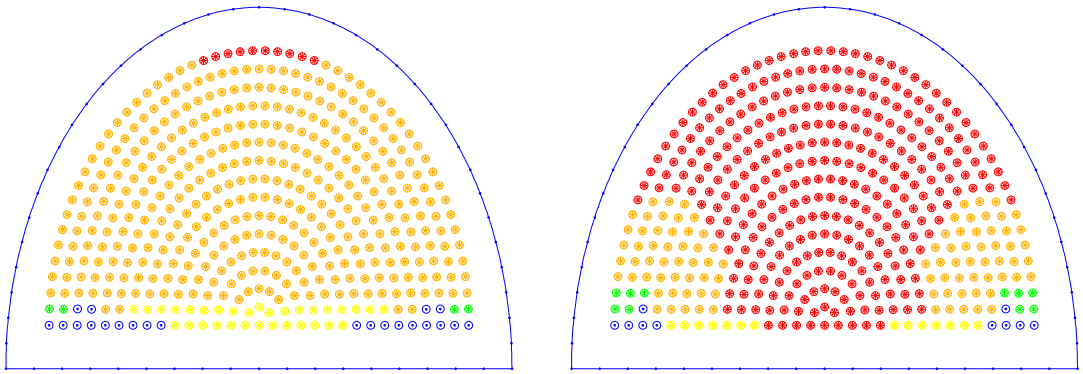

Figure 6.5 Stiffness reconstructions for circular, stiff inclusions (at $E^{II} = 150kPa$) at a damping ratio of $\zeta = 50\%$ within a 2D semi-elliptical geometry with shear actuation.

6.1.2.2 Variation in Geometry, Actuation Type and E^{II}

The reconstruction results obtained for different geometry and actuation types are, in general, very similar to those results shown previously. They also change similarly with damping ratio. However, these results are worth mentioning, as some small additional effects and trends can be illustrated.

Figure 6.6 shows the reconstruction results obtained for the 2D rectangular geometry for the case of stiff inclusions at $\zeta = 10\%$. Similar to the semi-ellipse, the results are very accurate, particularly at large inclusion sizes. However, areas of less accurate reconstructions show up in the $R = 5\ mm$ and $3\ mm$ cases more intensely than in the semi-elliptical case. In particular, there are some failed reconstructions in the $3\ mm/50\ Hz$ case. The shape of those inaccurate reconstruction areas has changed and is again observed to be different for each actuation frequency.

The difference in reconstructions due to change in the type of actuation is illustrated in Figure 6.7. This figure shows the results obtained for the identification of E^{II} at a damping ratio of $\zeta = 10\%$, when a shear actuation is applied at the geometry's bottom side in the horizontal x_1-direction. In comparison to the same case with longitudinal actuation in Figure 6.1, the results show slightly improved convergence accuracy, as the areas with increased reconstruction error, particularly in the small inclusion case, are decreased. This improvement is not necessarily significant, but has been observed consistently in all simulated cases with higher damping ratio, as well as the type of geometry.

Finally, Figure 6.8 shows the reconstruction results in the 2D semi-elliptical test-geometry obtained for the simulation of a *healthy* case with a reference in-

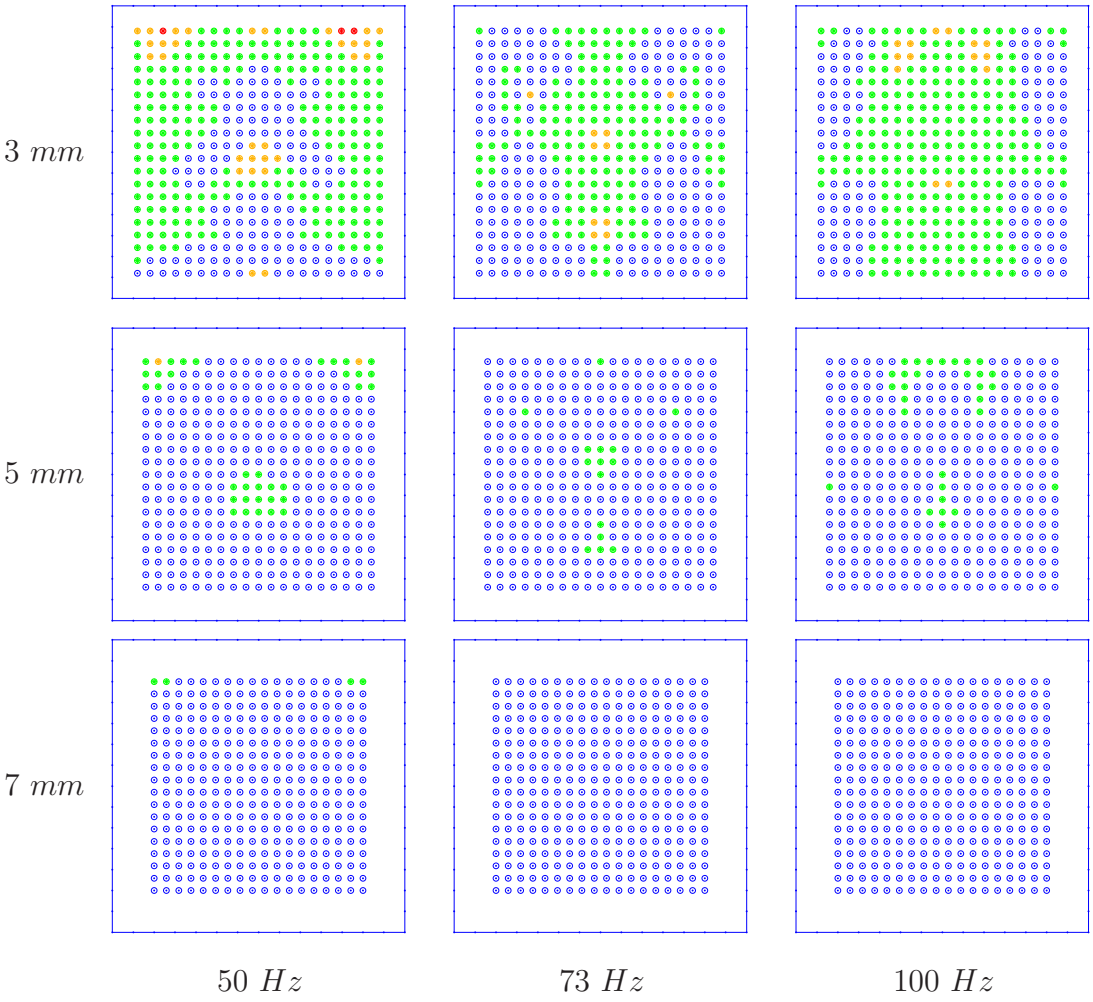

Figure 6.6 Stiffness reconstructions for circular, stiff inclusions (at $E^{II} = 150kPa$) within a 2D rectangle with longitudinal actuation at a damping ratio of $\zeta = 10\%$.

clusion stiffness of $E^{II} = 30kPa$. There is no major difference compared to the reconstruction behavior in Figure 6.1. However, it appears that, again, a slightly better accuracy is achieved, as less accurate areas are decreased in size.

6.1.2.3 Stiffness Reconstruction in 3D Cases

Reconstructions for inclusion elasticity in the case of three-dimensional test-geometries have also been conducted to resemble the observations made in the 2D geometries. For this reason, particular reconstruction cases were picked to compare changes in behavior with respect to damping ratio, inclusion size, geometry, actuation type and frequency. The background material parameters used here are also those given in Table 6.2 and reconstruction results are displayed in Figures 6.9 and 6.10.

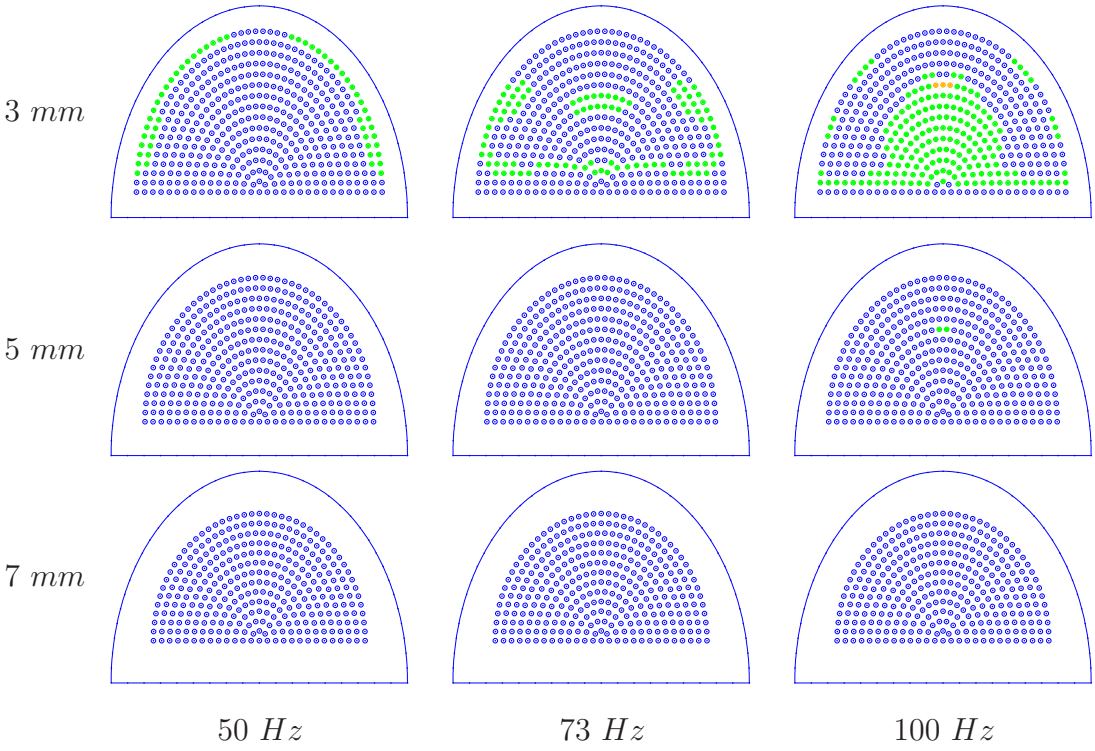

Figure 6.7 Stiffness reconstructions for circular, stiff inclusions (at $E^{II} = 150kPa$) within a 2D semi-ellipse with shear actuation at a damping ratio of $\zeta = 10\%$.

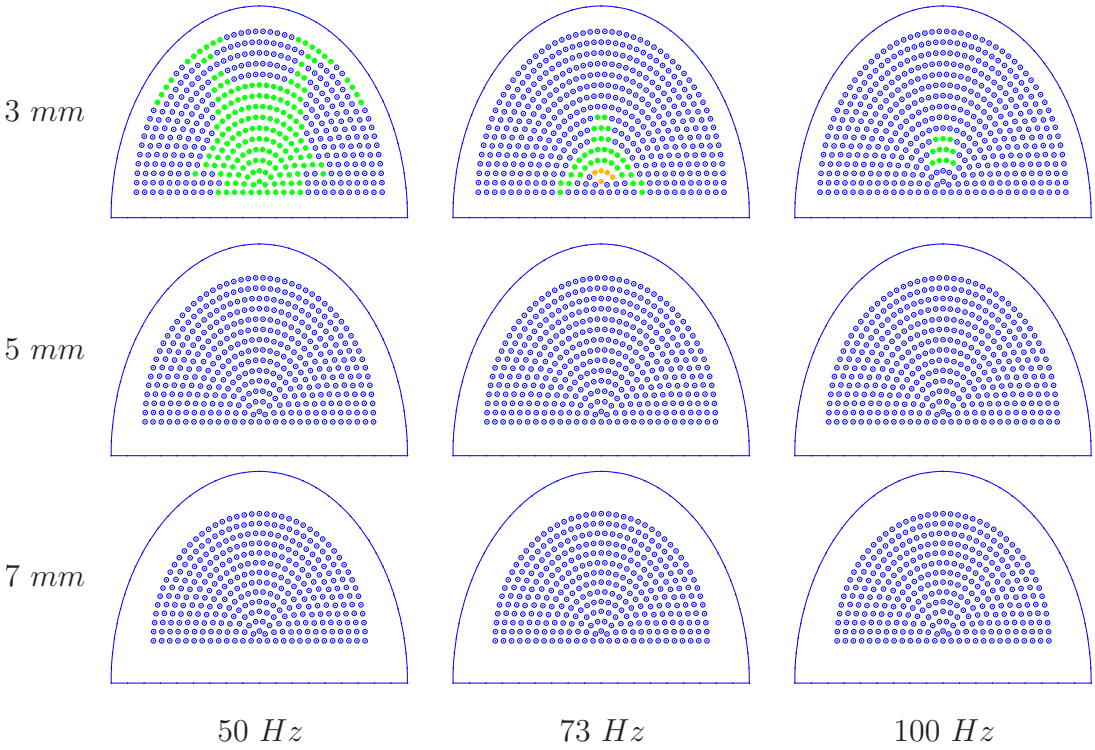

Figure 6.8 Stiffness reconstructions for circular, *healthy* inclusions ($E^{II} = 30kPa$) within a 2D semi-ellipse with longitudinal actuation at a damping ratio of $\zeta = 10\%$.

Figure 6.9 illustrates the accuracy of stiffness reconstructions in the case of a 3D semi-ellipsoid with an embedded spherical inclusion of size $R = 3\ mm$, when reconstructions are performed at 50 Hz and 100 Hz for three different damping levels, $\zeta = 10\%,\ 30\%$ and 50%. In this three-dimensional case the same observations are made as already seen in the equivalent 2D cases. With increasing damping ratio, the stiffness reconstructions become increasingly difficult with convergence to less accurate results. Similarly, reconstructions performed at the lower frequency appear to achieve better results compared to the same case at higher frequency.

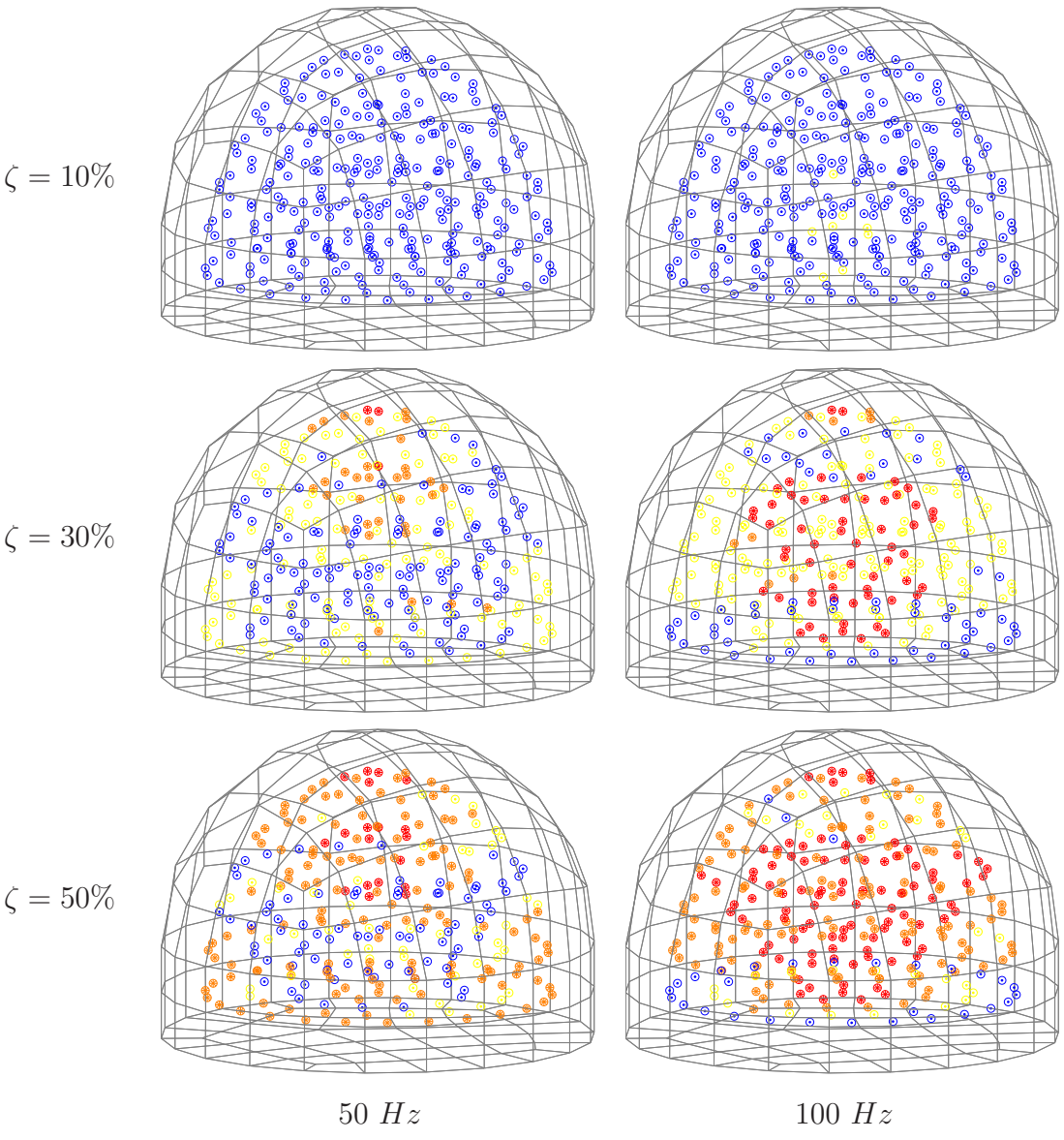

Figure 6.9 Reconstruction accuracy for inclusion stiffness in a longitudinally actuated 3D semi-ellipsoid for a given variation in damping ratio, ζ, and actuation frequency, Ω.

Figure 6.10 shows the inclusion stiffness reconstructions in the case of a 3D cylindrical geometry, where changes exhibited by different actuation type and different inclusion sizes are illustrated. Figure 6.10 (a) shows the stiffness reconstructions for a $R = 3\ mm$ inclusion case with $\zeta = 50\%$ and actuated longitudinally at $50Hz$, where Figure 6.10 (b) shows the same geometry in the same specifications, but with shear actuation. Interestingly, the longitudinal actuation case has achieved slightly more accurate results and less failure cases than the shear actuation case, which is the opposite of what was observed in the 2D geometries.

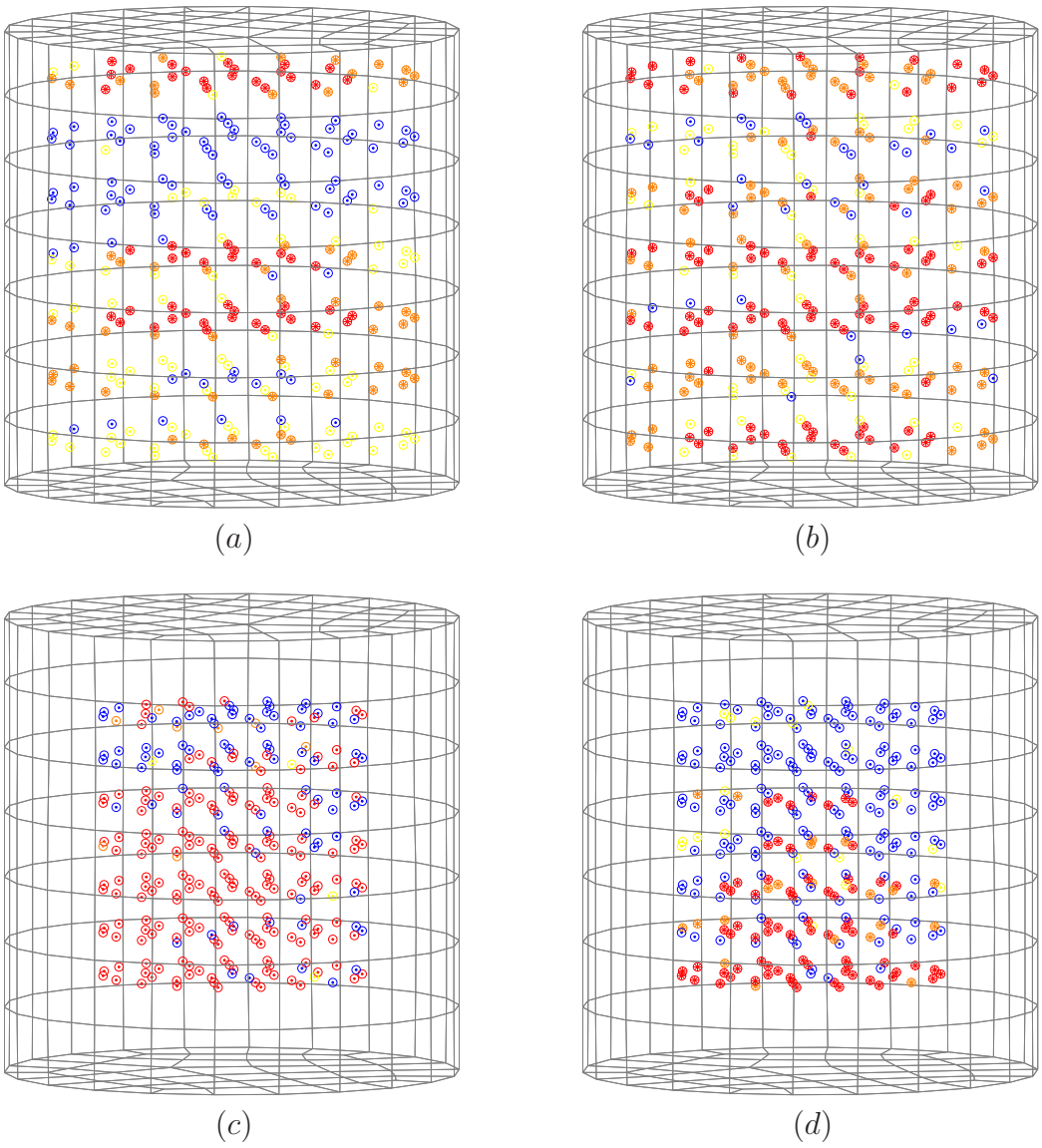

Figure 6.10 Reconstruction for inclusion stiffness in 3D cases, (a) from longitudinal and (b) from shear actuation at 50 Hz and $\zeta = 50\%$, as well as (c) for a $R = 3\ mm$ and (d) an $R = 8\ mm$ circular inclusion at 100 Hz longitudinal actuation and $\zeta = 30\%$.

Figures 6.10 (c) and (d) illustrate the differences in reconstruction accuracy in the case of differently sized inclusions. In particular, Figure 6.10 (c) uses a 3 mm inclusion and (d) an 8 mm inclusion within the 3D geometry, with $\zeta = 30\%$ and 100 Hz longitudinal actuation. The observations that accurate reconstruction occurs or is achievable in larger inclusion cases, is confirmed in this 3D case.

6.1.3 Discussion

It can be generally stated that reconstructions for inclusion stiffness were successful. Differences occurred in the accuracy of the reconstructed results and were influenced to different degrees by the varied parameters. The specific observations are discussed in the following:

- One of the most influential parameters for the reconstruction accuracy is the amount of damping, represented by the damping ratio, ζ. While reconstructions for E^{II} with low attenuation from damping, $\zeta \leq 10\%$, generally achieve rather accurately converged results, the increase of damping influence leads to areas of decreased reconstruction accuracy within the domain. These areas grow with increasing ζ in both size and reconstruction error. At high damping influence, $\zeta \geq 50\%$ (see Figures 6.3 and 6.9), distinct areas can be recognized where reconstructions have failed with respect to a margin of 25% in error. In a first estimation, a proportional relation between damping ratio and reconstruction accuracy may be assumed. This observation has been made consistently in 2D and 3D geometries.

  It is worth noting that the values for ζ assumed in this investigation are to a degree arbitrary choices. Hence, only the determination of the damping parameter by clinical studies will deliver objective information about the range of values likely to occur.

- The inclusion size, here characterized by the radial size, R, of a circular or spherical inclusion has been identified as a similarly important parameter with influence on the reconstruction accuracy. Where inclusions of larger size, $R \geq 5$ mm, have generally lead to reasonably accurate reconstruction results in 2D cases, often with less than 5% error, the reconstruction of stiffness of small inclusions becomes less accurate. Sizes of $R = 3$ mm show reconstruction errors of up to 10% even with little influence from damping ($\zeta = 10\%$). This result confirms the interpretations made in the study on

surface motion errormaps in Section 3.2, where inclusions of $R \leq 2\ mm$ were found to produce errormaps with undistinguishable, noisy characteristics that prohibit a systematic inverse identification of the parameters.

- Differences in reconstruction accuracy have also been found in inverse calculations at different actuation frequencies and at different actuation types. While it can be stated that some configurations produced better reconstructions results at a low actuation frequency, meaning smaller areas of inaccurate reconstructions, the same is the case for other reconstructions at higher actuation frequency. Similarly, where shear actuation in 2D cases has shown better results than longitudinal actuation, the opposite appears to be the case in 3D geometries. Further investigations with larger scale may be required here, to achieve more detailed observations and draw consistent conclusions.

- It can further be noted, that the shape of areas with less accurate reconstruction results varies with both frequency and actuation type, as well as with the type of geometry. However, the shape appears to remain qualitatively the same in case of changes in inclusion size. This result is meaningful as these areas may be related to a distinct mode-shape of a geometry excited from a certain actuation and at a certain frequency.

- Reconstruction behavior for *healthy* cases with only slightly raised values of inclusion stiffness compared to the surrounding material was consistently found to be more accurate than the reconstruction behavior for inclusions cases with lesions of increased stiffness. While this result may be influenced by the better quality of the initial guess used here, trials with higher start values also lead to similarly improved reconstruction accuracies.

- While stiffness reconstruction in the three-dimensional cases show all behaviors also encountered in the 2D cases, apart from differences due to actuation type, it appears that the accuracy of convergence results is generally slightly lower than in the 2D cases. This result occurs despite using the same parameters and (absolute) inclusion sizes. However, one should note that the relative inclusion sizes with respect to the size of the geometry, was not the same. In particular, the relation V_{incl}/V_{total} was smaller in the 3D cases, than the relation A_{incl}/A_{total} in 2D geometries. Thus, this result might have been anticipated.

6.1.4 Conclusions

The identification of inclusion stiffness, E^{II}, at otherwise well known material and geometric parameters, has been simulated in a variety of scenarios. The purpose was to test the ability of the applied algorithm to successfully identify both an inclusion with similar material parameters as the surrounding material, representing a healthy case, and a high-stiffness inclusion for the detection of a cancerous case. These scenarios included the change in several possible conditions including the damping ratio, ζ between values of 10% and 50%, as well as a shear and a longitudinal actuation type. Furthermore, those reconstruction scenarios have been tested at different inclusion sizes and different actuation frequencies.

These reconstructions for inclusion stiffness, E^{II}, have generally lead to results with reconstruction accuracies that are reasonable for the interpretation in a clinical setting. This includes particularly the differentiation between a healthy and a malignant tumor case. The overall reasonably successful reconstructions of inclusion stiffness particularly in healthy cases could be interpreted as an indication for a good specificity of this reconstruction method with a good ability in the identification of healthy cases.

However, the inclusion size, R, and damping ratio, ζ, have been found, in cases, to cause failure of convergence to stiffness values with acceptable accuracy. Often, high damping or small inclusion sizes are critical and result in reconstruction errors over 25% occurring in expanded areas of the simulated grid. This behavior can occur for all simulated frequencies and for different actuation types. Hence, these values may be regarded as limits for the reliable reconstruction from harmonic surface motion.

The rather large number of failed reconstructions particularly for cases representing a small malignant tumor at high damping levels could, therefore, also be interpreted as an indication for a lowered sensitivity of this reconstruction algorithm. Hence, patients with a very small stiff tumor may not be identified reliably, if the effective damping ratio of breast tissue exceeds such high damping ratios ($\zeta \geq 50\%$).

A potential solution for the reconstruction of inclusions in these *hidden* areas may be the use of several data-sets for the objective function. These data-sets may contain measured surface motions obtained at several actuation frequencies and/or several actuation types. The use of several data-sets would introduce a large amount of extra computational cost, but may lead to more accurate reconstruction results in critical cases.

6.2 Reconstruction for Inclusion Parameters

The precise identification of inclusion related parameters within the domain is a very important task in the DIET system. Needless to say, the failure to identify the correct values would be misleading in the clinical interpretation and could lead to serious potentially negative outcomes for a patient. From the other perspective, the correct identification of a potential inclusion would be of large diagnostic value. Follow-up examinations, such as a punch biopsy, could possibly be kept to a minimum. This in turn would allow a quick decision on a treatment plan and minimize the risk of further progress of the disease.

This section deals with the reconstruction of inclusion parameters within the given domain, in particular the inclusion location, P, the radial size, R, and the inclusion stiffness. In this section, background material parameters are generally assumed to be known exactly. Additionally, the inclusion's Poisson ratio, ν^{II}, density, ρ^{II}, as well as the inclusion's damping parameters, α^{II} and β^{II}, are assumed identical to their counterparts for the background material.

6.2.1 Reconstruction Setup

In Section 3.2, errormaps for the spatial position of an inclusion have been shown to be highly nonlinear and to contain a large number of local minima (see Figure 3.14). Therefore, even neglecting the influence from different inclusion sizes or stiffness values, a number of solutions for the inclusion location may possibly be found in a specific reconstruction problem. Some trial Gauss-Newton reconstructions for the inclusion size and stiffness purposely performed assuming a wrong inclusion location confirmed the obvious results: a wrong inclusion location causes significant error in the reconstruction of other inclusion parameters, particularly R and E^{II}. Results of such reconstruction cases can generally be observed not only to be inaccurate, but often reflect entirely opposing circumstances of the solution reality.

Given these reasons, it is obviously important to obtain as much knowledge as practically possible of at least several local solutions in a specific reconstruction case to provide the ability to qualitatively differentiate between reconstruction results. Creating a detailed errormap, that allows differentiation between local and global solutions with certainty, is prohibitive from a practical and from a computational cost point of view. The use of a gradient descent based reconstruction is far superior, but the choice of a number of quality start values is

crucial to enable differentiation of the global minimum.

The technique applied here to achieve the successful reconstruction of the inclusion parameters ($P,\ R,\ E^{II}$) is outlined in the pseudo-code in Table 6.5 and is essentially a hybrid method of Grid-Search combined with the Gauss-Newton method. In particular, it involves the execution of a coarse Grid-Search in the inclusion parameters of choice, but with focus on the inclusion location. Thereby, the choice of a reasonable resolution is a trade-off. The search needs to be fine enough to be able to catch the nonlinearity of the errormap, but should be as coarse as possible to keep computational costs minimal.

Following the Grid-Search, the extraction of N_{min} local minima from the resulting errormap supplies the start values, each of which are subsequently used in a Gauss-Newton reconstruction. A final comparison of the displacement error values of the converged solutions is then used for the differentiation between the correct global and other local solutions. The overall method is thus a hybrid optimization approach.

(1) Load mesh and boundary conditions from Input files, load all input parameters ($\boldsymbol{\theta}^0$, Ω, ...)
(2) Setup a feasible parameter-grid including the inclusion size, R, stiffness, E^{II}, and the spatial dimension according to the geometry type and inclusion size at a feasible resolution with respect to the expected number of local minima.
(3) Perform Grid-Search:
- Obtain errormap for the given grid
- Extract N_{min} local minima from the resulting errormap and save them as start values $\boldsymbol{\theta}^0$

(4) *FOR ALL* start values, $\boldsymbol{\theta}^0$, *DO*:
- Perform Gauss-Newton reconstruction algorithm for selected inclusion parameters out of $P,\ R,\ E^{II}$

END DO
(5) Compare error value, Ψ, from all (max. N_{min}) converged Gauss-Newton reconstructions and write to file

Table 6.5 Illustration of the program procedure for the reconstruction of inclusion parameters ($P,\ R,\ E^{II}$) from a combined Grid-Search and Gauss-Newton algorithm.

In the following, reconstruction results from this program are presented for the identification for the geometric inclusion parameters, location, P, and size R. Those reconstructions only illustrate and prove the ability and performance of the

algorithm. This analysis is thus followed by a short study for the simultaneous reconstruction of P, R and E^{II} to assess the clinical use this method.

6.2.2 Reconstruction for Inclusion Locations

The reconstruction process from the program in Table 6.5 was tested for inclusion locations using all test geometries in 2D and 3D. Two different inclusion locations are simulated with sizes varied between $R = 5\ mm$ and $R = 3\ mm$. For forward calculations, $E^I = 20\ kPa$, $\nu = 0.49$, $\rho = 1000\ kg/m^3$, $\zeta = 10\%$ and $E^{II} = 150\ kPa$ were used for material parameters to generate the reference displacement values, $\mathbf{u}^\star$, on the outer surface.

In all cases, the reconstructions lead to the successful identification of the correct inclusion position, as long the Grid-Search was performed at a sufficient resolution. As an example of the reconstructions, Figure 6.11 shows the 2D rectangular geometry with an inclusion of (a) $R = 5\ mm$ and (b) $R = 3\ mm$ in two different locations.

The reference displacements, $\mathbf{u}^\star$, were then used to reconstruct the inclusion location using the program outlined in Table 6.5 at different resolutions for the Grid-Search. Since the inclusion size, as well as its stiffness, were assumed to be known, Grid-Search was performed only in the spatial domain before the detailed reconstruction with Gauss-Newton.

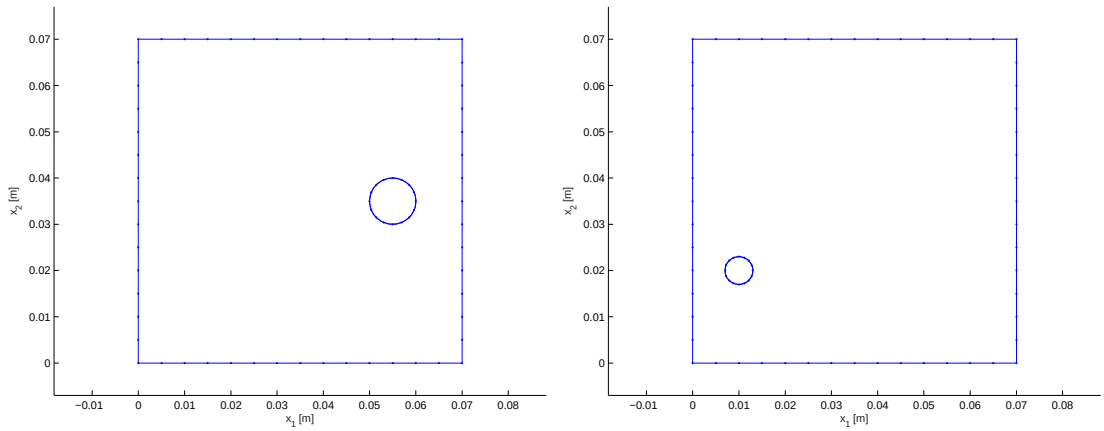

(a) (b)

Figure 6.11 Solutions for reconstruction in the inclusion's location for circular inclusions of size (a) $R = 5\ mm$ and (b) $R = 3\ mm$ in a 2D rectangular geometry.

6.2.2.1 Results

The reconstruction results for the $R = 5\ mm$ and the $R = 3\ mm$ inclusions in the rectangular geometry are shown in Figures 6.12 and 6.13, respectively. On the left of each figure the errormap resulting from the coarse Grid-Search is shown within the outlined geometry and with the extracted local minima highlighted with a yellow star and numbered in the order of extraction. On the right side of each figure, the path of the Gauss-Newton descent is highlighted by yellow dots from the numbered starting values towards their converged solution that is also highlighted with a yellow star. This path is plotted over the detailed errormap, to illustrate the descent process.

Each reconstruction was carried out at three different levels of coarseness in the Grid-Search. In these figures Grid-Search resolution increases from top to bottom: (a) at a resolution, h, of $h = 3\ cm$ (resulting in 9 grid-points, where forward solutions are required), (b) at a $h = 2\ cm$ resolution (16 grid-points) and (c) $h = 1.2\ cm$ resolution (25 grid-points).

In Figure 6.12, the resolutions in (a) and (b) lead to a maximum of two minima to be extracted as start values, whereas in (c), the requested number of start values, $N_{min} = 3$, can be extracted. However, the Gauss-Newton reconstructions identify the global minimum, and, therefore, the correct inclusion location in all cases with the first start value.

In contrast, in the more difficult $R = 3\ mm$ inclusion case shown in Figure 6.13, the coarseness of the first Grid-Search leads to the recognition of only one start value. The subsequently Gauss-Newton reconstruction, in this case, does not converge to the correct inclusion location, but stopped iterating. The reason for this result is the presence of a shallow, local minimum in the vicinity of this first start value that cannot be recognized in this contour plot. However, both the higher resolutions in (b) and (c) supply start values that subsequently lead to the successful identification of the inclusion location.

To illustrate the reconstruction process in the three-dimensional case, Figure 6.14 (a) shows the results obtained in the semi-ellipsoidal geometry for the case of a $R = 5\ mm$ inclusion. In this figure, the geometry is outlined as a coarse mesh. Within this mesh, the 139 grid-points simulated in the Grid-Search are plottet as blue dots, with the Gauss-Newton path from two selected start values plottet as yellow dots converging towards their closest local solution highlighted with a red star. Also in this case, the first selected start value returns the correct solution indicated by a sphere at the position $P^{\star} = (0.01, -0.01, 0.02)^T\ m$.

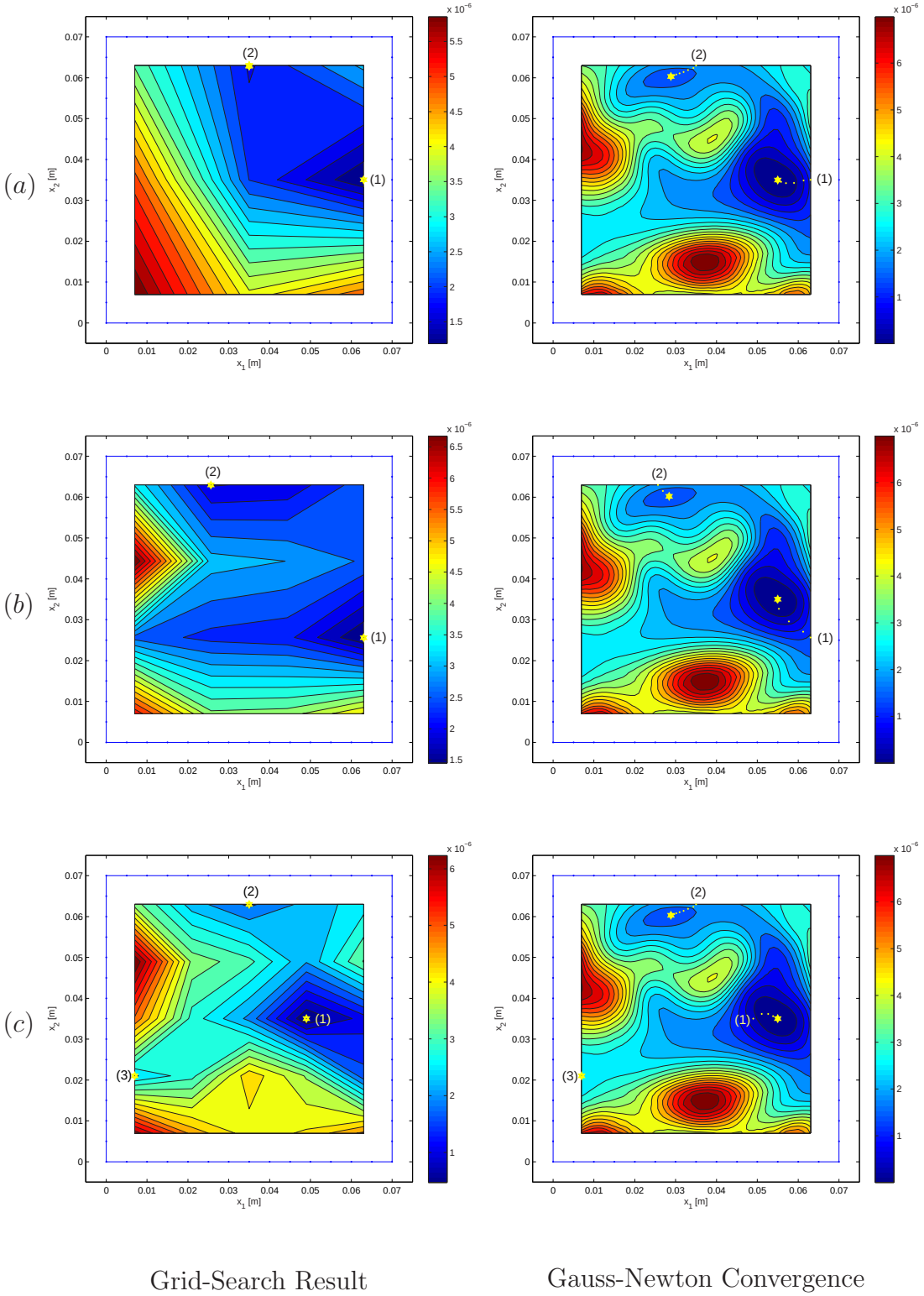

Figure 6.12 Reconstruction results for the identification of an inclusion's locations ($R = 5\ mm$) from combined Grid-Search and Gauss-Newton methods executed for three different Grid-Search resolutions, (a) $h = 3\ cm$, (b) $h = 2\ cm$ and (c) $h = 1.2\ cm$.

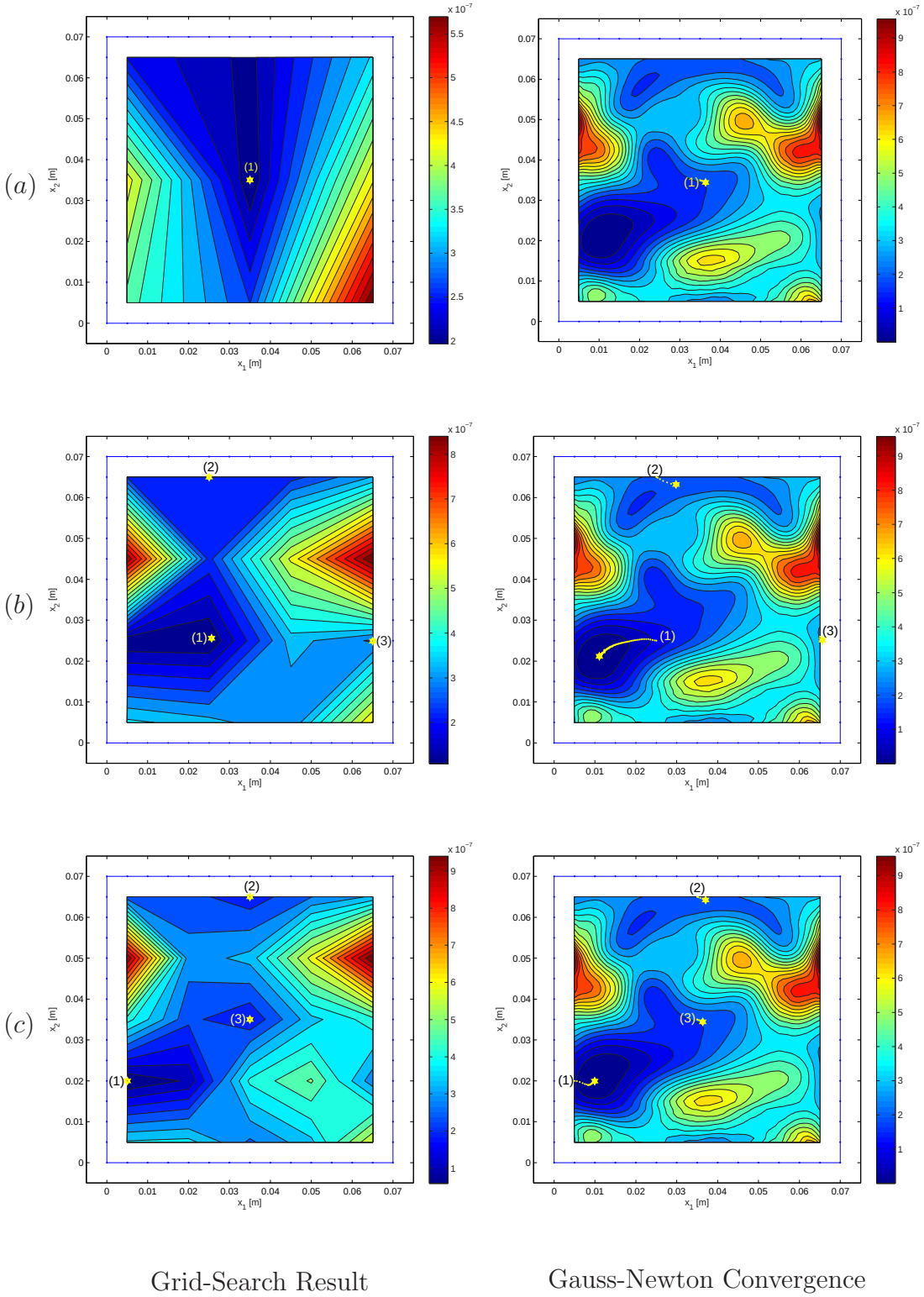

Figure 6.13 Reconstruction results for the identification of an inclusion's locations ($R = 3\ mm$) from combined Grid-Search and Gauss-Newton methods executed for three different Grid-Search resolutions, (a) $h = 3\ cm$, (b) $h = 2\ cm$ and (c) $h = 1.2\ cm$.

In Figure 6.14 (b), the convergence behavior of the inclusion case is illustrated. The number of 74 iterations is large, but in this small inclusion case, the displacement error caused is not overly large. Thus, low error margins are necessary for exact convergence, as occurred in this case to $\Psi = 1 \cdot 10^{-13}$. However, iterations could have been stopped at approximately 15, where the inclusion location was already converged to a position less than 0.5 mm off its true solution location, $P^{\star}$.

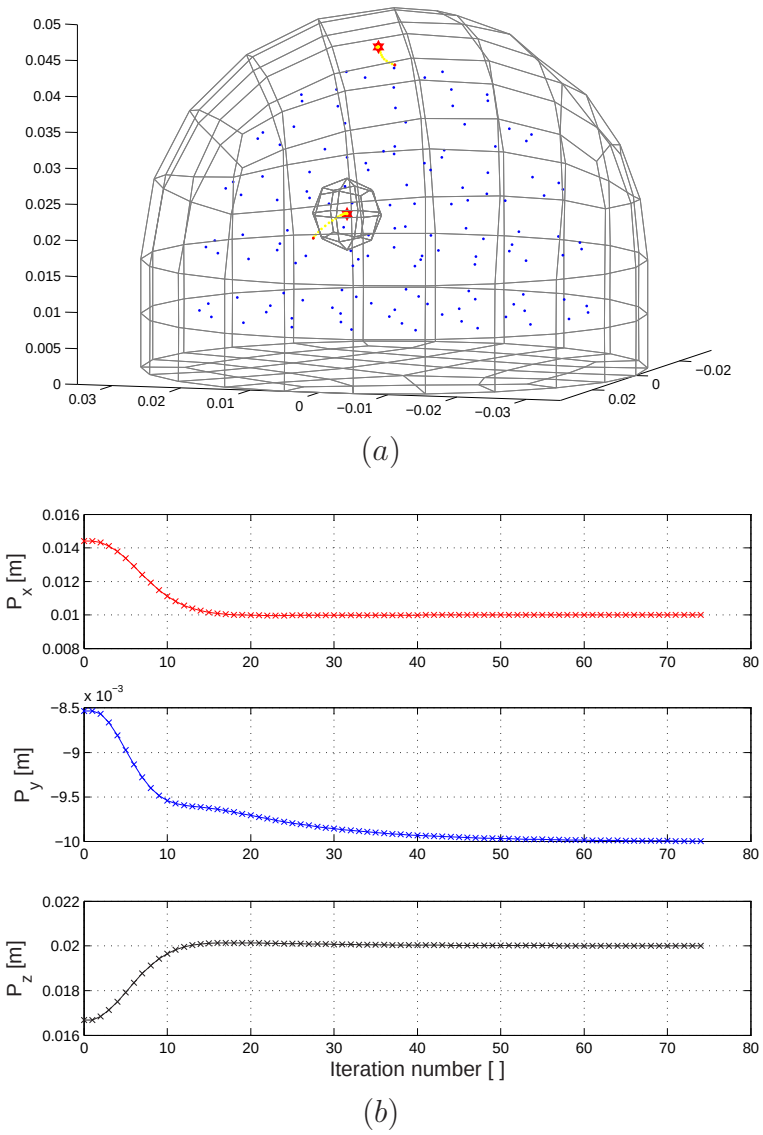

Figure 6.14 Sample reconstruction behavior for the location of an inclusion of size $R = 5\ mm$ in a 3D semi-ellipsoidal domain. (a) shows simulation points from Grid-Search plotted as blue dots and the subsequent Gauss-Newton path plotted in yellow dots converging towards their closest local solution, first of which is the correct inclusion location. (b) illustrates the general convergence behavior in each coordinate.

6.2.2.2 Discussion

In general, no significant, qualitative differences were found in the accuracy of the converged solutions between two- or three-dimensional geometries. However, compared to 2D cases, 3D reconstructions generally require more than double the number of iterations to converge. It also appears that the objective function in the three-dimensional case contains a larger number of local minima, which requires a reasonably fine Grid-Search.

As a summarizing result, it can be stated that the correct identification of inclusion locations is possible in any case at this low damping ratio. However, successful reconstruction depends on the resolution of the Grid-Search and therefore the quality of the start values that result from the Grid-Search. In particular, the search for small inclusions requires a reasonably fine resolution to subsequently yield the global solution. Particularly, in 3D geometries, this search does not represent an insubstantial computational effort.

6.2.3 Reconstructions for Inclusion Size

Similar to the reconstruction for single material parameters in Chapter 5, some reconstructions were performed for the inclusion size, R, of a circular/spherical inclusion using the test geometries. These reconstruction cases serve as a form of verification of this implementation and are thus illustrated only briefly.

Four inclusion cases of size $R^\star = 5\ mm$ are illustrated here for each of the 2D and 3D test geometries. For material parameters, $E^I = 20\ kPa$, $\nu = 0.49$, $\rho = 1000\ kg/m^3$, $\zeta = 10\%$ and $E^{II} = 150\ kPa$ were used to generate reference displacements using a longitudinal actuation in the vertical direction at 1 mm amplitude. As start values, $R^0 = 3\ mm$ and $R^0 = 8\ mm$ were used for reconstructions for the size, while all remaining parameters including the location were known exactly.

Figure 6.15 illustrates these reconstructions starting with $R^0 = 3\ mm$ as simple convergence plots. It can be stated that all reconstructions in R converge accurately to their correct solution with small iteration numbers. Unlike the location case, there is no convergence speed advantage observed in the 2D geometries compared to the 3D cases. Hence, while the results are not shown, it can be concluded that inclusion size by itself is a robustly identified parameter with this approach.

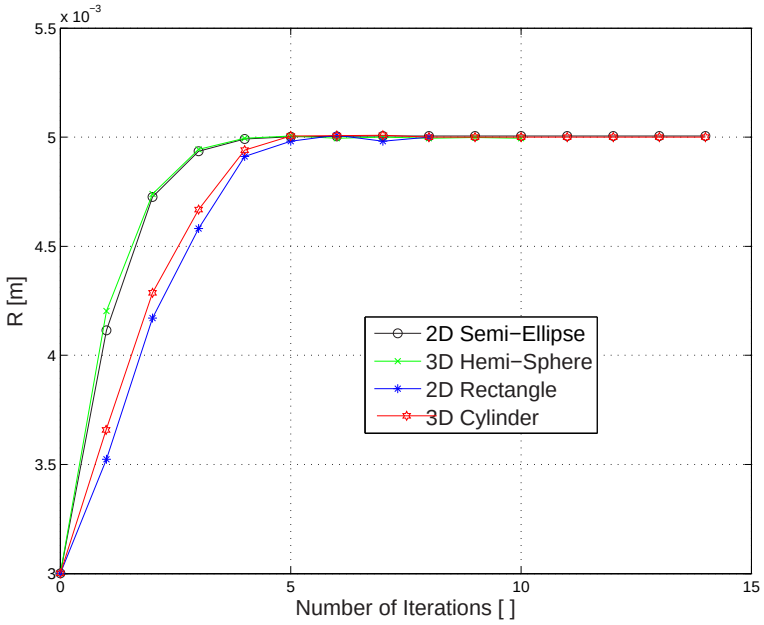

Figure 6.15 Reconstruction of inclusion size of a $R = 5\ mm$ inclusion within the 2D and 3D test geometries.

6.2.4 Simultaneous Reconstruction of P, R and E^{II}

The reconstruction of the inclusion size, its location and stiffness value is of critical importance for the DIET screening system. All of these parameters are true variables that are not known prior to screening. Unless clear suspicion exists from pre-assessment, they cannot be estimated. The study presented in this section provides not only a general knowledge about the reconstruction behavior and capabilities of the inversion algorithm, but also information about the problem sensitivity with respect to start values in the inclusion parameters, R and E^{II}.

A number of problems were simulated that simultaneously reconstruct P, R and E^{II}. For this problem, the program from Table 6.5 was used to perform a coarse Grid-Search only for the inclusion location at fixed initial guesses for R and E^{II} chosen at plausible values over the entire physiological range. Three start values determined from the resulting errormap were used subsequently for simultaneous Gauss-Newton reconstruction in all three inclusion parameters. The best converged solution with the smallest resulting displacement error resulting from one of the three Gauss-Newton reconstructions was interpreted as the algorithm result.

Due to the computational speed advantages, this study was performed with the two-dimensional test geometries. However, this choice should be understood

to be no limitation to the generality of results. This assumption should hold as in all prior analysis there have been no substantial differences in the reconstruction behavior between 2D and 3D geometries.

The first test geometry used was the 2D rectangle with a $R = 5\ mm$ inclusion, shown previously in Figure 6.11 (a). Additionally, the 2D semi-elliptical geometry, as shown in Figure 6.16, has been investigated with (a) a circular inclusion of $R = 3\ mm$ located at $P = (0.01, 0.03)^T\ m$ and (b) an elliptical inclusion at the same location and with semi-axis parameters, $a = 6\ mm$ and $b = 4\ mm$, and rotated 30° in space. The surface area of the ellipse thus corresponds to the same area occupied by a circle with a radius $R \approx 4.9\ mm$.

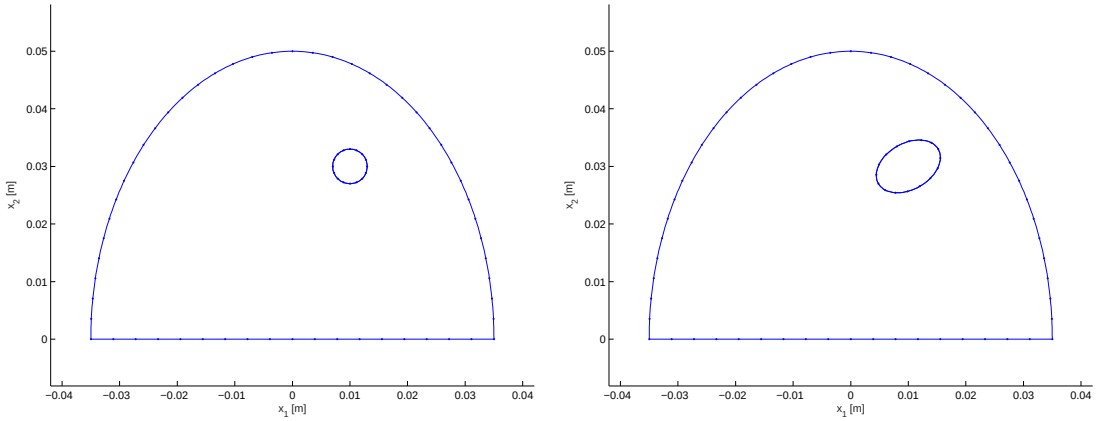

Figure 6.16 Solution geometries used for simultaneous reconstruction of P, R and E^{II}.

As the last test geometry for this type of reconstruction, the semi-elliptical geometry was used without the presence of an inclusion to simulate a healthy breast. However, the same reconstructions for the identification of a *potential* inclusion were performed. This test is thus used to asses the algorithms clinically important ability to differentiate between healthy and cancerous cases.

In forward simulations for the generation of reference displacements, $\mathbf{u}^\star$, the background material parameters in Table 6.6 have been used:

$\rho^\star$	=	$1000\ kg/m^3$
$E^{I\star}$	=	$20\ kPa$
$\nu^\star$	=	0.49
$\alpha^\star$	=	$31\ rad/s$
$\beta^\star$	=	$0.0003\ s/rad$

Table 6.6 Background material parameters used in the reconstruction studies for inclusion parameters P, R and E^{II}.

For the inclusion stiffness in the 2D rectangular geometry, $E^{II\star} = 200\ kPa$ was used, where all other 2D semi-ellipse cases used $E^{II\star} = 150\ kPa$.

6.2.4.1 Results

The results of these studies are reasonably detailed in each parameter, and include:

- The number of the start value, i_{min}, that converged to the best solution with the smallest displacement error,
- The initial displacement error, Ψ_0 (in m^2), evaluated at this particular start value,
- The resulting displacement error, $\tilde{\Psi}$ (in m^2), at the converged solution,
- The inclusion location in coordinates of its center, $\tilde{P}_x$, $\tilde{P}_y$ (in mm),
- The resulting radial inclusion size, $\tilde{R}$ (in mm),
- The converged inclusion stiffness, $\tilde{E}^{II}$ (in kPa),

While the detailed reconstruction results are given in Appendix A in tabularized form, results are summarized here: Table 6.7 (a) illustrates the results for the rectangular geometry and Tables (b) and (c) contain the results for the semi-elliptical geometry with a circular and an elliptical inclusion, respectively. Finally, Table 6.7 (d) shows the results for the healthy case.

To summarize the reconstruction outcomes, a classification scheme was defined according to the following conditions:

- **Exact:** Reconstruction results were classified as *exact* if all parameters converged to the correct solution with only negligible deviation. This class can be interpreted as the true and global solution to the computational problem and is denoted in Table 6.7 with a green tick (√).
- **Clinical 1:** The second category represents the most cases and shows deviation in some parameters. While this deviation is computationally relevant, this class contains only solutions that still indicate the clinically correct interpretation. Particularly, this means that the presence of a cancerous, stiff inclusion is recognized with a significantly increased stiffness value in

comparison to healthy tissue values in the close vicinity of the correct location and approximately the correct size. In the healthy case, this outcome can be formulated as the identification of inclusion parameters that either vanish in size or have similar stiffness values as healthy tissue. The results can thus be formulated in terms of maximally tolerated deviations from the inclusion parameters:

$$\begin{aligned} ||R^\star - \tilde{R}|| &\leq 3\ mm \\ ||P^\star - \tilde{P}|| &\leq 5\ mm \\ \frac{||E^{II\star} - \tilde{E}^{II}||}{||E^{II\star}||} &\leq 50\% \end{aligned}$$

This class is denoted with a blue tick ($\surd$).

- **Clinical 2:** Category three is essentially the same as the second category and still points towards the correct clinical diagnosis. However, this class covers cases where the inclusion stiffness value has increased beyond reasonable values, but inclusion sizes and locations are still identified correctly. This class thus does not represent a reconstruction failure in the clinical sense and is denoted with a blue ring ($\bigcirc$).

- **Failure:** The last class represents failure not only in the computational sense, but also in the clinical problem. In particular, this is the case, when a stiff inclusion is not identified with increased stiffness values and reasonable size, or when results from a healthy breast indicate a cancerous inclusion with increased stiffness values. These false result in both cases are denoted with a red crossed circle, $\otimes$.

6.2.4.2 Discussion

The illustration of reconstruction results in Table 6.7 is fairly self explanatory. In general, it can be stated that almost all inclusion cases have been successfully identified in a clinical sense and there have been only few reconstruction failures. However, since the details are listed only in the Appendix, some key findings need to be emphasized here.

The accuracy of inclusion reconstructions was in general very good, particularly in the geometric parameters. Both parameters, P and R, have converged to very small reconstruction errors, even in cases where the inclusion stiffness has

E_0^{II} $[kPa]$	Inclusion size R_0 $[mm]$ 3	5	7	10
50	✓	✓	✓	✓
100	○	✓	✓	✓
150	○	✓	✓	✓
200	○	✓	✓	✓
250	○	✓	✓	⊗

(a)

E_0^{II} $[kPa]$	Inclusion size R_0 $[mm]$ 2	4	6	8
50	✓	✓	✓	⊗
100	○	✓	⊗	⊗
150	○	✓	⊗	⊗
200	○	✓	⊗	⊗
250	○	✓	○	⊗

(b)

E_0^{II} $[kPa]$	Inclusion size R_0 $[mm]$ 2	4	6	8
50	✓	✓	○	○
100	○	✓	○	○
150	✓	✓	✓	⊗
200	○	○	✓	⊗
250	✓	○	✓	⊗

(c)

E_0^{II} $[kPa]$	Inclusion size R_0 $[mm]$ 2	4	6	8
50	✓	✓	✓	✓
100	✓	✓	✓	✓
150	✓	✓	✓	✓
200	✓	✓	✓	✓
250	✓	✓	✓	✓

(d)

Table 6.7 Reconstruction results for inclusion parameters P, R and E^{II} of a potential inclusion: (a) a circular ($R = 5\ mm$) in a 2D rectangular geometry, (b) a circular ($R = 3\ mm$) and (c) an elliptical inclusion ($a = 6\ mm,\ b = 4\ mm$) in a 2D semi-elliptical geometry and (d) no inclusion (healthy case) in a 2D semi-elliptical geometry. Green and blue ticks refer to the successful reconstructions, blue circles refer to successful results in a clinical sense and red crossed circles indicate reconstruction failure.

converged to values far from its true value. Reconstruction errors for P are at a maximum of the order 0.1 mm and for R at a maximum of 0.5 mm, which are clinically insignificant.

The inclusion stiffness is reconstructed accurately for only in the few cases rated as the computational (*Exact*) reconstruction solutions. The *Clinical 1* cases that make the majority of all simulated problems show relative errors of up to 50% in inclusion stiffness and some cases, rated *Clinical 2*, show reconstructed stiffness values of over 10–20 times the reference value. However, in all such cases that are not rated as reconstruction failures, the stiffness value was always

increased, correctly indicating a cancerous case. Therefore, these solutions, while not computationally exact, are clinically of use.

Few reconstruction failures occurred. Most of them are in the difficult $R = 3\ mm$ inclusion case. These cases fail generally in all parameters, size, location and stiffness. However, such cases are easily identified as failures due to an increased remaining displacement error (order between $O(10^{-6})$ and $O(10^{-9})$) in comparison to successful cases (converged errors of order $O(10^{-11})$).

All failure cases have some features in common. Some specific start values, particularly for the inclusion size, R_0, have been chosen much too large in comparison to the true solution value, $R^\star$. In these cases, the reconstruction behavior tends to prioritize a descent of inclusion stiffness before approaching the correct size. This decline in stiffness value, in turn, compensates the influence from the too large assumed inclusion on the overall displacement error. Convergence thus occurs towards a too large inclusion with decreased stiffness, instead of the stiffer and smaller inclusion intended.

Similarly, reconstruction cases with too small inclusion sizes for start values have shown competition between R and E^{II} in convergence behavior. Stiffness values have adjusted to much higher values, often 10–20 times higher than the true stiffness solution, compensating for a too small inclusion size. This particular behavior can be confirmed by the errormap in R and E^{II} shown in Figure 6.17 for a 2D rectangle with a $R^\star = 5\ mm$ and $E^{II\star} = 150\ kPa$ inclusion.

This errormap explains the competing characteristics between these parameters. The highlighted section in the dark minimal error area shows displacement error values of the order $1 \cdot 10^{-10}$, which causes the current Gauss-Newton algorithm to stop iterating at a point in this area when there is no significant improvement in error value to achieve. This behavior occurs particularly when only approximate Jacobian matrices are obtained, as done in this work using simple finite difference techniques. A method for more accurate Jacobian matrices would improve this convergence behavior.

At the same time, as better start values in R have obviously lead to successful reconstructions, it can also be observed that initial displacement errors, Ψ_0, from Grid-Search with inclusion sizes closer to the correct value have been approximately one order less than those cases leading to failure. Hence, these failures could also be overcome by expanding the Grid-Search to two or more inclusion sizes. This approach would result in more initial computational effort, but would lead to better quality start values that would likely be able to better guarantee

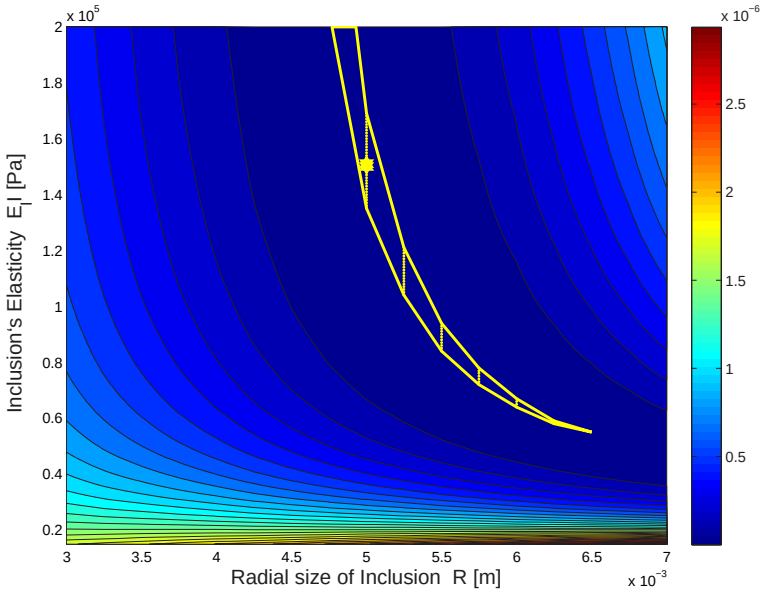

Figure 6.17 Displacement errormap (values in m^2) for the inclusion size, R, and inclusion stiffness, E^{II}, with reference to $R^\star = 5\ mm$ and $E^{II\star} = 150\ kPa$. The yellow highlighted zone refers to error values under $1 \cdot 10^{-10}\ m^2$.

correct reconstruction solutions, as long as background material parameters are known exactly.

Reconstructions for a circular inclusion, where the solution inclusion shape was actually elliptic, are difficult to rate. However, there are only few cases that can be rated failures. In addition, these cases should be easily circumvented by including R into the Grid-Search. Interestingly, similar characteristics as observed in the circular cases have been found with good convergence in the location. The inclusion size appears to be identified as a value not far from that of a radial inclusion size, whose circular surface area corresponds to the area covered by the elliptical inclusion shape. It should be noted that both the initial and converged objective function value have increased approximately one to two orders in magnitude for this case in comparison to the strictly circular case.

The reconstructions for inclusions in the healthy case have been very successful. Despite the algorithm converging to an existing inclusion of some more or less arbitrary size in all cases, they are rated as computationally sound with exact results. This good result is due to the inclusion stiffness having converged to the same stiffness value of the background material without exception.

This case resembles the healthy case as a homogeneous domain and has thus converged to displacement errors of the order $O(10^{-11})$ or even below. In contrast

to high stiffness inclusion cases, it is notable in most of these healthy cases that the second or even third start value found by the Grid-Search algorithm has lead to the most accurate solution with minimal displacement error. Interestingly, the first start value rarely lead to the minimal solution.

6.3 Summary

The effective identification of inclusion parameters within a domain with well known material parameters requires a more sophisticated reconstruction technique. In particular, hurdles placed by the nonlinear characteristics in the surface displacement error based objective function, especially those due to the inclusion location, are overcome using a combined algorithm approach. This approach uses first a Grid-Search for the inclusion location to find likely positions for a potential inclusion. These positions are subsequently used as start values in an accurate Gauss-Newton reconstruction.

Using this hybrid approach, investigations made here for the reconstruction of each geometric inclusion parameter, P and R, by itself were successful in all 2D and 3D cases simulated. While the inclusion stiffness, E^{II}, reconstruction accuracy has been shown to decline for increased damping ratios and for small inclusions (see Section 6.1), similar effects are expected here, although detailed investigations are still to be carried out for the parameters P and R to confirm this behavior.

The clinically most interesting case of simultaneous reconstruction of all three inclusion parameters, P, R and E^{II}, has been investigated using 2D geometries. These reconstructions show results that are very promising with respect to clinical application and can be summarized as follows:

- Healthy cases, that is cases where surface displacements from homogeneous domains have been used as reference displacements to reconstruct a potential inclusion, have, without exception, found convergence to occur to a small sized inclusion with the same elastic material parameters as the surrounding tissue and with high solution accuracy. These outcomes are computationally equivalent to the healthy, homogeneous case and can be rated highly successful. This outstanding result indicates that a surface based inclusion identification in a DIET system could potentially be realized with a particularly high specificity (minimal false negatives).

- Inclusion cases with high stiffness have, in summary, not always been identified with high numerical accuracy. However, most of such cases have been found to at least indicate the correct clinical result, showing an inclusion identified in the correct location and with a significantly increased stiffness value when compared to healthy tissue stiffness values.

- Failures to identify cancerous inclusion cases have been found to occur only for highly overestimated start values in the inclusion size. From the same results it is clear that these failures can easily be eliminated by including the inclusion size into the Grid-search algorithm, to supply a globally better start value.

- Improvements to the convergence behavior to more accurate solutions particularly in the inclusion parameters, R and E^{II}, may be achieved by determining the Jacobian matrix with more accurate analytically orientated methods, rather than using computationally simple, but inaccurate, finite difference methods.

- An investigation with respect to the accuracy in the reconstruction of the inclusion stiffness parameter alone has shown difficulties to occur for very small inclusions and for increased damping ratios. In such cases, areas develop within the domain in a mode-shape like manner, where reconstructions first become inaccurate and then fail with respect to a defined error margin. These areas grow together with decreasing inclusion size and with increasing damping ratio.

Chapter 7

Combined Background and Inclusion Identification

Breast tissue has been found to be variable not only in the long term with increasing age, but also on a monthly basis due to varying hormone levels associated with the menstrual cycle. [4, 154]. It has also been recognized in Section 3.2 that such background material parameters have an effect on the accuracy of inclusion parameter reconstructions. Hence, the knowledge of these background material parameters is an important requirement that should be considered before commencing a computationally expensive inclusion parameter search. Additionally, in any initial clinical trials it will be particularly difficult to estimate background parameters, since the existence of any additional nonlinear dependencies are entirely unknown at this point. Thus, this chapter closes the loop between reconstruction problems for homogeneous domains and domains with an embedded inclusion, particularly when the scenario includes no knowledge of both background material parameters and the potential presence of an inclusion prior to model identification.

7.1 Fully Combined Three Step Reconstruction Algorithm

In general, in a real breast cancer screening situation there is no specific knowledge about the presence of a stiff, cancerous inclusion within the breast. In a healthy case, the reconstruction for the homogeneous domain material parameters may therefore be sufficient if the model reflects the physics accurately and reconstruction leads to extremely small displacement error values. The presence of an inclusion within the breast can thus be understood as some disturbance to

the homogeneous system.

The amount of this disturbance will most significantly depend on the size of the inclusion in relation to the rest of the domain. In an undiagnosed cancer case, the size of an inclusion will likely be at or beneath a palpable size, and can thus be assumed to be relatively small. Therefore, it is a practical approach to neglect a potentially present inclusion in the initial situation, and reconstruct or estimate the surrounding background material parameters in the first step of an algorithm.

If an inclusion exists, the background material parameters resulting from this approach will be inaccurate to some degree. There will also be some level of displacement error remaining. However, the material parameter values obtained may be sufficiently accurate to achieve a smaller resulting displacement error from the additional subsequent introduction of an inclusion in the right location, with the right size and stiffness. Hence, it may provide a prime starting point to identify a better reflection of the true physical system in this case.

The algorithm proposed here to implement this approach is outlined in Table 7.1 and consists of three main steps. The first step reconstructs the background material parameters assuming a homogeneous domain and using a Gauss-Newton algorithm with plausible material parameters for breast tissue as the starting values. The results of this step are a parameter set (a) including E^I, ν, α and β. At this point, it is assumed that the material parameter values of ν, α and β maintain the same values for both background and inclusion material. This equality is also the case for the density, ρ, which is assumed to be known prior to reconstruction. The second step conducts a Grid-Search for the inclusion location, P, and circular/spherical size, R, followed by the extraction of a number of N_{min} minima from the resulting coarse errormap. These minima are used together with the solutions from Step (1) as start values in a Gauss-Newton algorithm in the third step. The third step thus involves the precise determination of a set, (b), of inclusion parameters P, R and E^{II} similar to the study in Chapter 6. The result with the lowest displacement error of these last Gauss-Newton reconstructions is thus interpreted as the solution of the problem.

Note that this algorithm could easily be extended to the more precise identification of both background and inclusion parameters by allowing a modification of step three, where all material parameters are allowed to vary simultaneously using a gradient descent based method. This approach could, for example, include a variation of damping parameters and Poisson ratio between different regions.

(1)
- Load mesh (with inclusion) and boundary conditions from input files, load all input parameters as well as start relevant values ($\boldsymbol{\theta}_0$, Ω, ...)
- Reduce mesh to single region mesh
- Perform Gauss-Newton for background parameters E^I, ν, α and β (a) and save for use in subsequent reconstructions
- Expand mesh to multi region mesh to incorporate inclusion

(2)
- Setup a feasible parameter-grid in inclusion size, R, and spatial location, P, according to the geometry type and at a feasible resolution with respect to the expected number of local minima.
- Perform Grid-Search based on background parameters obtained in step (1):
  - Obtain errormap for the given grid
  - Extract N_{min} local minima from the resulting errormap and save them as start values $\boldsymbol{\theta}^0$

(3)
- *FOR ALL* start values, $\boldsymbol{\theta}^0$, *DO*:
  - Perform Gauss-Newton reconstruction algorithm for inclusion parameters P, R, and E^{II} (b)

  END DO
- Compare error value, Ψ, from all (max. N_{min}) converged Gauss-Newton reconstructions and write to file

Table 7.1 Illustration of the three step program procedure for the combined reconstruction of (a) the background material parameters (E^I, ν, α, β) and (b) the inclusion parameters (P, R, and E^{II}) from a combined Gauss-Newton–Grid-Search–Gauss-Newton algorithm.

However, while the resulting algorithm needs to achieve clinically relevant results, it will also have to keep computational costs within affordable limits. Thus, the investigations shown here are restricted to the inclusion variables, P, R, and E^{II}, as described in the program layout.

7.2 Simulation Case Study

To demonstrate the reconstruction algorithm's capabilities, a small case study was conducted for a 2D and a 3D geometry case. This study investigated the reconstruction accuracy and reliability with respect to stiff inclusions at several sizes. For this purpose, the 2D semi-elliptical and the 3D semi-ellipsoidal geometry were meshed with an embedded inclusion, whose size was varied between

$R = 0, \ldots, 10\ mm$ in steps of 1 mm. Each of these cases were forward simulated using the material parameters from Table 7.2 to generate surface reference displacements, $\mathbf{u}^\star$. The case $R = 0\ mm$ represents the healthy case and was forward simulated as a homogeneous domain.

	Simulated Forward Solution Parameters $\boldsymbol{\theta}^\star$	
	2D Semi-Ellipse	3D Semi-Ellipsoid
E^I	$27.5\ kPa$	$27.5\ kPa$
ν	0.49	0.49
ρ	$950\ kg/m^3$	$950\ kg/m^3$
α	$31.4\ rad/s$	$62.8\ rad/s$
β	$0.0003\ s/rad$ $\Big\} \zeta = 10\%$	$0.00016\ s/rad$ $\Big\} \zeta = 10\%$
E^{II}	$250\ kPa$	$250\ kPa$
Act.	longitudinal at $f = 50\ Hz$	longitudinal at $f = 100\ Hz$

Table 7.2 Solution parameters used for the generation of reference displacements, $\mathbf{u}^\star$, for the identification of background and inclusion parameters in a three-step reconstruction algorithm.

These reference displacements were subsequently used to reconstruct the complete domain parameters using the three step reconstruction program from Table 7.1. The start values used for these reconstruction simulations are given in Table 7.3 in terms relevant to the individual algorithm steps. In step (2) this means, in particular, the setup of the spatial grid for inclusion locations, P, in terms of a certain resolution and the grid in the inclusion size, R. Note that the Grid-Search is at this point of the algorithm based on the solutions found for the background material parameter reconstructions in step (1). Similarly, in step (3), the initial values for the reconstruction of P, R and E^{II} are automatically selected from steps (1) and (2).

The reconstruction results of this study are presented in summarized form in the following subsections, (a) with an analysis for the reconstruction of background material parameters in step (1) and (b) for the inclusion specifications resulting from step (2)–(3). The specific results are presented in tabularized form in Appendix B, where the initial and final objective function values are also listed.

7.2.1 Background Estimation Results

Figure 7.1 shows the results obtained for simultaneous reconstruction of E, ν and ζ, together with a relative error defined for each background parameter analogue to Equation 6.1.2.

Alg.-Step		Start Values $\boldsymbol{\theta}_0$	
		2D Semi-Ellipse	3D Semi-Ellipsoid
(1)	E_0^I	25 kPa	25 kPa
	ν_0	0.5	0.5
	α_0	16.2 rad/s } $\zeta = 5\%$	31.4 rad/s } $\zeta = 5\%$
	β_0	0.00016 s/rad }	0.00012 s/rad }
(2)	E_0^{II}	100 kPa	100 kPa
	Res.(P)	10 mm	10 mm
	R_0	[3, 5, 7] mm	[2, 4, 6, 8] mm
(3)		Start values automatically assigned as local minima out of errormap from step (2) with background solution from step (1)	

Table 7.3 Start values, $\boldsymbol{\theta}_0$, used in the individual algorithm steps for the identification of background and inclusion parameters by a combined three-step reconstruction algorithm.

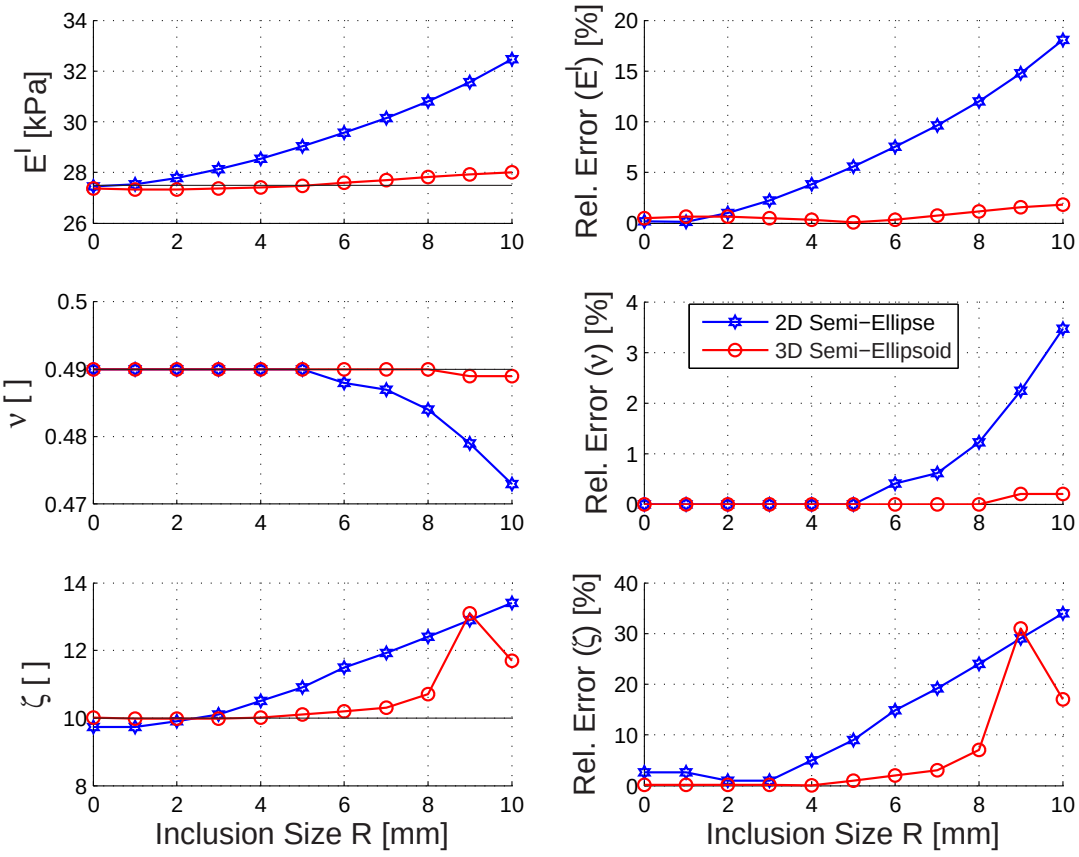

Figure 7.1 Background material parameter estimation for E, ν and ζ, while neglecting the presence of an inclusion of size $R = 0, \ldots, 10$ mm. Reconstruction results are given with the according relative errors from comparison to the reference parameter values.

Reconstructions for an overall Poisson's ratio, ν, consistently achieve very accurate results in the 3D case, where a maximum relative error of less than 1% is observed for the largest inclusion case. In the 2D case, this estimation becomes less accurate when inclusions reach sizes of $R = 5\ mm$ and larger and the Poisson ratio result is then systematically below the reference value. However, the maximum relative error amounts only 3.5% given a large inclusion of $R = 10mm$.

Estimations for Young's modulus, E^I, show similar behavior. While reconstructions in the 3D case achieve results close the the reference value, showing a relative error of approximately 2% for the large inclusion case, the 2D reconstructions experience a significantly larger divergence. This divergence from the correct result consistently grows with inclusion size in an exponential manner and causes a relative error of 18% for an inclusion of $R = 10\ mm$.

The largest relative discrepancy between reference value and reconstruction result is observed in the estimation for the damping ratio, ζ. While the 3D cases still lead to reasonable approximations in ζ with $\epsilon_{rel} < 5\%$ up to inclusion sizes of $R = 7\ mm$, error values increase significantly for larger inclusions. The 2D reconstruction cases can again be seen to diverge from the reference value starting at sizes of $R = 4\ mm$ and leading up to a relative error of approximately 34% for the largest inclusion case.

7.2.2 Inclusion Identification Results

This section shows results for the reconstruction of inclusion parameters in the case of inaccurately determined background material parameters. In general, similar behavior is observed, as seen previously in Section 6.2.4. It thus makes sense to reflect reconstruction results in a qualitative way, rather than illustrating accurate reflections of the reconstructed values. Therefore, these results are summarized, using an interpretation from a clinical point of view.

Table 7.4 illustrates the reconstruction success according to the classification also used in Section 6.2.4, in summary:

- **Exact:** A green tick ($\checkmark$) denotes the globally correct and computationally accurate solution with negligible variation in some parameters.

- **Clinical 1:** Denoted with a blue tick ($\checkmark$) are reconstruction results with

slight deviations tolerated within the limits

$$\begin{aligned} ||R^\star - \tilde{R}|| &\leq 3\ mm \\ ||P^\star - \tilde{P}|| &\leq 5\ mm \\ \frac{||E^{II\star} - \tilde{E}^{II}||}{||E^{II\star}||} &\leq 50\%. \end{aligned}$$

- **Clinical 2:** A blue ring (◯) covers cases with significant error (larger than tolerated in the previous category) in at least one reconstruction parameter, but with a correct clinical interpretation or diagnosis.
- **Failure:** Reconstruction failures are denoted with a red crossed circle, ⊗, meaning both significant error in reconstruction parameters as well as a misleading diagnostic value.

Note also that the reconstruction results in Table 7.4 display the best solution obtained from either algorithm step (1) with background material reconstruction only or from algorithm step (3) with combined background material and inclusion identification. The *better* solution is thereby determined by choosing the solution with a smaller reconstruction error ($\Psi^{(1)}$ or $\Psi^{(3)}$) remaining when iterations were stopped at each algorithm step. This approach thus helps to discriminate healthy ($R = 0\ mm$) cases from cancerous cases.

	Radial inclusion size, $R[mm]$										
	0	1	2	3	4	5	6	7	8	9	10
$2D$	√	⊗	√	√	√	◯	◯	◯	◯	◯	◯
$3D$	√	⊗	√	◯	√	√	◯	◯	◯	◯	◯

Table 7.4 Clinical interpretation of results obtained for inclusion parameter identification in the case of inaccurately estimated background material parameter values.

Table 7.4 clearly shows a large success rate in such reconstruction cases for inclusions that were performed with inaccurate background material parameter values. While computationally acceptable reconstruction results were achieved only for inclusions with sizes approximately between $R = 2\ mm$ and $R = 5\ mm$, it can be noted that any case with inclusions $R \geq 2\ mm$ have lead to a clinically correct interpretation.

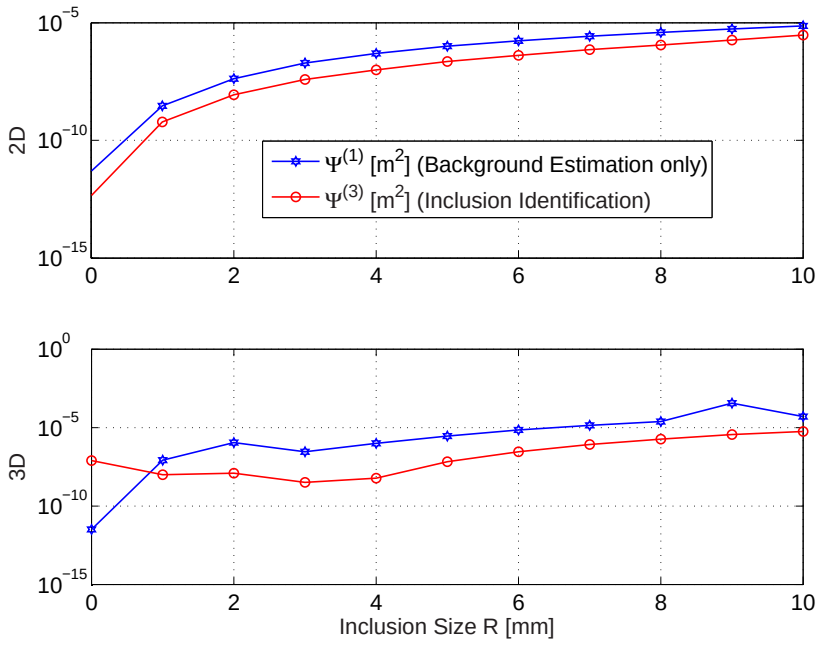

Figure 7.2 Remaining displacement error values (blue, $\Psi^{(1)}$) after reconstruction for background material only and (red, $\Psi^{(3)}$) after reconstruction for an inclusion.

In both the 2D and 3D case the small inclusion of $R = 1\ mm$ fails to be reconstructed. Importantly, the reconstruction for the $R = 0\ mm$ healthy case has lead to a computationally accurate result, leading also to the correct clinical interpretation. While the displacement error, $\Psi^{(3)}$, of the 2D reconstruction has in this case assumed its minimal value after introducing an inclusion of the same material parameters as the background material, the 3D case achieved the best solution with minimal error only after the reconstruction for background material. The introduction of a small inclusion has, in this case, not resulted in a modulus value that was approaching the background material value accurately enough and has thus resulted in a converged, but increased, objective function value.

The converged values for the displacement error residual are shown in Figure 7.2 for the 2D and 3D cases. The blue line shows the values $\Psi^{(1)}$ after iterations were terminated for the reconstruction of background material parameters only. The red line shows the converged error residual, $\Psi^{(3)}$, related to the reconstruction solutions, where an inclusion case was considered.

In general, the converged error residual shows increased values for larger inclusion cases. With only one exception, the residuals, $\Psi^{(3)}$, have lead to a better solution when compared to reconstruction cases for background material parameters only. This exception is the 3D case where no inclusion was present. While in

the equivalent 2D case, the elastic modulus of the inclusion has approached the value of the background modulus, this is not the case in 3D, where an increased elasticity value of the fictitious inclusion remains in the converged solution, which has lead to the increased error value.

7.2.3 Discussion

This approach combining background material estimation and inclusion identification shows promising results for a potential application in a general, clinically blind surface motion based breast screening system. From a clinical point of view, all inclusion cases with sizes $R \geq 2\ mm$ were successfully identified in all geometric parameters position and size of a circular/spherical inclusion as well as in a significantly increased stiffness value. These minimum values are below the $R = 5\ mm$ average detection size.

It was found that in the reconstruction for larger inclusion cases the estimation for background material parameter becomes less accurate. This result is due to the increasing influence of the growing inclusion size on the surface motion pattern. However, since this influence is globally increased, the accuracy of the background material parameters appears to become less important, as reasonable reconstruction results are still obtained for inclusion parameters.

There remains a possibility that very large inclusion sizes may become more difficult to recognize with these methods compared to smaller cases due to the growing global influence on motion behavior. However, such cases could probably be excluded as irrelevant for an application in the proposed DIET breast cancer screening method. In particular, these larger sizes would become easier to detect by manual palpation methods and, above $R = 8 - 10\ mm$, obviate the early detection goal in developing the system.

In contrast, small inclusions show little motion changes on the geometry's surface. In such cases, background material parameters can be determined more accurately. This increased accuracy in turn leads to an improved inclusion identification process, with less error in both Grid-Search and subsequent Gauss-Newton technique. Hence, even small inclusions down to sizes $R \geq 2\ mm$ could successfully be identified in elastic modulus, size and location.

Importantly, the healthy case can be understood to be successfully identifiable. This case could be determined directly from the algorithm's first step for background parameter estimation. If this estimation can be achieved resulting

with very small error residuals, $\Psi^{(1)}$, the presence of, at the least, a larger inclusion can be excluded. A further strong argument to distinguish successfully between healthy and inclusion cases is the subsequently performed search for a computationally introduced small inclusion, if no improvement in the resulting error value for $\Psi^{(3)}$ can be achieved.

A drawback is the sensitivity to which an inclusion stiffness can be reconstructed. The behavior identified in Chapter 6, where reconstructions tend to yield either smaller inclusion values with an overestimated elasticity value or larger inclusions with an underestimated elastic modulus compared to the reference value, can be confirmed here for the 3D case. However, this behavior does not appear to significantly affect the clinical interpretation of the reconstructed result given the large constrast in stiffness.

It should be noted, that material and inclusion reconstructions in this chapter have been performed assuming a damping ration of only 10%. This parameter was purposely chosen low to obtain general knowledge of the algorithm's reconstruction behavior, while not concealing these general effects by decreased reconstruction accuracies, as seen in Section 6.1.

7.3 Summary

In this chapter, a three step reconstruction approach was introduced for the solution of the elastographic inverse problem from surface motion. This algorithm combined a Gauss-Newton based estimation of background material parameters with a subsequent Grid-Search for a potential inclusion. This second step was followed by a more accurate Gauss-Newton reconstruction for the circular/spherical inclusion parameters.

The main findings highlighted the successful identification of an inclusion within a domain, where a vague material parameter estimate for the background material is the only knowledge existing prior to reconstruction. Furthermore, homogeneous material cases without an inclusion were successfully differentiated from inclusion cases. Stiff inclusions cases with radial sizes between 2 mm and 10 mm have been identified in both a 2D and a 3D geometry with great accuracy in the inclusion's size and location within the overall domain. Determination of specific inclusion stiffness values for use in a clinical interpretation was achieved with satisfactory accuracy.

The combination of background material and inclusion parameter identification has shown positive effects when reconstructing for inclusion cases of different size. While an approximate estimation for background material parameters appears to be sufficient for the identification of large inclusions, small inclusions could also be identified as better estimates of the background material parameters became available.

Chapter 8

Experimental Studies

Testing the developed algorithms on experimentally gathered silicon phantom surface motion data is a vital step towards the employment of a DIET breast screening system. Measured data can be corrupted with errors in actuation, noise in measurement, and camera resolution, as well as computational accuracy in the three-dimensional reconstruction of the motion data. In addition, surface motion data can be effected by incomplete or variable density of fiducial markers [120]. It is important to know the algorithms performance under the influence of all such errors and variations thereof. Furthermore, such studies can provide insight into the accuracy of how well the model reflects the actual behavior of the physical system.

8.1 Current Experimental System

The work by Peters and Brown *et al.* parallel to this thesis has lead to a functional image capture system, capable of delivering three-dimensional surface motion data of a longitudinally actuated object with an accuracy of order $O(10^{-4})$ m. While the process of image capture is described in principle in Section 1.4 of this thesis, details are provided by Peters and Brown [89, 120].

Figure 8.1 shows a photo of the present DIET image capture setup. In this picture, a transparent cylindrical silicon phantom with a colored spherical inclusion in its center is placed on top of an actuator capable of longitudinal harmonic actuation in the vertical (x_3) direction. Five cameras surrounding the phantom are employed to take pictures of the surface and deliver the data to the (not shown) imaging computer for three-dimensional surface motion data reconstruction. Note also the circular arrangements of LED lights around the cameras for illumination of the object at discrete points in time.

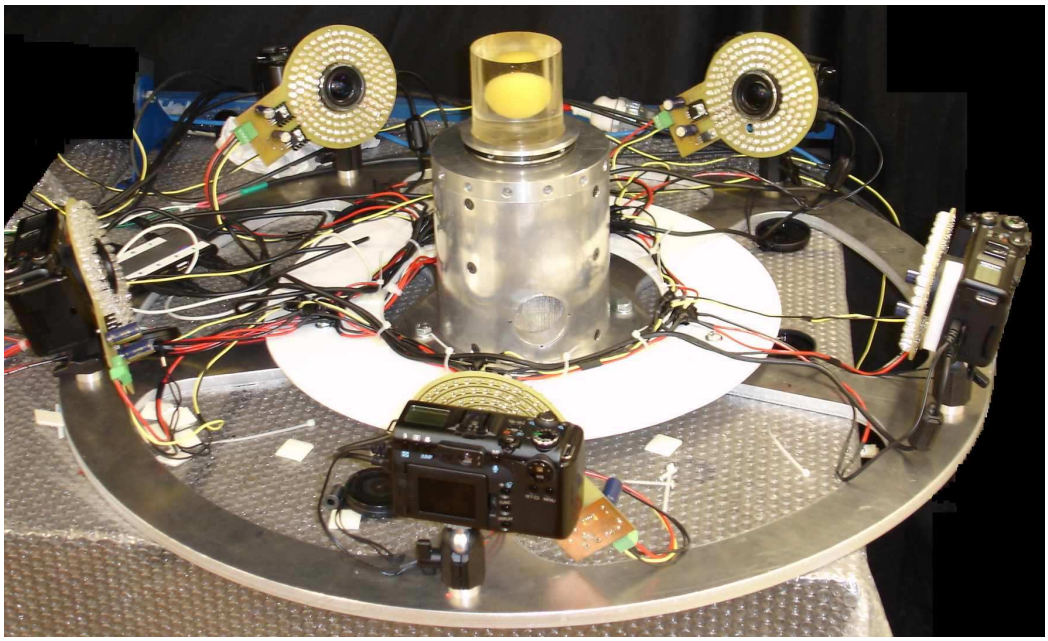

Figure 8.1 Current DIET image capture system setup using five cameras and a cylindrical silicon phantom with a centrally located inclusion.

Using the camera setup as illustrated in Figure 8.1, motion data sets could be taken of a breast phantom similar in shape to a semi-ellipsoidal geometry containing a stiff inclusion. Using a circular metal plate that was cast into the cross-sectional side of the phantom during production, this phantom could be mounted upside down mimicking a hanging breast. Prepared with markers on the surface for motion tracking, the phantom was placed in touch with the longitudinal actuator beneath, indenting the phantom slightly. This clinically focused experimental setup is illustrated in Figure 8.2, which is an image taken from one of the digital cameras taken at $t_0 = 0\ s$ during the image capture process.

8.1.1 Phantom Material

According to similar experimental research in the field, Peters [89] used a soft silicon gel as an appropriate material to cast breast phantoms. This material could easily be prepared by mixing a two-component silicon base according to certain ratios to achieve different resulting material stiffness. This initially liquid mixture was cast into plastic molds, where a vulcanizing process occurred at room temperature over a settling period of 6–12 hours, after which the material was stable and the phantom ready for experimentation.

Various phantoms were manufactured using two different material component

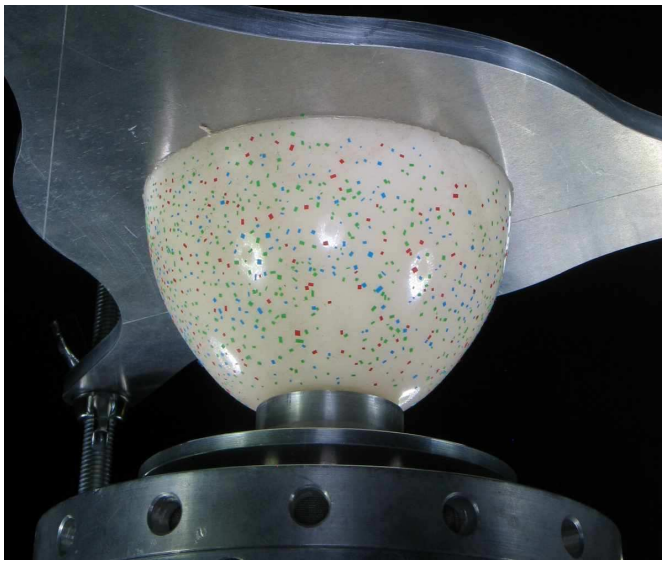

Figure 8.2 Silicon breast phantom during image capturing, as seen by one of the five digital cameras. The phantom is mounted over the vertical actuator with markers sticking to its surface for motion tracking purposes.

ratios to produce one *soft* and one *hard* mixture. Resulting samples were used to determine estimates of the material property values. Where values for the density were easily obtained by measuring a sample's weight and volume, values for Young's modulus were obtained using a series of static compression tests [89]. These tests revealed a linear elastic material behavior for statically applied strain rates between $\varepsilon = 0.025$ and $\varepsilon = 0.1$. Due to the manufacturer's specification, the Poisson's ratio was assumed to be near incompressibility. Importantly, no information was available with respect to the material damping behavior.

Table 8.1 provides an overview of the material data for each of the two silicon materials to the degree known or estimated. These values must be considered carefully and should be considered estimates, rather than precise reflections of the true parameters. In particular, there is no available knowledge with respect to the dynamic material behavior or other possible nonlinearities. More specifically, Peters [89] indicates that the silicone stiffness values may be overestimated by up to 10%.

8.2 Data – Mesh Correlation

A surface motion data set supplied by the current image capture system consists of N subsets of motion data. With respect to a global coordinate system, $\mathbf{x}$,

Parameter	*Soft* Silicone	*Hard* Silicone
E	32 kPa	135 kPa
ν	near incompressible	near incompressible
ρ	975 kg/m^3	1045 kg/m^3
ζ	unknown	unknown

Table 8.1 Estimated silicone material parameters used for the production of breast phantoms. The soft silicone is used for the breast tissue and the hard silicone for inclusions, yielding an approximately 4x contrast in stiffness.

each of these subsets describes a motion path, $\mathbf{z}_{\mathbf{q}}(t)$, observed by one of the N randomly distributed points, $\underline{\mathbf{q}}$, marked on the surface of the object in question. Each motion path is supplied in the form of discrete measurements of the global position, $\mathbf{z}^{\star}_{\mathbf{q}}(t_j)$, recorded at M discrete points in time, $t_j \in [0,\ \Delta t,\ \ldots,\ T-\Delta t]$, where $\Delta t = T/M$ and T is the oscillation period to the actuation frequency, f. Thus, the time $t_j = 0$ relates to the point $t = 0$ of a time-harmonic actuation of the form $\sin(\Omega t)$, where $\Omega = 2\pi f$.

To compare measured displacement data and displacements obtained from a BEM forward solution in using the surface displacement based objective function, Ψ, several steps are required to convert this data into a BEM compatible format. These steps are detailed in the following subsections. The outcome is then used in a BEM inverse problem analysis.

8.2.1 Path Conversion to Complex Displacements

The first requirement is to convert the measured data to a BEM compatible format. For this purpose, the nonlinear Gauss-Newton method was used in a simplified form without regularization techniques to obtain an analytical expression of the measured motion path. In particular, this task includes obtaining a real valued amplitude and phase angle for the oscillation of a surface point, $\underline{\mathbf{q}}$, in each coordinate direction. This expression was then converted to a complex number format to be directly comparable to motion data determined by forward solutions by the BEM.

In general, BEM displacement data, $\mathbf{u}$, are given as the complex valued amplitudes, $\hat{\mathbf{u}}$, of a harmonically oscillating surface node point in the form:

$$\mathbf{u} = \hat{\mathbf{u}} e^{-i\Omega t}, \tag{8.1}$$

where Ω is the rotational frequency and i is the imaginary unit. The true dis-

placement solution of this point is considered the real part of $\mathbf{u}$. Converting the complex amplitude to polar coordinates and using Euler's conversion for $e^{-i\Omega t}$, the real part of Equation 8.1 can be rewritten as a real valued time-harmonic oscillation:

$$\mathfrak{Re}\{\mathbf{u}\} = |\hat{\mathbf{u}}| \cos(\Omega t - \boldsymbol{\varphi}), \tag{8.2}$$

with the real valued amplitude, $|\hat{\mathbf{u}}|$, and a phase shift, $\boldsymbol{\varphi}$, given for each coordinate direction as:

$$|\hat{u}_j| = \sqrt{\mathfrak{Re}\{\hat{u}_j\}^2 + \mathfrak{Im}\{\hat{u}_j\}^2} \quad \text{and} \quad \tan\varphi_j = \frac{\mathfrak{Im}\{\hat{u}_j\}}{\mathfrak{Re}\{\hat{u}_j\}}. \tag{8.3}$$

In contrast, the measured data consist of the global coordinates, $\mathbf{z}^\star_{\mathbf{q}}(t_j)$, of a motion path recorded at M distinct points in time and does not contain the random surface points, $\underline{\mathbf{q}}^\star$, to which the path is related[1]. However, this measured path can be fitted to an analytic description assuming a damped time-harmonic oscillation of point $\underline{\mathbf{q}}^\star$:

$$\mathbf{z}_{\mathbf{q}}(t) = \underline{\mathbf{q}}^\star + |\underline{\hat{\boldsymbol{u}}}^\star| \cos(\Omega t - \underline{\boldsymbol{\varphi}}^\star), \tag{8.4}$$

where $|\underline{\hat{\boldsymbol{u}}}^\star|$ is the real valued amplitude and $\underline{\boldsymbol{\varphi}}^\star$ is the phase angle correlated to the measured data. This motion path is illustrated in Figure 8.3 (a).

For a given actuation frequency, f, the surface point's global position on the motion path at any of the measured times, t_j, can be expressed as:

$$\mathbf{z}_{\mathbf{q}}(t_j) = \underline{\mathbf{q}}^\star + |\underline{\hat{\boldsymbol{u}}}^\star| \cos(\Omega t_j - \underline{\boldsymbol{\varphi}}^\star), \quad j = 1, \ \ldots, \ M. \tag{8.5}$$

Using the measured data, $\mathbf{z}^\star_{\mathbf{q}}(t_j)$, and the analytic expression, $\mathbf{z}_{\mathbf{q}}(t_j)$, from Equation 8.5 an objective function based on the euclidian norm of their difference can be defined:

$$\Psi_M = \|\mathbf{z}^\star_{\mathbf{q}}(t_j) - \mathbf{z}_{\mathbf{q}}(t_j)\|_2. \tag{8.6}$$

Placing a simple bounding-box around the measured three-dimensional elliptic motion path supplies a first estimate of the real valued displacement am-

[1]The reason for path data lacking the relation to a surface point, $\underline{\mathbf{q}}^\star$, is a result of the image processing. In particular, for points close to one another, motion paths will overlap at different times. It thus becomes difficult to track the specific motion path origin using only images.

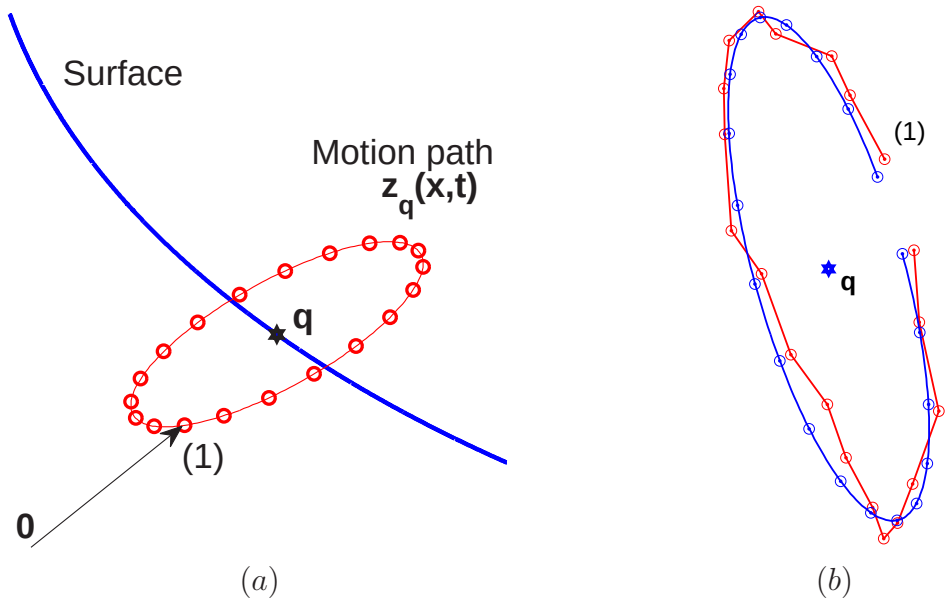

Figure 8.3 (a) General description of a motion path, $\mathbf{z}_\mathbf{q}(\mathbf{x}, t)$, of a point, $\mathbf{q}$, on the surface of an oscillating object; (b) the motion path (blue) and related center, $\mathbf{q}$, resulting from fitted displacement measurements, where "(1)" indicates the first data point at $t = 0$.

plitudes, $|\underline{\hat{\boldsymbol{u}}}^\star_0|$, as initial guesses for the motion in each coordinate direction. Similarly, the center of this bounding box can be used as an initial guess for the surface point, $\underline{\mathbf{q}}^\star_0$. A start value for the phase angles, $\underline{\boldsymbol{\varphi}}^\star_0$, can be estimated by inverting the following expression for each coordinate component, k:

$$\cos(\underline{\varphi}^\star_{0_k}) = \frac{\left(\mathbf{z}^\star_\mathbf{q}(t_j) - \underline{\mathbf{q}}^\star_{0_k}\right)}{|\underline{\hat{\boldsymbol{u}}}^\star_{0_k}|}, \tag{8.7}$$

where care needs to be taken with respect to the quadrant of the first data point relative to $\underline{\mathbf{q}}^\star_0$ and the direction of the motion path, so that the initial velocity at $t_j = 0$ is thus considered indirectly. Figure 8.3 (b) illustrates an example of a reconstructed motion path (blue) obtained and its center, $\underline{\mathbf{q}}^\star$, from the measured data points (red), showing a close fit between measurements and the fitted expression.

This procedure is performed for each of the N motion paths. The fitted expressions for amplitude and phase are then subsequently converted to real and imaginary part of a complex amplitude, $\underline{\hat{\boldsymbol{u}}}^\star$, describing the time-harmonic motion of any of the random surface points. Hence, the data now represents surface motion data compatible to that delivered by the BEM.

8.2.2 Identification of Data Points on the Surface Mesh

The second data pre-processing requirement is the correlation of a measured data point to its location within a mesh of the surface. This task includes the identification of both the surface element in this mesh and the point's position on this element in intrinsic coordinates. Since quadratic surface elements were used in this work, this correlation is also defined by a nonlinear reconstruction problem.

Despite the improved convergence of the mesh with respect to the geometry, when compared to a linear element mesh, it still cannot be guaranteed that measured points, $\underline{\mathbf{q}}^{\star}$, match the surface exactly. Considering the added influence of noise, it is generally expected that a small distance exists between the measured data and the meshed surface. Hence, this data correlation problem is related to the same inverse problem encountered in the sub-segmentation procedure for near-singular elements in the BEM forward solution (see Section 2.3.3.2), where a point on a surface element is identified as the closest surface point to a collocation point located elsewhere in space. However, the difference in the correlation problem is that not only one but a choice of several surface elements may exist. This situation occurs, when a data point is very close to a boundary between elements, as can be also seen in Figure 8.4.

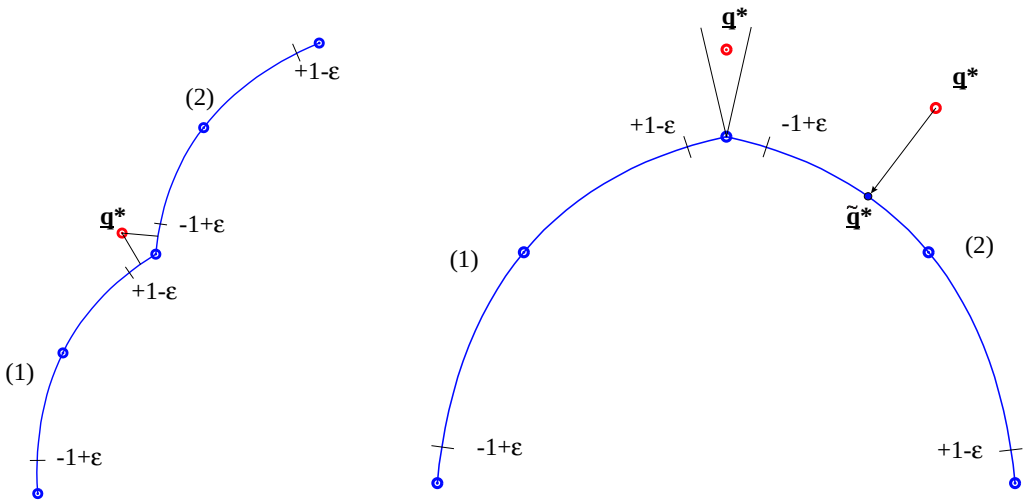

Figure 8.4 Correlation of measured data points, $\underline{\mathbf{q}}^{\star}$, to points on a surface mesh in element intrinsic coordinates. Critical points close to the edge of an element are disregarded from further use.

The choice of elements is easily narrowed down by the numerical identification of the node of the mesh closest to the data point. With respect to this node, all of it's neighboring elements need to be considered as elements potentially including this data point. Therefore, a nonlinear reconstruction is performed for each of these elements to identify a point, $\underline{\tilde{\mathbf{q}}}^{\star}(\boldsymbol{\eta})$, closest to a data point, $\underline{\mathbf{q}}^{\star}$, using an objective function based on the distance between these two points:

$$\Psi_{\mathbf{q}} = \|\underline{\tilde{\mathbf{q}}}^{\star}(\boldsymbol{\eta}) - \underline{\mathbf{q}}^{\star}\|_2. \tag{8.8}$$

Hence, this procedure returns the intrinsic coordinates, $\boldsymbol{\eta}$, of point $\underline{\tilde{\mathbf{q}}}^{\star}(\boldsymbol{\eta})$ for each element considered. The correct element number is then identified by ruling out cases where this reconstruction has led to intrinsic coordinates that were not within the limits $\boldsymbol{\eta} \in \{-1,\ 1\}$. These limits, thus, exclude points that are physically located outside the boundaries of the element.

Figure 8.4 illustrates that in some cases, particularly for coarse meshes, there may still remain a choice between element numbers. Hence, an acceptable limits for the intrinsic coordinates, $\boldsymbol{\eta}$, has been defined tighter, using $\tilde{\eta} \in \{-1+\varepsilon,\ 1-\varepsilon\}$, where ε was chosen $\varepsilon = 0.01$. In cases where this condition leads to no element being found related to a particular data point, this data point was eliminated from further use.

8.2.3 Data Extrapolation to Nodal Mesh Description

Theoretically, every parameter required in the elastographic inverse problem is now defined. The parameter reconstruction could easily commence with its objective function (see Equation 4.4) evaluated at every identified data point, $\underline{\tilde{\mathbf{q}}}^{\star}(\boldsymbol{\eta})$. In particular, this task requires displacements to be calculated at these data points from forward solutions, by quadratic interpolation, whenever the error functional needs to be evaluated. This technique introduces relatively little additional computational effort and has been used successfully by Peters [89] in an FEM-based reconstruction algorithm.

However, as data points are randomly and densely distributed on the geometry's surface, it often occurs that points are very close to each other. In such cases, several equations of the system may become exceedingly similar in their numerical values. These similar equations and values can lead to increased ill-conditioning of the inverse system equations. In contrast, the nodal values of a converged mesh describe both the geometry and related surface deformations

fully in a linearly independent system. If the inverse system is evaluated on the nodes of the mesh, this numerical ill-conditioning can thus be minimized or avoided.

Further, the reconstruction algorithm developed in the previous chapters is based on the evaluation of the displacement error objective function at the nodal values of a surface mesh. It is thus desirable to maintain this evaluation for better comparability of the tested inverse algorithm to its performance when using experimental data. Therefore, a third data pre-processing step was developed to extrapolate the complex motion amplitudes obtained at the measured points to the amplitudes of the given nodal locations of the mesh. This goal was achieved using a linear least squares technique combined with principles of finite element calculations.

Consider an element with a random number, $N_m^{(el)}$, of measurement points, $\underline{\tilde{\mathbf{q}}}^\star(\boldsymbol{\eta})$, whose intrinsic coordinates, $\boldsymbol{\eta}_q$, and whose complex displacement values, $\underline{\hat{\boldsymbol{u}}}^\star$, are known. These displacements can be defined in an isoparametric formulation as the interpolation of the nodal displacement values, $\hat{\mathbf{u}}_k^\star$, based on the element's nodal shape functions, ϕ_k. Hence, for each measured point of this element, one can write:

$$\underline{\hat{\boldsymbol{u}}}_j^\star = \phi_k(\boldsymbol{\eta}_q)\,\hat{\mathbf{u}}_k^\star, \quad j = 1,\ \ldots,\ N_m^{(el)}, \tag{8.9}$$

where summation over k applies.

Then one can conceive these $N_m^{(el)}$ equations in the sense of a local element matrix of a finite element formulation. Therefore, once can rewrite Equation 8.9 for each single measurement in a global sense:

$$\{\underline{\boldsymbol{u}}^\star\} = [\Phi]\,\{\mathbf{u}^\star\}, \quad j = 1,\ \ldots,\ N_m. \tag{8.10}$$

In Equation 8.10, $\{\underline{\boldsymbol{u}}^\star\}$ is a vector that contains all measured displacement amplitudes of size $(N_m \cdot N_{dof} \times 1)$, where N_{dof} is the number of degrees of freedom in each measurement; $\{\mathbf{u}^\star\}$ is the vector of the unknown nodal displacement amplitudes and is of size $(N_n \cdot N_{dof} \times 1)$, N_n being the number of nodes on the mesh's outer boundary. Finally, $[\Phi]$ is a rectangular matrix of size $(N_m \cdot N_{dof} \times N_n \cdot N_{dof})$ that contains only values of the interpolating polynomials evaluated at the intrinsic coordinates of each measured point.

Pre-multiplying Equation 8.10 with $[\Phi]^T$ yields:

$$\underbrace{\left[\Phi\right]^T \{\underline{\boldsymbol{u}}^\star\}}_{\mathbf{b}} = \underbrace{\left[\Phi^T \Phi\right]}_{\mathbf{A}} \{\mathbf{u}^\star\}, \tag{8.11}$$

where the left hand side can be reduced to a vector, $\mathbf{b}$, that is now of size $(N_n \cdot N_{dof} \times 1)$ and $\mathbf{A}$ is a square matrix of size $(N_n \cdot N_{dof} \times N_n \cdot N_{dof})$.

Before solving this system, the matrix $\mathbf{A}$ in Equation 8.11 needs to be further manipulated to account for the boundary conditions prescribed to the mesh. In particular, single equations are related to specific nodes of the mesh, where Dirichlet boundary conditions are prescribed. These equations must be substituted by their known displacement solution to account for these boundary conditions. After this operation, Equation 8.11 can be solved for the complex nodal displacements, $\mathbf{u}^\star$:

$$\mathbf{u}^\star = \mathbf{A}^{-1}\mathbf{b}, \tag{8.12}$$

where these displacement values are now readily usable in the elastographic inverse problem to evaluate the objective function on a nodal basis.

Figure 8.5 illustrates a simulated test of this procedure using a 3D hemispherical geometry, where eight data points were randomly generated from a nodal displacement solution on each element of the free surface. Figure 8.5 (a) shows these data points as red dots on the surface that is indicated as a grey wiremesh. Figure 8.5 (b) shows the geometry in its displaced configuration, where the nodal displacements were obtained from the extrapolation procedure. A visual inspection shows the same motion qualities that were seen in the originally displaced solution, with no change in magnitude.

As a quality measure of the extrapolated nodal displacement solution, the objective function of the elastographic inverse problem (Equation 4.4) was used. Comparing the original displacement forward solution to the extrapolated solution in this case yielded an error value of $3.26 \cdot 10^{-15}\ m^2$, which is a value very close to machine precision and thus effectively zero.

Note that this proposed technique necessitates the availability of a minimum number of measurements, such that an equation exists for each degree of freedom of each surface node. Therefore, a sequence of elements in a row without available measurements will lead to failure of this technique due to singular equations in the system. Having said that, it is important to realize that sparse data can also cause failure to occur. However, this type of failure will occur only in localized

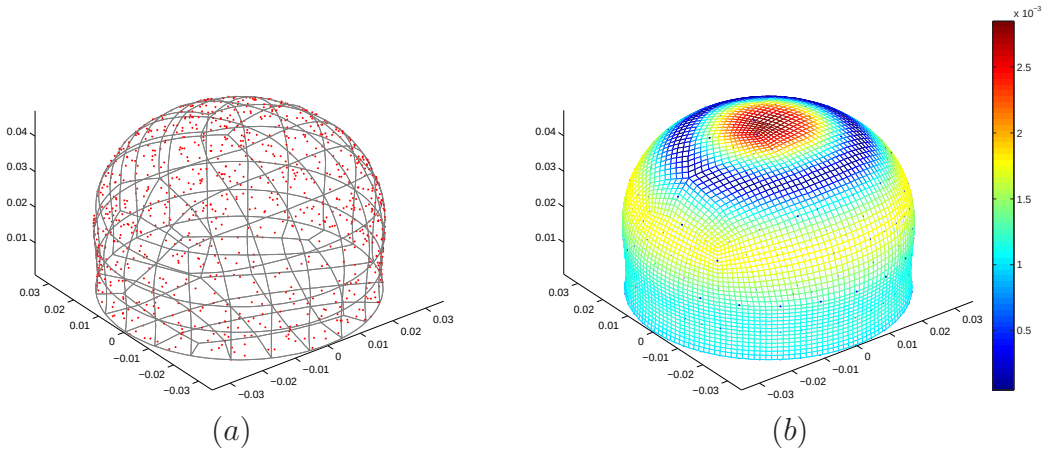

Figure 8.5 Extrapolation of displacements from random data points (a) to nodal displacement amplitudes of the mesh (b). (The color-coding refers to displacement amplitudes in m).

areas of the mesh, due to the finite influence of single equations. In such cases, this technique has similar advantages as classic finite element techniques.

8.3 Full Volume Breast Phantom Reconstruction

Although a variety of motion data-sets are available for a number of different phantom geometries, not many were suitable for direct use in the BEM reconstruction algorithm using the currently implemented techniques. More specifically, some phantoms exhibit larger sections on the surface where no motion measurements were available. This issue can occur, when surface markers were used too sparsely in particular locations or when blind spots appear over surface sections that do not allow for two sufficiently intersecting views by a camera pair. These circumstances can cause the data-extrapolation to fail due to insufficiently available motion data in limited sections of the phantom surface.

The *best* data set with the most complete available surface motion data was obtained for the breast phantom in Figure 8.2. The overall dimensions of this phantom were obtained via a surface scan and Solid Works' geometric recognition tool and are shown in the drawing in Figure 8.6.

This phantom contained a stiff inclusion of approximately spherical shape and a size of approximately $R \approx 7.5\ mm$. This inclusion was located centrally with respect to the vertical x_3 dimension of the phantom and approximately at a radial distance of 30 mm from the phantom's center in the $x_1 - x_2$ plane.

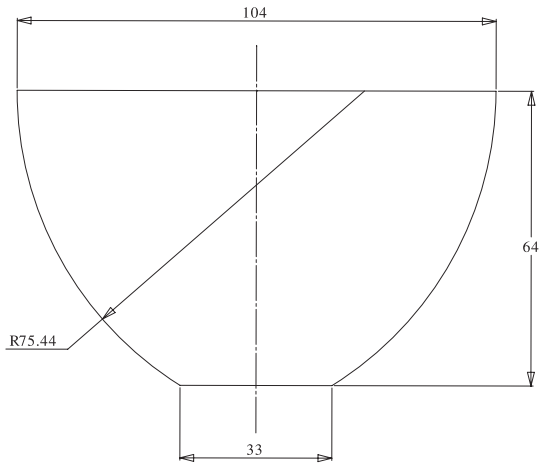

Figure 8.6 Overall dimensions of the breast phantom geometry

Approximate material parameters are given in Table 8.1. Precise knowledge of the inclusion parameters could not be supplied due to the inevitable inaccuracies occurring in the manufacturing process.

Motion data was measured for a longitudinal and sinusoidal actuation applied through the circular connection between the actuator and the bottom side of the phantom with an amplitude of 0.75 mm at 100 Hz, as illustrated in Figure 8.2.

8.3.1 Motion Data Manipulation

Figure 8.7 illustrates the results from the motion data preprocessing stages. In particular, the reconstructed locations of data points on the surface mesh of this phantom are shown in Figure 8.7 (a). It can be seen that a larger fraction of the surface on the back side of the phantom do not contain sufficient motion data points. There are more such sections near actuator connection.

Figure 8.7 (b) shows the result of the extrapolation procedure. It did not fail, but shows obvious areas at the top and bottom edges of the phantom, where the extrapolation was locally unsuccessful. These issues are also a result of local areas of sparse data points.

To make use of this data set a manual correction was performed. As actuation was applied with an amplitude of 0.75 mm, it is not expected that measured displacement values would yield more than 1 mm in amplitude. Therefore, the resulting nodal motion data was searched and any displacement values with amplitudes over 1 mm in either coordinate direction was set to a *zero* magnitude.

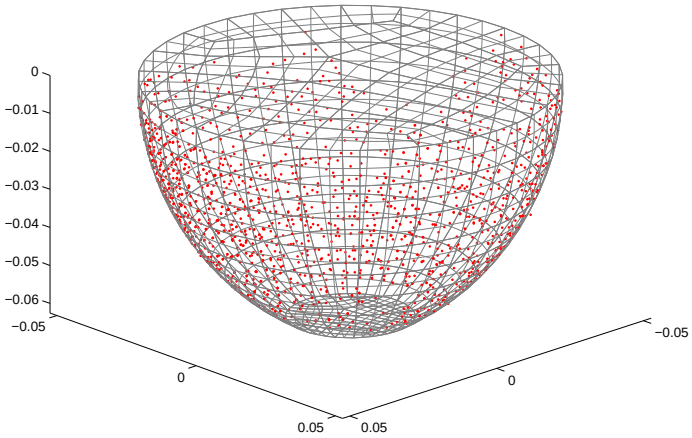

(a)

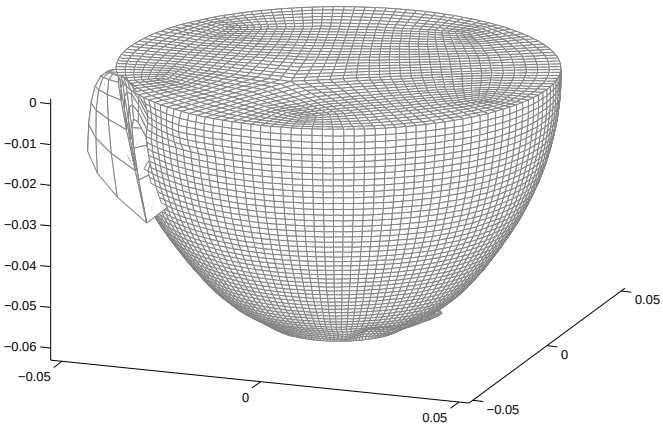

(b)

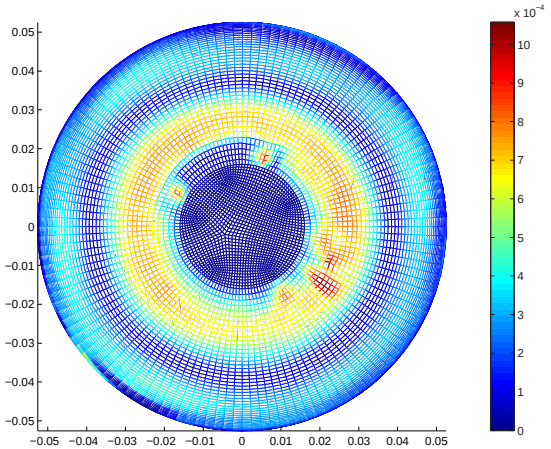

(c)

Figure 8.7 (a) Reconstructed locations of motion data points on the breast phantom surface, (b) resulting surface displacements from extrapolation, (c) resulting surface motion after manual correction of blind spots.

This criteria affected a total of 21 displacement values (out of 1035). To avoid errors in the inverse problem from such manipulated data these values were neglected in the objective function by setting the according surface motion error values to zero.

The remaining motion is plotted in Figure 8.7 (c) as viewed from the bottom of the phantom to allow a qualitative view of the entire measured surface. The color coding in this figure represents the motion amplitudes at $t = 0\ s$. The corrected areas can be recognized at the coordinates $(-0.03,\ -0.04)\ m$ at the top edge and $(-0.01,\ 0.02)\ m$ at the bottom edge. Some localized areas remain with more distorted displacement values.

Overall, the majority of the surface shows a clear motion image. As expected, (largely) longitudinal waves propagate from the bottom actuated side to the top of the phantom. Clearly, displacement amplitudes decrease rapidly, indicating some amount of damping in the material.

8.3.2 Phantom Reconstruction Results

Reconstructions were performed for this data set using the two techniques described in Chapters 6 and 7. In particular, **Case A** used the combined three-step reconstruction of background and inclusion parameters, as described in Table 7.1. However, in Case A, the Grid-Search step was carried out with a fixed value for the radial inclusion size. Therefore, the algorithm was repeated for several values of inclusion sizes. **Case B** employed the techniques for the identification of inclusion parameters only, as described Table 6.5.

The reconstruction results of Case A are given in Tables 8.2 and 8.3 according to the algorithm steps. All of the runs of Case A used common start values for the background material parameters. Thus, the reconstructions lead to the same material parameter results shown in Table 8.2.

Case A	Step (1) – Background Material Reconstruction	
(a)	Start Value	Reconstructed Value
E^I	$30\ kPa$	$26.9\ kPa$
ν	0.49	0.4943
α	$20.0\ rad/s$	$1.2\ rad/s$
β	$0.000125\ s/rad$ $\}\ \zeta = 5.5\%$	$4.57 \cdot 10^{-5}\ s/rad$ $\}\ \zeta = 1.5\%$
(ρ)	$(1000\ kg/m^3)$	$(1000\ kg/m^3)$

Table 8.2 Reconstruction results for the background material parameters (algorithm step (1) for the breast phantom.

In summary, the value for the reconstructed elastic modulus appears close to the parameter value obtained from mechanical testing. Peters *at al.* emphasized that the true solution value from mechanical testing, $E = 32\ kPa$, is likely overestimated by 10%. The result obtained here is slightly below this indication, but still in an acceptable range. Furthermore, Poisson's ratio, ν, converged to a value even closer to incompressibility than initially assumed. Interestingly, the damping parameters, α and β, decreased to a yield a damping ratio of $\zeta = 1.5\%$, which is an unexpected result below what might have been expected from Figures 8.7.

Table 8.3 contains the subsequent results for the identification of the inclusion parameters determined from Grid-Search and Gauss-Newton reconstruction. Although, all results apart from the $R = 10\ mm$ case indicate the presence of an inclusion with increased stiffness, the results appear inconsistent in all inclusion parameters.

The inclusion location has been found similar and close to the true location in the first two ($R = 5\ mm$ and $R = 6.6\ mm$) cases, but is reasonably different in both of the other results. The x_3 coordinate of the location is too *high* in all cases. In contrast, the results for the inclusion sizes are all close to their initial guess, which is a similar result as observed in the simulation studies of Chapters 5 and 7.

The fact that the algorithm converged in all cases with final objective function values $\tilde{\Psi}$ of $O(10^{-4}\ m^2)$ is not an indication for strong results. However, this value may reflect differences in initial shape and nonlinearity in response. Hence, larger objective function values are to be expected in comparison to simulation case studies.

Case A (b)	Step (3) – Inclusion Reconstruction for			
	$R = 5\ mm$	$R = 6.6\ mm$	$R = 8.3\ mm$	$R = 10\ mm$
$\tilde{E}^{II}\ [kPa]$	42.6	48.7	77.5	28.0
$\tilde{P}\ [mm]$	$\begin{pmatrix} -8.5 \\ 26.4 \\ -17.1 \end{pmatrix}$	$\begin{pmatrix} -8.0 \\ 38.1 \\ -14.0 \end{pmatrix}$	$\begin{pmatrix} 21.5 \\ 8.2 \\ -17.0 \end{pmatrix}$	$\begin{pmatrix} -4.2 \\ 22.4 \\ -19.2 \end{pmatrix}$
$\tilde{R}\ [mm]$	5.3	6.9	8.1	8.8
$\tilde{\Psi}^{(3)}\ [m^2]$	$1.4 \cdot 10^{-4}$	$1.3 \cdot 10^{-4}$	$1.7 \cdot 10^{-4}$	$1.6 \cdot 10^{-4}$

Table 8.3 Subsequent reconstruction results for inclusion parameters of the breast phantom (algorithm step (2) and (3): Grid-Search and Gauss-Newton).

Table 8.4 shows the reconstruction results for inclusion parameters in case B, where background material parameters have been fixed to the values closer to those determined from mechanical testing and with an estimated 5.5% damping ratio. In contrast to Case A, Case B clearly indicates a significantly increased stiffness value at a size close to the solution. However, the inclusion location has in this case not been determined correctly. A similar motion error $\tilde{\Psi}$ of $O(10^{-4}\ m^2)$ may also not necessarily promote confidence in the obtained solution.

Case B – Inclusion Reconstruction			
Start Values		Reconstruction Results	
E^I	$30\ kPa$	$\tilde{E}^{II}$	$96.1\ kPa$
ν	0.49	$\tilde{R}$	7.0
α	$20.0\ rad/s$	$\tilde{P}$	$\begin{pmatrix} -13.6 \\ -23.3 \\ -41.3 \end{pmatrix} mm$
β	$0.000125\ s/rad$ $\Big\} \zeta = 5.5\%$		
ρ	$975\ kg/m^3$	$\tilde{\Psi}$	$1.4 \cdot 10^{-4}\ m^2$

Table 8.4 Reconstruction results and start values for inclusion identification at fixed background material parameters.

8.3.3 Discussion

The reconstruction for background material parameters has lead to reasonable parameter results that are comparable to the values obtained from mechanical testing. In the reconstruction for inclusion parameters, all cases generally determined solutions that indicate the presence of an inclusion with a considerably increased stiffness value in comparison to the background parameters. However, results of inclusion parameter reconstruction are also inconsistent when compared to one another. None of the cases have converged to error function values below $O(10^{-4}\ m^2)$ and could thus be rated as either inconclusive or even as reconstruction failures, when compared to simulation study cases. Numerous factors would have contributed to these reconstruction results:

- The accuracy of motion measurements is vital to successful reconstruction. This accuracy has been estimated to be at $O(10^{-4}\ m)$ [120]. If motion measurement takes place at an actuation amplitude of $0.75\ mm$, this actuation is not significantly higher in amplitude than measurement accuracy and is thus a serious concern for the usability of this particular data set.

- Results for the reconstruction of a point motion path from the measured data appear to be a robust step in data processing that would likely lead to a degree of elimination of measurement error by averaging effects. In contrast, the motion data extrapolation procedure described in Section 8.2.3 is in itself an ill-conditioned inverse problem, where small errors in the measured displacement data may lead to significant error in the reconstructed nodal displacement value. The use of this technique may therefore be disadvantageous in this problem.

- Sparse availability of data points in areas have been found to lead to significant error in the extrapolation procedure. The fact that some data had to be eliminated from the nodal displacement data set is a disadvantage, as the available motion information is reduced. In particular, this loss of information in specific areas may conceal important effects or may even cause or mimic similar effects that an inclusion might have on the overall motion behavior.

- In contrast to simulation studies in the foregoing chapters, the breast phantom was subject to a large area with fixed zero Dirichlet boundary conditions and actuated using a small circular device. While this scenario may be closer to a realistic screening situation, a certain, inevitable data loss has occurred. Additionally, the smaller actuation area and smaller actuation amplitude can be interpreted as a decreased amount of actuation energy delivered to the phantom. This can be illustrated, for example, with an expression for the delivered strain energy. In turn, less motion occurs in the object and damping effects are increased. While this effect may possibly not immediately lead to vital consequences, optimization of these actuation parameters, also with respect to areas of resonant motion, would achieve better motion data results.

- The true physical motion behavior of the breast phantom may be inaccurately reflected by a purely linear elastic model. These kind of discrepancies are always to be expected. However, a true estimation of a model mismatch can only be evaluated, once accurate geometry and motion data is available.

- An increased final motion error value may well be expected in experimental tests, particularly when compared to the according simulation studies. Factors, such as nonlinear material behavior or geometry mismatches, will contribute to these accumulated values.

- Data measurement has not been performed at optimized actuation conditions. The actuation frequency, 100 Hz, is a very fast and, thus, enhancing the impact of damping, as pointed out in Chapter 3. Additionally, the small actuation amplitude would also have contributed to a reduced opportunity to reliably identify the inclusion.

All these factors or combinations thereof would have contributed to the inconclusive reconstruction results achieved here. However, while some particular factors will have more significant relevance, it cannot be pointed out conclusively, which ones these are.

Importantly, this experimental study was performed only on a single motion data set and, therefore, cannot be representative. It is obvious that the reconstruction technique must be tested and verified on a variety of improved motion data sets.

8.4 Summary

A number of processing steps of the available motion data has been developed. In particular this included the nonlinear reconstruction of a surface point's motion path and its conversion to a complex description. Furthermore, a number of steps have been taken to correlate the measured motion data to a surface mesh of a given phantom shape. Once this correlation has been completed, another step was introduced to extrapolate the measured random data points on the surface to the nodal displacements of the mesh.

These techniques developed have been tested on a silicone phantom with an idealized breast shape. All these data processing steps showed a plausible outcome for the given actuation scenario. However, testing the reconstruction algorithms from Chapters 6 and 7 for the identification of both background and inclusion parameters has lead to not fully satisfying results. The reconstruction of the background material parameters of the breast phantom may be rated successful. However, as accurate knowledge of the silicon material parameters is unavailable, an objective comparison and evaluation of the algorithm performance is currently not possible.

The reconstruction of inclusion parameters has led to results that do indicate the presence of an inclusion with increased stiffness. However, in general, these results are inconclusive. The relatively high final motion error values of

$O(10^{-4}\ m^2)$ indicate that a significant inaccuracy is likely present in the current problem setup. A large number of possibilities for this inaccuracy has been identified, but cannot be classified from this single experimental test. To determine the relevant reasons for these inaccuracies, systematic experimental testing needs to be performed on a large amount of motion data sets taken at optimized actuation conditions.

Chapter 9

Conclusions

This thesis presented the successful development of several algorithms for the solution of the elastographic inverse problems from time-harmonic surface motion data based on the BEM. These algorithms consider various configurations for the reconstruction of all relevant mechanical material parameters of a proportionally damped elastic solid as well as the reconstruction of parameters describing a circular or spherical inclusion with increased stiffness within the domain. This chapter highlights the main findings throughout the algorithm development phase and presents conclusions that can be drawn with respect to the algorithm's application to a DIET breast cancer screening system, which was the target application of this research.

9.1 Reconstruction Algorithm Developments

The BEM for harmonic elasticity was employed as the forward solver in this inverse problem. Therefore, a region-based reconstruction approach was dictated for the identification of piecewise constant material parameters. This region-based approach, however, introduced significant computational advantages to the BEM's use in the inverse problem, where only partial updates of the BEM system matrices were required and yielded significant computational savings.

The algorithm development was performed in a systematic manner from reconstruction of homogeneous material parameters up to the combined identification of background and inclusion parameters. The reconstruction of these parameters was, in all cases, achieved using surface displacement data only. In particular, three major reconstruction algorithms are the result of these developments.

Algorithm 1 – Isotropic Homogeneous Material Identification

The Gauss-Newton method was used to implement the simultaneous reconstruction of the material parameters α, β, E ν and ρ of a homogeneous isotropic material. Simulation studies verified the implementation and have highlighted important reconstruction behaviors:

- The reconstruction behavior for the proportional damping parameters α and β is dominated by initial convergence to the damping ratio, ζ, before convergence is achieved to the correct damping parameters.
- The inverse solution for density and elasticity at the same time is not unique. Solutions for these two parameters result in combinations of E and ρ that resemble the same wave speeds, c_s and c_p, determined by the material parameters of the true solution. Either ρ or E is required to be known initially to achieve correct identification results for the other parameter.
- The elastic modulus, E, is a parameter in this particular reconstruction problem that causes significant nonlinearities or non-convex characteristics in the surface motion error based objective function. Convergence to local minima in E must be avoided by the use of quality start values.

Algorithm 2 – 2-Step Identification of Inclusion Parameters

The identification of the geometric inclusion parameters is an extremely nonlinear problem with a large number of local minima, particularly in the identification of an inclusion location. These nonlinearities were overcome using a novel hybrid 2-step algorithm. This algorithm used a systematic Grid-Search in P and R of a stiff circular or spherical inclusion, followed by the more accurate reconstruction of these parameters including the inclusion's elastic modulus, E^{II}, with a Gauss-Newton gradient descent technique. The following reconstruction behaviors were found to be important:

- The Grid-Search resolution is vital to the successful identification of the global problem solution. It is advantageous to keep this resolution low and reconstruct for several local minima extracted from the resulting coarse errormap.
- Increased levels of material damping inhibit the successful identification of an inclusion and can cause reconstructions to fail. This failure occurs in

different areas of the geometric domain depending on the geometry shape and material as well as the actuation parameters.

- The actuation parameters, frequency and actuation type, as well as geometry shape, inclusion size and stiffness have effects on the success of the reconstruction. For the successful identification of an arbitrary inclusion, multiple surface motion data-sets with varied actuation parameters appear to be vital.

- A competitive reconstruction behavior occurs in cases of stiff inclusions between the inclusion elasticity and the inclusion size. Results can tend to slightly smaller inclusion sizes but extremely increased stiffness values, or to slightly larger inclusion sizes with decreased stiffness values when compared to the true inclusion stiffness solution. However, in comparison to the background material, these stiffness values are still found significantly increased.

Algorithm 3 – 3-Step Identification of Background and Inclusion

A clinical environment may require the identification of both background material parameters and inclusion parameters. This was achieved using a novel hybrid 3-step reconstruction algorithm. For the relatively small inclusions targeted, the estimation of background material parameters by reconstruction for a single homogeneous domain was implemented as the first step in a hybrid 3-step algorithm. This step was followed by a Grid-Search for a potential circular/spherical inclusion with a third refined reconstruction step with a Gauss-Newton method.

- The accuracy of background material estimation for E, ν, α and β strongly depends on inclusion size and stiffness. However, this estimation is accurate enough to successfully identify inclusions of sizes between 0 and 10 mm in radial size.

- The resulting motion error values after background and after inclusion reconstructions provide a basis to differentiate between the quality of the results. These results can be used as a strong indication for the differentiation between global of local solutions.

- The incorporation of accurate background material parameter estimation supports the successful identification of small sized inclusions. At low damp-

ing levels, inclusions with a 5–6 times increase in stiffness could be successfully identified for sizes $R \geq 2\ mm$.

- Reconstructing for an inclusion in cases where the solution did not contain an inclusion resulted in convergence behavior towards small inclusion sizes with inclusion stiffness values approaching the value of the background stiffness successfully resembling the case of a homogeneous domain. In these cases, the resulting minimal motion errors can be interpreted as a strong indication for the successful identification of healthy patients.

9.2 Experimental Data Processing

For the use of the reconstruction algorithms, a number of data-processing techniques were developed to correlate the DIET system specific motion measurements to a boundary element mesh.

- A nonlinear reconstruction technique was developed for the fitting of position data that was measured over one oscillation period to an elliptic motion path of a surface point in three-dimensional space. This motion was converted to the BEM compatible complex data format.

- The identification and correlation of a measured surface point to a given boundary mesh with quadratic surface elements was achieved by a second nonlinear gradient descent based reconstruction method that minimized the distance between an element and the data point in element intrinsic space.

- A motion data extrapolation procedure was developed based on a least square fitting procedure and in the sense of a finite element method obtaining nodal values of motion data from the motion measurements at arbitrary places on the surface.

These data pre-processing steps were found to be individually robust, as long as sufficient coverage of measured data points exists on the surface of a geometry. An elastographic reconstruction trial that was performed on a first data set obtained by the DIET image capture system of a silicone based breast phantom resulted in inconclusive reconstruction results. While this result is due to a large number of factors that cannot be classified from this single experimental test, it does indicate that this system still requires significant improvements.

9.3 Clinical Conclusions

In summary, all these algorithms have successfully proven their applicability for a surface motion based material and inclusion parameter identification. Particularly Algorithm 1 and 2 are relevant and are readily applicable in the DIET breast cancer screening system. Reconstruction results as achieved in simulation are very promising to be successful in both experimental testing and clinical application.

In particular, in simulation, the algorithms presented have shown very strong results in the identification of a *healthy* patient case where no inclusion is present. This case can be reconstructed with high accuracy and therefore indicates a potentially high specificity of this method, meaning a small number of false negatives. This technique could be used as a contradictive approach to breast cancer screening that excludes the potential presence of an inclusion with confidence, when the reconstruction for a homogeneous material can be achieved with high accuracy.

Stiff inclusion cases have also been identified with the implemented algorithms with great confidence. While inclusion locations have been found with great accuracy, the inclusion size and stiffness value were not reconstructed accurately with current techniques. However, in a clinical sense, the results obtained in such cases would usually still indicate the correct solution of a present inclusion with increased stiffness. Hence, this result also indicates a potentially good sensitivity of the resulting method.

A serious, but, at this stage, unknown limitation to the realization of a DIET breast cancer screening system could be posed by high levels of damping in biological breast tissue. In such cases, the reconstruction accuracy declines rapidly and the resulting motion scattering effects are attenuated before reaching the surface. The clinical realization of a DIET breast cancer system will depend strongly on what level of damping actually exists in real breast tissue.

However, the fact that material and inclusion identification could be performed with better quality results than current standard breast cancer screening methods is encouraging. These results are also comparable to competing elastographic methods but could be achieved with a reduced amount of measured data and computational advantages. Therefore, further development of this method and the DIET screening system should continue.

Chapter 10

Future Work

The work presented in this thesis, particularly with respect to the simulation studies presented in Chapters 5 – 7, has shown significant potential for the use in a DIET breast cancer screening system. However, these simulation studies also highlighted aspects in the implemented algorithm that require improvements. In this chapter, suggestions are made for algorithm improvements towards a better performance and towards the successful use of these algorithms in experimental and clinical studies. Future developments towards a better model representation of the underlying physics are included. Furthermore, important research direction for the potential application in a DIET breast cancer screening system are highlighted.

10.1 Algorithm Improvements

Both of the developed hybrid algorithms, Algorithm 1 and 2, have been shown suitable and immediately applicable for material and inclusion parameter identification in a surface motion based DIET breast cancer screening system. However, simulation studies have highlighted areas, where technical algorithm improvements are required or have large potential to improve the overall algorithm performance. These improvements are summarized in some detail in this section.

Computational Techniques

- The inverse problem sensitivity and, in particular, the calculation of the Jacobian matrix has been performed using a finite difference method and, thus, yielding inaccurate approximations. This calculation should, in the future, be replaced by more sophisticated methods. This could include an

analytical differentiation of the forward problem fundamental solutions with respect to a material parameter and, hence, yield a semi-analytical expression for the computation of the according Jacobian columns. In addition, sensitivities with respect to geometric changes for the inclusion mesh are advantageous to be obtained by adjoint methods [104]. Particularly in cases of small error changes over larger variable ranges, such as encountered in the inverse solution for inclusion parameters E^{II} and R, these improved sensitivities could lead to major improvements in the inverse solution accuracy.

- More sophisticated regularization techniques, as can be found, for example, in BEM based crack identification problems, could yield improvements with respect to the reconstruction behavior in this ill-posed and ill-conditioned inverse problem.

- The use of a radial basis function approach for the discretization of inclusions has recently shown significant potential when employed in similar inverse problems. These basis functions could be a step towards the more realistic identification of arbitrarily shaped inclusions.

- Particularly in the expected case of high damping, it may be necessary to expand the inverse algorithms to consider multiple motion data sets from several actuation scenarios. These scenarios should include several actuation frequencies, and actuation at several different surface areas to provide excitation in all parts of the entire volume.

Computational Efficiency

Significant computational savings have been made in this work by the use of partial system matrix updates in the repeated evaluation of BEM forward solutions. However, the solution of a single problem, particularly in 3D space, still requires significant computer resources.

Advances in computer technology are evidently leading towards parallelized computer architectures, even for personal computers, where quad core machines are the current standard. Therefore, the parallelization of the developed algorithms would yield to significant time reductions to determine clinically relevant results with the DIET system. Additionally, open source software for Message Passing Interface (MPI) parallelization is readily available.

In this implementation, both the forward and inverse problems have strong parallelization potential. A particularly straightforward parallelization case would, for example, be the Grid-Search routine in Algorithms 1 and 2, where simple looping can be reduced to an execution on parallel machines. Furthermore, the gradient descent techniques would profit immensely, if the matrix assembly of the BEM forward problem was performed in parallel.

Model Improvements

Currently, a model has been implemented that uses an isotropic, piecewise homogeneous, elastic material with proportional damping for the representation of harmonic vibrations of breast tissue. It is to be expected that the different tissue types involved, as described in 1, exhibit more sophisticated dynamic behavior.

In particular, anisotropic effects from fibrous tissues will be relevant, as will be other nonlinear material effects. Also, complicated mechanical interactions between the skin and tissue may play a role. Furthermore, the interior boundary conditions at the breast tissue interface with the rib cage will be interesting future research towards a better understanding of the complicated biological tissue behavior.

Although the successful recognition of a single inclusion with increased stiffness would lead to major further clinical investigations before diagnosis, the potential case of multiple lesions must be considered as a clinically relevant case in future research. The presence of multiple inclusions may significantly disturb the reconstruction algorithm behavior with respect to a single inclusion and could lead to diagnostic failures. On the other hand, the successful determination of such a multiple inclusion case, as can be achieved with a multiple region based BEM, would provide a major diagnostic value.

Parallel to this study, reconstruction techniques based on basic FE methods have been developed for reconstructions in the DIET application. While these methods were limited to material stiffness reconstruction of the background and inclusion material, these techniques have shown promising results in experimental phantom studies [89]. Particularly with respect to sophisticated future model improvements incorporating, for example, an anisotropic material model or effects from the skin, affecting only finite regions of the breast, it is proposed to use hybrid BEM-FEM formulations within a multiple region based framework. This approach would combine the advantages of both BEM and FEM in this particular research.

Experimental Techniques

While algorithms have been developed for all preprocessing requirements of the DIET specific motion data, the application of the inverse Algorithms 1 and 2, have not yet succeeded, due to a number of circumstances. At this point, the following recommendations can be made that can be achieved in a short to medium term.

- Motion data needs to be taken at output optimized settings. In particular, this goal includes recording motion at near resonant frequencies with increased actuation amplitudes to obtain a maximized signal-to-noise ratio.
- Further optimization for the recording of motion data includes to expand the presence of fiducial markers to the complete observed surface. An increase in the number of cameras with improved resolution will contribute to the minimization of measurement error.
- The reconstruction algorithms should be executed with error function evaluation performed directly on the measured data point by interpolation of the nodal displacement values. This step eliminates an additional source of error that may have been introduced by the ill-conditioned data extrapolation procedure.
- A systematic phantom testing regimen is suggested, starting with data sets from homogeneous phantoms with clear knowledge of its material parameters, before proceeding to the more difficult inclusion identification problem.
- To support the automation of motion data capture with the subsequent data inversion to stiffness information, the current surface data measurement system could easily be used for an automated surface recognition and surface mesh generation.

10.2 Future Clinical Developments

With respect to the future development of the DIET system in the short term and its potential clinical realization in the long term, a number of steps require attention. Using the algorithms developed this study has provided important reconstruction behaviors relevant to the implementation and realization of a material identification scheme such as required for the DIET system. Additionally,

general limits of such a reconstruction scheme have been highlighted with respect to reconstruction accuracy and the minimally identifiable inclusion size.

However, these studies were performed successfully in simulation only. To corroborate the validity of these findings, they urgently require confirmation from experimental testing. While some reconstruction behaviors, such as those with respect to damping or non-uniqueness, may be confirmed through a small number of basic tests, the confirmation of reconstruction limitations will require large scale testing due to the large variability and dependencies observed in the involved parameters.

These large scale studies require accurate knowledge of all parameters of the material being used including the material stiffness, Poisson ratio, density and damping parameters. The reproducibility of the results must be guaranteed for a large range and numerous combinations of the different material parameters.

In the medium term, it would be beneficial to obtain motion data sets from real, healthy, and cancerous breasts. Such data sets would present significant challenges to the implemented methods. However, they would provide vital information for the applicability of the developed methods. In particular, this information includes data or results on the real observed attenuation behavior, the accuracy of the elastic material model, and the validity of boundary conditions. This step is vital to the long term developments and long term feasibility of the DIET system.

Appendix A

Reconstruction Results for P, R and E^{II}

According to the reconstruction problems for the inclusion parameters location, P, size, R, and inclusion stiffness, E^{II} simulated in Section 6.2.4, the detailed reconstruction results are listed here in tabularized form. In these tables, the main axis label the start values R_0 and E_0^{II}, for which firstly a coarse spatial Grid-Search was performed for the inclusion location, P. After extracting three minima from the resulting errormap as start values, a Gauss-Newton reconstruction in all three variables P, R and E^{II} was performed for each of these start values. The table fields then contain the best converged solution achieved by one of these three start values. Details of each reconstruction are given:

- The number of the start value, i_{min}, that converged to the best solution with the smallest displacement error,
- The initial displacement error, Ψ_0 (in m^2), evaluated at this particular start value,
- The resulting displacement error, $\tilde{\Psi}$ (in m^2), at the converged solution,
- The inclusion location in coordinates of its center, $\tilde{P}_x$, $\tilde{P}_y$ (in mm),
- The resulting radial inclusion size, $\tilde{R}$ (in mm),
- The converged inclusion stiffness, $\tilde{E}^{II}$ (in kPa),

where the true solution values, geometry and actuation data for each table are described in detail in Section 6.2.4. Note that parameters that converged to values far from their true solution are highlighted in orange color if the clinical interpretation would still be correct and red color if the clinical interpretation would lead to a wrong diagnosis.

E_0^{II} $[kPa]$	Inclusion size R_0 $[mm]$ 3	5	7	10
50	$i_{min}=1$ $\Psi_0=1.4e{-}6$ $\tilde{\Psi}=8.3e{-}13$ $\tilde{P}_x=55$ $\tilde{P}_y=35$ $\tilde{R}=5.02$ $\tilde{E}^{II}=191.2$	$i_{min}=1$ $\Psi_0=5.6e{-}7$ $\tilde{\Psi}=2.1e{-}11$ $\tilde{P}_x=54.9$ $\tilde{P}_y=35$ $\tilde{R}=5.19$ $\tilde{E}^{II}=147.7$	$i_{min}=1$ $\Psi_0=1.8e{-}8$ $\tilde{\Psi}=3.2e{-}11$ $\tilde{P}_x=55$ $\tilde{P}_y=35$ $\tilde{R}=5.2$ $\tilde{E}^{II}=147.8$	$i_{min}=1$ $\Psi_0=9.5e{-}7$ $\tilde{\Psi}=2.1e{-}11$ $\tilde{P}_x=55$ $\tilde{P}_y=35$ $\tilde{R}=5.2$ $\tilde{E}^{II}=147.8$
100	$i_{min}=1$ $\Psi_0=1.0e{-}6$ $\tilde{\Psi}=8.8e{-}11$ $\tilde{P}_x=55$ $\tilde{P}_y=35$ $\tilde{R}=4.7$ $\tilde{E}^{II}=543.2$	$i_{min}=1$ $\Psi_0=9.3e{-}8$ $\tilde{\Psi}=3.3e{-}11$ $\tilde{P}_x=55$ $\tilde{P}_y=35$ $\tilde{R}=5.2$ $\tilde{E}^{II}=147.8$	$i_{min}=2$ $\Psi_0=1.3e{-}6$ $\tilde{\Psi}=3.2e{-}11$ $\tilde{P}_x=55$ $\tilde{P}_y=35$ $\tilde{R}=5.2$ $\tilde{E}^{II}=147.8$	$i_{min}=3$ $\Psi_0=1.8e{-}6$ $\tilde{\Psi}=3.2e{-}11$ $\tilde{P}_x=55$ $\tilde{P}_y=35$ $\tilde{R}=5.2$ $\tilde{E}^{II}=147.8$
150	$i_{min}=1$ $\Psi_0=9.0e{-}7$ $\tilde{\Psi}=1.3e{-}10$ $\tilde{P}_x=55$ $\tilde{P}_y=35$ $\tilde{R}=4.5$ $\tilde{E}^{II}=2757$	$i_{min}=1$ $\Psi_0=3.7e{-}8$ $\tilde{\Psi}=1.0e{-}12$ $\tilde{P}_x=55$ $\tilde{P}_y=35$ $\tilde{R}=5.0$ $\tilde{E}^{II}=182$	$i_{min}=1$ $\Psi_0=7.5e{-}7$ $\tilde{\Psi}=2.1e{-}11$ $\tilde{P}_x=55$ $\tilde{P}_y=35$ $\tilde{R}=5.2$ $\tilde{E}^{II}=147.8$	$i_{min}=1$ $\Psi_0=1.6e{-}6$ $\tilde{\Psi}=3.2e{-}11$ $\tilde{P}_x=55$ $\tilde{P}_y=35$ $\tilde{R}=5.2$ $\tilde{E}^{II}=147.8$
200	$i_{min}=1$ $\Psi_0=8.4e{-}7$ $\tilde{\Psi}=1.2e{-}10$ $\tilde{P}_x=55$ $\tilde{P}_y=35$ $\tilde{R}=4.6$ $\tilde{E}^{II}=1765$	$i_{min}=1$ $\Psi_0=2.5e{-}8$ $\tilde{\Psi}=1.4e{-}13$ $\tilde{P}_x=55$ $\tilde{P}_y=35$ $\tilde{R}=5.0$ $\tilde{E}^{II}=197$	$i_{min}=1$ $\Psi_0=9.8e{-}7$ $\tilde{\Psi}=2.1e{-}11$ $\tilde{P}_x=55$ $\tilde{P}_y=35$ $\tilde{R}=5.19$ $\tilde{E}^{II}=147.7$	$i_{min}=2$ $\Psi_0=1.6e{-}6$ $\tilde{\Psi}=2.1e{-}11$ $\tilde{P}_x=55$ $\tilde{P}_y=35$ $\tilde{R}=5.19$ $\tilde{E}^{II}=147.7$
250	$i_{min}=1$ $\Psi_0=8.e{-}7$ $\tilde{\Psi}=1.4e{-}10$ $\tilde{P}_x=55$ $\tilde{P}_y=35$ $\tilde{R}=4.5$ $\tilde{E}^{II}=3196$	$i_{min}=1$ $\Psi_0=2.5e{-}8$ $\tilde{\Psi}=8.4e{-}13$ $\tilde{P}_x=55$ $\tilde{P}_y=35$ $\tilde{R}=4.95$ $\tilde{E}^{II}=218.1$	$i_{min}=3$ $\Psi_0=1.1e{-}6$ $\tilde{\Psi}=3.2e{-}11$ $\tilde{P}_x=55$ $\tilde{P}_y=35$ $\tilde{R}=5.2$ $\tilde{E}^{II}=147.8$	$i_{min}=1$ $\Psi_0=1.7e{-}6$ $\tilde{\Psi}=1.2e{-}6$ $\tilde{P}_x=53.4$ $\tilde{P}_y=50.3$ $\tilde{R}=5.$ $\tilde{E}^{II}=28.1$

Table A.1 Reconstruction results for parameters P, R and E^{II} of a circular inclusion within a 2D rectangular geometry. (Solution: $P^\star=(55,\ 35)^T\ mm$, $R^\star=5\ mm$, $E^{II\star}=200\ kPa$).

E_0^{II} $[kPa]$	Inclusion size R_0 $[mm]$ 2	4	6	8
50	$i_{min}=1$ $\Psi_0=5.0e{-}7$ $\tilde{\Psi}=1.4e{-}13$ $\tilde{P}_x=10$ $\tilde{P}_y=30$ $\tilde{R}=3.04$ $\tilde{E}^{II}=135$	$i_{min}=1$ $\Psi_0=1.5e{-}7$ $\tilde{\Psi}=1.0e{-}12$ $\tilde{P}_x=10$ $\tilde{P}_y=30$ $\tilde{R}=3.17$ $\tilde{E}^{II}=106$	$i_{min}=3$ $\Psi_0=7.5e{-}7$ $\tilde{\Psi}=9.9e{-}13$ $\tilde{P}_x=10$ $\tilde{P}_y=30$ $\tilde{R}=3.17$ $\tilde{E}^{II}=106$	$i_{min}=1$ $\Psi_0=7.4e{-}7$ $\tilde{\Psi}=2.9e{-}7$ $\tilde{P}_x=18$ $\tilde{P}_y=34$ $\tilde{R}=8.0$ $\tilde{E}^{II}=28$
100	$i_{min}=1$ $\Psi_0=3.5e{-}7$ $\tilde{\Psi}=1.5e{-}11$ $\tilde{P}_x=10$ $\tilde{P}_y=30$ $\tilde{R}=2.7$ $\tilde{E}^{II}=809.2$	$i_{min}=1$ $\Psi_0=1.3e{-}7$ $\tilde{\Psi}=1.0e{-}12$ $\tilde{P}_x=10$ $\tilde{P}_y=30$ $\tilde{R}=3.17$ $\tilde{E}^{II}=106$	$i_{min}=2$ $\Psi_0=6.3e{-}7$ $\tilde{\Psi}=1.4e{-}9$ $\tilde{P}_x=10.3$ $\tilde{P}_y=29.8$ $\tilde{R}=5.8$ $\tilde{E}^{II}=30.9$	$i_{min}=2$ $\Psi_0=1.1e{-}6$ $\tilde{\Psi}=6.8e{-}7$ $\tilde{P}_x=23.5$ $\tilde{P}_y=26.4$ $\tilde{R}=8.0$ $\tilde{E}^{II}=28.9$
150	$i_{min}=1$ $\Psi_0=3.0e{-}7$ $\tilde{\Psi}=1.6e{-}11$ $\tilde{P}_x=10$ $\tilde{P}_y=30$ $\tilde{R}=2.7$ $\tilde{E}^{II}=1546$	$i_{min}=1$ $\Psi_0=1.9e{-}7$ $\tilde{\Psi}=9.8e{-}13$ $\tilde{P}_x=10$ $\tilde{P}_y=30$ $\tilde{R}=3.17$ $\tilde{E}^{II}=106.7$	$i_{min}=2$ $\Psi_0=7.8e{-}7$ $\tilde{\Psi}=4.8e{-}10$ $\tilde{P}_x=10.3$ $\tilde{P}_y=29.8$ $\tilde{R}=5.8$ $\tilde{E}^{II}=30.1$	$i_{min}=1$ $\Psi_0=1.3e{-}6$ $\tilde{\Psi}=7.1e{-}7$ $\tilde{P}_x=-25$ $\tilde{P}_y=17.1$ $\tilde{R}=8.0$ $\tilde{E}^{II}=30.4$
200	$i_{min}=1$ $\Psi_0=2.7e{-}7$ $\tilde{\Psi}=1.5e{-}11$ $\tilde{P}_x=10$ $\tilde{P}_y=30$ $\tilde{R}=2.7$ $\tilde{E}^{II}=1279.4$	$i_{min}=1$ $\Psi_0=2.4e{-}7$ $\tilde{\Psi}=9.8e{-}13$ $\tilde{P}_x=10$ $\tilde{P}_y=30$ $\tilde{R}=3.17$ $\tilde{E}^{II}=106.7$	$i_{min}=3$ $\Psi_0=1.4e{-}6$ $\tilde{\Psi}=6.5e{-}7$ $\tilde{P}_x=18.3$ $\tilde{P}_y=34.2$ $\tilde{R}=6.0$ $\tilde{E}^{II}=39.5$	$i_{min}=1$ $\Psi_0=1.5e{-}6$ $\tilde{\Psi}=1.4e{-}6$ $\tilde{P}_x=-26.9$ $\tilde{P}_y=17.1$ $\tilde{R}=8.0$ $\tilde{E}^{II}=46.9$
250	$i_{min}=1$ $\Psi_0=2.6e{-}7$ $\tilde{\Psi}=1.6e{-}11$ $\tilde{P}_x=10$ $\tilde{P}_y=30$ $\tilde{R}=2.7$ $\tilde{E}^{II}=2101$	$i_{min}=1$ $\Psi_0=2.8e{-}7$ $\tilde{\Psi}=1.e{-}12$ $\tilde{P}_x=10$ $\tilde{P}_y=30$ $\tilde{R}=3.17$ $\tilde{E}^{II}=106.4$	$i_{min}=3$ $\Psi_0=1.5e{-}6$ $\tilde{\Psi}=1.4e{-}11$ $\tilde{P}_x=10$ $\tilde{P}_y=30$ $\tilde{R}=2.65$ $\tilde{E}^{II}=1863$	$i_{min}=3$ $\Psi_0=3.8e{-}6$ $\tilde{\Psi}=9.0e{-}7$ $\tilde{P}_x=-13.7$ $\tilde{P}_y=18$ $\tilde{R}=2.2$ $\tilde{E}^{II}=1623.7$

Table A.2 Reconstruction results for parameters P, R and E^{II} of a circular inclusion within a 2D semi-elliptical geometry. (Solution: $P^\star=(10,\ 30)^T\ mm$, $R^\star=3\ mm$, $E^{II\star}=150\ kPa$).

E_0^{II} $[kPa]$	Inclusion size R_0 $[mm]$ 2	4	6	8
50	$i_{min}=1$ $\Psi_0=5.5e{-}6$ $\tilde{\Psi}=5.4e{-}9$ $\tilde{P}_x=10.1$ $\tilde{P}_y=29.9$ $\tilde{R}=5.4$ $\tilde{E}^{II}=90.4$	$i_{min}=1$ $\Psi_0=2.6e{-}6$ $\tilde{\Psi}=5.4e{-}9$ $\tilde{P}_x=10.1$ $\tilde{P}_y=29.9$ $\tilde{R}=5.39$ $\tilde{E}^{II}=92.1$	$i_{min}=1$ $\Psi_0=7.6e{-}7$ $\tilde{\Psi}=6.7e{-}9$ $\tilde{P}_x=10.1$ $\tilde{P}_y=29.9$ $\tilde{R}=6.3$ $\tilde{E}^{II}=56.2$	$i_{min}=1$ $\Psi_0=1.3e{-}6$ $\tilde{\Psi}=7.2e{-}9$ $\tilde{P}_x=10$ $\tilde{P}_y=29.8$ $\tilde{R}=6.7$ $\tilde{E}^{II}=49.9$
100	$i_{min}=2$ $\Psi_0=4.8e{-}6$ $\tilde{\Psi}=6.5e{-}9$ $\tilde{P}_x=10.1$ $\tilde{P}_y=29.9$ $\tilde{R}=4.4$ $\tilde{E}^{II}=2862$	$i_{min}=1$ $\Psi_0=1.4e{-}6$ $\tilde{\Psi}=5.4e{-}9$ $\tilde{P}_x=10.1$ $\tilde{P}_y=29.9$ $\tilde{R}=5.4$ $\tilde{E}^{II}=91.4$	$i_{min}=1$ $\Psi_0=1.0e{-}6$ $\tilde{\Psi}=5.9e{-}9$ $\tilde{P}_x=10.1$ $\tilde{P}_y=29.9$ $\tilde{R}=5.7$ $\tilde{E}^{II}=76.4$	$i_{min}=1$ $\Psi_0=2.0e{-}5$ $\tilde{\Psi}=7.6e{-}9$ $\tilde{P}_x=10$ $\tilde{P}_y=29.9$ $\tilde{R}=6.7$ $\tilde{E}^{II}=49.9$
150	$i_{min}=2$ $\Psi_0=4.6e{-}6$ $\tilde{\Psi}=6.4e{-}9$ $\tilde{P}_x=10.1$ $\tilde{P}_y=29.9$ $\tilde{R}=6.2$ $\tilde{E}^{II}=58.9$	$i_{min}=1$ $\Psi_0=1.1e{-}6$ $\tilde{\Psi}=3.8e{-}9$ $\tilde{P}_x=10.1$ $\tilde{P}_y=29.9$ $\tilde{R}=5.4$ $\tilde{E}^{II}=91.1$	$i_{min}=2$ $\Psi_0=1.5e{-}6$ $\tilde{\Psi}=5.5e{-}9$ $\tilde{P}_x=10.1$ $\tilde{P}_y=29.9$ $\tilde{R}=5.57$ $\tilde{E}^{II}=80.5$	$i_{min}=1$ $\Psi_0=1.5e{-}6$ $\tilde{\Psi}=1.5e{-}6$ $\tilde{P}_x=18.3$ $\tilde{P}_y=34.2$ $\tilde{R}=8.0$ $\tilde{E}^{II}=134.7$
200	$i_{min}=1$ $\Psi_0=4.4e{-}6$ $\tilde{\Psi}=6.5e{-}9$ $\tilde{P}_x=10.1$ $\tilde{P}_y=29.9$ $\tilde{R}=4.4$ $\tilde{E}^{II}=1425$	$i_{min}=1$ $\Psi_0=1.0e{-}6$ $\tilde{\Psi}=6.3e{-}9$ $\tilde{P}_x=10.1$ $\tilde{P}_y=29.8$ $\tilde{R}=4.5$ $\tilde{E}^{II}=637$	$i_{min}=1$ $\Psi_0=1.8e{-}6$ $\tilde{\Psi}=6.0e{-}9$ $\tilde{P}_x=10.1$ $\tilde{P}_y=29.9$ $\tilde{R}=5.9$ $\tilde{E}^{II}=68.8$	$i_{min}=1$ $\Psi_0=1.5e{-}6$ $\tilde{\Psi}=1.5e{-}6$ $\tilde{P}_x=18.3$ $\tilde{P}_y=34.2$ $\tilde{R}=8.0$ $\tilde{E}^{II}=125.4$
250	$i_{min}=1$ $\Psi_0=7.1e{-}6$ $\tilde{\Psi}=5.4e{-}9$ $\tilde{P}_x=10.1$ $\tilde{P}_y=29.9$ $\tilde{R}=5.4$ $\tilde{E}^{II}=91.7$	$i_{min}=1$ $\Psi_0=9.30e{-}7$ $\tilde{\Psi}=6.5e{-}9$ $\tilde{P}_x=10.1$ $\tilde{P}_y=29.8$ $\tilde{R}=4.4$ $\tilde{E}^{II}=2011$	$i_{min}=1$ $\Psi_0=2.0e{-}6$ $\tilde{\Psi}=5.4e{-}9$ $\tilde{P}_x=10.1$ $\tilde{P}_y=29.9$ $\tilde{R}=5.5$ $\tilde{E}^{II}=86.7$	$i_{min}=1$ $\Psi_0=1.5e{-}6$ $\tilde{\Psi}=1.5e{-}6$ $\tilde{P}_x=18$ $\tilde{P}_y=34.2$ $\tilde{R}=8.0$ $\tilde{E}^{II}=132.4$

Table A.3 Reconstruction results for parameters P, R and E^{II} in case of an elliptical inclusion (of semi-axes parameters a, b and rotation ϑ) within a 2D semi-elliptical geometry. (Solution: $P^\star=(10,\ 30)^T\ mm$, $a^\star=6\ mm$, $b^\star=4\ mm$, $\vartheta^\star=30°$ and $E^{II\star}=150\ kPa$).

E_0^{II}	Inclusion size R_0 $[mm]$			
$[kPa]$	2	4	6	8
50	$i_{min} = 3$ $\Psi_0 = 8.4e{-9}$ $\tilde{\Psi} = 2.6e{-10}$ $\tilde{P}_x = 0.5$ $\tilde{P}_y = 4.3$ $\tilde{R} = 1.5$ $\tilde{E}^{II} = 20.8$	$i_{min} = 3$ $\Psi_0 = 1.1e{-7}$ $\tilde{\Psi} = 2.9e{-11}$ $\tilde{P}_x = 4.0$ $\tilde{P}_y = 4.4$ $\tilde{R} = 2.1$ $\tilde{E}^{II} = 20.6$	$i_{min} = 1$ $\Psi_0 = 4.6e{-7}$ $\tilde{\Psi} = 1.0e{-12}$ $\tilde{P}_x = -9.3$ $\tilde{P}_y = 7.0$ $\tilde{R} = 6.0$ $\tilde{E}^{II} = 20.1$	$i_{min} = 2$ $\Psi_0 = 1.7e{-6}$ $\tilde{\Psi} = 1.3e{-11}$ $\tilde{P}_x = 4.8$ $\tilde{P}_y = 42.0$ $\tilde{R} = 8.0$ $\tilde{E}^{II} = 20.1$
100	$i_{min} = 2$ $\Psi_0 = 1.3e{-8}$ $\tilde{\Psi} = 2.5e{-11}$ $\tilde{P}_x = -5.7$ $\tilde{P}_y = 9.4$ $\tilde{R} = 1.6$ $\tilde{E}^{II} = 20.2$	$i_{min} = 3$ $\Psi_0 = 2.2e{-7}$ $\tilde{\Psi} = 4.2e{-11}$ $\tilde{P}_x = 3.7$ $\tilde{P}_y = 43.6$ $\tilde{R} = 2.6$ $\tilde{E}^{II} = 20.6$	$i_{min} = 2$ $\Psi_0 = 1.1e{-6}$ $\tilde{\Psi} = 6.8e{-11}$ $\tilde{P}_x = 0.0$ $\tilde{P}_y = 7.0$ $\tilde{R} = 6.0$ $\tilde{E}^{II} = 20.1$	$i_{min} = 3$ $\Psi_0 = 2.0e{-5}$ $\tilde{\Psi} = 2.7e{-11}$ $\tilde{P}_x = 18$ $\tilde{P}_y = 30.0$ $\tilde{R} = 2.1$ $\tilde{E}^{II} = 20.2$
150	$i_{min} = 2$ $\Psi_0 = 1.7e{-8}$ $\tilde{\Psi} = 2.5e{-11}$ $\tilde{P}_x = -5.4$ $\tilde{P}_y = 9.5$ $\tilde{R} = 1.6$ $\tilde{E}^{II} = 20.2$	$i_{min} = 1$ $\Psi_0 = 1.1e{-6}$ $\tilde{\Psi} = 3.6e{-11}$ $\tilde{P}_x = 4.0$ $\tilde{P}_y = 44.7$ $\tilde{R} = 1.9$ $\tilde{E}^{II} = 20.7$	$i_{min} = 2$ $\Psi_0 = 1.4e{-6}$ $\tilde{\Psi} = 6.8e{-11}$ $\tilde{P}_x = 0$ $\tilde{P}_y = 7.0$ $\tilde{R} = 6.0$ $\tilde{E}^{II} = 20.1$	$i_{min} = 3$ $\Psi_0 = 2.6e{-5}$ $\tilde{\Psi} = 3.2e{-11}$ $\tilde{P}_x = 1.9$ $\tilde{P}_y = 23.2$ $\tilde{R} = 2.9$ $\tilde{E}^{II} = 20.1$
200	$i_{min} = 2$ $\Psi_0 = 1.9e{-8}$ $\tilde{\Psi} = 2.5e{-11}$ $\tilde{P}_x = -5.4$ $\tilde{P}_y = 9.5$ $\tilde{R} = 1.6$ $\tilde{E}^{II} = 20.2$	$i_{min} = 2$ $\Psi_0 = 9.6e{-8}$ $\tilde{\Psi} = 3.9e{-11}$ $\tilde{P}_x = 10$ $\tilde{P}_y = 5.5$ $\tilde{R} = 2.2$ $\tilde{E}^{II} = 20.5$	$i_{min} = 3$ $\Psi_0 = 3.4e{-7}$ $\tilde{\Psi} = 2.6e{-11}$ $\tilde{P}_x = 8.6$ $\tilde{P}_y = 15.6$ $\tilde{R} = 3.3$ $\tilde{E}^{II} = 20.0$	$i_{min} = 3$ $\Psi_0 = 3.2e{-5}$ $\tilde{\Psi} = 6.2e{-8}$ $\tilde{P}_x = -28.0$ $\tilde{P}_y = 7.0$ $\tilde{R} = 8.0$ $\tilde{E}^{II} = 18.4$
250	$i_{min} = 2$ $\Psi_0 = 2.1e{-8}$ $\tilde{\Psi} = 2.5e{-11}$ $\tilde{P}_x = -5.5$ $\tilde{P}_y = 9.5$ $\tilde{R} = 1.6$ $\tilde{E}^{II} = 20.2$	$i_{min} = 3$ $\Psi_0 = 3.7e{-7}$ $\tilde{\Psi} = 1.0e{-12}$ $\tilde{P}_x = 8.7$ $\tilde{P}_y = 15.2$ $\tilde{R} = 3.3$ $\tilde{E}^{II} = 20.1$	$i_{min} = 2$ $\Psi_0 = 1.6e{-6}$ $\tilde{\Psi} = 6.6e{-11}$ $\tilde{P}_x = 0$ $\tilde{P}_y = 7.0$ $\tilde{R} = 6.0$ $\tilde{E}^{II} = 20.0$	$i_{min} = 3$ $\Psi_0 = 3.2e{-5}$ $\tilde{\Psi} = 2.0e{-11}$ $\tilde{P}_x = 16.0$ $\tilde{P}_y = 22.9$ $\tilde{R} = 2.8$ $\tilde{E}^{II} = 20.1$

Table A.4 Reconstruction results for parameters P, R and E^{II} in a healthy case without inclusion.

Appendix B

Background and Inclusion Identification Results

A simulation study was conducted in Chapter 7 to demonstrate the capabilities of a three step reconstruction algorithm illustrated in Table 7.1 for background estimation and inclusion identifications at differently sized inclusions. Stepwise, this algorithm determines first a set of background material parameters:

(a): E^I = Background Young's modulus
ν = Background Poisson ratio
α = Background inertial damping parameter
β = Background viscous damping parameter

using a Gauss-Newton approach and neglecting the existence of a potentia inclusion. Note that α, β, ν and ρ are assumed to be equal for both region. Secondly, a coarse Grid-Search is conducted in R and P, searching for a stiff inclusion, leading to three sets of start values for inclusion parameters:

(b): E^{II} = Inclusion Young's modulus
R = Radial inclusion size
P = Inclusion location

is more accurately determined in a third Gauss-Newton step of the algorithm.

Tables B.1–B.4) present the detailed solutions in terms of the parameter sets (a) and (b) obtained by the different algorithm steps. The solutions also list the initial and final displacement error value, Ψ, of each converged solution. Note that the solutions listed for each reconstruction is the *best* solution determined with minimal error.

R	Reconstructed Solution, $\tilde{\boldsymbol{\theta}}$
0	(a) $\Psi_0^{(1)} = 2.4e{-}6$ $\tilde{\Psi}^{(1)} = 5.0e{-}12$ $\tilde{E}^I = 27.45$ $\tilde{\nu} = 0.49$ $\tilde{\alpha} = 28.6$ $\tilde{\beta} = 0.00033$ } $\zeta = 9.74\%$ (b) $\Psi_0^{(3)} = 3.2e{-}8$ $\tilde{\Psi}^{(3)} = 4.5e{-}13$ $\tilde{P} = (-23.4,\ 31)^T$ $\tilde{R} = 2.3$ $\tilde{E}^{II} = 27.51$
1	(a) $\Psi_0^{(1)} = 2.5e{-}6$ $\tilde{\Psi}^{(1)} = 2.9e{-}9$ $\tilde{E}^I = 27.54$ $\tilde{\nu} = 0.49$ $\tilde{\alpha} = 28.6$ $\tilde{\beta} = 0.00033$ } $\zeta = 9.74\%$ (b) $\Psi_0^{(3)} = 8.1e{-}8$ $\tilde{\Psi}^{(3)} = 6.1e{-}10$ $\tilde{P} = (12.5,\ 31.8)^T$ $\tilde{R} = 3.2$ $\tilde{E}^{II} = 31.4$
2	(a) $\Psi_0^{(1)} = 2.9e{-}6$ $\tilde{\Psi}^{(1)} = 4.2e{-}8$ $\tilde{E}^I = 27.77$ $\tilde{\nu} = 0.49$ $\tilde{\alpha} = 28.7$ $\tilde{\beta} = 0.00034$ } $\zeta = 9.9\%$ (b) $\Psi_0^{(3)} = 2.0e{-}8$ $\tilde{\Psi}^{(3)} = 8.7e{-}9$ $\tilde{P} = (12.5,\ 31.9)^T$ $\tilde{R} = 1.96$ $\tilde{E}^{II} = 157.6$
3	(a) $\Psi_0^{(1)} = 3.5e{-}6$ $\tilde{\Psi}^{(1)} = 1.9e{-}7$ $\tilde{E}^I = 28.12$ $\tilde{\nu} = 0.49$ $\tilde{\alpha} = 29.0$ $\tilde{\beta} = 0.00035$ } $\zeta = 10.1\%$ (b) $\Psi_0^{(3)} = 8.0e{-}8$ $\tilde{\Psi}^{(3)} = 3.9e{-}8$ $\tilde{P} = (12.6,\ 32.0)^T$ $\tilde{R} = 2.9$ $\tilde{E}^{II} = 175.14$
4	(a) $\Psi_0^{(1)} = 4.5e{-}6$ $\tilde{\Psi}^{(1)} = 4.9e{-}7$ $\tilde{E}^I = 28.55$ $\tilde{\nu} = 0.49$ $\tilde{\alpha} = 29.5$ $\tilde{\beta} = 0.00037$ } $\zeta = 10.5\%$ (b) $\Psi_0^{(3)} = 1.6e{-}7$ $\tilde{\Psi}^{(3)} = 1.0e{-}7$ $\tilde{P} = (12.6,\ 32.1)^T$ $\tilde{R} = 3.4$ $\tilde{E}^{II} = 219.5$
5	(a) $\Psi_0^{(1)} = 5.9e{-}6$ $\tilde{\Psi}^{(1)} = 1.0e{-}6$ $\tilde{E}^I = 29.04$ $\tilde{\nu} = 0.49$ $\tilde{\alpha} = 30.07$ $\tilde{\beta} = 0.00039$ } $\zeta = 10.9\%$ (b) $\Psi_0^{(3)} = 4.3e{-}7$ $\tilde{\Psi}^{(3)} = 2.2e{-}7$ $\tilde{P} = (12.8,\ 32.3)^T$ $\tilde{R} = 4.3$ $\tilde{E}^{II} = 1726.2$

Table B.1 Entire domain parameter reconstruction results for a circular inclusion in a 2D semi-elliptical geometry – part A (Solution: (1) $E^I = 27.5\ kPa$, $\nu = 0.49$, $\zeta = 10\%$ with (2) $P^\star = (10,\ 30)^T\ mm$, $E^{II^\star} = 250\ kPa$ for inclusion sizes $0\ mm \leq R \leq 5\ mm$).

R	Reconstructed Solution, $\tilde{\boldsymbol{\theta}}$
6	(a) $\Psi_0^{(1)} = 7.8e{-}6$ $\tilde{\Psi}^{(1)} = 1.7e{-}6$ $\tilde{E}^I = 29.57$ $\tilde{\nu} = 0.488$ $\tilde{\alpha} = 30.75$ $\tilde{\beta} = 0.00042$ } $\zeta = 11.49\%$ (b) $\Psi_0^{(3)} = 5.9e{-}7$ $\tilde{\Psi}^{(3)} = 4.1e{-}7$ $\tilde{P} = (13.1,\ 32.4)^T$ $\tilde{R} = 5.1$ $\tilde{E}^{II} = 1744$
7	(a) $\Psi_0^{(1)} = 1.0e{-}5$ $\tilde{\Psi}^{(1)} = 2.6e{-}6$ $\tilde{E}^I = 30.15$ $\tilde{\nu} = 0.487$ $\tilde{\alpha} = 31.5$ $\tilde{\beta} = 0.00044$ } $\zeta = 11.92\%$ (b) $\Psi_0^{(3)} = 1.1e{-}5$ $\tilde{\Psi}^{(3)} = 7.1e{-}7$ $\tilde{P} = (13.0,\ 32.4)^T$ $\tilde{R} = 5.6$ $\tilde{E}^{II} = 4357$
8	(a) $\Psi_0^{(1)} = 1.3e{-}5$ $\tilde{\Psi}^{(1)} = 3.8e{-}6$ $\tilde{E}^I = 30.8$ $\tilde{\nu} = 0.484$ $\tilde{\alpha} = 31.8$ $\tilde{\beta} = 0.00047$ } $\zeta = 12.4\%$ (b) $\Psi_0^{(3)} = 2.4e{-}6$ $\tilde{\Psi}^{(3)} = 1.1e{-}6$ $\tilde{P} = (13.2,\ 32.4)^T$ $\tilde{R} = 6.4$ $\tilde{E}^{II} = 4976$
9	(a) $\Psi_0^{(1)} = 1.7e{-}5$ $\tilde{\Psi}^{(1)} = 5.3e{-}6$ $\tilde{E}^I = 31.56$ $\tilde{\nu} = 0.479$ $\tilde{\alpha} = 32.3$ $\tilde{\beta} = 0.0005$ } $\zeta = 12.9\%$ (b) $\Psi_0^{(3)} = 3.1e{-}6$ $\tilde{\Psi}^{(3)} = 1.8e{-}6$ $\tilde{P} = (13.1,\ 32.2)^T$ $\tilde{R} = 6.7$ $\tilde{E}^{II} = 7630$
10	(a) $\Psi_0^{(1)} = 2.3e{-}5$ $\tilde{\Psi}^{(1)} = 7.4e{-}6$ $\tilde{E}^I = 32.47$ $\tilde{\nu} = 0.473$ $\tilde{\alpha} = 32.1$ $\tilde{\beta} = 0.00053$ } $\zeta = 13.4\%$ (b) $\Psi_0^{(3)} = 4.8e{-}6$ $\tilde{\Psi}^{(3)} = 3.0e{-}6$ $\tilde{P} = (10.3,\ 30.4)^T$ $\tilde{R} = 5.3$ $\tilde{E}^{II} = 21715$

Table B.2 Entire domain parameter reconstruction results for a circular inclusion in a 2D semi-elliptical geometry – part B (Solution: (1) $E^I = 27.5\ kPa$, $\nu = 0.49$, $\zeta = 10\%$ with (2) $P^\star = (10,\ 30)^T\ mm$, $E^{II^\star} = 250\ kPa$ for inclusion sizes $6\ mm \leq R \leq 10\ mm$).

R	Reconstructed Solution, $\tilde{\boldsymbol{\theta}}$	R	Reconstructed Solution, $\tilde{\boldsymbol{\theta}}$
0	(a) $\Psi_0^{(1)} = 6.9e{-}5$ $\tilde{\Psi}^{(1)} = 3.1e{-}12$ $\tilde{E}^I = 27.37$ $\tilde{\nu} = 0.49$ $\tilde{\alpha} = 48.9$ $\tilde{\beta} = 0.000195$ } $\zeta = 10.02\%$ (b) $\Psi_0^{(3)} = 9.2e{-}8$ $\tilde{\Psi}^{(3)} = 7.7e{-}8$ $\tilde{P} = (1.8,\ 3.8,\ 45.7)^T$ $\tilde{R} = 2.1$ $\tilde{E}^{II} = 74.9$	3	(a) $\Psi_0^{(1)} = 6.8e{-}5$ $\tilde{\Psi}^{(1)} = 2.8e{-}7$ $\tilde{E}^I = 27.36$ $\tilde{\nu} = 0.49$ $\tilde{\alpha} = 48.8$ $\tilde{\beta} = 0.000194$ } $\zeta = 9.98\%$ (b) $\Psi_0^{(3)} = 6.1e{-}8$ $\tilde{\Psi}^{(3)} = 3.1e{-}9$ $\tilde{P} = (9.8,\ -14.8,\ 24.9)^T$ $\tilde{R} = 3.8$ $\tilde{E}^{II} = 71.6$
1	(a) $\Psi_0^{(1)} = 6.7e{-}6$ $\tilde{\Psi}^{(1)} = 8.3e{-}8$ $\tilde{E}^I = 27.32$ $\tilde{\nu} = 0.49$ $\tilde{\alpha} = 48.8$ $\tilde{\beta} = 0.000194$ } $\zeta = 9.98\%$ (b) $\Psi_0^{(3)} = 1.6e{-}8$ $\tilde{\Psi}^{(3)} = 1.0e{-}8$ $\tilde{P} = (-0.1,\ -0.16,\ 38.5)^T$ $\tilde{R} = 1.7$ $\tilde{E}^{II} = 63.5$	4	(a) $\Psi_0^{(1)} = 7.1e{-}5$ $\tilde{\Psi}^{(1)} = 9.6e{-}7$ $\tilde{E}^I = 27.41$ $\tilde{\nu} = 0.49$ $\tilde{\alpha} = 48.8$ $\tilde{\beta} = 0.000195$ } $\zeta = 10.01\%$ (b) $\Psi_0^{(3)} = 2.7e{-}7$ $\tilde{\Psi}^{(3)} = 6.0e{-}9$ $\tilde{P} = (10.0,\ -15.0,\ 26.1)^T$ $\tilde{R} = 4.15$ $\tilde{E}^{II} = 163.2$
2	(a) $\Psi_0^{(1)} = 6.7e{-}5$ $\tilde{\Psi}^{(1)} = 1.1e{-}6$ $\tilde{E}^I = 27.33$ $\tilde{\nu} = 0.49$ $\tilde{\alpha} = 48.8$ $\tilde{\beta} = 0.000194$ } $\zeta = 9.98\%$ (b) $\Psi_0^{(3)} = 1.8e{-}8$ $\tilde{\Psi}^{(3)} = 1.2e{-}8$ $\tilde{P} = (9.7,\ -14.2,\ 24.7)^T$ $\tilde{R} = 2.2$ $\tilde{E}^{II} = 182.9$	5	(a) $\Psi_0^{(1)} = 7.6e{-}5$ $\tilde{\Psi}^{(1)} = 2.9e{-}6$ $\tilde{E}^I = 27.48$ $\tilde{\nu} = 0.49$ $\tilde{\alpha} = 49.0$ $\tilde{\beta} = 0.000197$ } $\zeta = 10.1\%$ (b) $\Psi_0^{(3)} = 9.4e{-}7$ $\tilde{\Psi}^{(3)} = 6.5e{-}8$ $\tilde{P} = (10.0,\ -15.2,\ 25.1)^T$ $\tilde{R} = 4.8$ $\tilde{E}^{II} = 328.32$

Table B.3 Entire domain parameter reconstruction results for a spherical inclusion in a 3D semi-ellipsoidal geometry – part A (Solution: (1) $E^I = 27.5\ kPa$, $\nu = 0.49$, $\zeta = 10\%$, (2) $P^\star = (10,\ -15,\ 25)^T\ mm$, $E^{II^\star} = 250\ kPa$ for inclusion sizes $0\ mm \leq R \leq 5\ mm$).

R	Reconstructed Solution, $\tilde{\boldsymbol{\theta}}$
6	(a) $\Psi_0^{(1)} = 8.5e{-}5$ $\tilde{\Psi}^{(1)} = 6.8e{-}6$ $\tilde{E}^I = 27.59$ $\tilde{\nu} = 0.49$ $\tilde{\alpha} = 49.5$ $\tilde{\beta} = 0.0002$ } $\zeta = 10.2\%$ (b) $\Psi_0^{(3)} = 2.3e{-}6$ $\tilde{\Psi}^{(3)} = 2.8e{-}7$ $\tilde{P} = (10.0,\ -15.2,\ 25.0)^T$ $\tilde{R} = 5.6$ $\tilde{E}^{II} = 403.8$
7	(a) $\Psi_0^{(1)} = 9.8e{-}5$ $\tilde{\Psi}^{(1)} = 1.4e{-}5$ $\tilde{E}^I = 27.7$ $\tilde{\nu} = 0.49$ $\tilde{\alpha} = 50.4$ $\tilde{\beta} = 0.0002$ } $\zeta = 10.3\%$ (b) $\Psi_0^{(3)} = 2.8e{-}6$ $\tilde{\Psi}^{(3)} = 8.0e{-}7$ $\tilde{P} = (10.0,\ -15.3,\ 25.0)^T$ $\tilde{R} = 6.5$ $\tilde{E}^{II} = 402.3$
8	(a) $\Psi_0^{(1)} = 1.1e{-}4$ $\tilde{\Psi}^{(1)} = 2.4e{-}5$ $\tilde{E}^I = 27.82$ $\tilde{\nu} = 0.49$ $\tilde{\alpha} = 51.7$ $\tilde{\beta} = 0.00021$ } $\zeta = 10.7\%$ (b) $\Psi_0^{(3)} = 6.3e{-}6$ $\tilde{\Psi}^{(3)} = 1.8e{-}6$ $\tilde{P} = (10.1,\ -15.4,\ 24.9)^T$ $\tilde{R} = 7.3$ $\tilde{E}^{II} = 497.4$
9	(a) $\Psi_0^{(1)} = 1.3e{-}4$ $\tilde{\Psi}^{(1)} = 3.6e{-}4$ $\tilde{E}^I = 27.93$ $\tilde{\nu} = 0.489$ $\tilde{\alpha} = 53.6$ $\tilde{\beta} = 0.00028$ } $\zeta = 13.1\%$ (b) $\Psi_0^{(3)} = 1.4e{-}5$ $\tilde{\Psi}^{(3)} = 3.4e{-}6$ $\tilde{P} = (10.1,\ -15.4,\ 24.7)^T$ $\tilde{R} = 8.1$ $\tilde{E}^{II} = 595.2$
10	(a) $\Psi_0^{(1)} = 1.5e{-}4$ $\tilde{\Psi}^{(1)} = 5.0e{-}5$ $\tilde{E}^I = 28.0$ $\tilde{\nu} = 0.489$ $\tilde{\alpha} = 56$ $\tilde{\beta} = 0.00023$ } $\zeta = 11.7\%$ (b) $\Psi_0^{(3)} = 2.2e{-}5$ $\tilde{\Psi}^{(3)} = 5.7e{-}6$ $\tilde{P} = (10.13,\ -15.4,\ 24.7)^T$ $\tilde{R} = 8.9$ $\tilde{E}^{II} = 797.0$

Table B.4 Entire domain parameter reconstruction results for a spherical inclusion in a 3D semi-ellipsoidal geometry – part A (Solution: (1) $E^I = 27.5\ kPa$, $\nu = 0.49$, $\zeta = 10\%$, (2) $P^\star = (10,\ -15,\ 25)^T\ mm$, $E^{II^\star} = 250\ kPa$ for inclusion sizes $0\ mm \leq R \leq 5\ mm$).

References

[1] J. Ferlay, P. Autier, M. Boniol, M. Heanue, M. Colombet, and P Boyle. Estimates of the cancer incidence and mortality in Europe in 2006. *Annals of Oncology*, 18(3):581–92, 2007.

[2] A. Jemal, R. Siegel, E. Ward, Y. Hao, J. Xu, T. Murray, and M.J. Thun. Cancer statistics, 2008. *CA: A Journal for Clinicians*, 58(2):71–96, 2008.

[3] D. Hanahan and R.A. Weinberg. The hallmarks of cancer. *Cell*, 100:57–70, 2000. Review Article.

[4] D.B. Kopans. *Breast Imaging*. Lippincott–Ravens, Philadelphia, PA, USA, second edition, 1998.

[5] P.J. Lynch and C.C. Jaffe. Image: Breast anatomy. `http://patricklynch.net`.

[6] T. Suzuki, M. Toi, S. Saji, K. Horiguchi, T. Aruga, E. Suzuki, S. Horiguchi, N. Funata, K. Karasawa, and N. Kamata. Early breast cancer. *International Journal of Clinical Oncology*, 11(2):108–19, April 2006.

[7] F.L. Greene, D.L. Page, I.D. Fleming, A. Fritz, C.M. Balch, D.G. Haller, and M. Morrows, editors. *AJCC Cancer Staging Manual*. Lippincott Raven, 1997.

[8] V.C. Cokkinides, A. Samuels, E.M. Ward, and M.J. Thun. *Cancer Prevention & Early Detection Facts & Figures*. American Cancer Society, 2004.

[9] National Comprehensive Cancer Network. *Breast Cancer: Treatment Guidelines for Patients*. 2005.

[10] H.-J. Koubenec. Brustkrebs Info. `http://www.brustkrebs-info.de`.

[11] Canadian Cancer Society. Breast self-examination: What you can do. 2005.

[12] L. Holmberg, A. Ekbom, E. Calle, A. Mokdad, and T. Byers. Breast cancer mortality in relation to self–reported use of breast self–examination: A cohort study of 450,000 women. *Breast Cancer Research and Treatment*, 43:137–40, 1997.

[13] P.A. Newcomb, N.S. Weiss, B.E. Storer, D. Scholes, B.E. Young, and L.F. Voigt. Breast self-examination in relation to the occurence of advanced breast cancer. *Journal of the National Cancer Institute*, 83(4):260–65, 1991.

[14] J.E. Joy, E.E. Penhoet, and D.B. Petitti, editors. *Saving Women's Lives: Strategies for Improving Breast Cancer Detection and Diagnosis*. The National Academic Press, Washington DC, 2005.

[15] A. Asghari and M.K. Nicholas. Pain during mammography: The role of coping strategies. *Pain*, 108:170–79, 2004.

[16] R. Sapir, M. Patlas, S.D. Strano, I. Hadas-Halpern, and N.I. Cherny. Does mammography hurt? *Journal of Pain and Symptom Management*, 25(1):53–63, 2003.

[17] S.K. Moore. Better breast cancer detection. *IEEE Spectrum*, 38:50–54, 2001.

[18] Denise Grady. In shift to digital, more repeat mammograms. New York Times Online, `http://www.nytimes.com/2008/04/10/health/10scan.html`, 2008.

[19] Tara Parker-Pope. Mammograms, new and old. New York Times Online, `http://well.blogs.nytimes.com/2008/04/10/mammograms-new-and-old/`, 2008.

[20] K.D. Schulz and U.S. Albert et. al. Manual der Konzentrierten Aktion zur Leitlinie Brustkrebs-Früherkennung in Deutschland. `http://www.senologie.org`, 2001.

[21] Craig A. Beam, Peter M. Layde, and Daniel C. Sullivan. Variability in the interpretation of screening mammograms by us radiologists: Findings from a national sample. *Archives of Internal Medicine*, 156:209–13, 1996.

[22] S. Gupta. A new breast cancer test. `http://www.time.com/time/magazine/article/0,9171,1565516,00.html`, 2006.

[23] M. Yaffe. What should be the burden of proof for acceptance of a new breast-cancer screening technique. *The Lancet*, 364(9440):1111–12, 2004.

[24] O. Olsen and P.C. Gtzsche. Cochrane review on screening for breast cancer with mammography. *The Lancet*, 358:1340–42, 2001.

[25] V.L. Ernster and J. Barcley. Increases in ductal carcinoma in situ (dcis) of the breast in relation to mammography: A dilemma. *Journal of the National Cancer Institute*, 22:151–56, 1997.

[26] S. Diekmann and F. Diekmann. Mammography screening in Germany. *Radiologe*, 48(1):17–25, January 2008.

[27] D. Lister, A.J. Evans, H.C. Burell, R.W. Blamey, A.R. Wilson, S.E. Pinder, I.O. Ellis, C.W. Elston, and J. Kollias. The accuracy of breast ultrasound in the evaluation of clinically benign discrete, symptomatic breast lumps. *Clinical Radiology*, 53(7):490–92, 1998.

[28] N.V. Ruiter, G.F. Schwarzenberg, M. Zapf, R. Liu, R. Stotzka, and H. Gemmeke, editors. *3D Ultrasound Computer Tomography: Results with a clinical Breast Phantom*. 2006 IEEE Ultrasonics Symposium, 2006.

[29] J. Safir, J.L. Zito, M.E. Gershwind, D. Faegenburg, C.E. Tobin, P.D. Cayea, W.J. Wortman, L.M. Sclafani, and V.E. Maurer. Contrast-enhanced breast MRI for cancer detection using a commercially available system – a perspective. *Clinical Imaging*, 22:162–79, 1998.

[30] L. Irwig, N. Houssami, and C. van Vliet. New technologies in screening for breast cancer: a systematic review of their accuracy. *British Journal of Cancer*, 90:2118–22, 2004.

[31] E. Warner, D.B. Plewes, R.S. Shumak, G.C. Catzavelos, L.S. Di Prospero, M.J. Yaffe, V. Goel, P.L. Chart, E. Ramsay, D.E.C. Cole, G.A. Taylor, M. Cutrara, T.H. Samuels, J.P. Murphy, J.M. Murphy, and S.A. Narod. Comparison of breast magnetic resonance imaging, mammography , and ultrasound for surveillance of women at high risk for hereditary breast cancer. *Journal of Clinical Oncology*, 19:3524–31, 2001.

[32] L. Liberman. Breast cancer screening with MRI - What are the data for patients at high risk? *New England Journal of Medicine*, 351:497–500, 2004.

[33] N.M. Desouza, R. Dina, G.A. McIndoe, and W.P. Soutter. Cervical cancer: Value of an endovaginal coil magnetic resonance imaging technique in detecting small volume disease and assessing parametrial extension. *Gynecologic Oncology*, 2006.

[34] W.C. Amalu. Nondestructive testing of the human breast: The validity of dynamic stress testing in medical infrared breast imaging. In *Proceedings of the 26th Annual International Conference of the IEEE EMBS*, San Francisco, CA, September 2004.

[35] Y.R. Parisky, A. Sardi, R. Hamm, K. Hughes, L. Esserman, S. Rust, and K. Callahan. Efficacy of computerized infrared imaging analysis to evaluate mammographically suspicious lesions. *American Journal of Roentgenology*, 180:263–269, 2002.

[36] Pacific Chiropractic and Research Center. Breast thermography – online. `http://www.breastthermography.com`.

[37] W.C. Amalu, W.B. Hobbins, J.F. Head, and R.L. Elliot. *Infrared Imaging of the Breast — An Overview*, chapter 25. Taylor and Francis, 2006.

[38] T.J.C., J.C. Meij, J.C. de Munck, and R.M. Heethaar. The electric resistivity of human tissues (100 hz-10 mhz): A meta-analysis of review studies. *Physiological Measurement*, 20:1–10, 1999.

[39] Y. Zou and Z. Guo. A review of electrical impedance techniques for breast cancer detection. *Medical Engineering and Physics*, 25(2):79–90, March 2003.

[40] V. Cherepenin, A. Karpov, A. Korjenevsky, A. Mazaletskaya, D. Mazourov, and D. Meister. A 3D Electrical Impedance Tomography (EIT) system for breast cancer detection. *Physiological Measurement*, 22:9–18, 2001.

[41] N.K. Soni, A. Hartov, C. Kogel, S.P. Poplack, and K.D. Paulsen. Multifrequency electrical impedance tomography of the breast: New clinical results. *Physiological Measurement*, 25:301–14, 2004.

[42] A.E. Cerussi, A.J. Berger, F. Bevilacqua, N. Shah, D. Jakubowski, J. Butler, R.F. Holcombe, and B.J. Tromberg. Sources of absorption and scattering contrast for near infrared optical mammography. *Academic Radiology*, 8:211–18, 2001.

[43] S. Fantini, E.L. Heffer, E.P. Vivian andA. Sassaroli, and L. Ning. Spatial and spectral information in optical mammography. *Technology in Cancer Research and Treatment*, 4(5):471–82, 2005.

[44] X. Intes, J. Ripoll, Y. Chen, S. Nioka, A.G. Yodh, and B. Chance. In vivo continuous-wave optical breast imaging enhanced with indocyanine green. *Medical Physics*, 30(6):1039–47, 2003.

[45] H. Rinneberg, D. Grosenick amd K.T. Moesta, J. Mucke, B. Gebauer, C. Stroszczynski, H. Wabnitz, M. Moeller, B. Wassermann, and P.M. Schlag. Scanning time-domain optical mammography: detection and characterization of breast tumors in vivo. *Technology in Cancer Research and Treatment*, 4(5):483–96, 2005.

[46] H. Dehghani, M.M. Doyley, B.W. Pogue, S. Jiang, J. Geng, and K.D. Paulsen. Breast deformation modelling for image reconstruction in near infrared optical tomography. *Physics in Medicine and Biology*, 49:1131–45, March 2004.

[47] A.P. Sarvazyan, A.R. Skovaroda, S.Y. Emelianov, J.B. Fowlkes, J.G. Pipe, R.S. Adler, R.B. Boxton, and P.L. Carson. Biophysical bases of elasticity imaging. *Acoustical Imaging*, 21:223–40, 1995.

[48] A.P. Sarvazyan. Mechanical imaging: A new technology for medical diagnostics. *International Journal of Medical Informatics*, 49(2):195–216, 1998.

[49] T.A. Krouskop, T.M. Wheeler, F. Kallel, B.S. Garra, and T. Hall. Elastic moduli of breast and prostate tissues under compression. *Ultrasonic Imaging*, 20(4):260–74, 1998.

[50] A. Samani, J. Bishop, C. Luginbuhl, and D.B. Plewes. Measuring the elastic modulus of ex vivo small tissue samples. *Physics in Medicine and Biology*, 48:2183–98, 2003.

[51] A. Samani, J. Zubovits, and D.B. Plewes. Elastic moduli of normal and pathological human breast tissues: An inversion technique based investigation of 169 samples. *Physics in Medicine and Biology*, 52(6):1565–76, 2007.

[52] P.S. Wellman, Robert D. Howe, Edward Dalton, and Kenneth A. Kern. Breast tissue stiffness in compression is correlated to histological diagnosis. Technical report, University of Connecticut School of Medicine, 1999.

[53] A. Samani and D.B. Plewes. An inverse problem solution for measuring the elastic modulus of intact ex vivo breast tissue tumours. *Physics in Medicine and Biology*, 52:1247–60, 2007.

[54] J. Ophir, I. Cespedes, H. Ponnekanti, Y. Yazdi, and X. Li. Elastography: A quantitative method for imaging the elasticity of biological tissues. *Ultrasonic Imaging*, 13:111–34, 1991.

[55] Kevin J. Parker, Lawrence S. Taylor, and Sheryl Gracewski. A unified view of imaging the elastic properties of tissue. *The Journal of the Acoustical Society of America*, 117(5):2705–12, 2005.

[56] K.D. Paulsen, P.M. Meaney, and L.C. Gilman, editors. *Alternative Breast Imaging: Four Model-Based Approaches*. Springer, 2005.

[57] J. Ophir, S.K. Alam, B. Garra, F. Kallel, E. Komofagou, T. Krouskop, and T. Varghese. Elastography: Ultrasonic estimation and imaging of the elastic properties of tissues. In *Proceedings of the Institution of Mechanical Engineers*, pages 203–33, 1999.

[58] J. Ophir, F. Kallel, T. Varghese, E. Konofagou, S.K. Alam, T. Krouskop, B. Garra, and R. Righetti. Elastography. *Comtes Rendus de l'Academie des Sciences Series IV Physics*, 2:1193–1212, 2001.

[59] R.M. Lerner, S.R. Huang, and K.J. Parker. "sonoelasticity" images derived from ultrasound signals in mechanically vibrated tissues. *Ultrasound in Medicine and Biology*, 16:231–39, 1990.

[60] F. Lee, J.P. Bronson, R.M. Lerner, K.J. Parker, S-R. Huang, and J.B. Roach. Sonoelastic imaging: Results in in vitro tissue specimens. *Radiology*, 181:237–39, 1990.

[61] R.G. Barr. Clinical applications of a real-time elastography technique in breast imaging. In *Proceeding of the 5th International Conference on the Ultrasonic Measurement and Imaging of Tissue Elasticity*, Utah.

[62] H. Frey. Realtime elastography. a new ultrasound procedure for the reconstruction of tissue elasticity. *Radiologe*, 43(10):850–55, 2003.

[63] J. Bercoff, S. Chaffai, M. Tanter, L. Sandrin, S. Catheline, M. Fink, J.L. Gennisson, and M. Meunier. In vivo breast tumor detection using transient elastography. *Ultrasound in Medicine and Biology*, 29(10):1387–96, 2003.

[64] J. Bercoff, M. Tanter, and M. Fink. Supersonic shear imaging: A new technique for soft tissues elasticity mapping. *IEEE Transactions on Ultrasonics, Ferroelectrics, and Frequency Control*, 51:396–409, 2004.

[65] J.E. Lindop, G.M. Treece, A.H. Gee, and R.W. Prager. 3D elastography using freehand ultrasound. *Ultrasound in Medicine and Biology*, 32(4):529–45, 2006.

[66] S. Park, S.R. Aglyamov, W.G. Scott, and S.Y. Emelianov. Strain imaging using conventional and ultrafast ultrasound imaging: Numerical analysis. *IEEE Transactions on Ultrasonics, Ferroelectrics, and Frequency Control*, 54(5):987–95, 2007.

[67] E. Konofagou, B. Garra, and J. Ophir. Benign and malignant in vivo breast tumor. `http://www.uth.tmc.edu/schools/med/rad/elasto/slides/breastinvivo/images/img001.jpg`, 2008.

[68] P.E. Barbone and J.C. Bamber. Quantitative elasticity imaging: What you can do and cannot be inferred from strain images. *Physics in Medicine and Biology*, 47:2147–64, 2002.

[69] P. Barbone, N. Gokhale, M. Richards, A. Oberai, and M. Doyley. Simultaneous elastic image registration and elastic modulus reconstruction. In *Proceedings of the 2004 International Symposium on Biomedical Imaging: From Nano to Macro*, pages 543–46, 2004.

[70] P.E. Barbone and N. Gokhale. Elastic modulus imaging: On the uniqueness and nonuniqueness of the elastography inverse problem in two dimensions. *Inverse Problems*, 20:283–96, 2004.

[71] M.M. Doyley, S. Srinivasan, S.A. Pendergrass, Z. Wu, and J. Ophir. Comparative evaluation of strain-based and model-based modulus elastography. *Ultrasound in Medicine and Biology*, 31(6):787–802, 2005.

[72] D. B. Plewes, J. Bishop, A. Samani, and J. Sciarretta. Visualization and quantification of breast cancer biomechanical properties with magnetic resonance elastography. *Phys Med Biol*, 45(6):1591–610, 2000.

[73] E.E.W. Van Houten, M.I. Miga, J.B. Weaver, F.E. Kennedy, and K.D. Paulsen. Three-dimensional subzone-based reconstruction algorithm for MR elastography. *Magnetic Resonance in Medicine*, 45(5):827–37, 2001.

[74] E.E.W. Van Houten, M.M. Doyley, F.E. Kennedy, J.B. Weaver, and K.D. Paulsen. Initial in vivo experience with steady-state subzone-based MR elastography of the human breast. *Journal of Magnetic Resonance Imaging*, 17(1):72–85, 2003.

[75] E.E.W. Van Houten, M.M. Doyley, F.E. Kennedy, K.D. Paulsen, and J.B. Weaver. A three parameter mechanical property reconstruction algorithm for MR-based elastic property imaging. *IEEE Transactions on Medical Imaging*, 24(3):311–24, March 2005.

[76] R. Sinkus, J. Lorenzen, D. Schrader, M. Lorenzen, M. Dargatz, and D. Holz. High-resolution tensor MR elastography for breast tumour detection. *Physics in Medicine and Biology*, 45(6):1649–64, 2000.

[77] A. Manduca, T.E. Oliphant, M.A. Dresner, J.F. Greenleaf, and R.L. Ehman. Comparative evaluation of inversion algorithms for magnetic resonance elastography. In *IEEE International Symposium on Biomedical Imaging*, pages 997–1000, 2002.

[78] A. Manduca, D.S. Lake, S.A. Kruse, and R.L. Ehman. Spatio-temporal directional filtering for improved inversion of MR elastography images. *Med Image Anal*, 7(4):465–73, 2003.

[79] R. Sinkus, M. Tanter, T. Xydeas, S. Catheline, J. Bercoff, and M. Fink. Viscoelastic shear properties of in vivo breast lesions measured by MR elastography. *Magnetic Resonance in Medicine*, 23(2):159–65, 2005.

[80] P.E. Barbone and A.A. Oberai. Elastic modulus imaging: Some exact solutions of the compressible elastography inverse problem. *Physics in Medicine and Biology*, 52(6):1577–93, 2007.

[81] Salavat R. Aglyamov, Andrei R. Skovoroda, Hua Xie, Kang Kim, Jonathan M. Rubin, Matthew O'Donnell, Thomas W. Wakefield, Daniel Myers, and Stanislav Y. Emelianov. Model-based reconstructive elasticity imaging using ultrasound. *International Journal of Biomedical Imaging*, 2007.

[82] R.F. Havre, E. Elde, O.H. Gilja, S. Odegaard, G.E. Eide, K. Matre, and L.B. Nesje. Freehand real-time elastography: Impact of scanning parameters on image quality and in vitro intra- and interobserver validations. *Ultrasound in Medicine and Biology*, 2008.

[83] E. Tohno and E. Ueno. Current improvements in breast ultrasound, with a special focus on elastography. *Breast Cancer*, 15(3):200–204, 2008.

[84] Q.L. Zhu, Y.X. Jiang, J.B. Liu, H. Liu, Q. Sun, Q. Dai, and X. Chen. Real-time ultrasound elastography: It's potential use in assessment of breast lesions. *Ultrasound in Medicine and Biology*, 2008.

[85] M.D. McGarry and E.E.W. Van Houten. Use of a Rayleigh damping model in elastography. *Medical and Biological Engineering and Computing*, 2008.

[86] M.A. Green, L.E. Bilston, and R. Sinkus. In vivo brain viscoelastic properties measured by magnetic resonance elastography. *NMR in Biomedicine*, 2008.

[87] H. Wang, J.B. Weaver, M.M. Doyley, F.E. Kennedy, and K.D. Paulsen. Optimized motion estimation for MRE data with reduced motion encodes. *Physics in Medicine and Biology*, 53(8):2181–96, 2008.

[88] K. Uffmann and M.E. Ladd. Actuation systems for MR elastography: design and applications. *IEEE Engineering in Medicine and Biology Magazine*, 27(3):28–34, 2008.

[89] A. Peters. *Digital Image-Based Elasto-Tomography: Mechanical Property Reconstruction from Surface Measured Displacement Data.* PhD thesis, University of Canterbury, Christchurch, New Zealand, 2007.

[90] A. Peters, A. Milsand, J. Rouzé L. Ray, J.G. Chase, and E.E.W. Van Houten. Digital image-based elasto-tomography: Proof of concept studies for surface based mechanical property reconstruction. *JSME International Journal*, 47(4):1117–23, 2004.

[91] M. Tanaka. Applications of the boundary element method to some inverse problems in engineering mechanics. In *Inverse Problems in Engineering: Theory and Practice – 3rd Int. Conference on Inverse Problems in Engineering*, 1999.

[92] 5^{th} International Congress on Computational Mechanics. *Recent Applications of the BEM to some inverse problems in Engineering*, Limassol, June–July 2005.

[93] P.K. Banerjee. *The Boundary Element Methods in Engineering.* McGraw-Hill, second edition, 1981.

[94] S. Babaeizadeh, D.H. Brooks, and D. Isaacson. A 3D boundary element solution to the forward problem of electrical impedance tomography. In *Proceedings of the 26th Annual Conference of the IEEE EMBS*, San Francisco, CA, USA, September 2004.

[95] A.J. Nowak. The boundary elements in inverse thermal problems with phase change. Transactions of the Wessex Institute, 1996.

[96] D. Lesnic, L. Elliott, and D.B. Ingham. Application of the boundary element method to inverse heat conduction problems. *International Journal of Heat and Mass Transfer*, 39(7):1503–17, 1996.

[97] L. Yan, C.-L. Fu, and F.-L. Yang. The method of fundamental solutions for the inverse heat source problem. *Engineering Analysis with Boundary Elements*, 32(3):216–22, 2007.

[98] Bong-Ki Kim and Jeong-Guon Ih. On the reconstruction of the vibro-acoustic field over the surface enclosing an interior space using the boundary element method. *Journal of the Accoustic Society*, 100(5):3003–3016, 1995.

[99] S.-C. Kang and J.-G. Ih. On the accuracy of nearfield pressure by the acoustic boundary element method. *Journal of Sound and Vibration*, 233(2):353–358, 1999.

[100] X. Zhao and S.F. Wu. Reconstruction of vibro-acoustic fields using hybrid nearfield acoustic holography. *Journal of Sound and Vibration*, 282(3):1183–99, 2003.

[101] M. Tanaka, M. Nakamura, and T. Nakano. Application of boundary element method to elastodynamic inverse problems: In case of using dynamic strain responses as additional information. *Transactions of the Japan Society of Mechanical Engineers. C*, 56(530):2583–88, 1990.

[102] T. Burczyński. Applications of BEM in sensitivity analysis and optimization. *Computational Mechanics*, 13(1):29–44, 1993.

[103] T. Burczyński, G. Kuhn, H. Antes, and M. Nowakowski. Boundary element formulation of shape sensitivity analysis for defect identification in free vibration problem. *Engineering Analysis with Boundary Elements*, 19:167–75, 1997.

[104] Guillermo Rus and Rafael Gallego. Boundary integral equation for inclusion and cavity shape sensitivity in harmonic elastodynamics. *Engineering Analysis with Boundary Elements*, 29:77–91, 2005.

[105] V. Mallardo and C. Alessandri. Inverse problems in the presence of inclusions and unilateral constraints: a boundary element approach. *Computational Mechanics*, 26(6):571–81, 2000.

[106] D. S. Schnur and N. Zabaras. Finite element solution of two-dimensional inverse elastic problems using spatial smoothing. *International Journal for Numerical Methods in Engineering*, 30(1):57–75, 1990.

[107] D. S. Schnur and N. Zabaras. An inverse method for determining elastic material properties and a material interface. *International Journal for Numerical Methods in Engineering*, 33(10):2039–57, 1992.

[108] H.T. Liu, L.Z. Sun, and G. Wang. Tomography-based 3D anisotropic elastography using boundary measurements. *IEEE Transactions in Medical Imaging*, 24(10):1323–33, 2005.

[109] L. Marin, L. Elliott, D. B. Ingham, and D. Lesnic. Parameter identification in isotropic linear elasticity using the boundary element method. *Engineering Analysis with Boundary Elements*, 28(3):221–33, 2004.

[110] Zhongyan Lin. On the determination of radially dependent λ coefficients. *SIAM Journal on Applied Mathematics*, 58(3):875–903, 1998.

[111] G. Nakamura and G. Uhlmann. Inverse problems at the boundary for an elastic medium. *SIAM Journal on Mathematical Analysis*, 26(2):263–279, 1995.

[112] M. Ikehata. The linearization of the Dirichlet to Neumann map in anisotropic plate theory. *Inverse Problems*, 11:165–81, 1995.

[113] G. Nakamura and K. Tanuma. A nonuniqueness theorem for an inverse boundary value problem in elasticity. *SIAM Journal on Applied Mathematics*, 56(2):602–610, 1996.

[114] L. Huang, X. Sun, Y. Liu, and Z. Cen. Parameter identification for two-dimensional orthotropic material bodies by the boundary element method. *Engineering Analysis with Boundary Elements*, 28(2):109–21, 2003.

[115] T. Lauwagie, H. Sol, G. Roebben, W. Heylen, S. Yinming, and O. Van Der Biest. Mixed numerical-experimental identification of elastic properties of orthotropic metal plates. *NDT & E International*, 36(7):487–95, 2003.

[116] P. Heyliger, P. Ugander, and H. Ledbetter. Anisotropic elastic constants: Measurement by impact resonance. *Journal of Materials in Civil Engineering*, 13(5):356–63, 2001.

[117] R.G. Brown, J.G. Chase, and E.E.W. Van Houten. Discrete colour-based euclidean-invariant signatures for feature tracking in a diet-based cancer-screening system. In *Proceedings of the SPIE International Conference on Medical Imaging*, CA, USA, February 2007. SPIE.

[118] A. Peters, H.-U. Berger, J.G. Chase, and E.E.W. Van Houten. Digital image-based elasto-tomography: Nonlinear mechanical property reconstruction of homogeneous gelatine phantoms. *International Journal of Information and System Sciences*, 2(4):512–21, 2006.

[119] A. Peters, J.G. Chase, and E.E.W. Van Houten. Digital image elasto-tomography: Mechanical property estimation of silicone phantoms. *Medical and Biological Engineering and Computing*, 46(3):205–212, March 2008.

[120] Richard Brown. *Three-dimensional motion capture for the DIET breast cancer imaging system.* PhD thesis, University of Canterbury, Christchurch, New Zealand, 2008.

[121] H. Helmholtz. Theorie der Luftschwingungen in Röhren mit offenen Enden. *Reine Angewandte Mathematik*, 57:1 – 72, 1860.

[122] G. Kirchhoff. Zur Theorie der Lichtstrahlen. *Annalen der Physik*, 18:663 – 695, 1883.

[123] C. Somigliana. Sulle equazioni dell' elasticitá. *Ann. Mat. Serie II*, 17:37 – 64, 1889 – 1890.

[124] I. Fredholm. Sur une classe d'equations fonctionelles. *Acta Mathematica*, 27:365 – 390, 1903.

[125] R.P. Banaugh and W. Goldsmith. Diffraction of steady acoustic waves by surfaces of arbitrary shape. *Journal of the Acoustical Society of America*, 35(10):1590–1601, 1963.

[126] R.P. Banaugh and W. Goldsmith. Diffraction of steady elastic waves by surfaces of arbitrary shape. *Journal of Applied Mechanics*, 30:589–97, 1963.

[127] J. C. Lachat and J. O. Watson. Effective numerical treatment of boundary integral equations: a formulation for three-dimensional elasto-statics. *International Journal for Numerical Methods in Engineering*, 10:991–1005, 1976.

[128] J.O. Watson. Boundary elements from 1960 to the present day. *Journal of Boundary Elements*, 1(1):34–46, 2003.

[129] G. Beer. *Programming the Boundary Element Method - An Introduction for Engineers*. Wiley, 2001.

[130] W. Thomson (Lord Kelvin). A note on the integration of the equations of equilibrium of an elastic solid. *Cambridge and Dublin Mathematical Journal*, 1848.

[131] S. Ahmad. *Linear and Nonlinear Dynamic Analysis by the Boundary Element Method*. PhD thesis, State University of New York at Buffalo, NY, USA, 1986.

[132] M. Abramowitz and I.A. Stegun. *Handbook of Mathematical Functions with Formulas, Graphs, and Mathematical Tables*. Dover, New York, ninth Dover printing, tenth GPO printing edition, 1964.

[133] E. Trefftz. Ein Gegenstück zum Ritzschen Verfahren. In *Proceedings of the 2^{nd} Congress in Aplied Mechanics*, page 131, Zürich, 1926.

[134] G. Beer and J.O. Watson. *Introduction to Finite and Boundary Element Methods for Engineers*. Wiley, Chichester, 1995.

[135] C.A. Brebbia and J. Dominguez. *Boundary Elements – An Introductory Course*. McGraw-Hill, 1992.

[136] K.-J. Bathe. *Finite-Elemente-Methoden*. Springer Verlag, Berlin, 2002.

[137] O.C. Zienkiewicz and R.L. Taylor. *The Finite Element Method I*, volume Volume 1: The Basis. Butterworth Heinemann, 5th edition, 2000.

[138] A.H. Stroud and D. Secrest. *Gaussian Quadrature Formulas*. Prentice-Hall, Englewood Cliffs, NJ, 1966.

[139] G.D. Manolis and D.E. Beskos. *Boundary Element Methods in Elastodynamics*. Pentice-Hall, 1988.

[140] M. Guigiani. Computing principal value integrals in 3d bem for time-harmonic elastodynamics – a direct approach. *Communications in applied numerical methods*, 8:141–149, 1992.

[141] A. Sommerfeld. *Partial Differential Equations in Physics*. Academic Press, New York, 1949.

[142] O.C. Zienkiewicz and R.L. Taylor. *The Finite Element Method II*, volume Volume 2: Solid Mechanics. Butterworth Heinemann, 2000.

[143] J. Nocedal and S.J. Wright. *Numerical Optimization*. Springer, 1999.

[144] A. Peters, S. Wortmann, R. Elliott, M. Staiger, J.G. Chase, and E.E.W. Van Houten. Digital image-based elasto-tomography: First experiments in surface based mechanical property estimation of gelatine phantoms. *JSME International Journal*, 48(4):562–69, 2005.

[145] J. Lorenzen, R. Sinkus, M. Biesterfeldt, and G. Adam. Menstrual-cycle dependence of breast parenchyma elasticity: estimation with magnetic resonance elastography of breast tissue during the menstrual cycle. *Investigative Radiology*, 38(4):236–40, 2003.

[146] R. Horst and P.M. Pardalos. *Introduction to Global Optimization*. Kluwer Academic Publishers, Dordrecht, 1995.

[147] P. Spellucci. *Numerische Verfahren der Nichtlinearen Optimierung*. Birkhäuser Verlag, 1993.

[148] D.A. Coley. *An Introduction to Genetic Algorithms for Scientists and Engineers*. World Scietific, River Edge, N.J., 1999.

[149] A. Neumeier. Complete search in continuous global optimization and constraint satisfaction. *Acta Numerica*, 2004.

[150] P. Spellucci. Einführung in die Stetige Optimierung – Kurzskript zur Vorlesung. Darmstadt University of Technology, 2004.

[151] J.R. Shewchuck. An introduction to the conjugate gradient method without the agonizing pain. `http://www.cs.cmu.edu/~jrs/jrspapers.html`, Carnegie Mellon University, Pittsburgh, PA, 1994.

[152] A.N. Tikhonov and V.Y. Arsenin. *Solutions of ill-posed problems*. Wiley, New York, 1977.

[153] H.W. Engl, M. Hanke, and A. Neubauer. *Regularization of Inverse Problems*. Kluwer Academic Publishers, Dordrecht, 2000.

[154] A. Hartov, N.K. Soni, and Keith D Paulsen. Variation in breast eit measurements due to menstrual cycle. *Physiological Measurements*, 25:295–299, 2004.